THE EVALUATION OF NARCCAP REGIONAL CLIMATE MODELS USING THE NORTH AMERICAN REGIONAL REANALYSIS

By

Adam Blake Cinderich

A THESIS

Submitted to
Michigan State University
in partial fulfillment of the requirements
for the degree of

MASTER OF SCIENCE

Geography

2012

ABSTRACT

THE EVALUATION OF NARCCAP REGIONAL CLIMATE MODELS USING THE NORTH AMERICAN REGIONAL REANALYSIS

By

Adam Blake Cinderich

Understanding the extent of future climate change is highly dependent on the use of climate models to assess the degree and rate of change. More recently, dynamic downscaling has been employed with the use of regional climate models (RCMs) as an alternative to statistical downscaling. However, while RCMs provide a much finer resolution, they have still been shown to exhibit bias within their simulations. In order to understand the biases and uncertainties that exist within the RCMs, simulations of current climate must first be evaluated using past climatic data. In this study, a comparative analysis examining mean surface-air temperature and daily accumulated precipitation differences between RCM projections from the North American Regional Climate Change Assessment Program (NARCCAP) and reanalysis data from the North American Regional Reanalysis (NARR) is performed for the contiguous United States (CONUS). NCEP-driven RCM runs from 1981-2000 were validated to discern the biases that exist solely due to the RCM. To evaluate RCM simulations at a regional level, the domain is then further divided into 5 sub-regions: Northeast (NE), Southeast (SE), Northwest (NW), Southwest (SW) and the Great Lakes Region (GLR). The Great Lakes Region was chosen in addition to the four main sub-regions as future climate change is expected to impact future water resources and agricultural production within this region. Results indicate that RCM performance varies from region to region and season to season.

To my loving wife, parents, grandparents, and siblings who gave me the confidence, support and education I needed to achieve this goal.

ACKNOWLEDGEMENTS

I would like to thank my advisor Dr. Sharon Zhong for her teachings, guidance and review of this thesis; Dr. Joseph J. Charney for his assistance with data management, computer programming, and GrADS; Xindi Bian for his assistance with data management and processing; Dr. Julie Winkler, Dr. Lifeng Luo, and Dr. Jeff Andresen for their constructive edits, and the Research Work Unit NRS-06 of the USDA Forest Service for providing the computer server resources needed to complete this work. I would also like to extend thanks to my fellow graduate students, especially David Young, Perdinan, Jovanka Nikolic and Kristin Adams for the camaraderie that was formed over the past 2 years. This research was partially funded by the USDA Forest Service through Joint Venture Agreement with Michigan State University 02-JV-11231300-084.

TABLE OF CONTENTS

LIST OF TABLES.	ix
LIST OF FIGURES	xii
LIST OF EQUATIONS.	xx
CHAPTER I	
INTRODUCTION	1
CHAPTER II	
REVIEW OF THE LITERATURE.	
a. Regional climate models as a tool for climate change assessment	
b. Validation of regional climate models	
1. Validations in the Arctic	
2. Validations in Asia	
3. Validations in Europe	
4. Validations in North America.	
c. Climate change impacts of the Great Lakes region	14
CHAPTER III	
METHODOLOGY	17
a. Study area	17
b. Data sources	18
1. NARCCAP	18
2. NARR	22
c. Data Analysis	23
1. Spatial plots	
2. Annual cycles	
3. Statistics	24
3.1 Bias	25
3.2 Mean absolute error	26
3.3 Root mean square error	26
3.4 Spatial correlation	
CHAPTER IV	
RESULTS	27
a. Contiguous United States	
1. Spatial distribution of mean surface-air temperatures	
1.1 Spring	
1.2 Summer	
1.3 Autumn.	
1.4 Winter	
1.5 Summary	

	2.	Spatial distribution of mean surface-air temperature differences	33
		2.1 Spring	33
		2.2 Summer	35
		2.3 Autumn	36
		2.4 Winter	
		2.5 Summary	
	3.	Statistics and annual cycle of mean surface-air temperature	
	4.	Spatial distribution of daily accumulated precipitation	
	т.	4.1 Spring	
		4.1 Spring	
		4.3 Autumn	
		4.4 Winter	
	_	4.5 Summary	
	5.	Spatial distribution of daily accumulated precipitation differences	
		5.1 Spring	
		5.2 Summer	
		5.3 Autumn	51
		5.4 Winter	54
		5.5 Summary	56
	6.	Statistics and annual cycle of daily accumulated precipitation	57
b.		east	
		Statistics and annual cycle of mean surface-air temperature	
		Statistics and annual cycle of daily accumulated precipitation	
C		east	
С.	1	Statistics and annual cycle of mean surface-air temperature	
	1. 2	Statistics and annual cycle of daily accumulated precipitation	
a		, , , , , , , , , , , , , , , , , , , ,	
a.	NOTHIN	west	
	1.	Statistics and annual cycle of mean surface-air temperature	
		Statistics and annual cycle of daily accumulated precipitation	
e.	South	west	
	1.	Statistics and annual cycle of mean surface-air temperature	
	2.	Statistics and annual cycle of daily accumulated precipitation	63
f.	Great 1	Lakes Region	66
	1.	Spatial distribution of mean surface-air temperature	65
		1.1 Spring	65
		1.2 Summer	67
		1.3 Autumn	69
		1.4 Winter	71
		1.5 Summary	
	2.	Spatial distribution of mean surface-air temperature differences	
	2.	2.1 Spring	
		2.1 Spring 2.2 Summer	
		2.3 Autumn.	
		2.5 Autumn	
	2	2.5 Summary	
	3.	Statistics and annual cycle of mean surface-air temperature	84

4	. Spatial distribution of daily accumulated precipitation	
	4.1 Spring	84
	4.2 Summer	86
	4.3 Autumn	88
	4.4 Winter	90
	4.5 Summary	92
5	. Spatial distribution of daily accumulated precipitation differences	
	5.1 Spring	
	5.2 Summer	
	5.3 Autumn	97
	5.4 Winter	99
	5.5 Summary	101
6	. Statistics and annual cycle of daily accumulated precipitation	102
CHAPTER	V	
	IONS	103
	mary	
	Contiguous United States.	
	1.1 Mean surface-air temperature	
	1.2 Daily accumulated precipitation	
2	2. Great Lakes Region	
	2.1 Mean surface-air temperature	
	2.2 Daily accumulated precipitation	
b. Limi	tations and Future Research	
A DDENIDIN		
APPENDIX Spatiai di	A LOTS	111
	iguous United States Temperatures	
	. Monthly mean surface-air temperature	
2	Monthly mean surface-air temperature differences.	
h Conti	iguous United States Precipitation.	
	Daily accumulated precipitation.	
	Daily accumulated precipitation differences	
	Lakes Region Temperatures.	
	. Monthly mean surface-air temperature	
	Monthly mean surface-air temperature differences	
	Lakes Region Precipitation	
	Daily accumulated precipitation	
	Daily accumulated precipitation differences	
APPENDIX		200
ANNUAL C		
	iguous United States	
	neast	
	neast	212

e.	Southwest		
f.		Lakes Region	
		Č	
APPI	ENDIX	C	
STA	FISTICS	S	215
a.	Contig	guous United States	
	1.	Monthly mean surface-air temperature	216
		Daily accumulated precipitation	
b.	North	east	220
		Monthly mean surface-air temperature	
		Daily accumulated precipitation	
c.		east	
		Monthly mean surface-air temperature	
		Daily accumulated precipitation	
d.		west	
		Monthly mean surface-air temperature	
		Daily accumulated precipitation	
e.		west	
		Monthly mean surface-air temperature	
		Daily accumulated precipitation	
f.		Lakes Region	
		Monthly mean surface-air temperature	
		Daily accumulated precipitation	
		2 m², m²	
DEE	EDENIC	rec	240

LIST OF TABLES

Table 1.	NARCCAP-RCM characteristics (NCAR 2009)	20
Table C.1.	Monthly mean surface-air temperature bias for the CONUS domain	.216
Table C.2.	MAE for monthly mean surface-air temperatures for the CONUS domain	.216
Table C.3.	RMSE for monthly mean surface-air temperatures for the CONUS domain	.217
Table C.4.	Monthly mean surface-air temperature correlations between each RCM and NARR for the CONUS domain.	.217
Table C.5.	Daily accumulated precipitation bias for the CONUS domain	.218
Table C.6.	MAE for daily accumulated precipitation for the CONUS domain	.218
Table C.7.	RMSE for daily accumulated precipitation for the CONUS domain	.219
Table C.8.	Daily accumulated precipitation correlations between each RCM and NARR the CONUS domain.	
Table C.9.	Monthly mean surface-air temperature bias for the NE domain	220
Table C.10.	MAE for monthly mean surface-air temperatures for the NE domain	.220
Table C.11.	RMSE for monthly mean surface-air temperatures for the NE domain	.221
Table C.12.	Monthly mean surface-air temperature correlations between each RCM and NARR for the NE domain	221
Table C.13.	Daily accumulated precipitation bias for the NE domain	.222
Table C.14.	MAE for daily accumulated precipitation for the NE domain	222
Table C.15.	RMSE for daily accumulated precipitation for the NE domain	223
Table C.16.	Daily accumulated precipitation correlations between each RCM and NARR the NE domain.	
Table C.17.	Monthly mean surface-air temperature bias for the SE domain	.224
Table C.18.	MAE for monthly mean surface-air temperatures for the SE domain	.224
Table C.19.	RMSE for monthly mean surface-air temperatures for the SE domain	225

Table C.20.	Monthly mean surface-air temperature correlations between each RCM and NARR for the SE domain	.225
Table C.21.	Daily accumulated precipitation bias for the SE domain	226
Table C.22.	MAE for daily accumulated precipitation for the SE domain	226
Table C.23.	RMSE for daily accumulated precipitation for the SE domain	227
Table C.24.	Daily accumulated precipitation correlations between each RCM and NARR the SE domain.	for 227
Table C.25.	Monthly mean surface-air temperature bias for the NW domain	.228
Table C.26.	MAE for monthly mean surface-air temperatures for the NW domain	228
Table C.27.	RMSE for monthly mean surface-air temperatures for the NW domain	229
Table C.28.	Monthly mean surface-air temperature correlations between each RCM and NARR for the NW domain.	229
Table C.29.	Daily accumulated precipitation bias for the NW domain	230
Table C.30.	MAE for daily accumulated precipitation for the NW domain	230
Table C.31.	RMSE for daily accumulated precipitation for the NW domain	231
Table C.32.	Daily accumulated precipitation correlations between each RCM and NARR the NW domain.	for 231
Table C.33.	Monthly mean surface-air temperature bias for the SW domain	232
Table C.34.	MAE for monthly mean surface-air temperatures for the SW domain	232
Table C.35.	RMSE for monthly mean surface-air temperatures for the SW domain	233
Table C.36.	Monthly mean surface-air temperature correlations between each RCM and NARR for the SW domain.	233
Table C.37.	Daily accumulated precipitation bias for the SW domain	234
Table C.38.	MAE for daily accumulated precipitation for the SW domain	234
Table C.39.	RMSE for daily accumulated precipitation for the SW domain	235

Table C.40.	Daily accumulated precipitation correlations between each RCM and NARR the SW domain.	for 235
Table C.41.	Monthly mean surface-air temperature bias for the GLR domain	236
Table C.42.	MAE for monthly mean surface-air temperatures for the GLR domain	236
Table C.43.	RMSE for monthly mean surface-air temperatures for the GLR domain	237
Table C.44.	Monthly mean surface-air temperature correlations between each RCM and NARR for the GLR domain	237
Table C.45.	Daily accumulated precipitation bias for the GLR domain	.238
Table C.46.	MAE for daily accumulated precipitation for the GLR domain	238
Table C.47.	RMSE for daily accumulated precipitation for the GLR domain	239
Table C.48.	Daily accumulated precipitation correlations between each RCM and NARR the GLR domain.	for 239

LIST OF FIGURES

Fig. 1.	Processes included within, and the structure of, the CESM (Adapted from: University Corporation for Atmospheric Research 2012)5
Fig. 2.	Six model domains including the: (a) CONUS, (b) NE, (c) SE, (d) NW, (e) SW, and (f) GLR
Fig. 3.	NARCCAP-RCM domains (NCAR 2009)19
Fig. 4.	NARR domain and its topography at a spatial resolution of 32-km (Mesinger et al 2006)
Fig. A.1.1.1.	Mean January surface-air temperatures from (a) NARR, (b) CRCM, (c) ECP2, (d) HRM3, (e) MM5I, and (f) WRFG for the CONUS domain
Fig. A.1.1.2.	Mean February surface-air temperatures from (a) NARR, (b) CRCM, (c) ECP2, (d) HRM3, (e) MM5I, and (f) WRFG for the CONUS domain113
Fig. A.1.1.3.	Mean March surface-air temperatures from (a) NARR, (b) CRCM, (c) ECP2, (d) HRM3, (e) MM5I, and (f) WRFG for the CONUS domain
Fig. A.1.1.4.	Mean April surface-air temperatures from (a) NARR, (b) CRCM, (c) ECP2, (d) HRM3, (e) MM5I, and (f) WRFG for the CONUS domain
Fig. A.1.1.5.	Mean May surface-air temperatures from (a) NARR, (b) CRCM, (c) ECP2, (d) HRM3, (e) MM5I, and (f) WRFG for the CONUS domain
Fig. A.1.1.6.	Mean June surface-air temperatures from (a) NARR, (b) CRCM, (c) ECP2, (d) HRM3, (e) MM5I, and (f) WRFG for the CONUS domain
Fig. A.1.1.7.	Mean July surface-air temperatures from (a) NARR, (b) CRCM, (c) ECP2, (d) HRM3, (e) MM5I, and (f) WRFG for the CONUS domain
Fig. A.1.1.8.	Mean August surface-air temperatures from (a) NARR, (b) CRCM, (c) ECP2, (d) HRM3, (e) MM5I, and (f) WRFG for the CONUS domain
Fig. A.1.1.9.	Mean September surface-air temperatures from (a) NARR, (b) CRCM, (c) ECP2, (d) HRM3, (e) MM5I, and (f) WRFG for the CONUS domain120
Fig. A.1.1.10.	Mean October surface-air temperatures from (a) NARR, (b) CRCM, (c) ECP2, (d) HRM3, (e) MM5I, and (f) WRFG for the CONUS domain
Fig. A.1.1.11.	Mean November surface-air temperatures from (a) NARR, (b) CRCM, (c) ECP2, (d) HRM3, (e) MM5I, and (f) WRFG for the CONUS domain122

Fig. A.1.1.12.	Mean December surface-air temperatures from (a) NARR, (b) CRCM, (c) ECP2, (d) HRM3, (e) MM5I, and (f) WRFG for the CONUS domain
Fig. A.1.2.1.	January mean surface-air temperature differences between (a) CRCM, (b) ECP2, (c) HRM3, (d) MM5I, (e) WRFG, and NARR for the CONUS domain124
Fig. A.1.2.2.	February mean surface-air temperature differences between (a) CRCM, (b) ECP2, (c) HRM3, (d) MM5I, (e) WRFG, and NARR for the CONUS domain125
Fig. A.1.2.3.	March mean surface-air temperature differences between (a) CRCM, (b) ECP2, (c) HRM3, (d) MM5I, (e) WRFG, and NARR for the CONUS domain126
Fig. A.1.2.4.	April mean surface-air temperature differences between (a) CRCM, (b) ECP2, (c) HRM3, (d) MM5I, (e) WRFG, and NARR for the CONUS domain127
Fig. A.1.2.5.	May mean surface-air temperature differences between (a) CRCM, (b) ECP2, (c) HRM3, (d) MM5I, (e) WRFG, and NARR for the CONUS domain128
Fig. A.1.2.6.	June mean surface-air temperature differences between (a) CRCM, (b) ECP2, (c) HRM3, (d) MM5I, (e) WRFG, and NARR for the CONUS domain129
Fig. A.1.2.7.	July mean surface-air temperature differences between (a) CRCM, (b) ECP2, (c) HRM3, (d) MM5I, (e) WRFG, and NARR for the CONUS domain
Fig. A.1.2.8.	August mean surface-air temperature differences between (a) CRCM, (b) ECP2, (c) HRM3, (d) MM5I, (e) WRFG, and NARR for the CONUS domain131
Fig. A.1.2.9.	September mean surface-air temperature differences between (a) CRCM, (b) ECP2, (c) HRM3, (d) MM5I, (e) WRFG, and NARR for the CONUS domain132
Fig. A.1.2.10.	October mean surface-air temperature differences between (a) CRCM, (b) ECP2, (c) HRM3, (d) MM5I, (e) WRFG, and NARR for the CONUS domain133
Fig. A.1.2.11.	November mean surface-air temperature differences between (a) CRCM, (b) ECP2, (c) HRM3, (d) MM5I, (e) WRFG, and NARR for the CONUS domain134
Fig. A.1.2.12.	December mean surface-air temperature differences between (a) CRCM, (b) ECP2, (c) HRM3, (d) MM5I, (e) WRFG, and NARR for the CONUS domain135
Fig. A.2.1.1.	January daily accumulated precipitation from (a) NARR, (b) CRCM, (c) ECP2, (d) HRM3, (e) MM5I, and (f) WRFG for the CONUS domain
Fig. A.2.1.2.	February daily accumulated precipitation from (a) NARR, (b) CRCM, (c) ECP2, (d) HRM3, (e) MM5I, and (f) WRFG for the CONUS domain137
Fig. A.2.1.3.	March daily accumulated precipitation from (a) NARR, (b) CRCM, (c) ECP2, (d) HRM3, (e) MM5I, and (f) WRFG for the CONUS domain

Fig. A.2.1.4.	April daily accumulated precipitation from (a) NARR, (b) CRCM, (c) ECP2, (d) HRM3, (e) MM5I, and (f) WRFG for the CONUS domain
Fig. A.2.1.5.	May daily accumulated precipitation from (a) NARR, (b) CRCM, (c) ECP2, (d) HRM3, (e) MM5I, and (f) WRFG for the CONUS domain
Fig. A.2.1.6.	June daily accumulated precipitation from (a) NARR, (b) CRCM, (c) ECP2, (d) HRM3, (e) MM5I, and (f) WRFG for the CONUS domain
Fig. A.2.1.7.	July daily accumulated precipitation from (a) NARR, (b) CRCM, (c) ECP2, (d) HRM3, (e) MM5I, and (f) WRFG for the CONUS domain
Fig. A.2.1.8.	August daily accumulated precipitation from (a) NARR, (b) CRCM, (c) ECP2, (d) HRM3, (e) MM5I, and (f) WRFG for the CONUS domain
Fig. A.2.1.9.	September daily accumulated precipitation from (a) NARR, (b) CRCM, (c) ECP2 (d) HRM3, (e) MM5I, and (f) WRFG for the CONUS domain144
Fig. A.2.1.10.	October daily accumulated precipitation from (a) NARR, (b) CRCM, (c) ECP2, (d) HRM3, (e) MM5I, and (f) WRFG for the CONUS domain145
Fig. A.2.1.11.	November daily accumulated precipitation from (a) NARR, (b) CRCM, (c) ECP2 (d) HRM3, (e) MM5I, and (f) WRFG for the CONUS domain146
Fig. A.2.1.12.	December daily accumulated precipitation from (a) NARR, (b) CRCM, (c) ECP2, (d) HRM3, (e) MM5I, and (f) WRFG for the CONUS domain147
Fig. A.2.2.1.	January daily accumulated precipitation differences between (a) CRCM, (b) ECP2, (c) HRM3, (d) MM5I, and (e) WRFG, and NARR for the CONUS domain.
Fig. A.2.2.2.	February daily accumulated precipitation differences between (a) CRCM, (b) ECP2, (c) HRM3, (d) MM5I, and (e) WRFG, and NARR for the CONUS domain
Fig. A.2.2.3.	March daily accumulated precipitation differences between (a) CRCM, (b) ECP2, (c) HRM3, (d) MM5I, and (e) WRFG, and NARR for the CONUS domain150
Fig. A.2.2.4.	April daily accumulated precipitation differences between (a) CRCM, (b) ECP2, (c) HRM3, (d) MM5I, and (e) WRFG, and NARR for the CONUS domain151
Fig. A.2.2.5.	May daily accumulated precipitation differences between (a) CRCM, (b) ECP2, (c) HRM3, (d) MM5I, and (e) WRFG, and NARR for the CONUS domain152
Fig. A.2.2.6.	June daily accumulated precipitation differences between (a) CRCM, (b) ECP2, (c) HRM3, (d) MM5I, and (e) WRFG, and NARR for the CONUS domain153

Fig. A.2.2.7.	July daily accumulated precipitation differences between (a) CRCM, (b) ECP2, (c) HRM3, (d) MM5I, and (e) WRFG, and NARR for the CONUS domain154
Fig. A.2.2.8.	August daily accumulated precipitation differences between (a) CRCM, (b) ECP2, (c) HRM3, (d) MM5I, and (e) WRFG, and NARR for the CONUS domain
Fig. A.2.2.9.	September daily accumulated precipitation differences between (a) CRCM, (b) ECP2, (c) HRM3, (d) MM5I, and (e) WRFG, and NARR for the CONUS domain
Fig. A.2.2.10.	October daily accumulated precipitation differences between (a) CRCM, (b) ECP2, (c) HRM3, (d) MM5I, and (e) WRFG, and NARR for the CONUS domain
Fig. A.2.2.11.	November daily accumulated precipitation differences between (a) CRCM, (b) ECP2, (c) HRM3, (d) MM5I, and (e) WRFG, and NARR for the CONUS domain
Fig. A.2.2.12.	December daily accumulated precipitation differences between (a) CRCM, (b) ECP2, (c) HRM3, (d) MM5I, and (e) WRFG, and NARR for the CONUS domain
Fig. A.3.1.1.	Mean January surface-air temperatures from (a) NARR, (b) CRCM, (c) ECP2, (d) HRM3, (e) MM5I, and (f) WRFG for the GLR domain
Fig. A.3.1.2.	Mean February surface-air temperatures from (a) NARR, (b) CRCM, (c) ECP2, (d) HRM3, (e) MM5I, and (f) WRFG for the GLR domain
Fig. A.3.1.3.	Mean March surface-air temperatures from (a) NARR, (b) CRCM, (c) ECP2, (d) HRM3, (e) MM5I, and (f) WRFG for the GLR domain
Fig. A.3.1.4.	Mean April surface-air temperatures from (a) NARR, (b) CRCM, (c) ECP2, (d) HRM3, (e) MM5I, and (f) WRFG for the GLR domain
Fig. A.3.1.5.	Mean May surface-air temperatures from (a) NARR, (b) CRCM, (c) ECP2, (d) HRM3, (e) MM5I, and (f) WRFG for the GLR domain
Fig. A.3.1.6.	Mean June surface-air temperatures from (a) NARR, (b) CRCM, (c) ECP2, (d) HRM3, (e) MM5I, and (f) WRFG for the GLR domain
Fig. A.3.1.7.	Mean July surface-air temperatures from (a) NARR, (b) CRCM, (c) ECP2, (d) HRM3, (e) MM5I, and (f) WRFG for the GLR domain
Fig. A.3.1.8.	Mean August surface-air temperatures from (a) NARR, (b) CRCM, (c) ECP2, (d) HRM3, (e) MM5I, and (f) WRFG for the GLR domain

Fig. A.3.1.9.	Mean September surface-air temperatures from (a) NARR, (b) CRCM, (c) ECP2, (d) HRM3, (e) MM5I, and (f) WRFG for the GLR domain
Fig. A.3.1.10.	Mean October surface-air temperatures from (a) NARR, (b) CRCM, (c) ECP2, (d) HRM3, (e) MM5I, and (f) WRFG for the GLR domain
Fig. A.3.1.11.	Mean November surface-air temperatures from (a) NARR, (b) CRCM, (c) ECP2, (d) HRM3, (e) MM5I, and (f) WRFG for the GLR domain
Fig. A.3.1.12.	Mean December surface-air temperatures from (a) NARR, (b) CRCM, (c) ECP2, (d) HRM3, (e) MM5I, and (f) WRFG for the GLR domain
Fig. A.3.2.1.	January mean surface-air temperature differences between (a) CRCM, (b) ECP2, (c) HRM3, (d) MM5I, (e) WRFG, and NARR for the GLR domain
Fig. A.3.2.2.	February mean surface-air temperature differences between (a) CRCM, (b) ECP2, (c) HRM3, (d) MM5I, (e) WRFG, and NARR for the GLR domain
Fig. A.3.2.3.	March mean surface-air temperature differences between (a) CRCM, (b) ECP2, (c) HRM3, (d) MM5I, (e) WRFG, and NARR for the GLR domain
Fig. A.3.2.4.	April mean surface-air temperature differences between (a) CRCM, (b) ECP2, (c) HRM3, (d) MM5I, (e) WRFG, and NARR for the GLR domain
Fig. A.3.2.5.	May mean surface-air temperature differences between (a) CRCM, (b) ECP2, (c) HRM3, (d) MM5I, (e) WRFG, and NARR for the GLR domain
Fig. A.3.2.6.	June mean surface-air temperature differences between (a) CRCM, (b) ECP2, (c) HRM3, (d) MM5I, (e) WRFG, and NARR for the GLR domain
Fig. A.3.2.7.	July mean surface-air temperature differences between (a) CRCM, (b) ECP2, (c) HRM3, (d) MM5I, (e) WRFG, and NARR for the GLR domain
Fig. A.3.2.8.	August mean surface-air temperature differences between (a) CRCM, (b) ECP2, (c) HRM3, (d) MM5I, (e) WRFG, and NARR for the GLR domain
Fig. A.3.2.9.	September mean surface-air temperature differences between (a) CRCM, (b) ECP2, (c) HRM3, (d) MM5I, (e) WRFG, and NARR for the GLR domain180
Fig. A.3.2.10.	October mean surface-air temperature differences between (a) CRCM, (b) ECP2, (c) HRM3, (d) MM5I, (e) WRFG, and NARR for the GLR domain181
Fig. A.3.2.11.	November mean surface-air temperature differences between (a) CRCM, (b) ECP2, (c) HRM3, (d) MM5I, (e) WRFG, and NARR for the GLR domain182
Fig. A.3.2.12.	December mean surface-air temperature differences between (a) CRCM, (b) ECP2, (c) HRM3, (d) MM5I, (e) WRFG, and NARR for the GLR domain183

Fig. A.4.1.1.	January daily accumulated precipitation from (a) NARR, (b) CRCM, (c) ECP2, (d) HRM3, (e) MM5I, and (f) WRFG for the GLR domain
Fig. A.4.1.2.	February daily accumulated precipitation from (a) NARR, (b) CRCM, (c) ECP2, (d) HRM3, (e) MM5I, and (f) WRFG for the GLR domain
Fig. A.4.1.3.	March daily accumulated precipitation from (a) NARR, (b) CRCM, (c) ECP2, (d) HRM3, (e) MM5I, and (f) WRFG for the GLR domain
Fig. A.4.1.4.	April daily accumulated precipitation from (a) NARR, (b) CRCM, (c) ECP2, (d) HRM3, (e) MM5I, and (f) WRFG for the GLR domain
Fig. A.4.1.5.	May daily accumulated precipitation from (a) NARR, (b) CRCM, (c) ECP2, (d) HRM3, (e) MM5I, and (f) WRFG for the GLR domain
Fig. A.4.1.6.	June daily accumulated precipitation from (a) NARR, (b) CRCM, (c) ECP2, (d) HRM3, (e) MM5I, and (f) WRFG for the GLR domain
Fig. A.4.1.7.	July daily accumulated precipitation from (a) NARR, (b) CRCM, (c) ECP2, (d) HRM3, (e) MM5I, and (f) WRFG for the GLR domain
Fig. A.4.1.8.	August daily accumulated precipitation from (a) NARR, (b) CRCM, (c) ECP2, (d) HRM3, (e) MM5I, and (f) WRFG for the GLR domain
Fig. A.4.1.9.	September daily accumulated precipitation from (a) NARR, (b) CRCM, (c) ECP2, (d) HRM3, (e) MM5I, and (f) WRFG for the GLR domain192
Fig. A.4.1.10.	October daily accumulated precipitation from (a) NARR, (b) CRCM, (c) ECP2, (d) HRM3, (e) MM5I, and (f) WRFG for the GLR domain
Fig. A.4.1.11.	November daily accumulated precipitation from (a) NARR, (b) CRCM, (c) ECP2, (d) HRM3, (e) MM5I, and (f) WRFG for the GLR domain194
Fig. A.4.1.12.	December daily accumulated precipitation from (a) NARR, (b) CRCM, (c) ECP2, (d) HRM3, (e) MM5I, and (f) WRFG for the GLR domain195
Fig. A.4.2.1.	January daily accumulated precipitation differences between (a) CRCM, (b) ECP2, (c) HRM3, (d) MM5I, and (e) WRFG, and NARR for the GLR domain.
Fig. A.4.2.2.	February daily accumulated precipitation differences between (a) CRCM, (b) ECP2, (c) HRM3, (d) MM5I, and (e) WRFG, and NARR for the GLR domain
Fig. A.4.2.3.	March daily accumulated precipitation differences between (a) CRCM, (b) ECP2, (c) HRM3, (d) MM5I, and (e) WRFG, and NARR for the GLR domain198

Fig.	A.4.2.4.	April daily accumulated precipitation differences between (a) CRCM, (b) ECP2, (c) HRM3, (d) MM5I, and (e) WRFG, and NARR for the GLR domain199
Fig.	A.4.2.5.	May daily accumulated precipitation differences between (a) CRCM, (b) ECP2, (c) HRM3, (d) MM5I, and (e) WRFG, and NARR for the GLR domain200
Fig.	A.4.2.6.	June daily accumulated precipitation differences between (a) CRCM, (b) ECP2, (c) HRM3, (d) MM5I, and (e) WRFG, and NARR for the GLR domain201
Fig.	A.4.2.7.	July daily accumulated precipitation differences between (a) CRCM, (b) ECP2, (c) HRM3, (d) MM5I, and (e) WRFG, and NARR for the GLR domain202
Fig.	A.4.2.8.	August daily accumulated precipitation differences between (a) CRCM, (b) ECP2, (c) HRM3, (d) MM5I, and (e) WRFG, and NARR for the GLR domain
Fig.	A.4.2.9.	September daily accumulated precipitation differences between (a) CRCM, (b) ECP2, (c) HRM3, (d) MM5I, and (e) WRFG, and NARR for the GLR domain
Fig.	A.4.2.10.	October daily accumulated precipitation differences between (a) CRCM, (b) ECP2, (c) HRM3, (d) MM5I, and (e) WRFG, and NARR for the GLR domain
Fig.	A.4.2.11.	November daily accumulated precipitation differences between (a) CRCM, (b) ECP2, (c) HRM3, (d) MM5I, and (e) WRFG, and NARR for the GLR domain
Fig.	A.4.2.12.	December daily accumulated precipitation differences between (a) CRCM, (b) ECP2, (c) HRM3, (d) MM5I, and (e) WRFG, and NARR for the GLR domain
	Fig. B.1.	Monthly mean surface-air temperatures for the CONUS domain209
	Fig. B.2.	Daily accumulated precipitation for the CONUS domain209
	Fig. B.3.	Monthly mean surface-air temperatures for the NE domain
	Fig. B.4.	Daily accumulated precipitation for the NE domain
	Fig. B.5.	Monthly mean surface-air temperatures for the SE domain
	Fig. B.6.	Daily accumulated precipitation for the SE domain
	Fig. B.7.	Monthly mean surface-air temperatures for the NW domain

Fig.	B.8.	Daily accumulated precipitation for the NW domain	.212
Fig.	B.9.	Monthly mean surface-air temperatures for the SW domain	.213
Fig.	B.10	Daily accumulated precipitation for the SW domain	.213
Fig.	B.11	Monthly mean surface-air temperatures for the GLR domain	.214
Fig.	B.12	Daily accumulated precipitation for the GLR domain	.214

LIST OF EQUATIONS

3.3.1.
$$RMSE = \left\{ \frac{1}{N_k} \sum_{i=1}^{N_k} \left[\Phi_{RCM}(i) - \Phi_{NARR}(i) \right]^2 \right\}^{1/2} \qquad$$

Chapter I - Introduction

Climate change is now being viewed as a reality of today as opposed to the future of tomorrow. The impacts that climate change may bring are expected to cause several complications to climate sensitive systems, such as natural resources, forestry and agriculture (Southworth et al. 2002). With agriculture topping the list of economic practices in the Great Lakes Region (GLR), the impacts of climate change on this region's crops have been the focus of many recent studies (Andresen et al. 2001; Southworth et al. 2002; Winkler et al. 2002).

Understanding climate change is highly dependent on the use of climate models to assess not only what variables are expected to change but at what rate they are expected to change. Atmospheric-Oceanic Global Climate Models (AOGCMs), also known as General Circulation Models (GCMs), although valuable for assessing processes and phenomena at the global and synoptic scales, are not as effective at the regional scale due to their coarse resolution. For this reason, scientists employ Regional Climate Models (RCMs), with finer resolutions, to capture smaller-scale processes and phenomena occurring at the regional level.

However, before RCMs can be used to simulate future climates, a comprehensive understanding of how well they simulate the current climate must first be achieved. Knowing whether a particular RCM consistently over- or under-predicts temperature, precipitation or any other meteorological variable is important as this will justify any modifications that must be made to the model before future simulations can be performed. Several RCM validations studies have already been completed using data from continents spanning the globe including the Arctic (Wu et al. 2007; Ma et al. 2008), Asia (Feng and Fu 2006; Kim et al. 2008), Europe (Walter et al. 2006; Rivington et al. 2008; Kotroni et al. 2008; Kostopoulou et al. 2009) and North America

(Markovic et al. 2009; Lueng et al. 2003; Lueng et al. 2003; Gutowski et al. 2010; Music and Caya 2007; Caldwell 2010).

Unfortunately, regional RCM validation studies are lacking specifically within the GLR. This hole in the literature is the basis upon which this study is derived. The goals of this research are twofold and are as follows: (1) To fill the gaps within the literature by assessing the skill of leading RCMs in their ability of simulating mean surface-air temperatures and daily accumulated precipitation in the CONUS, and specifically the GLR, and (2) To provide quantitative estimates of mean surface-air temperature and daily accumulated precipitation biases and their spatial and temporal variations, for the leading RCMs, for future use in climate impact studies over the GLR.

It is hoped that through the completion of this research, the following research questions will be answered: (1) How well do RCM simulations, driven by NCEP reanalysis, describe the current mean surface-air temperature and daily accumulated precipitation patterns of the CONUS (and subsequent sub-regions: NE, SE, NW, SW) and the GLR?, and (2) Which, if any, RCM(s) consistently outperform(s) the others in representing the current mean surface-air temperature and daily accumulated precipitation patterns of the CONUS (and subsequent sub-regions: NE, SE, NW, SW) and the GLR? To answer these research questions, simulations from five RCMs (CRCM, ECP2, HRM3, MM5I, and WRFG) from the North American Regional Climate Change Assessment Program (NARCCAP) (Mearns et al. 2009) for the period of 1981-2000 will be validated against the North American Regional Reanalysis (NARR) (Mesinger et al. 2006) data from the same period.

This thesis will be organized as follows. First, a review of the literature will be presented in Chapter II, which includes a brief discussion about the benefits of RCMs over

AOGCMs, the existing work that has been done to evaluate RCM performance in the Arctic, Asia, Europe and North America, and a brief discussion on climate change and its associated potential effects on the GLR. Next, the methodology of this research, including the study areas of choice, the datasets being utilized and the analyses being performed will be presented in Chapter III. Chapter IV describes the results from the data analysis including statistical analyses. Finally, concluding remarks, including a summary of the results, a discussion of the study limitations and future research, will be presented in Chapter V.

Chapter II – Review of the Literature

a. Regional Climate Models as a Tool for Climate Change Assessment

Climate models are the primary tools used by climatologists to better understand future climates. Two main classifications of climate models exist based on their resolution: (1) atmospheric-oceanic global climate models (AOGCMs) and (2) regional climate models (RCMs). Based on the fundamental laws of physics, and parameterized, or adjusted to account for sub-grid processes, AOGCMs are the most comprehensive type of climate models as they include several physical processes and relationships on a global scale. Such processes found within AOGCMs, as shown in Fig. 1 for the Community Climate System Model (CCSM) (UCAR 2011), include but are not limited to (1) atmospheric and oceanic dynamics, (2) radiative and cloud processes, (3) surface processes and (4) sea ice models. Although GCMs provide a holistic understanding of the Earth's atmospheric and oceanic systems and the interactions that occur between them and have been a primary tool for producing future climate projections, the scale of GCMs can prove to be difficult when the trends being studied occur on a sub-grid scale. Most GCMs have a resolution on the order of ~200km (CCSP 2008). To better study these subgrid processes and develop climate change scenarios for a specific region, scientists employ limited-area models, also known as regional climate models or RCMs, with several tens of kilometers as opposed to several hundreds of kilometers as their horizontal resolution. In addition to a finer spatial scale that better resolves complex topography, land use and land-water contrasts, RCMs also better represent physical processes such as turbulence and convection.

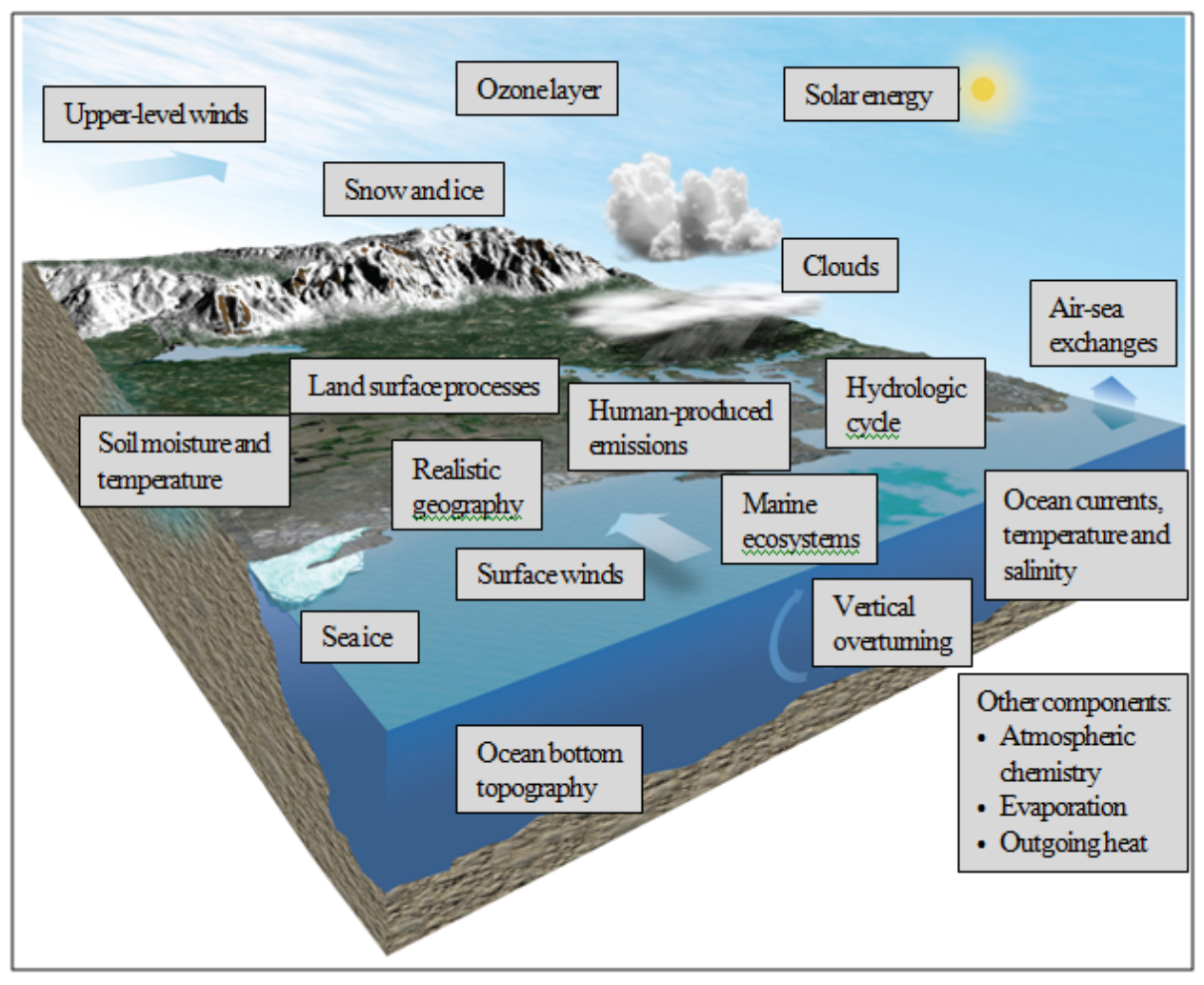


Fig. 1. Processes included within, and the structure of, the CESM (Adapted from: University Corporation for Atmospheric Research 2012).

"For interpretation of the references to color in this and all other figures, the reader is referred to the electronic version of this thesis"

One way RCMs are used is by nesting them within GCMs, a process known as dynamic downscaling whereby the output from a GCM is used to drive RCM simulations through lateral boundary conditions. Alternatively, RCMs can be run independently of GCMs, with boundary conditions provided by observational data sets or large-scale reanalyses. Regardless of the method used, RCMs prove to be more useful at the regional scale because they can better resolve topography, land use and land cover heterogeneity, and land-water contrasts. They are also better able to resolve small to mesoscale atmospheric processes that cannot be or are poorly

resolved by GMCs and generally result in greater accuracy, specifically for meteorological parameters that have high spatial variability (CCSP 2008).

b. Validation of Regional Climate Models

Before RCMs can be used to develop future climate scenarios, validation studies must be conducted to see how well the model performs in representing current climate. The underlying assumption is that if the RCMs can accurately take past data and model it into the future to recreate our current climate, then the basis on which we use them to predict future climate is justified.

Many studies have been conducted to evaluate the performance of regional climate models by various institutions and research facilities from several regions of the world. It is believed that once a climate model has been created and tested in a particular region, it cannot simply be taken to a drastically different geographic location with the expectation that it will perform as good as or better than when it was run in the original location. Such a "home field" advantage has limited the number of validation studies deemed useful for this research. However, the methodologies and findings of these evaluations may still prove to be useful and thus will be included in this review. Evaluations from the Arctic, Asia, Europe and finally North America will be discussed in the following sub-sections.

1) Validations in the Arctic

A study conducted by Wu et al. (2007) for the western Arctic performed a comparative analysis of surface climate between surface observations and climate model simulations. Five data sets were utilized: (1) NCEP-NCAR reanalysis data, (2) European Centre for Medium-

Range Weather Forecasts (ERA-40) reanalysis data, (3) Willmott-Matsuura (WM) climatology data, (4) Global Precipitation Climatology Project (GPCP) data and (5) Xie-Arkin global precipitation data. These data sets were used to validate climate simulations generated by the Penn State-National Center for Atmospheric Research (NCAR) Mesoscale Model (MM5) (Grell et al. 1994). The MM5 was run with a resolution of 50km for the western Arctic domain as part of the Western Arctic Linkage Experiment (WALE) that was devised to examine parts of western Canada and Alaska in a previous study (McGuire et al. 2008).

The model output for sea-level pressure, surface-air temperature and precipitation was compared to observational data sets with climatological means from 1992 to 2001. Seasonality, interannual variability and trends were the main focus of the evaluation. It was found that sea-level pressure was represented fairly well by the RCM, with a few minor differences found between the RCM and ERA-40, where the RCM simulated lower pressure values in the winter and fall seasons but higher pressure values in the spring and summer. The mean annual pressure of the MM5 was also found to be 0.44 hPa greater than the mean annual pressure of the ERA-40. In regards to mean temperatures, the MM5 consistently underestimated the temperature with mean annual temperatures of -7.49°, -4.24°, -4.85°, and -5.62°C for the MM5, ERA-40, NNR and WM, respectively. Finally, precipitation comparisons reveal that although the correlations between the MM5 and the GPCP, Xie-Arkin and WM were 0.83, 0.83, 0.66, respectively, the MM5 places the precipitation minimum in June while the datasets all indicate the minimum precipitation occurring in spring (Wu et al. 2007).

A subsequent study conducted in this region by Ma et al. (2008), also utilized a version of the MM5 model. This study however employed a land-surface model in the MM5 to examine the effects that the land surfaces may have on climate and atmospheric chemistry. Once the

land-surface model was incorporated, the model became known as the MM5+LSM. The study concluded that the MM5+LSM was very skillful in reproducing sea-level pressure, temperature, and dew-point temperature near the surface and in the vertical but did not represent the wind speeds very well (Ma et al. 2008).

2) Validations in Asia

In 2006, an inter-comparison project focused on validating precipitation in a monsoon zone for several RCMs in Asia was completed. Various RCMs were utilized from China, Japan, Korea, the USA and Australia and were run from July 1988 to December 1998. To validate the model output, 903 observation stations containing monthly precipitation were used. The results of the study concluded that, although most of the models were able to capture the spatial distribution of precipitation, they were not able to capture the intensity and location of the rain belt core that shows up in the observations. They were, however, able to capture the general shift of the rain belt from north to south but with a wide range among the different models. Finally, most of the models were also able to accurately represent the interannual variability of precipitation (Feng and Fu 2006).

Kim et al. (2008) conducted a study to examine the temporal and spatial distribution of precipitation and low-level temperature over East Asia. The RCM, known as the Mesoscale Atmospheric Simulation (MAS), was run from 1979-2000 and then compared to observational data gathered from the Climate Research Unit (CRU) at the University of East Anglia and the CPC Merged Analysis Precipitation (CMAP). Results showed that the model simulation and CMAP were generally in fairly good agreement with each other, but indicated that the model slightly overestimated temperatures over the

ocean. To examine the skill of the model in capturing the progression of the monsoon, the movement of the precipitation was examined. It appeared that the model simulation tended to advance the movement somewhat faster than what the CMAP analysis showed. Finally, extreme rainfall events were analyzed. Results demonstrated that the model simulation did fairly well at reproducing extreme precipitation events with correlation coefficients of 0.84 and 0.89 for the two year and five year extreme events, respectively. However it was noted that the CMAP was fairly coarse in its resolution and tended to reduce the local maxima.

3) Validations in Europe

Validation studies similar to those conducted in the Arctic and Asia have also been done in various locations throughout Europe. A study by Walter et al. (2006) investigated how high resolution RCMs would capture wind velocities in Germany. The underlying goal of this research was to validate the models with the hope of being able to run them for future decades should the models prove to be accurate. Three different RCMs were employed for this study: REMO RCM (two versions 5.0 and 5.1) (Jacob and Podzun 1997; Jacob 2001), the Climate Limited Area Model (CLM) (Doms and Schaettler 1999) and Multiscale Climate Chemistry Model MCCM/MM5 based on the Penn State MM5 model (Dudhia 1993). Observational data were obtained from every German Meteorological Service climate station available at any given time, ranging from 73 stations in 1951 to 113 stations in 2001. Results concluded that the RCMs did perform fairly well overall with differences in the modeled and observed wind speeds on the order of +/- 1.0 ms⁻¹ (Walter et al. 2006).

A project similar to the German study, conducted by Rivington et al. (2008) in the UK, evaluated model projections from the Hadley Centre's HadRM3 that were presented in the

UKCIP02 climate change scenarios report against 15 meteorological observation stations from 1960-1990. Variables such as temperature, precipitation, and solar radiation were investigated. The results of this study revealed that the HadRM3 represented maximum temperature fairly well while minimum temperature values tended to be overestimated which also resulted in extreme low temperature events not being captured very well. In addition to problems with temperature, precipitation proved to be somewhat challenging for the HadRM3 as well. The RCM tended to model too many small precipitation events causing a severe underestimation in the number of days without any precipitation. Finally, in regards to solar radiation, the HadRM3 was found to overestimate solar radiation in a systematic way for parts of the domain, while performing fairly well in others.

That same year, a study by Kotroni et al. (2008), was conducted for the Eastern Mediterranean in which current climate simulations were evaluated against surface station data from 1961-1990. The PRECIS model (Jones et al. 2004), also known as the HadRM3P, was used in this study. After comparing the model output to station data, it appeared that the mean, maximum temperature and minimum temperature were all underestimated by the model during the winter season, but they were all overestimated during the summer season. The models appeared to underestimate the seasonal rainfall between the months of September and February. It was hypothesized that this underestimation was due to the fact that the model failed to represent cyclone activity within the domain during the same time frame.

Following the studies by Rivington et al. (2008) and Kotroni et al. (2008), a study was conducted by Kostopoulou et al. (2009) to examine the performance of the Aire Limitée Adaptation Dynamique Développement International (ALADIN) on daily maximum and minimum temperatures, as well as extreme warm and cold events. This RCM, developed in

France, and described in Déqué and Somot (2007) and Radu et al. (2008), was validated using observed temperature data from 53 meteorological stations located throughout the Balkin Peninsula and western Turkey. It was found that the RCM overestimated temperatures in the northern part of the region and underestimated temperatures in the southernmost parts. RCM seasonality performance was also noted as the model had difficulties accurately representing minimum temperatures, showing a cold bias, in the fall and winter seasons. In regards to extreme events, the RCM overestimated the frequency of warm spells and underestimated the frequency of cold spells.

4) Validations in North America

As previously mentioned, it is believed that most models would not perform as well in other geographic regions when compared to the region in which they were developed. Although the methodologies and findings of the previously discussed studies from the Arctic, Asia, and Europe did prove to be interesting, this final section examines RCM performance in North America, as the regions of interest in this study lie completely within the North American continent. While radiation simulations have been evaluated from RCM output, most studies conducted for North America investigate surface-air temperature and precipitation, with precipitation being the most widely studied variable as it has a high level of spatial variability.

A study by Markovic et al. (2009) investigated how well three different RCMs were able to represent the surface radiation budget over North America. The three RCMs examined were the Canadian Regional Climate Model (CRCM) (Caya and Laprise 1999), the limited area model version of the Global Environmental Model (GEM-LAM) (Côté et al. 2008) and the Rossby Centre RCM (RCA3) (Jones et al. 2004 and Kjellström et al. 2005). Used to validate the models

were the ERA40, NARR and derived values from the International Satellite Cloud Climatology Project (ISCCP) (Zhang et al. 2004). Results showed that overall the mean incoming solar radiation for the winter months of December, January and February were represented best by the GEM-LAM. The RCA3 and CRCM were found to underestimate the downwelling longwave radiation.

Multiple RCM studies examining the hydrology of North America have been conducted (Leung et al. 2003; Music and Caya 2007). A study conducted by Leung et al. (2003) examined the hydroclimate of the western United States by comparing NCEP-NCAR reanalysis-driven regional climate simulations from the MM5 against the NCEP-NCAR reanalysis data for 1981-2000. The results showed that while the RCM did simulate seasonal means and extreme precipitation, there were observable biases within the simulations. The study found that during the cold season, the simulations overestimated precipitation over parts of the Intermountain West while underestimations were observed during the warm season in parts of the Southwest. In the northern half of the U.S. during the warm season, the simulations showed a lower frequency of precipitation which led to lower than observed total precipitation amounts. A similar study conducted by Music and Caya (2007) also examined the hydroclimate of the United States but focused on the Mississippi River Basin and utilized the CRCM rather than the MM5. Comparing CRCM simulations with various parameterization schemes to three observational datasets, the results of the study concluded that when more complex physical parameterization schemes were employed, improvements in precipitation, evapotranspiration, moisture flux convergence, and terrestrial water storage were achieved.

Another study, also conducted in 2003 by Leung et al., investigated the Columbia and Sacramento-San Joaquin water budgets in the western United States by comparing RCM

simulations against reanalysis and observational data. This study utilized simulations from the MM5 and the Regional Spectral Model (RSM) (Juang and Kanamitsu 1994; Kanamitsu 2000), reanalysis data from the NCEP-NCAR reanalysis I (Kalnay et al. 1996), NCEP-DOE second Atmospheric Model Intercomparison Project (AMIP-II) reanalysis II (Kanamitsu et al. 2002) and European Centre for Medium-Range Weather Forecasts (ECMWF) reanalyses (Gibson et al. 1997), and observational precipitation data from the Global Precipitation Climatology Project (GPCP) (Huffman et al. 1997), observational stream flow data from the A. G. Crook Company for the Columbia basin and the California Department of Water Resources Data Exchange Center for the San Joaquin basin, and a subset of temperature and precipitation data from the National Oceanic and Atmospheric Administration (NOAA) Cooperative Observer (COOP) network created by Maurer et al. (2002). The results showed that differences in the spatial extent and magnitude of precipitation did exist, with differences in mean precipitation values within the basins between the regional simulations, reanalyses and observations nearly double the mean. It was noted that when comparing the simulations to the observational dataset, the ERA-driven RSM and MM5 simulations demonstrated the best mean precipitation approximations within the basins.

In addition to the overall water budget of the western United States, studies have also focused on winter season precipitation in this region. A study conducted by Caldwell (2010) examined reanalysis-forced RCM simulations, specifically in California. Using observations from 6 separate sources to compile a more complete data set, NCEP-driven RCM simulations from NARCCAP were evaluated. Results indicate that the simulations overestimated precipitation due to an over-prediction of extreme precipitation events. However, these results differ from another study also conducted in 2010 by Gutowski et al. which investigated extreme

monthly precipitation values in various regions throughout the United States. This study compared 18 years of cool season precipitation simulations from NARCCAP RCMs with observational data to determine the ability of the RCMs in capturing non-convective precipitation. Unlike the Caldwell study, which focused only on winter season precipitation, the results showed that in regions prone to topographically induced precipitation, specifically California, the models did simulate the frequency and magnitude of cool season extreme precipitation as well as the interannual variability. However, in the central United States surrounding the upper Mississippi River valley, the models were said to be in less agreement compared to the results from California.

c. Climate Change Impacts of the Great Lakes Region

Mean temperatures in the GLR have been increasing over the last few decades, with the most noticeable trends occurring during the winter season (Li et al. 2010). This increase in mean temperature has increased the length of the growing season because the last frost of Spring has been occurring by as much as one week sooner than before (Karl et al. 2009). In addition to changes in observed temperatures, changes in precipitation have also been noted. Both summer and winter precipitation have been above normal for the last 30 years in the GLR which has left this period as the wettest on record within the last 100 years. With average temperature and precipitation showing positive trends in the GLR, their potential impacts on the GLR environment have become a recent topic of discussion.

One area that is expected to be greatly impacted is agriculture. With \$15 billion in cash receipts annually for Michigan, Minnesota and Wisconsin alone, agricultural practices rank among the top of the region's economic practices (USDA-NASS 1997). In this context, potential

climate changes will have implications for agriculture, forestry and natural resources as they are all climate-sensitive systems (Southworth et al. 2002). Some suggest that these implications would actually result in better conditions for agriculture because a longer growing season would result in increased production and thus show a positive response to climate change in the GLR (Wuebbles and Hayhoe 2004). Other studies have found that even though agriculture may benefit overall from climate change, secondary effects may be observed such as the migration of pests from the south, changes in crop yield and areas of optimal crop production shifting to other geographic locations (NAST 2001; Watson et al. 1998; McCarthy et al. 2001).

To better understand the consequences of climate change on agriculture in the GLR, several case studies have been completed to assess the potential impacts on a specific crop. One such study by Andresen et al. (2001) utilized crop growth models for maize, soybean and alfalfa and concluded that wetter conditions resulted in higher crop yield and that the length of the growing season was an important factor, especially for the northern most parts of the GLR. A similar study by Southworth et al. (2000) examining maize yields concluded that the southern most parts of the GLR would experience a drop in maize yields because the increase in temperature would result in conditions too harsh for higher maize yields. However, it was also noted that northern areas could experience anywhere between a 10-50% increase in yield depending on the exact location and type of maize planted. Southworth et al. (2002) conducted a similar study focusing on soybean yields in the GLR and reported some similar results. They concluded that the future climate scenarios would lead to higher soybean yields in the northern and central locations. However, they also found that the southern locations would report lower soybean yields due to the fact that high temperatures were actually found to be a limiting factor.

Parallel studies have also explored these same questions regarding fruit production. A study by Winkler et al. (2002) examined future commercial fruit production for the decades of 2025-2034 and 2090-2099. The 2025-2034 assessment indicated a decrease in freezing temperature frequency but an increase in seasonal heat accumulation and growing season length, while the assessment completed for 2090-2099 suggested very large temperature increases. However, in both instances it is important to note that the authors are unclear as to whether the fruit crops will be more or less vulnerable to colder temperatures or if warmer temperatures will result in more insect generations within one growing season (Winkler et al. 2002). As all of the aforementioned studies have concluded, climate change in the GLR is expected to have substantial impacts, both positive and negative, on the agricultural community; it is because of this and because agriculture plays such a vital role in this region's economy that a better understanding of climate change impacts is desired.

Chapter III - Methodology

a. Study Area

Model evaluations were conducted for the contiguous United States (CONUS; 26.0°N-50.0°N and 65.0°W-125.0°W). In order to evaluate the regional performance of the RCMs, the following sub-regions were also chosen: Northeast (NE; 38.0°-50.0°N and 65.0°-95.0°W), Southeast (SE; 26.0°-37.5°N and 65.0°-95.0°W), Northwest (NW; 38.0°-50.0°N and 95.5°-125.0°W), Southwest (SW; 26.0°-37.5°N and 95.5°-125.0°W), and Great Lakes Region (GLR; 40.0°-50.0°N and 74.0-94.0°W). Figure 2 depicts each of the selected domains.

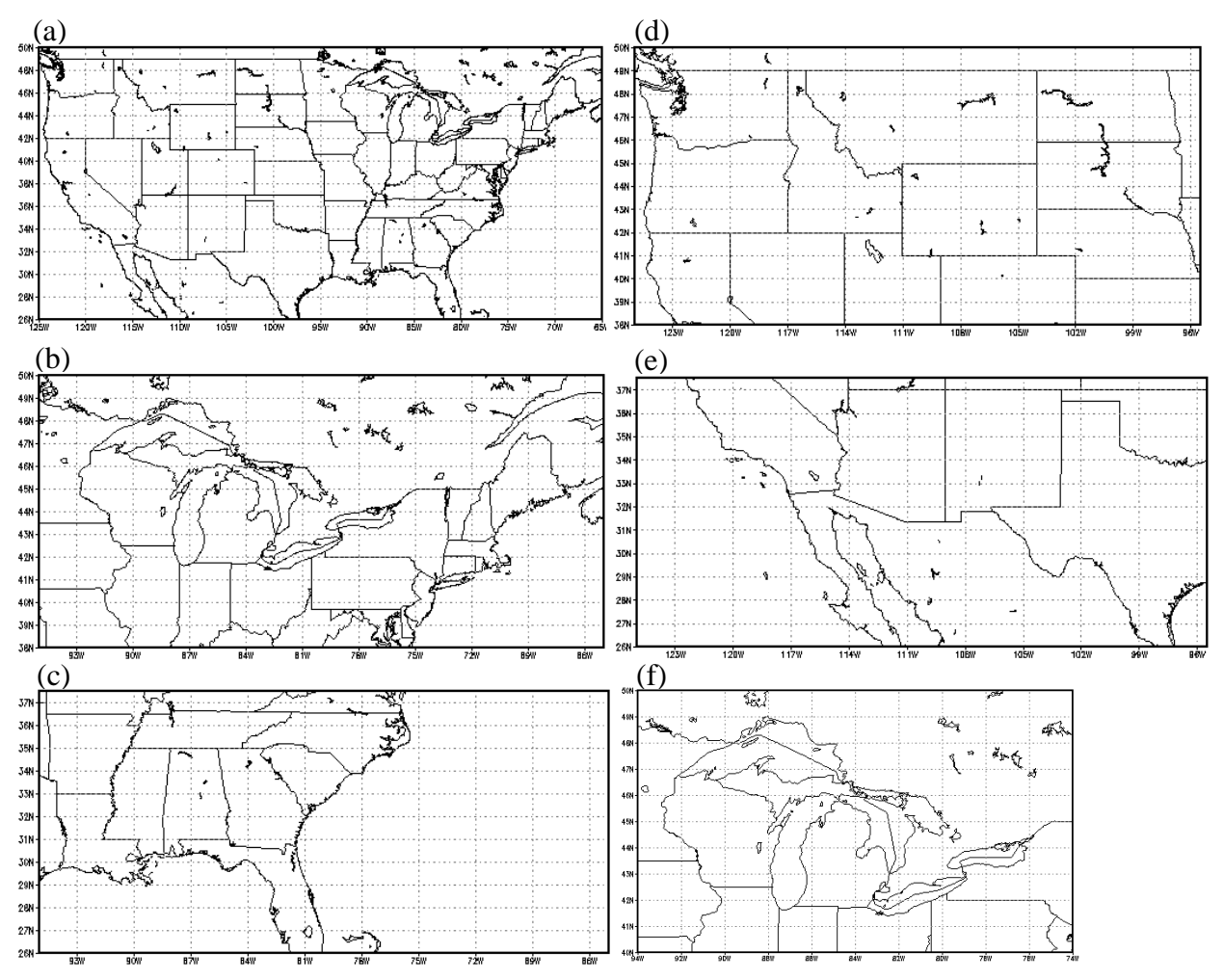


Fig. 2. Six model domains including the: (a) CONUS, (b) NE, (c) SE, (d) NW, (e) SW, and (f) GLR.

b. Data Sources

Two main data sets are used in this study. RCM simulations of current climate are obtained from the North American Regional Climate Change Assessment Program (NARCCAP). Reanalysis data are obtained from the North American Regional Reanalysis (NARR) archives.

1. NARCCAP

The first data set used in this study, NARCCAP, is a suite of climate models and is discussed in Mearns et al. (2009). The NARCCAP project was developed to examine the uncertainties that exist within the regional and global climate models commonly used in practice today, to develop and provide high resolution scenarios to be used in studies focusing on impacts assessment, and to build a stronger relationship between climate modelers from America, Canada and Europe. Since the project first began and the data have become available, many studies have been conducted utilizing this suite of climate models (Wang et al. 2009; Mailhot et al. 2011; Gutowski et al. 2010; Sain et al. 2010).

Simulations of current climate, available from 1979-2004, are driven by NCEP Reanalysis II, are available at a spatial resolution of 50-km, and cover the North American domain as shown in Fig. 3 (Mearns et al. 2007). The 5 RCMs being evaluated in this study are the (1) Canadian Regional Climate Model (CRCM), (2) Experimental Climate Prediction model, version 2 (ECP2), (3) Hadley Regional Model, version 3 (HRM3), (4) Mesoscale Model, version 5 run by the Iowa State University modeling group (MM5I), and (5) Weather Research and Forecasting model, using the Grell convective parameterization scheme (WRFG). Model characteristics for each RCM are discussed in Table 1.

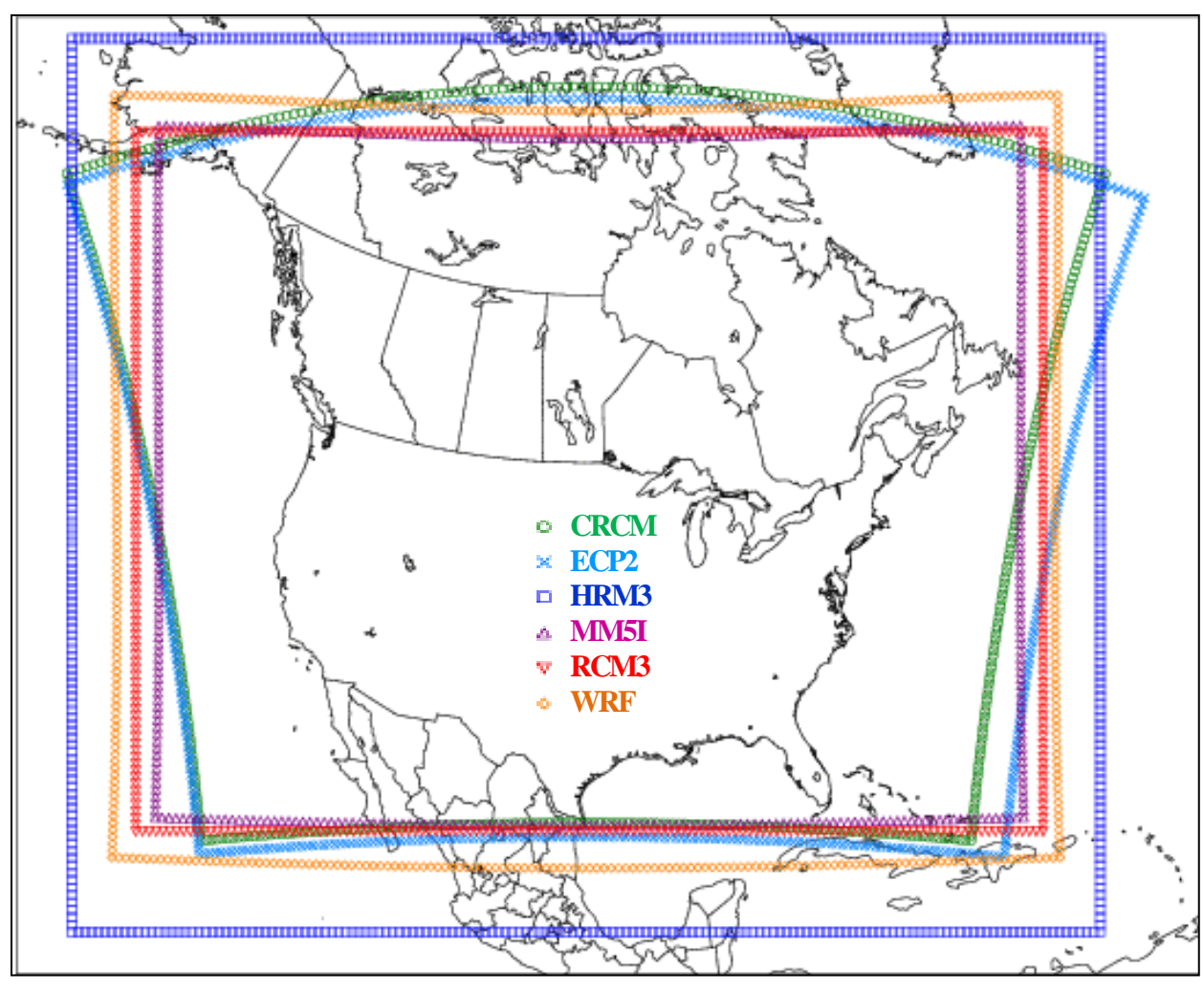


Fig. 3. NARCCAP-RCM domains (NCAR 2009).

	CRCM	ECPC/ECP2	HRM3	MM5I	RCM3	WRFP/WRFG
Dynamics	Nonhydrostatic, Compressible	Hydrostatic, Incompressible	Hydrostatic, Compressible	Nonhydrostatic, Compressible	Hydrostatic, Compressible	Nonhydrostatic, Compressible
Lateral Boundary Treatment	9 points (Davies 1976); spectral nudging of horizontal wind.	Pertubations relaxed at boundaries; spectral filter	4 points (Davies and Turner 1977)	4 points (linear relaxation)	12 points (exponential relaxation)	15 grid points (exponential relaxation)
Land Surface	CLASS	NOAH	MOSES	NOAH	BATS	NOAH
Thermal/Water Layers	3/3	4/4	4/4	4/4	1/3	4/4
Vegetation Types	21 vegetation classes	13 classes	53 classes (Wilson and Henderson- Sellers 1985)	16 classes from USGS SiB model	19 classes	24 classes from USGS
Boundary Layer	Local K, gradient Richardson number formulation	Hong-Pan non- local K	First order turbulent mixing	Hong-Pan (MRG) countergradient, non-local K	Non-local K, countergradient flux	Yonsei Univ. (explicit entrainment)
Explicit Moist Physics	Removal of supersaturation	Removal of supersaturation	Prognostic cloud liquid and ice; liquid potential temperature	Dudhia simple ice	SUBEX, prognostic cloud water	Prognostic cloud liquid and ice, rain, snow
Cumulus Perameterization	Mass Flux	Simplified Arawaka- Schubert	Mass Flux, including downdraft	Kain-Fritsch2 mass flux	Grell with Fritsch- Chappell closure	Kain-Fritsch2 mass flux [WRFP] / Grell [WRFG]
Number of Vertical Levels	29	28	19	23	18	35

Table 1. NARCCAP-RCM characteristics (NCAR 2009).

Table 1. cont'd

	Gal-Chen scaled-	Normalized	Hybrid terrain	Sigma	Terrain	Terrain
Type of Vertical	height	pressure	following &		following	following
Coordinate			pressure			
Original Grid	160 x 135	161 x 136	171 x 146	154 x 129	160 x 130	155 x 130
Size						
Sponge Zone	10	7 (x) / 10 (y)	8	15	13	10.5
Depth (gridpts)*						
Length of	900 Seconds	100 seconds	300 Seconds	120 seconds	150 Seconds	150 seconds
Timestep						
tasmin/tasmax	timestep	timestep	timestep	timestep	3-hourly	hourly
Calculation**						
Spectral	Yes	Yes	No	No	No	No
Nudging						

^{*} Sponge Zone Depth: Values given are depth along each edge. Total points removed from each dimension are twice the given values.

^{**} tasmin/tasmax Calculation: the frequency of the values from which daily minimum and maximum temperature values (variables tasmin and tasmax) are calculated. "Timestep" means that min and max values are updated on every internal timestep of the model. "Hourly" and "3-hourly" mean that min and max are calculated from tas values recorded at hourly/3-hourly intervals.

2. NARR

The second data set utilized in this study is the NARR from the National Center of Environmental Protection (NCEP) and is discussed in Mesinger et al. (2006). The NARR was created to improve upon the NCEP/NCAR and NCEP/DOE Global Reanalyses and includes improvements such as the more sophisticated Noah land surface model it employs and the improved data assimilation techniques used, specifically for precipitation, resulting from the use of an upgraded regional Eta model (Mesinger et al. 2006). The NARR covers the North American domain, as depicted in Fig. 5, and is available at a spatial resolution of 32-km, in 3-hourly time steps, over 29 pressure levels, and spans a period from 1 January 1979 to present day. These factors all contribute to the improved representation of climatological, meteorological and hydrological variables within NARR. As a result, this was chosen as the climate reference data set for this study.

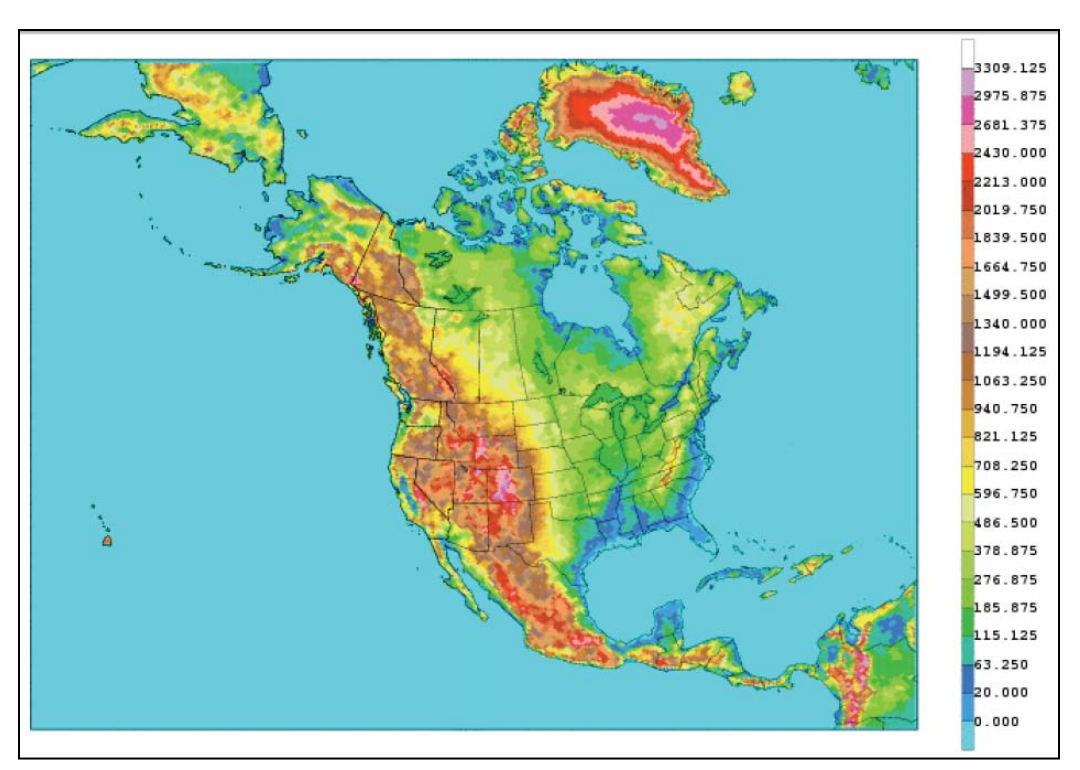


Fig. 4. NARR domain and its topography at a spatial resolution of 32-km (Mesinger et al. 2006).

c. Data Analysis

To accomplish the objectives of this study, a common grid spacing and common period of study were required of both data sets. With NARCCAP simulations available from 1979-2004 and the NARR available from 1979-present, the study period from 1981-2000 was chosen. This period takes into account the models' spin-up period that allows for all elements within the models to reach equilibrium and also allows for an even 20-year climatology for analysis.

With NARCCAP simulations available at a 50-km spatial resolution and the NARR available at a 32-km spatial resolution, a 0.5° latitude by 0.5° longitude common grid, with nominal grid spacing close to 50 km, was utilized. A bi-linear interpolation technique was used to re-grid the NARR data and NARCCAP output to this common grid.

For the temperature (T) at grid point (x, y), the bi-linear interpolation yields

$$T(x,y) \approx \frac{(x_2 - x)(y_2 - y)}{(x_2 - x_1)(y_2 - y_1)} T(x_1, y_1) + \frac{(x - x_1)(y_2 - y)}{(x_2 - x_1)(y_2 - y_1)} T(x_2, y_1) + \frac{(x_2 - x)(y - y_1)}{(x_2 - x_1)(y_2 - y_1)} T(x_1, y_2) + \frac{(x - x_1)(y - y_1)}{(x_2 - x_1)(y_2 - y_1)} T(x_2, y_2)$$

$$(1)$$

where $(x_1, y_1), (x_1, y_2), (x_2, y_1)$ and (x_2, y_2) are the four closest grid points to grid point (x, y). A similar bi-linear interpolation method was used for precipitation.

Agriculture within the GLR is of significant importance and as a result, the original intentions of this study were to validate various agriculturally significant variables in addition to the standard variables of temperature and precipitation. However, due to time constraints, the analysis presented herein focuses on monthly mean surface-air temperatures and daily accumulated precipitation as temperature and precipitation are two of the most important agriculturally significant variables and also serve as the basis for many derived indices. To evaluate the ability of each RCM in simulating these two variables, spatial plots and spatial

difference plots were created, annual cycles were analyzed and statistical measures were also computed.

1. Spatial Plots

To visually display mean temperatures and daily accumulated precipitation the Grid Analysis and Display System (GrADS) was utilized. Monthly spatial plots for both variables were generated for each RCM and NARR for the CONUS and GLR. These plots allow for an examination of the RCMs ability in capturing the observed spatial patterns of temperature and precipitation across the CONUS and all of the sub-regions. To better quantify the differences between the RCMs and NARR and determine how the differences vary spatially, spatial plots of RCM minus NARR at each grid point were also produced for both variables. These plots are provided in Appendix A for the CONUS and GLR. To save space, the spatial plots for the four sub-regions (NE, SE, NW and SW) are not shown since inferences for these regions can be easily drawn from the CONUS plots.

2. Annual Cycles

The annual cycle of each variable was created to examine how well each RCM captures the seasonal variability within each region and can be found in Appendix B. Unlike the spatial plots, the annual cycles for the 4 sub-regions, in addition to the CONUS and GLR, are also included and analyzed independently to better quantify RCM performance in each sub-region.

3. Statistics

Statistical analyses including: bias, mean absolute error (MAE), root mean square error (RMSE), and correlation coefficients between each RCM and NARR were computed and can be

found in Appendix C. Similar to the time series analyses, statistics have been generated for the 4 sub-regions, in addition to the CONUS and GLR to better quantify RCM performance in each sub-region.

3.1. Bias

The bias of each of the RCMs in simulating the NARR surface temperature is calculated for each grid point within each of the 6 domains using

$$B_i = \Phi_{RCM}(i) - \Phi_{NARR}(i)$$
 (3.1.1)

where B_i is the bias at grid point i, Φ denotes either monthly mean surface air temperature or daily accumulated precipitation. Subscript RCM and NARR, represent RCM or NARR values.

To obtain the domain-averaged bias, denoted B, the bias at individual grid point were then averaged over each of the six domains using 1

$$B = \frac{1}{Nk} \sum_{i}^{Nk} Bi$$
 (3.1.2)

where N_k is the total number of grid points for each of the six domains with k = 1, 2, ...6, representing the six domains.

3.2. Mean Absolute Error

To examine the magnitude of the differences between each RCM and NARR, regardless of direction, the MAE was calculated for each domain using

$$MAE = \frac{1}{N_k} \sum_{i=1}^{N_k} \left| \Phi_{RCM}(i) - \Phi_{NARR}(i) \right|$$
(3.2.1)

3.3 Root Mean Square Error

The RMSE was calculated for both temperature and precipitation for each domain using

$$RMSE = \left\{ \frac{1}{N_k} \sum_{i=1}^{N_k} \left[\Phi_{RCM}(i) - \Phi_{NARR}(i) \right]^2 \right\}^{1/2}$$
 (3.3.1)

3.4 Spatial Correlation

To examine the spatial correlation between the RCM simulated and NARR temperature and precipitation, the correlation coefficient is computed for each of the six domains using

$$Correl = \frac{\sum_{i=1}^{N_k} [\Phi_{RCM}(i) - \overline{\Phi}_{RCM}] [\Phi_{NARR}(i) - \overline{\Phi}_{NARR}]}{\sqrt{\sum_{i=1}^{N_k} [\Phi_{RCM}(i) - \overline{\Phi}_{RCM}]^2 \sum_{i=1}^{N_k} [\Phi_{NARR}(i) - \overline{\Phi}_{NARR}]^2}}$$
(3.4.1)

Chapter IV – Results

The results and discussions are organized by region, starting with the CONUS, followed by the four sub-regions, and finally the GLR. For the CONUS and GLR, the results are presented as follows. The spatial distribution of temperature and daily precipitation is first presented to examine the ability of the RCMs in describing the observed spatial pattern of these variables and their seasonal variations. To better quantify the differences at each grid point, a discussion of the mean biases over the study region exhibited by each model in each season is presented and an overall ranking of the RCMs based on model performance is presented. However, it should be noted that these rankings do not necessarily represent which models performed better overall, as the average of many small biases, both positive and negative, and the average of many large biases, both positive and negative, can offset one another thereby producing misleading results. To account for this, a qualitative analysis of the difference plots for each RCM is then discussed. Finally, to further quantify the performance of each model in simulating the monthly variations of NARR temperatures and precipitation, the annual cycles of domain averaged monthly mean temperature and daily accumulated precipitation between NARR and each of the RCMs are discussed. For the four sub-regions, spatial plots are not presented to save space since inferences can be easily drawn from the CONUS plots. Only the annual cycles and statistical analysis results are described for each sub-region.

While all spatial plots, annual cycle figures and statistics are presented by month, and available in Appendix A, Appendix B and Appendix C, respectively, the results are mostly aggregated to and discussed at the seasonal level. For the purposes of this study, spring is defined as March, April, May (MAM), summer as June, July, August (JJA), autumn as September, October, November (SON), and winter as December, January, February (DJF).

a. Contiguous United States

1. Spatial Distribution of Mean Surface-Air Temperatures

1.1 Spring

Spring temperatures from NARR (Figs. A.1.1.3.a, A.1.1.4.a, and A.1.1.5.a) depict the general north-south gradient with warmer temperatures extending further north along the western and eastern coasts in the SW and SE, respectively. As the spring months progress, warmer temperatures are also observed further north in the central part of U.S., extending from Texas to North Dakota in May. The warmest spring temperatures are consistently concentrated in the southern most parts of California, Arizona, New Mexico, Texas and Florida. Cooler temperatures are observed in the higher elevations of the Appalachian, Cascade, Sierra-Nevada and Rocky Mountains and are also observed over the waters of all 5 Great Lakes with the most noticeable lake temperature differences occurring in the latter part of spring in April and May.

While the RCM-simulated spatial patterns are in very good agreement with NARR for all spring months, differences in the northward migration of the warmer temperatures, the location and magnitude of the warmest temperatures in the southernmost regions of the domain, and the cooler temperatures of the Great Lakes, most noticeably in May, are observed. The strong skill of the RCMs in capturing the spatial distribution of the spring temperature across CONUS is also reflected by the high spatial correlation coefficients, which range from 0.89 to 0.98 (Table C.4). The correlations tend to decrease from March to May for all the models. In all spring months, the correlation between NARR and the CRCM is consistently lower than the other models.

1.2 Summer

Summer temperatures from NARR (Figs. A.1.1.6.a, A.1.1.7.a, and A.1.1.8.a) exhibit warmer temperatures in the southern regions extending northward in the central U.S. and cooler temperatures in the NE and NW. Similar to spring temperature patterns, the coolest temperatures are observed in the higher elevations of the Appalachian, Cascade, Sierra-Nevada and Rocky Mountains with these regions warming as the summer season progresses. The Great Lakes also show cooler temperatures, and a sharp land-water gradient; however this gradient decreases throughout the summer season and is only noticeable over Lake Superior during the month of August, as the other lakes have warmed and show a more zonal pattern.

All RCMs simulate broad-scale patterns reasonably well during the summer months but are overall less accurate when compared to the spring months. Most RCMs correctly simulate the cooler waters of the Great Lakes, the warmest temperatures in the south-central U.S., and the coolest temperatures in the Pacific Northwest. However, the CRCM, MM5I and WRFG in all months, and the ECP2 in June, falsely expand the cooler temperatures surrounding the higher elevations in the western CONUS. The MM5I is consistently better at correctly simulating the spatial pattern of temperatures in all summer months with correlation values of 0.93, 0.91 and 0.92 for June, July and August, respectively (Table C.4). Much like the spring, the CRCM shows the lowest level of skill in simulating the spatial pattern of summer temperatures with correlation values of 0.86, 0.84 and 0.86 for June, July and August, respectively. The HRM3 shows decreasing correlation values during the summer with values of 0.93, 0.90 and 0.89 for June, July and August, respectively, while the ECP2 and WRFG are relatively consistent with correlation values of 0.91 or 0.92 in each of the summer months.

1.3 Autumn

Autumn marks the warm to cold season transition with large changes in circulation patterns with temperatures from NARR (Figs. A.1.1.9.a, A.1.1.10.a, and A.1.1.11.a) showing the largest month to month variations. September temperatures depict spatial patterns similar to those of early summer with the warmest temperatures observed along the Gulf Coast and in the SE extending north and west into Oklahoma and Kansas as well as Arizona and California. Cooler temperatures are observed in the NE and NW regions as well as the Upper Midwest, most noticeably over the upper Great Lakes Region especially over Lake Superior. Cooler temperatures are also present over the higher elevations of the Appalachian, Cascade, Sierra-Nevada and Rocky Mountains. October temperatures from NARR show zonal pattern with slightly warmer temperatures extending northward from the Gulf of Mexico into the central U.S. Warmer temperatures are also seen in southern and west-central California. Cooler temperatures are observed within the higher elevations of the Appalachian and Rocky Mountains. However, noticeably cooler temperatures are not as well defined in the higher elevations of the Pacific Northwest. In November, consistent cool temperatures are seen across much of the CONUS with warmer temperatures extending inland only along the coastlines of the SW and SE. Slightly warmer temperatures are observed over the waters of the Great Lakes and cooler temperatures are observed over the higher elevations of the Cascade, Sierra-Nevada and Rocky Mountains but are not as well defined over the higher elevations of the Appalachians.

Despite the transitional nature of this season with large month-to-month variations, all models show improvements in the simulated spatial patterns when compared to the summer months, but some noticeable differences between NARR and the models do exist during autumn. The locations and magnitudes of the warmer temperatures within the southern CONUS vary

from model to model, especially in September and October. The spatial extent of the cooler temperatures associated with higher elevations in the western CONUS also varies, especially during the month of September. Differences between the simulated and NARR temperatures also exist within the north-central CONUS, but the magnitudes of the difference vary from model to model. All models show increasing skill in simulating the spatial pattern of temperatures as autumn progresses as the correlation coefficients are higher than the month before in all cases. The values of the correlation are considerably higher during autumn than the previous seasons with a seasonal mean correlation value of 0.97-0.98 among the models, compared to 0.85-0.92 for the summer season and 0.94-0.97 for the spring season (Table C.4).

1.4 Winter

Winter temperatures from NARR (Figs. A.1.1.1.a, A.1.1.2.a, and A.1.1.12.a) display a zonal pattern with warmer temperatures in the southern most portions of Florida, Texas, Arizona and California and colder Canadian air extending southward into the northern plains, GLR and NE. Colder temperatures are also observed in the higher elevations of the western CONUS, most noticeably in Colorado, Wyoming and Idaho. Finally, the Great Lakes appear several degrees warmer than the surrounding land throughout the winter months, especially in December and January. In February, the land-water temperature differences are visible but are not as prevalent, especially along the shorelines where the shallower waters lead to cooler temperatures closer to those observed over neighboring land.

With spatial correlation values of 0.96 or greater for all months and all RCMs during the winter months, all models, with the exception of WRFG, demonstrate the best spatial pattern of temperatures during this season as indicated by the highest seasonal mean spatial correlation values of 0.99, 0.99, 0.98, 0.99 and 0.97 for CRCM, ECP2, HRM3, MM5I and WRFG,

respectively (Table C.4). Interestingly, the CRCM is the only RCM with a spatial correlation value of 0.99 in each of the three winter months showing it to be much more reliable during the coldest months compared to the warmest months. Unlike the other seasons, where many differences are observed from the northward migration of warmer temperatures from the south, the winter season shows differences in the southward migration of colder temperatures from the north. The magnitude and extent of these colder temperatures in the north-central U.S. and NE regions do show some variations from model to model. Additionally, noticeable differences are observed in how far north the warmer temperatures extend from the southern plains into the northern plains and also in the areas surrounding the Rocky Mountains as some RCMs show a tendency for colder temperatures surrounding the highest elevations.

1.5 Summary

In general, the RCMs capture the spatial pattern of mean temperatures with slight differences in overall accuracy from model to model and season to season. During the spring season, the ECP2 and HRM3 have the greatest spatial accuracy, followed by the MM5I, WRFG and CRCM. In the summer, the ECP2, MM5I and WRFG all demonstrate the greatest accuracy followed by the HRM3 and CRCM. The months of autumn show a similar pattern with the ECP2, MM5I and WRFG, again, having the greatest spatial correlation values, and the CRCM and HRM3 both showing the least amount of accuracy. Finally, during the winter season, the CRCM, ECP2 and MM5I have the highest spatial correlations followed by the HRM3 and WRFG.

For all the models, better agreement in simulated and observed spatial distribution occurs in winter and autumn and the worst occurs in summer. The differences between the models are

relatively small except for the CRCM which shows relatively poor performance in spring, summer and autumn compared to other models, but the best performance in winter.

2. Spatial Distribution of Mean Surface-Air Temperature Differences

2.1 Spring

During the spring, average bias values range from -3.05K for the CRCM in April to +1.43K for the HRM3 in March (Table C.1). In March and April, the CRCM has the largest negative bias values followed by the MM5I and ECP2, with the WRFG having the smallest negative bias values and the HRM3 having the only positive bias values observed in the spring. In May, the CRCM and MM5I still have the largest negative bias values, in that order, but the WRFG surpasses the ECP2 with a slightly larger negative bias, while the HRM3 switches signs to a slightly negative bias of -0.33K. Ranking the models, from best to worst, according to mean spring biases, yields the following order (with their respective seasonal mean bias values): HRM3 (+0.45K), WRFG (-1.01K), ECP2 (-1.39K), MM5I (-2.26K) and CRCM (-2.88K).

The CRCM (Figs. A.1.2.3.a, A.1.2.4.a, and A.1.2.5.a) consistently underestimates CONUS temperatures with the largest underestimations occurring in the western CONUS. However, in all three months, the CRCM overestimates the Great Lake temperatures, especially along the western shores of Lake Superior and southern shores of Lake Michigan. The ECP2 (Figs. A.1.2.3.b, A.1.2.4.b, and A.1.2.5.b) shows both overestimations and underestimations in various parts of the CONUS with the spatial extent and magnitude of the underestimations more prevalent than the overestimations. Most of the underestimations occur in the western CONUS and parts of the SE, most noticeably in FL. However, the ECP2 does show little to no bias in

parts of the NE and central CONUS during all three months and overestimations in the northern plains during the month of March.

The HRM3 (Figs. A.1.2.3.c, A.1.2.4.c, and A.1.2.5.c) overestimates temperatures during the month of March, but progressively shows less of a warm bias during the months of April and May. The greatest overestimations are in the Midwest and northern plains in March and April while the most concentrated area of overestimation during the month of May shifts to the central CONUS. However, it should be noted that consistent underestimations are observed in parts of the SW, particularly in western TX and southern NM. The MM51 (Figs. A.1.2.3.d, A.1.2.4.d, and A.1.2.5.d) shows a similar pattern to that of the CRCM in that it consistently underestimates CONUS spring temperatures. However, the west coast does show isolated areas of little to no bias or slight overestimations, most notably in March and April. In addition, the MM51 overestimates the Great Lakes especially the western portion of Lake Superior and southern portion of Lake Michigan.

The WRFG (Figs. A.1.2.3.e, A.1.2.4.e, and A.1.2.5.e) shows a similar pattern to that of the HRM3 with areas of overestimation in the central CONUS most noticeable in March and April. However, unlike the HRM3, the WRFG underestimates most of the western CONUS in April and May. The areas of underestimation are concentrated to the western CONUS in all spring months with greater bias values concentrated in the SW region. The WRFG also underestimates temperatures slightly in the SE region, especially in May, with the greatest underestimations occurring in FL.

2.2 Summer

Average bias values for summer range from -2.56K from the WRFG in August to +0.67K from the HRM3 also in August, demonstrating a smaller range of errors when compared to spring (Table C.1). The WRFG has the largest negative bias values during the months of July and August with the CRCM overtaking the WRFG with a slightly larger negative bias in June. However, it should be noted that the mean bias values for the CRCM and WRFG in June are only +0.03K different at -2.16K and -2.13K, respectively. In all summer months, the MM5I and ECP2 exhibit the next largest negative biases, in that order, with the HRM3 demonstrating the smallest bias values. The HRM3, unlike the other models, shows positive biases but only in the months of July and August. Using the mean summer biases to rank the models, from best to worst, the following order (with their respective seasonal mean bias values) is achieved: HRM3 (+0.29K), ECP2 (-1.53K), MM5I (-2.11K), CRCM (-2.19K) and WRFG (-2.40K).

The CRCM (Figs. A.1.2.6.a, A.1.2.7.a, and A.1.2.8.a), in a similar fashion to the spring season, shows little to no bias in the central and NE regions with underestimations in the SE and western CONUS and overestimations along the west coast and over the Great Lakes. Like the CRCM, the ECP2 (Figs. A.1.2.6.b, A.1.2.7.b, and A.1.2.8.b) exhibits the largest underestimations in both spatial extent and magnitude in the western CONUS, smaller underestimations in the SE and overestimations over the Great Lakes. However, unlike the CRCM, the ECP2 shows the underestimations of the SE extending further north and west towards the Great Lakes Region and isolated pockets of overestimation in the western half of the CONUS.

HRM3 (Figs. A.1.2.6.c, A.1.2.7.c, and A.1.2.8.c) summer temperatures mimic a pattern similar to those of spring with the largest underestimates occurring in the SW and

overestimations during the first part of the season that decrease in magnitude and spatial extent as the season progresses. However, unlike the spring, the largest overestimations during the summer are concentrated in the central one-third of the CONUS as well as the NW. MM5I simulations exhibit negative biases throughout much of the CONUS with a small area in the south central U.S. showing little to no bias.

The MM5I (Figs. A.1.2.6.d, A.1.2.7.d, and A.1.2.8.d) and WRFG (Figs. A.1.2.6.e, A.1.2.7.e, and A.1.2.8.e) show similar patterns during the months of summer. Both RCMs show warmer lake surface temperatures compared to NARR and widespread underestimations across the CONUS with the greatest negative biases occurring in the western half of the country, specifically the SW. Both models depict a small region with little to no bias in the central part of the country but the size and placement of that region does vary between models. The MM5I shows little to no bias in the south-central U.S. in June and July with a slight movement north in August while the WRFG depicts a slightly larger area in the north-central U.S. in all summer months.

2.3 Autumn

During the autumn season, average bias values range from -2.64K from the MM5I in September to +1.21K from the HRM3 in November indicating a smaller range than the spring season but a larger spread than the summer season (Table C.1). The CRCM, MM5I and WRFG consistently exhibit the largest negative biases. The MM5I shows the largest negative bias in September but the performance of the CRCM declines as the season progresses, resulting in the largest negative biases in October and November. The ECP2 also has negative mean bias values in all autumn months but the values are significantly less, by almost 1K, in each case when compared to the MM5I and CRCM. The ECP2, MM5I and WRFG all show improvements

between September and November with negative bias values becoming less negative in all cases. The CRCM and HRM3 however, do not reflect the same consistent skill improvements each month, as the CRCM bias becomes more negative from September to October before improving in November, and the HRM3 bias becomes slightly less positive in October before the performance drops in November. Ranking the models, from best to worst, according to mean autumn biases, yields the following order (with their respective seasonal mean bias values):

ECP2 (-0.72K), HRM3 (0.76K), WRFG (-1.99K), MM5I (-2.22K) and CRCM (-2.50K).

During the autumn months, the CRCM (Figs. A.1.2.9.a, A.1.2.10.a, and A.1.2.11.a) and MM5I (Figs. A.1.2.9.d, A.1.2.10.d, and A.1.2.11.d) simulate cooler temperatures compared to NARR over much of the CONUS. The CRCM does show a broad region with little to no bias extending from Iowa to Louisiana in September while the MM5I shows a broad area in the NW where there was no bias or overestimations in isolated areas in November. The MM5I also depicts larger underestimations in the east-central part of the CONUS in September and October.

The ECP2 (Figs. A.1.2.9.b, A.1.2.10.b, and A.1.2.11.b), showing improvements from the summer months, exhibits larger regions of cooler-than-NARR temperatures in the west but not to the extent that was observed in the CRCM and MM5I. The model improves throughout October and November with fewer underestimations in the west, but does simulate a larger area of overestimations in the central CONUS as the summer progresses. The HRM3 (Figs. A.1.2.9.c, A.1.2.10.c, and A.1.2.11.c) shows almost all of the CONUS to be warmer than NARR in all months and all regions during the autumn season, with a few exceptions observed in the southcentral CONUS. These overestimations of temperature grow in spatial coverage and magnitude each month throughout the season.

WRFG (Figs. A.1.2.9.e, A.1.2.10.e, and A.1.2.11.e) shows a September and October pattern similar to that of the CRCM and MM5I with the largest negative biases concentrated in the southwest CONUS and small areas with little to no bias present in the central CONUS. However, in November the WRFG shows more warm biases in the northern plains. It should also be noted that all RCMs begin to show a cold bias over the Great Lakes in November, with the exception of the HRM3 which only shows a slight cool bias over Lakes Superior, Huron and Erie and a warm bias over parts of Lake Michigan.

2.4 Winter

With the average bias values ranging from -2.16K from the CRCM in February to +2.93K from the HRM3 in January, the winter season has the largest range of average bias values among the four seasons (Table C.1). Again, the CRCM has the largest negative bias and the HRM3 has the largest positive bias values in all three months. All other RCMs fall between the two extremes of the CRCM and HRM3 in each month. The ECP2 shows increasing negative biases from December to February although the bias values only change by -0.25K from -0.38K to -0.63K. Bias values from the MM5I show a change in the sign going from +0.40K in December to -0.53K in January, and then further decline in February to -1.11K. Unlike the other RCMs, the WRFG is the only model to consistently improve during the winter months. This improvement also results in the WRFG having the smallest bias value in February. Using the mean winter biases to rank the models, from best to worst, the following order (with their respective seasonal mean bias values) is achieved: WRFG (-0.38K), ECP2 (-0.47K), MM5I (-0.86K), CRCM (-1.81K) and HRM3 (+2.44K).

The CRCM (Figs. A.1.2.1.a, A.1.2.2.a, and A.1.2.12.a) exhibits cooler biases in the western CONUS much like the previous seasons. However, the spatial extent and magnitude of these biases is less in December and January. Also during these two months, little to slightly warm biases are shown in the north central U.S. that ends with little to no bias in this part of the CONUS in February. Underestimations are also observed in the SE, extending northward into parts of the Mid-Atlantic and NE in all months. All other RCMs demonstrate warmer biases in all winter months compared to the previous seasons. However, the spatial concentration and magnitude vary by model and month.

The ECP2 (Figs. A.1.2.1.b, A.1.2.2.b, and A.1.2.12.b) and WRFG (Figs. A.1.2.1.e, A.1.2.2.e, and A.1.2.12.e) show similar patterns during the winter months. Large areas of warm biases occur in the central CONUS, extending into the western part of the country. However, the western CONUS does not show as concentrated of an area of overestimations and progressively shows more sporadic pockets of over- and underestimations as the season progresses. The eastern half of the CONUS shows little bias in all three months with the exception of the WRFG in December, which shows slight cool biases in the NE region. The ECP2 and WRFG also express cool biases over the Great Lakes, with the WRFG being cooler than the ECP2 in all cases.

The HRM3 (Figs. A.1.2.1.c, A.1.2.2.c, and A.1.2.12.c) exhibits warm biases over the entire CONUS during the winter season with the largest biases occurring in January. The largest overestimations occur in the north-central CONUS in all cases. A few areas do exhibit little to no bias and include southern Texas and southern Florida in December and February, and southwestern Texas in January. The Great Lakes in December show few biases over Lake Michigan and slight underestimations over the other lakes. However, as the season progresses,

the Lakes begin to demonstrate fewer underestimations and more overestimations, resulting in warm biases over all 5 lakes in February.

Winter temperature biases from the MM5I (Figs. A.1.2.1.d, A.1.2.2.d, and A.1.2.12.d) resemble a pattern similar to the ECP2 and WRFG with a few noticeable differences. While the MM5I shows warm biases in the central CONUS and sporadic over- and underestimations in the western CONUS, the model also exhibits cool biases across much of the SE, extending as far north as Pennsylvania, and the largest biases occurring in southern Texas. The Great Lakes show cool biases in December that diminish throughout winter and result in overestimations over all 5 lakes, especially along the coastlines, in February.

2.5 Summary

In summary, RCM performance over the CONUS varies from season to season with some models representing mean temperatures better than others. During the spring, the HRM3 shows the least amount of bias followed by the WRFG, ECP2, MM5I and CRCM. In summer, the HRM3 continues to demonstrate the least amount of bias, followed by the ECP2, MM5I and CRCM with WRFG showing the lowest level of skill. During the autumn months, the ECP2 overtakes the HRM3 in overall skill, with the WRFG, MM5I and CRCM following. Finally, during the winter, the WRFG has the lowest mean bias value, followed by the ECP2, MM5I, CRCM and HRM3. In all seasons collectively, the HRM3 shows the least amount of bias, with the exception of winter, where it shows the largest amount of bias, and the CRCM consistently shows large bias values in all seasons. The WRFG exhibits more biases during the summer and autumn while showing the second lowest and lowest bias scores during the spring and winter,

respectively. The ECP2 shows consistently lower biases than the MM5I, however neither of these models exhibit the lowest or highest bias values in any season.

Overall, biases appear to be larger over the western CONUS where topography is more complex. In most cases, these biases are negative, although some isolated positive biases do exist and are frequently observed near the higher elevations of the Rocky, Cascade and Sierra-Nevada Mountain Ranges. The CRCM and MM5I show negative biases across the CONUS more frequently than the other RCMs while the HRM3 shows positive biases across the CONUS more frequently. However, all models show more positive biases during the winter season. Biases in the eastern half of the CONUS vary from model to model and season to season but with cool biases dominating in most cases. However, warm biases are observed over the Great Lakes throughout much of the year except during autumn when most models show little to no bias over the lake surfaces and in winter when the ECP2, MM5I and WRFG show negative biases over the lakes.

3. Statistics and Annual Cycle of Mean Surface-Air Temperature

Figure B.1 shows the annual cycle of monthly mean temperatures as simulated by each RCM and from NARR. As revealed by NARR temperatures, there is a distinct annual cycle with maximum temperatures occurring in July and August and minimum temperatures in January. All RCMs capture this annual cycle very well. The magnitudes of monthly mean temperatures, however, differ among the models and from NARR, and the differences vary by month but are within 5 K. Monthly, seasonal and annual bias values are given in Table C.1.

Except for the HRM3 which is consistently warmer than NARR throughout the year, all other models underestimate monthly mean temperature for all months of the year, with the

exception of a slightly positive bias of 0.20 K from WRFG in February. The ECP2 contains smaller biases as compared to the CRCM and MM5I, especially during the autumn and winter seasons where bias values from November to January are within half of a degree of NARR. The WRFG follows a pattern similar to the CRCM and MM5I during the summer and autumn seasons, but shows improvement during the winter and spring seasons, with the smallest bias values occurring from January to March, all of which are within 0.5 K of NARR. The HRM3 best simulates the trend of mean temperatures between April and October with the smallest bias values, all of which are less than 0.5 K except in August and September when bias values are greater than 0.5 K but less than 0.75 K. However, the HRM3 is the only model to demonstrate a warmer trend during any given month, with the exception of a slightly positive bias of 0.20 K from WRFG in Feb. The HRM3 is warmer than NARR in all months of the year except May and June, with the warmest biases occurring during the cooler months between November and March.

4. Spatial Distribution of Daily Accumulated Precipitation

4.1 Spring

The spring precipitation patterns, as depicted by NARR (Figs. A.2.1.3.a, A.2.1.4.a, and A.2.1.5.a), show the highest amounts along the coast of the Pacific NW, with sharp gradients observed along the Cascades. This elongated region of high precipitation recedes northward out of California and becomes concentrated in Oregon and Washington as the season progresses. A secondary maximum is observed in the SE centered over Alabama, Mississippi and Tennessee. This region of high precipitation fades with a gradient extending northwest and west, with a more westerly gradient shown in April and May. This region of high precipitation expands in

May, encompassing areas such as Iowa to the north and western Oklahoma and central Texas to the west. NARR also exhibits high precipitation over the peaks of the Rockies with little precipitation occurring in the SW.

Overall, most models capture the distribution of precipitation across CONUS with the highest values occurring in the SE and Pacific NW and a minimum in the SW. However, the areal coverage, magnitude and position do show large variations from model to model. Among the five RCMs, the CRCM shows the highest spatial correlation with NARR values in each month with 0.87, 0.87 and 0.83 for March, April and May, respectively while the HRM3 consistently exhibits the lowest skill, with correlation values of 0.71, 0.68 and 0.61 for the spring months (Table C.8).

4.2 Summer

Summer precipitation patterns from NARR (Figs. A.2.1.6.a, A.2.1.7.a, and A.2.1.8.a) show the region of higher precipitation along the coast of the Pacific NW that decreases throughout the summer, and an increase in precipitation, specifically in July and August, over the SW with the onset of the SW monsoon. In June, higher precipitation amounts are observed in the SE but also in the central CONUS extending as far north as Minnesota and as far south as the Gulf coast of Texas. However, as the summer season progresses, the precipitation maximum begins to separate and forms two isolated regions of high precipitation, one centered over northeastern Iowa and the other along the SE coastline from North Carolina to Louisiana. Lower precipitation values are also observed over the Great Lakes during all summer months.

All RCMs show difficulties in accurately representing the spatial pattern of precipitation during the summer months, most likely due to the localized nature of summer precipitation

which is not captured well by the RCMs at the current resolution of 50 km. More specifically, the RCMs are unable to correctly place the highest precipitation amounts in the eastern CONUS, the lowest precipitation amounts in the central CONUS and also inaccurately simulate the magnitude of precipitation along the coasts of the NW and SE. The CRCM exhibits the highest spatial correlation values in June and August, with the ECP2 having a slightly higher value in July (Table C.8). The lowest spatial correlations, similar to spring, are observed in all months by the HRM3. It should also be noted that all RCMs have their lowest summer correlation values in July.

4.3 Autumn

In autumn, highest precipitation amounts in NARR (Figs. A.2.1.9.a, A.2.1.10.a, and A.2.1.11.a) return to the Pacific NW by November and lower precipitation once again is found in the SW as the North American Monsoon retreats. Higher values of precipitation centered over the Kansas, Missouri, and Oklahoma border begins to expand and move towards the SW and sets up an east-to-west gradient over the central CONUS. Higher precipitation amounts in Florida and along the SE coastline in September also fade as the season progresses.

Overall, the RCMs perform better in autumn compared to summer, with the exception of the MM5I, but all RCM correlations are still less in autumn than they were during the spring (Table C.8). In general, the RCMs show skill in resolving the higher precipitation amounts on the windward side of the Cascades and the west-to-east gradient of increasing precipitation. The CRCM, ECP2 and WRFG show the best overall skill in simulating precipitation patterns in autumn with the CRCM and ECP2 being slightly better than WRFG overall. In addition, the

HRM3 and MM5I demonstrate the least skill overall with the HRM3 being slightly better in September and October and the MM5I being slightly better in November.

4.4 Winter

Winter precipitation patterns from NARR (Figs. A.2.1.1.a, A.2.1.2.a, and A.2.1.12.a) are similar to spring in the Pacific NW, with the highest amounts located along the coastline, which decreases westward becoming very small on the leeward side of the Cascade Mountains. Higher precipitation values are also observed in the SE with the highest amounts concentrated in and around Louisiana, Mississippi, and Alabama. As the season progresses, the higher amounts begin to expand eastward to include Georgia and northward to include Tennessee and parts of Kentucky. In all winter months, a noticeable gradient can also be discerned. This gradient originates in southern Texas and extends north and northeast through the central plains and into the Great Lakes region with a SW to NE orientation. The Great Lakes also show increased precipitation amounts along the eastern shores of Lakes Superior, Michigan and Huron in December and January but not in February as lake effect snow begins to diminish with cooler lake temperatures.

Most models capture the higher precipitation amounts in the Pacific NW, but do not show the lower amounts on the leeward side of the Cascades. The models also show large variations in the location and magnitude of the SE precipitation maxima. Most RCMs also depict a much wider gradient than is observed from NARR extending across the central part of the CONUS. The CRCM showed the highest skill in simulating precipitation in all months with correlation values of 0.84, 0.86 and 0.86 for December, January and February, respectively (Table C.8).

The CRCM was followed by the WRFG, ECP2 and MM5I. The HRM3 showed the poorest spatial correlations in all winter months.

4.5 Summary

Overall, the RCMs were able to simulate precipitation patterns but not with the same level of accuracy as the temperature simulations. Precipitation simulations show regional and local variations that vary by model and season. In the spring, the CRCM had the greatest spatial accuracy, followed by the ECP2, the MM5I and WRFG with identical correlation values, and the HRM3. A similar pattern was observed during the summer with the CRCM and ECP2 having the best correlation value followed by the MM5I, WRFG and HRM3. In autumn, model performances shifted with the ECP2 showing the highest spatial accuracy followed by the CRCM and WRFG. The MM5I had the lowest spatial correlation value during autumn, placing the HRM3 ahead of the MM5I during this season. During the months of winter, the CRCM again showed the highest spatial correlation value followed by the WRFG, ECP2, MM5I and HRM3.

The ECP2 and WRFG showed the same season skill pattern with correlation values highest during the winter, followed by spring, autumn and summer. The CRCM pattern was slightly different with spring surpassing winter, followed by autumn and summer. The HRM3, similar to the ECP2 and WRFG, showed the highest correlation values in winter. However, the HRM3 showed the lowest correlation values in spring and summer. Lastly, the MM5I, similar to the CRCM, demonstrated the highest spatial correlation in spring followed by winter, summer and autumn. Overall, the models tend to have high skill in simulating cold season precipitation

than warm season with all but MM5I showing the lowest skill in simulating summer precipitation pattern.

The most noticeable differences in the spatial distribution of precipitation across the CONUS are observed in the northwestern region of the CONUS, where the complex topography proved difficult for all RCMs overall. These differences in the western portion of the domain are largely due to highly localized regions of over and underestimations that are demonstrated in all simulations rather than the spatially consistent and smooth precipitation patterns observed from NARR. However, the eastern third of the CONUS also shows varying spatial accuracy as the highest concentrations of precipitation vary from model to model and month to month in this region. Moreover, differences are also observed in the NE as the RCMs falsely expand the regions of lower precipitation in some instances but falsely expand the regions of higher precipitation in others.

5. Spatial Distribution of Daily Accumulated Precipitation Differences

5.1 Spring

All models show positive biases in each of the spring months with average bias values ranging from +0.29mm for the HRM3 in May to +1.04mm for the ECP2 in March (Table C.5). The WRFG has the smallest bias value of +0.41mm in March while the HRM3 has the smallest bias values of +0.40mm and +0.29mm in April and May, respectively. The HRM3 and WRFG also consistently showed lower biases in all spring months compared to the other RCMs. In March and April, the CRCM and MM5I trail the HRM3 and WRFG, in that respective order. In May however, the MM5I and CRCM bias values are closer together with a slightly lower bias value from the MM5I. In all spring months the ECP2 has the largest bias values. Ranking the

models, from best to worst, according to mean spring biases, yields the following order (with their respective seasonal mean bias values): HRM3 (+0.37mm), WRFG (+0.40mm), CRCM (+0.52mm), MM5I (+0.62mm) and ECP2 (+0.90mm).

The CRCM (Figs. A.2.2.3.a, A.2.2.4.a, and A.2.2.5.a) shows both wet and dry biases across the CONUS during the spring, with more widespread dry biases. The larger wet biases are observed during the latter part of spring, specifically in May, and are concentrated in the western half of the CONUS as well as the Great Lakes region. Slight dry biases are shown along the Gulf Coast in Louisiana, Mississippi, Alabama and the panhandle of Florida in March and May, as well as Georgia in March and Texas and Oklahoma in May. The largest dry biases are shown over the higher elevations of the Cascade Mountains in Washington and the Sierra-Nevada Mountains in California, but these underestimations gradually fade away as spring progresses.

The ECP2 (Figs. A.2.2.3.b, A.2.2.4.b, and A.2.2.5.b) shows the largest overestimations of precipitation of all models during all of the spring months. The largest underestimations are observed in the NW, NE and GLR. However, these wet biases do decrease in both magnitude and spatial coverage as the season progresses. Similar to the CRCM, the ECP2 also shows a slight dry bias over the SE states along the Gulf Coast in March and May with the largest underestimations occurring in Texas and Louisiana in May.

The HRM3 (Figs. A.2.2.3.c, A.2.2.4.c, and A.2.2.5.c) exhibits both wet and dry biases with the former being slightly larger. These wet biases are concentrated in New Mexico and Texas, along the Rocky and Appalachian Mountain Ranges and in the NE and GLR. Dry biases are observed in the SE during all spring months, but the locations of these underestimations shift north and west to as far as Nebraska as the season progresses. The dry biases also increase in

magnitude from March to May. Underestimations of precipitation are also shown along the western coast of the CONUS with the greatest values occurring in western Washington, western Oregon and northern California. However, unlike the underestimations found in the SE, the underestimations along the West Coast decrease in magnitude from March to May.

The MM5I (Figs. A.2.2.3.d, A.2.2.4.d, and A.2.2.5.d) and WRFG (Figs. A.2.2.3.e, A.2.2.4.e, and A.2.2.5.e) demonstrate similar patterns during the spring season. Both models exhibit overestimations in the NW that are most noticeable in March and April. Overestimations are also observed in the NE and GLR in all spring months, which extend southward into parts of the SE in April and May. However, the MM5I and WRFG both show a dry bias over the SE during March, which shifts westward into the southern plains in April and May, resembling a pattern similar to the HRM3 in May. One discernable difference between the MM5I and WRFG is that the overestimations in the NE and along the East Coast are greater in both magnitude and spatial extent for the MM5I compared to the WRFG.

5.2 Summer

Average bias values for summer range from -0.21mm for the HRM3 in August to +0.60mm from the CRCM in June (Table C.5). Similar to the spring season, the HRM3 and WRFG have the lowest bias values overall during the summer months. Both the HRM3 and WRFG also demonstrate a similar bias pattern throughout summer in that the biases in both models go from being slightly positive, to near neutral with values of -0.01mm and 0.00mm, respectively, to slightly negative. The CRCM shows the largest biases in June and August with the MM5I showing a slightly larger positive bias in July. Using the summer biases to rank the models, from best to worst, the following order (with their respective seasonal mean bias values)

is achieved: HRM3 (-0.02mm), WRFG (+0.04mm), ECP2 (+0.35mm), MM5I (+0.52) and CRCM (+0.56).

During the summer, the CRCM (Figs. A.2.2.6.a, A.2.2.7.a, and A.2.2.8.a) is the only RCM to show large regions of excess precipitation over the western third of the CONUS between the Rocky Mountains and the West Coast. These overestimations, while spatially extensive, show localized maxima throughout much of the western CONUS but are seemingly located away from the coast. The CRCM also exhibits wet biases in the eastern third of the country, including the GLR, with the largest overestimations occurring in the SE. The central CONUS shows an area of underestimation from Texas to Minnesota during the summer, which increases in size and magnitude and shifts slightly to become centered over the Iowa-Missouri border as the season progresses.

The ECP2 (Figs. A.2.2.6.b, A.2.2.7.b, and A.2.2.8.b) shows a large area of overestimations in the eastern CONUS in all months while the greatest positive biases occur during the earlier part of summer in June. In the NW, underestimations are also shown in the highest elevations of the Cascade Mountains but these biases diminish and become almost neutral in August. In the central CONUS, the ECP2 demonstrates a dry bias in all months with the spatial extent spreading from parts of the SW and south-central plains in June to parts of the north-central CONUS and GLR in August. However, in all summer months, the ECP2 shows a distinct wet bias along the windward side of the Front Range in Colorado.

The HRM3 (Figs. A.2.2.6.c, A.2.2.7.c, and A.2.2.8.c) and WRFG (Figs. A.2.2.6.e, A.2.2.7.e, and A.2.2.8.e) exhibit very similar patterns, as well as similar average bias values, during the summer. Both RCMs show slight underestimations in the Mid-Atlantic shifting towards the NE, particularly in June and July, and slight underestimations in the highest

elevations of Colorado. Both RCMs also demonstrate large areas of underestimations in the central CONUS. In both cases, the underestimations reach their greatest spatial extent in August with the greatest underestimations shifting from the Texas-Louisiana border to the Minnesota-Iowa border as the season progresses. Both models also show dry biases over Florida and along the Gulf Coast during all summer months. However, while the HRM3 and WRFG show similar patterns, a few differences do exist. The HRM3 shows a larger region of overestimations in the Mid-Atlantic and parts of the SE in June and in the NE in July. The HRM3 also shows the underestimations in the central CONUS extending further north and west into Montana, Idaho and parts of Washington and Oregon.

The MM5I (Figs. A.2.2.6.d, A.2.2.7.d, and A.2.2.8.d) illustrates a widespread area with little to no bias in the western regions of the CONUS with only a few overestimations along the Rocky Mountains. The largest overestimations during all summer months occur in the SE, with the greatest biases occurring along the Appalachian Mountains. In the central CONUS, underestimations of precipitation are shown and progressively expand in spatial extent from June through August. In June, the underestimations are centered along an axis extending from Texas to southern Minnesota, while in August the area grows larger and is oriented from Arizona to Wisconsin, Michigan and Minnesota with the largest underestimations occurring in Arizona. Noticeable underestimations are also visible in the NE, including parts of Maine, Vermont, New Hampshire and New York during August.

5.3 Autumn

During autumn, average bias values range from -0.01mm from the HRM3 in October to +0.54mm from the ECP2 in November (Table C.5). The HRM3 shows the lowest bias values in

all autumn months. The CRCM, ECP2 and WRFG bias values do not show a distinct pattern, proving one model to be better than the others. However, the ECP2 and WRFG biases do progressively get larger as the season progresses. The MM5I exhibits the largest biases, excluding the month of November when the ECP2 demonstrates a higher bias value. Ranking the models, from best to worst, according to mean autumn biases, yields the following order (with their respective seasonal mean bias values): HRM3 (0.00mm), WRFG (+0.19mm), CRCM (+0.22mm), ECP2 (+0.28mm) and MM5I (+0.37mm).

In September, the CRCM (Fig. A.2.2.9.a) shows slight overestimations of precipitation over the Great Lakes and Ohio as well as parts of the Pacific NW in Washington and Oregon. Underestimations are also observed throughout Wyoming, Utah, Colorado, Arizona and New Mexico. However, these underestimations are sporadic and isolated in nature. Interestingly, while the Great Lakes show underestimations, the surrounding areas in Minnesota, Wisconsin and Michigan show overestimations. Additionally, the east coast, from Maine to North Carolina, Florida and the south central plains all demonstrate underestimations. The largest underestimations are observed in Nebraska and Missouri. In October, most of the CONUS has little to no bias with the exceptions of the extreme NW and eastern and Gulf coasts (Fig. A.2.2.10.a). In the NW, the largest underestimations of October are shown on the windward side of the Cascade Mountains while the leeward side demonstrates a larger area of overestimations. Along the eastern seaboard, slight overestimations are observed from Maine to Florida extending west into central Texas. In November, a similar pattern is observed along the eastern seaboard but with little to no bias along the North Carolina, South Carolina and Georgia coasts (Fig. A.2.2.11.a). In the NW, overestimations are still observed and with a greater magnitude

compared to October. However, unlike September and October, underestimations of as much as -5mm on the windward side of the Cascade Mountains are observed in November.

The ECP2 (Fig. A.2.2.9.b) in September shows little to no bias over the western and eastern thirds of the CONUS except for Colorado and Utah where the model shows a distinct wet bias on the windward side of the Rocky Mountains. Most of the central CONUS shows a dry bias, with the greatest underestimations in Oklahoma, eastern Kansas and Arkansas. In October, the central CONUS still exhibits underestimations but to a lesser extent compared to September as the magnitude is less and the spatial extent, centered over the Oklahoma, Texas, Arkansas and Louisiana border, is much smaller (Fig. A.2.2.10.b). The NW also shows a distinguishable difference in October, with wet biases extending into eastern Washington and Oregon on the leeside of the Cascade Mountains. Finally, in November, the ECP2 demonstrates underestimations in the SE extending from Arkansas and Louisiana to Georgia, overestimations in the NE from northern Kentucky to Maine, and both over- and underestimations in the NW (Fig. A.2.2.11.b). The greatest overestimations, much like the previous months, occur east of the Cascade Mountains. However, large underestimations of up to -4.5mm are observed along the windward slopes of the Cascade Mountains.

Autumn simulations from the HRM3 (Figs. A.2.2.9.c, A.2.2.10.c, and A.2.2.11.c) depict widespread dry biases over much of the CONUS in September and October with the greatest underestimations occurring in the Great Lake states of Wisconsin and Michigan, the south central CONUS and Florida. In October and November, the largest underestimations are found in the Pacific NW along the windward side of the Cascade Mountains, especially in western Washington. The large region of underestimations in the central CONUS decreases in spatial

extent and magnitude in November, while the east coast still shows underestimations from northern Maine to southern Florida.

The MM5I (Figs. A.2.2.9.d, A.2.2.10.d, and A.2.2.11.d) and WRFG (Figs. A.2.2.9.e, A.2.2.10.e, and A.2.2.11.e) demonstrate similar patterns in autumn. In September, both models depict little to no bias along the west coast, underestimations in the central CONUS with the greatest values occurring between Iowa and Oklahoma, and a few wet biases in the SE. However, the MM5I depicts the overestimations in the SE extending into Florida while the WRFG depicts underestimations in Florida. In October, the overestimations of the SE become only slight underestimations in some areas with others showing little to no bias. The underestimations of the central CONUS also show a decrease in magnitude and also a slight shift south and west to be centered over the Texas, Oklahoma and Arkansas. Also, Washington depicts slight overestimations on the eastern side of the state with underestimations occurring along the coast along the windward side of the Cascade Mountains. Finally, in November, both models show the underestimations of the central CONUS shifting towards the SE and the overestimations in the NW expanding eastward into parts of Montana and Wyoming and southward into California, Nevada and Utah. The underestimations west of the Cascade Range also intensify and are observed in Oregon as well.

5.4 Winter

Average bias values for winter range from +0.18mm from the HRM3 in December to +0.95 from the ECP2 in both January and February (Table C.5). The HRM3 has the lowest bias values in all winter months followed by the WRFG and CRCM. The ECP2 consistently demonstrates the highest bias values in all months during the winter season. One noticeable

trend across all models is that bias values generally increased, demonstrating degrading skill, as the season progresses. Using the winter biases to rank the models, from best to worst, the following order (with their respective seasonal mean bias values) is achieved: HRM3 (+0.27mm), WRFG (+0.35mm), CRCM (+0.37mm), MM5I (+0.54mm) and ECP2 (+0.86mm).

The CRCM (Figs. A.2.2.1.a, A.2.2.2.a, and A.2.2.12.a) in winter shows little to no bias across the central CONUS with slight overestimations in the NE, larger overestimations in the NW and slight underestimations in the SE. The underestimations in the NE are most noticeable in late winter but do not extend north of New York or south of Pennsylvania and Ohio, except in January when slight overestimations extend into West Virginia and Kentucky. The overestimations of the NW are greater in magnitude compared to those in the NW, but are mirrored by large underestimations on the windward side of the Cascade Mountains. A distinct pattern noticeable in winter from the CRCM is that all of the highest elevations in Washington, Oregon and California show a pattern similar to the Cascade Mountains with large underestimations of -4 to -5mm occurring on the west side of the mountains and overestimations of +4 to +5mm occurring on the east side of the mountains. The drier simulations of the SE intensify as the season progresses but remain spatially constant centered over the Gulf Coast states.

Of all the models, the ECP2 (Figs. A.2.2.1.b, A.2.2.2.b, and A.2.2.12.b) shows the largest overestimations in all winter months. The largest of these overestimations are shown in the NW and NE with slight overestimations in the north-central CONUS. In the SE, the ECP2 demonstrates overestimations along the Gulf coastline in December, but by February, these overestimations dissipate and only a small area remains over southern Louisiana and Mississippi. The HRM3 (Figs. A.2.2.1.c, A.2.2.2.c, and A.2.2.12.c) shows a distinctly different pattern

compared to the other models in winter. Unlike the other models that show little to no bias in the south-central CONUS, the HRM3 depicts overestimations in the south-central CONUS with the largest overestimations in southern Texas. The HRM3 also depicts a broad swath of underestimations along the east coast from Maine to Florida in December and January and from North Carolina to Florida in February. Finally, the HRM3 shows several isolated areas of underestimations from -2 to -5 mm along much of the west coast.

The MM5I (Figs. A.2.2.1.d, A.2.2.2.d, and A.2.2.12.d) and WRFG (A.2.2.1.e, A.2.2.2.e, and A.2.2.12.e) again show similar bias patterns. Both models, like the CRCM and ECP2 show the greatest overestimations in the Pacific NW. The MM5I and WRFG also show an isolated area of large underestimation as great as -5 mm in the NW corner of Washington in all three months of winter. Both models also depict dry biases over much of the SE centered over Louisiana, Mississippi and western Tennessee in all months with a slight wet bias over central and south Florida. Some differences between the MM5I and WRFG are also observed but vary from month to month. In December, the MM5I shows dry biases extending into the NE as far north as western Maine. The WRFG does show some dry biases in the NE but in a more sporadic and isolated manner compared to the MM5I. In January and February, the MM5I shows overestimations over the Great Lakes and parts of the surrounding states of Minnesota, Wisconsin, Michigan and New York while the WRFG only shows these overestimations to be present over Lakes Erie and Ontario.

5.5 Summary

In summary, CONUS precipitation biases show variations by season and model. In all seasons the HRM3 shows the lowest domain averaged mean bias value with the WRFG close

behind, followed by the CRCM, MM5I and ECP2 in spring and winter, the ECP2, MM5I and CRCM in summer and the CRCM, ECP2 and MM5I in autumn. Overall, wet biases are shown more frequently in the western CONUS with a few exceptions between July and October where little to no biases are observed or slight dry biases extend west from the central part of the CONUS. However, it should be noted that embedded within these large scale overestimations are isolated areas of underestimations that coincide with the windward side of the various western mountain ranges. Most of the dry biases are concentrated within the southeastern CONUS between November and March or the central CONUS between April and October. Of all the RCMs, the HRM3 consistently shows the greatest dry biases while the ECP2 and MM5I consistently show the greatest wet biases.

6. Statistics and Annual Cycle of Daily Accumulated Precipitation

Figure B.2 shows the annual cycle of daily accumulated precipitation as simulated by each RCM and from NARR. All models appear to overestimate daily precipitation in all months of the year with a few exceptions. Monthly, seasonal and annual bias values are given in Table C.5.

Unlike temperature, the NARR precipitation does not demonstrate seasonal variations in precipitation, but does show a slight late spring and early summer maximum during the month of June. All models capture the month to month variations and show a slight maximum during the month of June except the ECP2 which does not appear to capture the month to month variations, shows significantly higher precipitation values during the winter and spring seasons peaks in March. Of all of the RCMs, the CRCM, HRM3 and WRFG show the best agreement with the overall shape of the curve. However, it should be noted that the CRCM consistently

overestimates precipitation in all months, the HRM3 only overestimates precipitation from Jan-Jun but shows the smallest bias of all models from Sep-Dec and the WRFG shows a steady increase in precipitation from Jan-Jun rather than the actual fluctuations shown by NARR.

b. Northeast

1. Statistics and Annual Cycle of Mean Surface-Air Temperature

The seasonal pattern of mean temperatures from NARR exhibits maximum temperatures in July and August and minimum temperatures in January with a steady increase from January to June and a steady decrease from July to December (Fig. B.3). All models capture the seasonal cycle of mean temperatures in the NE showing peak temperatures in July and August and minimum temperatures in January. However, during the cold season from November to March, the HRM3 shows the largest deviation from the NARR temperature curve with consistently warmer temperatures. The CRCM and MM5I, on the other hand, are consistently cooler than NARR in all months of the year while the WRFG is cooler between May and January but then becomes warmer than NARR from February to April. Of all the models, the ECP2 most closely follows the NARR temperature cycle, with slightly cooler temperatures observed in June and July. All monthly, seasonal and annual bias values are offered in Table C.9.

2. Statistics and Annual Cycle of Daily Accumulated Precipitation

The annual cycle of NARR precipitation shows a steady but gradual increase from February to July, followed by slight fluctuations between July and November with relative minima in August and October and relative maxima in September and November, and a quick decline from November to an annual minimum in February (Fig. B.4). Most models are able to

capture the seasonal pattern of precipitation in the NE but with varying magnitudes, with the greatest differences observed between February and July. All of the models produce higher precipitation from December through July. The CRCM best captures the seasonal precipitation cycle of NARR, although the model does show higher precipitation amounts in all months of the year except for October when the model appears to correctly capture the magnitude of precipitation. The ECP2 also expresses a similar precipitation pattern but is consistently much higher than NARR and all other models from October to July and does not correctly simulate the slight increase in precipitation in September. The HRM3, MM5I and WRFG all show a less similar pattern with the most noticeable differences between February and July when NARR precipitation increases gradually and the models simulate more abrupt changes. The HRM3 peaks in May and begins to decline in June; the MM5I peaks in April and immediately shows a decrease in precipitation; and the WRFG peaks in June also showing an immediate decrease in precipitation. All monthly, seasonal and annual bias values are offered in Table C.13.

c. Southeast

1. Statistics and Annual Cycle of Mean Surface-Air Temperature

Mean temperatures from NARR depict a pattern similar to the NE, with minimum temperatures in January and peak temperatures in July and August (Fig. B.5). All models capture the seasonal cycle of mean temperatures well, but do show some consistent deviations from the NARR temperature curve. The HRM3 best simulates the NARR temperature pattern with only slight differences throughout the year. In March and April, as well as October through December, the HRM3 shows slightly cooler temperatures by less than 1K. The HRM3 also shows a slight overestimation of the peak temperatures in August by approximately 0.5K. The

curves from all other models are very close, especially from January through May when the curves are nearly overlap each other, and are consistently colder than NARR throughout the year. The CRCM, ECP2, MM5I and WRFG all show very similar values during the spring, autumn and winter seasons with the greatest spread occurring in the summer. Between June and August, the WRFG shows the lowest mean temperatures differing from NARR by as much as 2K, followed by the ECP2, MM5I and finally the CRCM which differs from NARR by less than 1K. All monthly, seasonal and annual bias values are offered in Table C.17.

2. Statistics and Annual Cycle of Daily Accumulated Precipitation

The annual cycle of daily accumulated precipitation time from NARR in the SE shows relatively steady precipitation amounts from January to March, a decrease in precipitation leading up to the lowest precipitation amounts in April, followed by increasing precipitation leading to a peak in June (Fig. B.6). Following the June maximum, precipitation slowly declines through the remainder of the year with a relatively constant period between July and September. All of the models overestimate the precipitation throughout the year except for CRCM which has slightly higher amounts in November and December. Among the 5 models, the MM5I has the largest differences from NARR, with summer and early autumn precipitation nearly doubling those of NARR. The ECP2 is in better agreement with the NARR precipitation pattern throughout the year compared to the MM5I; however, the model shows a false peak in August and a slight increase from November to December. The WRFG precipitation pattern differs the most from the rest of the models and from NARR in that it fails to capture the minimum in May and the maximum in June, but produces a pronounced maximum in September. The CRCM and HRM3 simulate a precipitation pattern most similar to NARR. Both models show a decrease in

April and May with a sharp increase during June. However, the models differ slightly from one another and NARR during the summer. The CRCM, after a slight decrease, shows an increase in precipitation peaking in August, while the HRM3 precipitation decreases from June to August but then shows a peak in September similar to the WRFG. All monthly, seasonal and annual bias values are offered in Table C.21.

d. Northwest

1. Statistics and Annual Cycle of Mean Surface-Air Temperature

An annual cycle similar to the other regions is observed in NW with maximum temperatures in July and August and minimum temperatures in December and January (Fig. B.7). In November and December, the rate of the decreasing temperatures is slower than those from August to October, and in January and February, the rate of increasing temperatures is also slower than those between March and July. All models capture the seasonal cycle of temperatures in the NW with shifts in the overall magnitude of the curve. The CRCM is the only model to remain cooler than NARR during all months of the year and the HRM3 is the only model to remain warmer than NARR throughout the year. It should also be noted that the CRCM has the largest underestimations in all months. The MM5I, while cooler than NARR from February to November, shows slightly warmer temperatures in December and January. The ECP2 and WRFG remain cooler than NARR between March and November, but similar to the MM5I, become warmer than NARR between December and February. All monthly, seasonal and annual bias values are shown in Table C.25.

2. Statistics and Annual Cycle of Daily Accumulated Precipitation

NARR precipitation in the NW shows a distinctly different pattern from those of NE and SE with a bimodal peak of precipitation in May and November and a minimum in August (Fig. B.8). From January to April, precipitation remains constant leading up to a sharp increase in precipitation to the May maximum. Between the two maxima in May and November, precipitation decreases to the minimum in August and gradually rises through November after which precipitation sharply decreases in December before leveling off in January. The CRCM, although showing greater precipitation than NARR in all months, does exhibit a similar curve compared to NARR. However, the model shows the minimum in September rather than August and also shows a slight decrease between January and April compared to the steady precipitation amounts of NARR during these months. The ECP2 however, is constant from January through May, missing the May maximum seen with NARR. The ECP2 precipitation is lower than NARR from June through September, but considerably higher during the rest of the year. The HRM3, MM5I and WRFG all show a decrease in precipitation between January and September with the HRM3 showing the lowest precipitation of all models. All three of these models produce greater precipitation amounts from December through April, but fall below the NARR precipitation curve in all other months. All monthly, seasonal and annual bias values are offered in Table C.29.

e. Southwest

1. Statistics and Annual Cycle of Mean Surface-Air Temperature

Mean temperatures from NARR in the SW also show maximum temperatures in July and August and minimum temperatures in December and January (Fig. B.9). All models capture the

seasonal cycle of temperatures but simulate cooler than NARR temperatures in all months of the year, excluding the HRM3. The HRM3 remains cooler than NARR in all months except November through February when temperatures are slightly warmer. However, the HRM3 simulates temperatures closest to NARR compared to all other models from March to October. The CRCM temperature curve is consistently the lowest of all models from October through May while the WRFG simulates the lowest temperatures of all models during the warm season from June through September. However, it should be noted that the WRFG, similar to NARR, is the only model to show the warmest temperatures in July followed by August. All other models show peak temperatures in August rather than July. All monthly, seasonal and annual bias values are offered in Table C.33.

2. Statistics and Annual Cycle of Daily Accumulated Precipitation

The annual cycle of daily accumulated precipitation from NARR in the SW demonstrates bimodal minima in April and November, with the April minimum showing the lowest precipitation amount (Fig. B.10). A gradual increase is observed from April to August when precipitation peaks, followed by a decrease in monthly precipitation to the second minimum in November. Following the November minimum, precipitation rises through February after which it levels off before falling to the first minimum in April. All models simulate the overall shape of the NARR precipitation curve between the two minima in November and April. However, all models show higher precipitation amounts during these months with the CRCM, ECP2 and HRM3 showing the largest overestimations. After the April minimum, model performance is highly variable in both shape and magnitude. The CRCM, among all of the models, has the largest overestimations by as much as +0.6 mm/day but does simulate a curve that best matches

the overall pattern of NARR. The WRFG shows relatively constant precipitation amounts from May to July before reaching a maximum close to that of NARR in August. However, the maximum is not preceded by a gradual increase as was the case for NARR. The WRFG also shows the second minimum to occur in October rather than November. The ECP2, HRM3 and MM5I all show less precipitation compared to NARR during the late summer and early autumn with the HRM3 and MM5I showing local minima rather than a maximum. The ECP2 shows a minimum in June and gradually rises throughout the remainder of the year before leveling off in January. All monthly, seasonal and annual bias values are offered in Table C.37.

f. Great Lakes Region

The following sections are presented to examine the spatial distribution of temperature and precipitation biases within the GLR. Similar to the CONUS, spatial plots and spatial difference plots for temperature and precipitation are presented. However, it is important to note that while the precipitation and precipitation difference color scales are the same as those used in the CONUS analysis, the temperature and temperature difference color scales used hereafter in the GLR analysis are different. Unique temperature color scales were chosen for each month within the GLR to obtain the greatest amount of detail and better identify the spatial variations that exist from month to month. A common temperature difference color scale for the GLR was used for all months, but contains a smaller range compared to the CONUS temperature difference color scale as the GLR did not show temperature differences as large as those observed within the CONUS. Because each month utilizes a unique color scale, the following temperature analyses will be discussed by month and presented by season as opposed to being

discussed by season only. The following precipitation analyses, however, will be discussed by season as the CONUS analyses were.

1. Spatial Distribution of Mean Surface-Air Temperatures

1.1 Spring

In March, NARR mean temperatures depict a fairly zonal pattern with warmer temperatures in the south and cooler temperatures to the north in Canada (Fig. A.3.1.3.a). Lakes Superior and Huron appear to fall within the zonal temperature bands of the lands west and east of the lakes, while Lakes Michigan, Ontario show warmer temperatures than the surrounding land and Lake Erie shows cooler temperatures compared to the surrounding land. Warmer temperatures are observed over the SE corner of Michigan as well as a small bull's eye of warm temperatures in the northern Lower Peninsula of Michigan. Cooler temperatures extend further south in central Pennsylvania along the Allegheny Mountains and in northeastern New York near the Adirondack Mountains.

In April, latitudinal temperature zones still exist but are not as strictly oriented in a north to south manner and do not extend across lake boundaries (Fig. A.3.1.4.a). While the temperature gradient is oriented north to south from Pennsylvania to Indiana, the gradient becomes oriented SE to NW across Wisconsin and Minnesota. All of the Great Lakes show cooler temperatures compared to the surrounding land. However, warmer temperatures are observed in the SW corner of Lake Michigan and the eastern-most portion of Lake Erie. Cooler temperatures are still shown to extend further south along the Allegheny and Adirondack Mountain ranges.

Finally, in May, NARR mean temperatures show a similar north-south gradient across the southern portion of the domain extending NW across Wisconsin and Minnesota and cooler

temperatures over all of the Great Lakes (Fig. A.3.1.5.a). Warmer temperatures extend further north in central Michigan and are also observed over the SE corner of the state. Warmer temperatures are also shown along the eastern and western edges of Lake Erie, as well as extreme SW Lake Michigan around the Chicago, Illinois metro area. It should also be noted that the Saginaw Bay demonstrates warmer temperatures similar to the surrounding land masses rather than the cooler waters of Lake Huron.

While all models produce the general north-south gradient, with warmer temperature in the south gradually decreasing to the north, differences in the northern extent of the warmer temperatures, especially in Michigan and Wisconsin, and differences in the southern extent of the cooler temperatures especially in the northeast part of the domain, exist. Differences are also observed over the Great Lakes as some models simulate warmer or cooler lake temperatures compared to NARR. All models show decreasing spatial correlation values in spring with the highest values in March and the lowest values in May (Table C.44). Among the models, the ECP2 shows the highest spatial correlations in March and April with values of 0.96 and 0.89, respectively, while the WRFG has the highest spatial correlation (0.85) in May. Although the WRFG has the highest spatial correlation in May, it shows the lowest spatial correlation value of 0.90 in March, signifying that the spatial accuracy of all the other models decreases at a much faster pace than WRFG through spring. In April, the MM5I shows the lowest spatial correlation with a value of 0.80 while the CRCM demonstrates the lowest level of skill in capturing the spatial pattern of temperatures in May.

1.2 Summer

June temperatures from NARR show the coolest temperatures over Lake Superior followed by Lake Huron, Lake Michigan, Lake Ontario and Lake Erie (Fig. A.3.1.6.a).

Extending from SE Lake Michigan, a small area of cooler temperatures is observed over land while a small area of warmer temperatures is observed extending over Lake Michigan from the Chicago, Illinois area. The warmest temperatures are observed in the southeast portion of Michigan's Lower Peninsula near the Detroit, Michigan metro area. Warmer temperatures also extend east onto the western edge of Lake Erie, and are also observed over northeastern Lake Ontario as well. North-to-south temperature gradients are still shown across Pennsylvania and in Michigan where warmer temperatures extend further north in the interior portions of the state. However, the temperature gradient in the western domain is also now oriented more north to south rather than southeast to northwest.

July temperatures from NARR indicate the lakes continuing to warm with Lakes Erie and Ontario showing the warmest temperatures of any lake (Fig. A.3.1.7.a). Warm temperatures also extend further north from the southern tip of Lake Michigan. Lakes Superior, Huron and northern Lake Michigan still have the coolest temperatures of the domain. Temperatures much warmer than the surrounding areas are again observed over the western and eastern edges of Lake Erie and just northeast of Lake Ontario with the warmest temperatures of the domain still shown near the Detroit metro area. A land temperature gradient pattern similar to June is observed over the southern domain with cooler temperatures extending south in central Pennsylvania.

In August, the warmest temperatures have shifted south with the most noticeable gradient northeast to the southwest observed in Indiana, Illinois and Iowa (Fig. A.3.1.8.a). The coolest

temperatures continue to be located over Lake Superior, although lake temperatures cooler than the surrounding land is observed over all of the lakes, but is least noticeable over Lake Huron. The warmer temperatures along the western coast of Lake Erie are still present, but the eastern shore of Lake Erie and just northeast of Lake Ontario show the warmer temperatures to be less spatially expansive compared to early summer.

All model simulations correctly produce the north-to-south temperature gradient across the GLR in the early part of summer and also correctly show the shifting of the north-to-south gradient to a southeast-to-northwest orientation in the latter part of the season, with slight variations in the tightness and position of the gradient. However, differences in the spatial representation of temperatures are observed throughout the region. Model simulations show cooler lake surface temperature compared to NARR in all summer months over Lake Superior as well as parts of the other lakes. All model simulations also show differences surrounding Lakes Erie and Ontario along the land-shore borders, most noticeable along the western shore of Lake Erie near the Detroit metro area. The CRCM, ECP2 and HRM3 show relatively consistent spatial correlation values in summer with July showing the lowest values, while the MM5I and WRFG show decreasing spatial correlation values in summer with the highest values in June and lowest in August (Table C.44). In June, the WRFG exhibits the highest spatial correlation with a value of 0.87, while in July, the WRFG and ECP2 both show the highest spatial correlation values of 0.86. In June and July, the CRCM and HRM3 have the least amount of skill in representing the spatial pattern of temperature with values of 0.84 in June and 0.83 in July. Finally, in August, the ECP2 shows the highest spatial correlation value of 0.87 while the MM5I shows the lowest value of 0.80.

1.3 Autumn

September temperatures from NARR show the general north-to-south temperature gradient returning with fewer lake temperature differences (Fig. A.3.1.9.a). Lakes Huron and Michigan now show a north to south temperature gradient as well, with warmer temperatures extending slightly further north over the lakes compared to the surrounding land. Lake Erie still shows warmer temperatures over all of the lake compared to the surrounding areas with Lake Ontario still showing slightly warmer temperatures along the northeast shore. The areas of cooler temperatures near the Appalachian and Adirondack Mountains have also expanded since the summer months. It should also be noted that while the warmer temperatures over southern Lake Michigan extend east into extreme southwest Lower Michigan, there is no longer a small area of warmer temperatures observed over the lake waters just east of Chicago as was previously noted during the summer.

In October, a similar pattern in the higher elevations of the eastern domain is observed (Fig. A.3.1.10.a). Lake Erie still shows the warmest temperatures located over the entire lake with Lakes Michigan, Huron and Ontario still showing warmer temperatures further north than the surrounding land. However, these warmer temperatures over Lake Michigan have now shifted east and are concentrated over the southeast corner of the lake. Cooler temperatures are now shown to extend over central Lake Michigan from the west with warmer temperatures shown in the northern part of the lake near the Traverse Bay. The higher elevations of New York and Pennsylvania also continue to demonstrate cooler temperatures relative to the surrounding lower elevations.

November temperatures show changes in the overall distribution of temperatures with all of the lakes now showing warmer temperatures than the surrounding lands (Fig. A.3.1.11.a).

The warmest lake, Erie, shows the most noticeable warm temperature extensions from the lake along the southern shores including the Cleveland, Ohio and Erie, Pennsylvania areas. The northeast region of Michigan's Lower Peninsula also shows warmer temperatures extending inland from Lake Huron. Lake Michigan still exhibits the warmest temperatures that have shifted slightly east from the center of the lake, extending inland along the southeast coast of the lake. Finally, similar to the previous months, the Appalachian and Adirondack Mountains maintain their relatively cooler temperatures in November.

All models show improvements in simulating the spatial pattern of mean temperatures in autumn compared to spring and summer. However, differences in the spatial pattern of temperatures are observed in the central part of the domain over Wisconsin and Michigan. Differences are also noticeable in the temperature gradient observed in the southwestern portion of the domain and also over Lake Michigan where the ECP2 and WRFG show a more zonal pattern than is observed in NARR. The CRCM and MM5I show increasing spatial correlation values through autumn while the other models show an increase only from September to October followed by a decrease (Table C.44). Following the peak value in October, the ECP2 and WRFG fall to a value lower than the correlation value of September, while the HRM3 also falls but to the same correlation value observed in September. In September, the CRCM and ECP2 show the highest spatial correlation value of 0.92 while the MM5I shows the lowest correlation value of 0.85. In October, the ECP2 correlation remains the highest but is joined by the WRFG rather than the CRCM, with a correlation value of 0.94. Finally, in November, the CRCM and MM5I have the highest spatial correlation with a value of 0.93 while the WRFG now shows the lowest spatial correlation value of 0.85 after showing the highest in the previous month.

1.4 Winter

NARR mean temperatures from December show the expected pattern of warmer lake surface temperatures and the overall north-to-south gradient over the rest of the domain (Fig. A.3.1.12.a). The warmest temperatures are still shown along the eastern side of the lakes, most specifically over Lakes Superior and Michigan. Warmer temperatures still extend east across the lake shore boundaries in southwest lower Michigan and south across the lake shore boundaries of Lakes Huron, Erie and Ontario. Temperatures in Michigan and Wisconsin appear more spatially homogeneous compared to the latter part of autumn when temperatures decrease with increasing latitude. Finally, the higher elevations of the Appalachian Mountains, while showing temperatures to deviate slightly from the relatively zonal pattern, do not show temperature variations as pronounced compared to autumn. It should be noted, however, that the Adirondack Mountains do continue to show noticeably cooler temperatures.

In January, declining winter temperatures cause the warmer lake temperatures to concentrate towards the center of the lakes, with warmer temperatures extending across the lakeshore boundaries in fewer locations compared to December (Fig. A.3.1.1.a). Parts of southern Lake Superior, southeastern Lake Michigan and southern Lake Ontario do show warmer temperatures crossing the lake boundaries onto neighboring land. As expected, Lake Erie shows the coolest temperatures due to the shallower water that is unable to store as much heat compared to the other Great Lakes. Temperatures across Michigan begin to show noticeable differences from those across Wisconsin. In previous months and seasons, temperatures in Michigan and Wisconsin demonstrated comparable values and spatial patterns. However, beginning in January, Michigan shows warmer temperatures across the entire state compared to Wisconsin, indicating that the surrounding lakes help to moderate temperatures in

the middle of winter. Finally, in the extreme northern portion of Michigan's Lower Peninsula, there is a distinct pocket of isolated warm temperatures that appears along the coast of Lake Huron that reaches values of up to 275K.

Finally, in February, NARR shows the warmer temperatures above the lake surfaces to become further concentrated in the centers of the lakes (Fig. A.3.1.2.a). Lake Erie continues to show the coolest temperatures with a more zonal temperature pattern over the lake while Lakes Michigan and Ontario show the warmest temperatures. The southern portion of the domain shows a distinct north-to-south temperature gradient from Pennsylvania to Iowa with noticeable deviations in the higher elevations of the eastern domain. Similar to January, Michigan and Wisconsin temperatures continue to show differences with warmer temperatures extending further north in Michigan than in Wisconsin. In addition, the distinct pocket of isolated warm temperatures along the coast of Lake Huron in northern Michigan become more isolated as it is no longer connected to the warmer lake temperatures over central Lake Huron.

The models depict the overall spatial distribution of mean temperatures in December. However, the HRM3 in January and February and the WRFG in all winter months do not capture the spatial pattern very well. The HRM3 and WRFG show a zonal temperature pattern with slightly warmer temperatures over the lake surfaces while NARR and the other RCMs show much warmer lake surface temperatures and relatively warmer land temperatures near the lake shores rather than a strictly zonal temperature gradient. However, it should be noted that while the CRCM, ECP2, MM5I and the HRM3 in December do show warmer lake surfaces, the spatial extent and magnitude of these warmer temperatures are not as large as those observed from NARR. All models show increasing correlation values as the winter season progresses (Table C.44). In all months, the WRFG shows the lowest spatial correlation values of 0.68, 0.73 and

0.84 in December, January and February, respectively. However, unlike the lowest correlation values which are all from one model, the highest spatial correlation values (0.91, 0.94, and 0.96) for December, January, and February belong to three different models (CRCM, MM5I and ECP2).

1.5 Summary

Overall, the accuracy of model performance is highly dependent upon the RCM and season. In spring, the ECP2, HRM3 and WRFG show the greatest spatial accuracy followed by the CRCM and the MM5I. In summer, the ECP2 and WRFG continue to show the greatest spatial accuracy, while the HRM3 performance declines, resulting in the HRM3, CRCM and MM5I all having the lowest spatial correlation values. In autumn, the CRCM and WRFG have the greatest correlation value followed by the ECP2 and MM5I and lastly the HRM3. In winter, the relative performance of the models in capturing spatial distributions appears to be reversed from those of spring and summer with the CRCM and MM5I showing the greatest spatial accuracy followed by the ECP2, HRM3 and WRFG. In most cases, the summer season proves most difficult for the RCMs in simulating the spatial distribution of mean temperature, with the exception of the WRFG which shows the lowest skill in winter. In contrast to the WRFG, all of the other RCMs actually show winter, as well as autumn, to have the best spatial representation of mean temperature patterns. The most noticeable differences in the spatial distribution of temperatures are observed in the eastern half of the domain where variations in the northern extent of warmer temperatures from Pennsylvania and in the southern extent of cooler temperatures exist. However, differences are also exhibited in the southern and southwestern

portions of the domain where the location of the temperature gradient varies by model and season.

2. Spatial Distribution of Mean Surface-Air Temperature Differences

2.1 Spring

Spring bias values range from -2.45K for the MM5I in April to +4.45 for the HRM3 in March (Table C.41). In March, the WRFG has the largest bias followed by the WRFG, CRCM, MM5I and ECP2. The MM5I shows the largest bias value in April, followed by the CRCM, HRM3, WRFG and ECP2. In May, the MM5I continues to show the largest bias again followed by the CRCM, and the ECP2, WRFG and HRM3. Ranking the models, from best to worst, according to their mean temperature biases results in the following order (with their respective seasonal mean bias values): ECP2 (-0.24K), WRFG (+1.54K), CRCM (-1.68K), MM5I (-1.77K) and HRM3 (+2.07K).

The CRCM (Figs. A.3.2.3.a, A.3.2.4.a, and A.3.2.5.a) consistently underestimates land surface temperatures across the GLR and overestimates lake surface temperatures over all of the Great Lake in all spring months. The largest cool biases are shown just north of Lake Erie's western shores in all months, as well as the Saginaw Bay area and just east of the Chicago metro area in April and May. The largest warm biases are exhibited during the latter part of spring and are focused in localized areas along the shorelines of Lakes Superior, Michigan and Huron, most noticeably in the southeast corner of Lake Michigan and eastern shore of Lake Erie in northwestern Pennsylvania. The ECP2 (Figs. A.3.2.3.b, A.3.2.4.b, and A.3.2.5.b) shows fewer biases in the earlier part of spring with increasing negative biases over the land surfaces through May. In all months, the model exhibits warm biases over the lake surfaces, especially in May.

However, in March parts of Lake Michigan exhibit little to no bias and Lake Ontario demonstrates cool biases. Similar to the CRCM, the largest cool biases from the ECP2 occur over the Saginaw Bay, western shore of Lake Erie and Chicago metro area, while the largest warm biases occur along the lakeshores.

The HRM3 (Figs. A.3.2.3.c, A.3.2.4.c, and A.3.2.5.c) exhibits warm biases over most of the domain in the first part of spring, especially in March. Warm biases are most noticeable in the western and northern portions of the domain with relatively smaller warm biases shown in the southern portion of the domain and over the lake surfaces. The only cool biases observed in March were observed over Lake Ontario, the western most part of Lake Erie and the northern tip of Michigan's Lower Peninsula. The warm biases continue across much of the domain in April but with a relatively smaller magnitude. The largest biases are observed along the shores of Lakes Superior and Michigan, specifically in the southeast corner of Lake Michigan. The coolest biases, like the CRCM, are observed over the Saginaw Bay and just east of the Detroit metro area. Finally, in May, the warm biases are not as large and cool biases are observed across the northern portion of the domain.

Spring temperatures from the MM5I (Figs. A.3.2.3.d, A.3.2.4.d, and A.3.2.5.d) show a pattern similar to the CRCM, with cool biases over most of the land surfaces and warm biases over the lake surfaces. The warm and cool biases increase in magnitude as the season progresses. One noticeable difference compared to the CRCM is that in March, the MM5I shows a somewhat small buffer zone with little to no bias surrounding the Great Lakes. Like all of the previous models, the coolest biases are observed over southeast Lower Michigan and the Saginaw Bay. However, relatively cooler biases are also observed in the northern portion of the domain in Canada. The warmest biases, also similar to the other models, are found along the

lake shores. The WRFG (Figs. A.3.2.3.e, A.3.2.4.e, and A.3.2.5.e) demonstrates a pattern similar to the HRM3 with most of the land surfaces showing warm biases in early spring, diminishing as the season progresses, and ultimately ending the spring season with little to no bias over much of the land surfaces. However, unlike the HRM3, the WRFG shows little to no bias or slightly cool biases over the lake surfaces in March, which then reverses to warm biases in the latter part of spring.

2.2 Summer

Bias values in the summer range from -2.37K for the MM5I in August to +0.72K for the HRM3 in August (Table C.41). In June, the CRCM shows the least amount of bias, followed by the WRFG, HRM3, ECP2 and MM5I. In July, the HRM3 demonstrates lowest bias value, followed by the CRCM, ECP2, WRFG and again the MM5I showing the largest mean bias value. Finally, in August, the ECP2 shows the smallest bias value followed by the HRM3, CRCM, WRFG and MM5I. Therefore, ranking the models, from best to worst, according to the domain averaged bias values of mean temperature results in the following order (with their respective seasonal mean bias values): HRM3 (+0.02K), CRCM (-0.62K), ECP2 (-0.78K), WRFG (-0.86K) and MM5I (-2.09K).

The CRCM (Figs. A.3.2.6.a, A.3.2.7.a, and A.3.2.8.a) and ECP2 (Figs. A.3.2.6.b, A.3.2.7.b, and A.3.2.8.b) show similar patterns during the summer months. Both models also show a pattern similar to their respective spring simulations, with isolated areas of localized warm or localized cool biases along the lake shores. These localized areas decrease in both frequency and magnitude as the season progresses. Both models also simulate most of the cool biases to be over the land surfaces and most of the warm biases to be over the lake surfaces.

However, differences are observed in the spatial extent and location of the cool land biases. The CRCM shows most of the cool biases in the northern domain over Canada and northern Michigan while the ECP2 shows the cool biases in the southern domain.

The HRM3 (Figs. A.3.2.6.c, A.3.2.7.c, and A.3.2.8.c) differs from the other model simulations in that large areas of warm biases are found over land in addition to the lake surfaces. In all months, the HRM3 simulates cool biases in the northeast part of the domain and warm biases in the southwest part of the domain. However, these warm biases are smaller in spatial extent and magnitude during the earlier part of summer and increase as the season progresses. Unlike the other model simulations, the Great Lakes now show one consistent bias pattern with warm biases over Lakes Superior, Huron and Ontario, and portions of Lake Michigan and little to no bias over Lake Erie in all summer months.

The MM5I (Figs. A.3.2.6.d, A.3.2.7.d, and A.3.2.8.d) and WRFG (Figs. A.3.2.6.e, A.3.2.7.e, and A.3.2.8.e) show similar bias patterns during the summer months with most land surfaces demonstrating cooler biases and most lake surfaces exhibiting warmer biases. Similar to the other model simulations, isolated areas of warm and cold biases are observed along the shores of lakes, most specifically Lakes Superior, Michigan and Huron; however, the frequency and magnitude of these isolated areas decreases as the season progresses. Both models simulate temperatures cooler than NARR where the Upper and Lower Peninsula's of Michigan meet as well as the western shore of Lake Erie. Both models also show the warmest lake biases over Lake Superior in all months. One notable difference between the models is that the WRFG shows little to no bias in the western and southwestern portions of the domain with slight warm biases shown in August over parts of Minnesota, Wisconsin and Iowa.

2.3 Autumn

Autumn bias values range from -2.90K for the MM5I in September to +1.78K for the HRM3 in November (Table C.41). During the months of September and October, the MM5I shows the largest bias values, followed by the CRCM, WRFG, HRM3 and ECP2. However, while the bias values follow a similar pattern in both months, it should be noted that the ECP2 changes signs from a negative to a positive mean bias. In November, the HRM3 now shows the largest bias followed by the CRCM, MM5I, WRFG and ECP2. Ranking the models, from best to worst, according to their respective mean bias values, the following order is obtained (with their respective seasonal mean bias values): MM5I (-2.20K), CRCM (-1.67K), WRFG (-1.25K), HRM3 (+1.14K) and ECP2 (+0.06K).

In autumn, the CRCM (Figs. A.3.2.9.a, A.3.2.10.a, and A.3.2.11.a) depicts cool biases over most of the land surfaces with the exception of the southwestern domain in September and the Iowa, Minnesota, Wisconsin border in November. Lake surface biases vary from month to month with warm biases over Lakes Superior, Michigan and Huron in September and October, changing to cool biases over Lakes Superior and Michigan and little to no biases over Lake Huron in November. However, in all autumn months, Lake Erie demonstrates cool biases while Lake Ontario shows slight warm biases over the western part of the lake and little to no bias over the central-most part of the lake. As the season progresses, isolated areas of relatively larger cool biases are shown along the lake shores, especially surrounding Lakes Superior, Huron and Erie.

The ECP2 (Figs. A.3.2.9.b, A.3.2.10.b, and A.3.2.11.b) shows warm biases in the western domain in parts of Minnesota, Iowa and Wisconsin and over Lake Superior. These warm biases increase in spatial coverage as the season progresses, expanding eastward across Lake Michigan

into Michigan and are also shown in parts of New York as well. However, in November, the warm biases dominate much of the land surface in the southern portion of the domain while all of the Great Lakes now exhibit cool biases with the exception of southwestern Lake Michigan. The greatest of these cool biases are observed over the northern portions of Lakes Superior and Huron.

The HRM3 (Figs. A.3.2.9.c, A.3.2.10.c, and A.3.2.11.c) shows the largest warm biases in both spatial extent and magnitude during all autumn months. In September the warm biases are observed over the western domain with the largest biases concentrated over the Minnesota, Wisconsin, and Iowa border while the cool biases are observed over Lake Erie and the northeast portion of the domain. A similar pattern is observed in October, however, with the warm biases over Lake Superior not as large and fewer cool biases over Canada. In November, warm biases are found over most of the land surfaces within the domain with the greatest biases concentrated in the western domain. The lake surfaces now show a different pattern, with most of the lakes, excluding Lake Michigan, showing little to no bias or slightly cool biases. Lake Michigan is the only lake that continues to demonstrate warm biases in the latter part of autumn.

Like the CRCM, the MM5I (Figs. A.3.2.9.d, A.3.2.10.d, and A.3.2.11.d) shows cool biases over the land surfaces across the entire domain, including Lakes Erie and Ontario. However, these cool biases decrease in both magnitude and spatial extent as the season progresses. The lake surfaces show varying difference patterns from month to month during autumn. In September, Lake Superior exhibits the only positive biases of the domain while Lakes Michigan and Huron show little to no cool biases over much of the lake surfaces. In October, however, Lake Michigan demonstrates the greatest warm biases with Lake Superior only showing positive biases in the center of the lake and little to no bias across the rest of the

lake surface. Finally, in November, all of the lake surfaces show cool biases with the exception of southwest Lake Michigan. The greatest underestimations in November are found along the northern shores of Lakes Superior and Huron, although it should be noted that isolated warm biases are observed along the coastlines of the Great Lakes.

The WRFG (Figs. A.3.2.9.e, A.3.2.10.e, and A.3.2.11.e) in September demonstrates cool biases over most of the domain with a few exceptions in the western domain, northern Lower Michigan and over Lakes Superior, Michigan and Huron. Lake Superior exhibits warm biases over the lake surface while Lakes Michigan and Huron show slight isolated warm biases but little to no bias over the rest of the lake surfaces. However, in October, warm biases over Lakes Superior and Huron are replaced by slight cool biases or no bias at all. Lake Michigan demonstrates a pattern similar to September, but the area of warm biases over central Lake Michigan has expanded in spatial extent. Over the land surfaces, cool biases are still shown with the western domain now also exhibiting cool biases. November shows a pattern different than the previous months, with warm biases found in the southwest portion of the domain, little to no biases in the south central portion of the domain and relatively cold biases over all of the Great Lakes. All 5 Great Lakes exhibit the coldest biases from the WRFG in this month, with Lake Superior showing the largest biases and southern Lake Michigan showing the smallest lake surface biases.

2.4 Winter

The winter season exhibits the largest range of biases of the year with values ranging from -1.85K for the WRFG in December to +5.93K for the HRM3 in February (Table C.41). Among the models, the HRM3 has the largest biases in all winter months. In December and

February, the WRFG and CRCM follow the HRM3, while in January the CRCM overtakes the WRFG with a larger bias value. The MM5I and ECP2 show the lowest bias values with the ECP2 having the lowest value in December and January, and the MM5I showing the lowest value in February. Therefore, ranking the models, from best, to worst, according to their mean bias values yields the following order (with their respective seasonal mean bias values): ECP2 (+0.05K), MM5I (-0.16K), WRFG (-0.27K), CRCM (-1.31K) and HRM3 (+4.93K).

December and January temperature biases from the CRCM (Figs. A.3.2.1.a, A.3.2.2.a, and A.3.2.12.a) demonstrate warm biases over the southwest corner of the domain, little to no biases extending southeast from northern Minnesota to Illinois and east into Ohio and cool biases across the northern and eastern regions of the domain. Isolated areas of cool and warm biases are observed along the coastlines of all 5 Great Lakes in these 2 months. The most noticeable warm biases are observed over the Saginaw Bay, western shores of Lake Erie and over Lake Nipigon in Canada, while the most noticeable cool biases are observed in the extreme southeast corner of Lake Michigan and along the coastline of Lake Superior. In February, most of the land surfaces exhibit cool biases except for a few locations in the western part of the domain and all 5 of the lakes now demonstrating warm biases.

The ECP2 shows cool biases over the lakes in the beginning of winter, with the largest underestimations shown over Lake Superior. However, in February, warm biases extend beyond the lake coastlines and onto the lake surfaces of Lakes Superior, Michigan, Huron and Erie resulting in only the centers of these lakes showing cool biases. Lake Ontario demonstrates cool biases in all winter months, with the largest bias in January. There are little to no biases over the land surfaces in the eastern half of the domain in December and warm biases over the western half of the domain. As the season progresses, these warm biases expand eastward, but are

mostly concentrated near the lake boundaries as central Wisconsin and central Michigan show little to no biases while the northeastern portion of the domain shows cool biases.

Of all the models, the HRM3 demonstrates the largest warm biases that increase in magnitude as the season progresses. In all months, the largest overestimations are concentrated over the western part of the domain. In December, all 5 lakes show cool biases or little to no biases. In January, these lake surface biases begin to change signs, from negative to positive, as Lakes Michigan, Huron and Erie and the central part of Lake Superior now show warm biases. In February, these warm biases now completely cover the lakes with cool biases no longer observed in the central part of the lakes. However, it should be noted that Lake Ontario, unlike the other lakes, exhibits cool biases in all winter months.

In December, the MM5I exhibits cool biases over the Great Lakes and the northeast and southeast regions of the domain with warm biases over the western most portion of the domain from Canada to Iowa. Warm biases are also observed along the coastlines of the lakes, most noticeably surrounding Lakes Superior and Michigan. However, in January, the warm biases of the western domain extend eastward into parts of Wisconsin, Michigan and Canada between Lakes Huron and Erie while the eastern portion of the domain now exhibits fewer cool biases. Warm biases continue to be shown along the coastlines of the lakes, while the surface of Lake Erie now shows a warm bias. Finally, in February, fewer warm biases are observed in the western domain while the cool biases in the eastern domain have increased in spatial extent. The majority of the Great Lakes surfaces, with the exception of Lake Ontario, now exhibit warm biases compared to the cool biases that were shown in the beginning of winter. It should also be noted that while the warm biases are now observed over the lakes, the warm biases that were observed in central Wisconsin and central Lower Michigan are no longer apparent.

2.5 Summary

In summary, some models demonstrate fewer biases than others, with model performances varying spatially and temporally throughout the year. In spring, the ECP2 shows the least amount of domain averaged bias, followed by the WRFG, CRCM, MM5I and HRM3. In summer, the HRM3 overtakes the ECP2 and demonstrates the lowest mean bias value followed by the CRCM, ECP2, WRFG and MM5I. Like spring, the ECP2 shows the least amount of averaged bias in autumn followed by the HRM3, WRFG, CRCM and MM5I. Finally, in winter, the ECP2 shows the lowest bias value now followed by the MM5I, WRFG, CRCM and HRM3. Overall, the ECP2 shows the lowest domain averaged bias values in all seasons. In most cases, summer and winter have the lowest domain averaged biases with the exceptions of the ECP2 in summer and the HRM3 in winter while spring offered relatively larger mean bias values overall compared to the other seasons, with exception of the MM5I which has its second lowest mean bias value during this month.

Overall, some general bias patterns, across all RCMs, exist in the GLR. From March to October all of the Great Lakes show warm biases which decrease in spatial extent and magnitude as the spring and summer seasons progress. However, from November to February, the lakes demonstrate cool biases overall with the greatest cool biases over the lakes observed between November and January. The exception to these cool lake biases is the HRM3, which demonstrates warm biases across much of the domain during these months. Of all the models, the HRM3 exhibits the greatest overestimations in both spatial extent and magnitude most noticeably between December and April. In addition to the HRM3, the WRFG also shows widespread overestimations concentrated mainly between February and April. Finally, in the

warm season between April and August, highly localized and isolated areas of over and underestimations along the lake coastlines are shown from all RCM simulations.

3. Statistics and Annual Cycle of Mean Surface-Air Temperature

NARR temperatures from the GLR depict maximum temperatures in July and the minimum temperature in January with temperatures gradually increasing from January to July and steadily declining from August to January (Fig. B.11). All models capture the seasonal cycle of mean temperatures with a few noticeable differences in winter and early Spring as well as Summer. The HRM3 temperatures are generally warmer than NARR, especially during the cold season from November through March with the warm bias as much as 5 K in January. Unlike the other models and NARR that show an annual peak in July, peak temperatures from the HRM3 occur in August instead. The other models all have lower temperatures throughout the year, except for the WRFG which is warmer than NARR from January through April. Among the models, the MM5I shows the greatest underestimations compared to NARR in all summer months. All monthly, seasonal and annual bias values are offered in Table C.41.

4. Spatial Distribution of Daily Accumulated Precipitation

4.1 Spring

March precipitation patterns from NARR demonstrate a general southeast-to-northwest gradient in precipitation with the higher precipitation amounts found in the southeast domain and the lowest precipitation amounts observed in the north and northwestern domain (Fig. A.4.1.3.a). Slightly lower precipitation amounts are also exhibited in eastern Wisconsin and just north of Lakes Erie and Ontario. However, lower precipitation amounts relative to the surrounding areas

are shown east of the Detroit metro area in Canada and along the New York – Canada border just north of Lake Ontario's northeastern shores.

In April, the precipitation gradient becomes more north-to-south oriented, rather than southeast-to-northwest, as the greater precipitation amounts are found in the entire southern domain and lower precipitation amounts are observed in the entire northern domain (Fig. A.4.1.4.a). However, higher precipitation amounts extend northward into Minnesota, Wisconsin and Michigan while lower precipitation amounts, relative to the surrounding land surfaces, are observed over all of the Great Lakes. These lake surface precipitation amounts remain relatively constant from March to April over all of the lakes except Lake Michigan, where slightly higher precipitation amounts are shown over the central part of the lake, but are still lower than values observed over the surrounding land.

In May, most of the land surfaces, including Canada, show increases in precipitation from April to May and as a result the lower precipitation values over the lake surfaces becomes more pronounced (Fig. A.4.1.5.a). However, slightly higher precipitation values are shown to extend onto the lake surfaces of Lake Michigan from the Chicago metro area. Land surfaces just west of Lakes Superior and Erie show the smallest precipitation values in May while the largest precipitation values are observed in the southwestern and southeastern areas of the domain. Finally, a broad west-to-east gradient appears in May over central Lower Michigan, with higher precipitation amounts shown to the west and lower precipitation amounts to the east.

All RCMs have difficulties in representing the spatial pattern of daily precipitation in spring with only one model, the CRCM, showing spatial correlation values above 0.70 in all months. The CRCM does show the greatest spatial accuracy in representing the precipitation gradients in early spring but fails to show the lower precipitation amounts over southern Lake

Michigan in April and extends the higher precipitation amounts west of the lakes further north compared to NARR. The HRM3 shows the lowest level of skill in simulating the spatial pattern of daily precipitation as precipitation amounts are shown to be highly localized and sporadic, rather than spatially consistent like NARR. The ECP2, MM5I and WRFG also show difficulties in simulating the spatial pattern of precipitation, but to a lesser extent than the HRM3. The most noticeable differences between the ECP2, MM5I and WRFG and NARR are the orientation of the temperature gradients and the lake surface temperatures. The CRCM has the highest spatial correlation values in all spring months with values of 0.78, 0.83, and 0.76 in March, April and May, respectively (Table C.48). The lowest spatial correlation value for March of 0.46 is from the MM5I. However, as the season progresses, the MM5I shows increasing skill while the HRM3 shows decreasing skill, resulting in the HRM3 having the lowest spatial correlation values of 0.43 and 0.37 in April and May, respectively.

4.2 Summer

Precipitation patterns from NARR in June show lower precipitation amounts over all of the Great Lakes, with the lowest precipitation amounts observed over the northwestern shore of Lake Erie (Fig. 4.1.6.a). The greatest precipitation amounts are found west of Lake Michigan in Wisconsin, Minnesota, Iowa and Indiana, with a few isolated regions also showing relatively higher precipitation amounts in Indiana, Ohio, Pennsylvania and New York. Precipitation amounts over Michigan show a north-to-south gradient with higher values along the Indiana and Ohio borders and the lowest amounts in the northeastern part of the state along the coast of Lake Huron.

In July, a precipitation pattern similar to June is observed with the lowest precipitation amounts again located over the Great Lakes (Fig. 4.1.7.a). The area of lower precipitation of the northwestern shore of Lake Erie has since expanded and now covers most of the western and central lake surfaces while lower precipitation amounts are also now exhibited over the extreme western shore of Lake Ontario. Lower precipitation amounts also extend west from the northwest shore of Lake Superior along the Canadian border. In the western domain, higher precipitation amounts have decreased in spatial extent, with the greatest amounts now west and north of the Quad Cities metro area while the higher amounts previously observed over Indiana, Ohio and Pennsylvania have decreased in magnitude and shifted south.

In August, precipitation decreases over the majority of the land surfaces while higher precipitations amounts, compared to the earlier part of summer, are observed over the lake surfaces along the coastline of Lake Michigan (Fig. 4.1.8.a). Enhanced precipitation is also shown along the eastern shores of Lakes Superior and Huron. The highest precipitation amounts are now concentrated in the western domain and have slightly shifted south and east, and again include the Quad Cities region. Indiana, Ohio and Pennsylvania no longer show isolated regions of relatively higher precipitation.

Summer simulations show an increased level of difficulty compared to spring in correctly representing the distribution of daily precipitation. In all summer months, all RCM simulations show the highest precipitation amounts across the southern and eastern areas of the domain rather than the western and southern areas as seen in NARR. In addition, the HRM3 and WRFG in July and all RCMs in August simulate the lowest precipitation values in the western part of the domain rather than over the lake surfaces.

As the summer season progresses, all RCMs show decreased skill with the highest correlation values occurring in June and the lowest values occurring in August (Table C.48). In each of the summer months, the MM5I shows the greatest spatial correlation values of 0.75, 0.48 and 0.40, in June, July and August, respectively. These values, which are the highest correlation values between any RCM and NARR, further attest to decreased model performance during the summer. The WRFG exhibits the lowest correlation value of 0.32 in June while the HRM3 exhibits the lowest correlation values of 0.15 and 0.11 in July and August, respectively. However, it should be noted that while the HRM3 demonstrated the lowest correlation value in August, all RCM correlation values, with the exception of the MM5I, were 0.15 or lower. The degraded performance of the RCMs in simulating summer season precipitation in this region is not surprising given the dominance of convective precipitation in summer and the relatively coarse resolution (50 km) of the RCMs that are insufficient for resolving local convection.

4.3 Autumn

September precipitation patterns from NARR demonstrate lower precipitation amounts over the central and western lake surfaces of the Great Lakes as well as isolated regions of Canada along the northern Minnesota and New York borders (Fig. 4.1.9.a). The lowest precipitation amounts are observed just east of the Detroit metro area and north of western Lake Erie in Canada. Higher precipitation amounts are shown in the southwestern, southeastern and north-central regions of the domain, with the highest amounts concentrated over central Wisconsin and New York and west central Michigan and the thumb of Michigan's Lower Peninsula.

In October, a somewhat more chaotic spatial pattern of precipitation is observed in the GLR (Fig. 4.1.10.a). The lowest precipitation amounts continue to be observed just north of Lake Erie's western shore while lower precipitation amounts are also shown over the central and western portions of the lake surfaces. Lower precipitation amounts are also now shown in Minnesota and parts of central Iowa, central Wisconsin, and into central Ohio and southwestern Pennsylvania. Higher precipitation amounts are depicted in western Michigan that parallel Lake Michigan's shoreline highlighting the importance of the lake as the cool season begins. Higher precipitation amounts are also observed downwind of the other Great Lakes with the highest amounts east of Lakes Superior and Ontario where the west-to-east fetch across the lake is longest.

November precipitation patterns show a general northwest-to-southeast gradient over the domain's land surfaces with the lowest precipitation amounts shown in Canada just north of the Minnesota border and the higher precipitation amounts located in New York, Pennsylvania and northern New Jersey (Fig. 4.1.11.a). All of the Great Lakes begin to show a west-to-east gradient of precipitation with lower amounts near the western shores and higher amounts near the eastern shores. The largest gradients are observed over Lakes Erie and Ontario, where the longer west-to-east fetch allows for more moisture to be evaporated and later deposited east of the lakes.

All RCMs show improvements as autumn progresses; however, differences in the spatial representation of daily precipitation do occur in all months. Throughout autumn, all RCMs show less precipitation in the western half of the domain and relatively higher precipitation amounts in the eastern half. This trend is most noticeable from the HRM3, MM5I and WRFG as these models show lower precipitation values extending further east than the CRCM and ECP2.

Additionally, the higher precipitation amounts that are simulated in the eastern half of the domain are highly isolated and scattered, especially for the HRM3. However, while the HRM3 and WRFG do show these isolated areas of higher precipitation, they are able to simulate the higher precipitation amounts that are observed over the Adirondack Mountains from NARR.

After correlation values reaching their minimum by the end of summer, all RCMs show increasing skill in representing the spatial patterns of precipitation throughout autumn with the lowest correlation values in September and the highest correlation values in November (Table C.48). The ECP2 shows the highest spatial correlation values of 0.22, 0.41 and 0.61 in September, October and November, respectively, with the MM5I and CRCM showing correlation values only 0.01 less than the ECP2 in October and November, respectively. Additionally, the CRCM shows the greatest improvement throughout autumn as correlation values rise from 0.19 in September to 0.60 in November. The WRFG shows the lowest correlation value of 0.11 in September, while the CRCM shows the lowest correlation value of 0.31 in October and the MM5I shows the lowest value of 0.41 in November.

4.4 Winter

Winter precipitation patterns from NARR remain relatively consistent December through February (Figs. A.4.1.1.a, A.4.1.2.a, and A.4.1.12.a). The region exhibits lower precipitation amounts across Minnesota, Wisconsin and Iowa as well as the regions north of Lakes Huron, Erie and Ontario in Canada with the lowest precipitation amounts observed to the north and west of Lake Superior. Higher precipitation amounts are shown in the southern part of the domain from Illinois to New Jersey and extend north into Michigan and the central GLR. Of these, the highest precipitation amounts are located across Pennsylvania, New York and New Jersey.

During the winter season, the important influences of the lakes on precipitation amounts east of the lake shores are visible. All months show increased precipitation on the eastern side of Lakes Superior and Huron, along the eastern shores of Lake Michigan extending inland to western Michigan, especially in the southwestern part of the state, and just southeast of Lake Erie near Erie, Pennsylvania and Buffalo, New York. The highest precipitation amounts, particularly in December and January, extend horizontally east of Lake Ontario towards the Adirondack Mountains.

The most noticeable differences between the RCMs and NARR occur in the eastern half of the domain, although some differences are shown in the western domain as all models vary in how far east the lower precipitation amounts are observed. In the eastern GLR, all models falsely expand the areas of higher precipitation south of Lake Erie into Ohio as well as Indiana and Illinois in some cases. All models also falsely expand the isolated regions of higher precipitation downwind from the lakes. The HRM3 precipitation plots show little to no discernable spatial patterns as the RCM simulates highly localized precipitation maxima and minima, rather than the smooth and spatially consistent precipitation patterns observed from NARR.

In all winter months, the CRCM is most skillful in capturing the spatial distribution of precipitation with the highest spatial correlation values among all RCMs of 0.69, 0.74 and 0.81 in December, January and February, respectively. The good performance of the CRCM is immediately followed by the ECP2, WRFG for all winter months. The HRM3 has the lowest spatial correlation coefficients of 0.43 and 0.45 in December and January, while the lowest value for February (0.54) belongs to the MM5I.

4.5 Summary

Similar to the CONUS as a whole, the RCMs demonstrate decreased accuracy in simulating the spatial distribution of precipitation compared to temperatures for the GLR. Precipitation accuracies are highly variable and are dependent on the RCM and month. In spring, the ECP2 demonstrates the greatest spatial accuracy followed by the CRCM, WRFG, MM5I and HRM3. In summer, the MM5I shows increased skill resulting in the highest spatial accuracy followed by ECP2, CRCM and the HRM3 and WRFG. In autumn, the WRFG demonstrates the highest spatial correlation value followed by the ECP2 and HRM3, MM5I and CRCM. In contrast to autumn, the CRCM shows the largest correlation value followed by the ECP2, WRFG, MM5I and HRM3 during winter months. As shown by these rankings, no one model consistently outperforms the others in all seasons in correctly simulating the spatial distribution of precipitation; however, the ECP2 was consistently within the top two in all seasons.

The most noticeable differences in the spatial distribution of precipitation in the GLR vary by season. During the spring, all RCM simulations exhibit variations in the orientation of the precipitation gradient demonstrated by NARR. In the summer, all model simulations show very low spatial accuracy due to the incorrect placement of the higher precipitation amounts. All RCMs place the greatest precipitation amounts in the eastern side of the domain while NARR shows the correct placement to be in the west-central domain. Autumn differences are shown over the entire domain as NARR depicts lower precipitation values over the lake surfaces while the RCMs simulate lower precipitation amounts extending into the eastern half of the domain. Finally, in winter, the RCMs falsely expand the area of higher precipitation east of Lakes Erie and Ontario.

Spatial Distribution of Daily Accumulated Precipitation Differences
 Spring

The CRCM (Figs. A.4.2.3.a, A.4.2.4.a, and A.4.2.5.a) shows slight wet biases over the south-central and northeastern domain in March that increase in spatial extent and magnitude as the season progresses. The largest wet biases are shown over southern Lake Michigan and Lakes Huron, Erie and Ontario. Relatively larger biases are also observed northeast of Lake Ontario and west of Lake Superior in the latter part of spring. The ECP2 (Figs. A.4.2.3.b, A.4.2.4.b, and A.4.2.5.b) shows wet biases over the entire domain, with these biases being the largest biases of any RCM in the spring. However, the thumb of Michigan's Lower Peninsula, as well as the Chicago metro area, are two noticeable locations showing little to no biases in April and May.

The HRM3 (Figs. A.4.2.3.c, A.4.2.4.c, and A.4.2.5.c) also exhibits wet biases over much of the domain. However, in the latter part of spring, little to no biases are shown in the southern portion of the domain with a few isolated areas with negative biases. These dry biases are shown over New Jersey and extend west into eastern Pennsylvania in March and April. Dry biases are also shown in the southwestern portion of the domain, specifically in Iowa, in April and May. The largest wet biases from the HRM3 are located over southern Lake Michigan, Lakes Erie and Ontario as well as a large number of isolated areas surrounding the Great Lakes.

The MM5I (Figs. A.4.2.3.d, A.4.2.4.d, and A.4.2.5.d) and WRFG (A.4.2.3.e, A.4.2.4.e, and A.4.2.5.e) show similar bias patterns during the spring season. Little to no biases are shown over much of the western and southern regions of the domain in March. However, wet biases are observed in the southern portion of the domain in April from the MM5I and also in May from the WRFG. The largest wet biases from the MM5I and WRFG are found over the lake surfaces, except for the WRFG in March where lakes Superior, Huron and Michigan show little to no

biases. Larger wet biases are also exhibited in the northeastern domain, especially from the MM5I in March and April, while little to no biases are shown in the northeastern domain from either model in May.

All models demonstrate wet biases in all spring months with average bias values ranging from +0.43mm for the WRFG in May to +1.60mm for the ECP2 in March (Table C.45). In March, the CRCM has the smallest bias value of +0.53mm while the WRFG shows the smallest bias values of +0.52mm and +0.43mm in April and May, respectively. The largest biases in March and April are both from the ECP2 with values of +1.60mm and +1.49mm, respectively. In May, however, the HRM3 shows the largest bias with a value of +0.98mm. Ranking the models in order, from best to worst, according to seasonal biases of daily precipitation (with their respective bias values) yields the following order: WRFG (+0.48mm), CRCM (+0.62mm), HRM3 (+0.81mm), MM5I (+0.85mm) and ECP2 (+1.27mm).

5.2 Summer

The CRCM (Figs. A.4.2.6.a, A.4.2.7.a, and A.4.2.8.a) in summer, exhibits wet biases in the northeastern domain that decrease in magnitude as the season progresses. Wet biases are also observed over all of the Great Lakes, but to a lesser extent over Lakes Michigan and Huron in August. Large wet biases are also shown west of Lake Superior, north of Lake Erie and to the northeast and southeast of Lake Ontario in New York state. Dry biases, on the other hand, are shown in the southwestern domain in all summer months. These dry biases, centered over Iowa, increase in magnitude and spatially expand as the season progresses.

The ECP2 (Figs. A.4.2.6.b, A.4.2.7.b, and A.4.2.8.b) shows a bias pattern in June, similar to that of spring. Wet biases are observed over the entire domain with larger values showing no

distinct pattern. However, as the season progresses these wet biases decrease in spatial coverage and magnitude across the eastern domain. By August, most of the wet biases are contained to the southeastern domain with the largest values north of Lake Erie, northeast of Lake Ontario and over Ohio. Dry biases are shown in the southwest corner of the domain beginning in July that spread north and east from Iowa to Minnesota, Wisconsin, northern Illinois and most of Lower Michigan.

The HRM3 (Figs. A.4.2.6.c, A.4.2.7.c, and A.4.2.8.c) and WRFG (Figs. A.4.2.6.e, A.4.2.7.e, and A.4.2.8.e) demonstrate similar bias patterns in all summer months. In June, the HRM3 shows dry biases over Minnesota and Iowa, little to no biases over Wisconsin and across the northernmost part of the domain and sporadic wet biases over the central, eastern and southern domain. The WRFG illustrates a similar pattern but with the wet biases in the eastern and central domain being spatially smoothed across the Canadian land surfaces and the dry biases in Wisconsin contained to the southern half of the state. In addition, both models show the largest wet biases over the lake surfaces. In July, a pattern similar to June is depicted, however, dry biases are now also shown over Wisconsin and the north-central domain in Canada. Both models also depict little to no biases over Illinois, Indiana, Michigan and Ohio as well as the northeastern region of the domain. Both models depict the largest wet biases over southern Lake Michigan as well as Lake Erie. In August, both models show little to no bias over the northeastern domain, and Lakes Superior, Michigan and Huron with the greatest biases over southeastern Lake Michigan and Lake Erie. Notable differences are observed between the HRM3 and WRFG in August in eastern New York where the HRM3 illustrates isolate areas of overestimations near the Adirondack Mountains. However, dry biases continue to expand

eastward and are now observed over parts of Illinois, Indiana, and Michigan, with the greatest dry biases centered over the Minnesota, Wisconsin and Iowa border.

The MM5I (Figs. A.4.2.6.d, A.4.2.7.d, A.4.2.8.d) shows very little bias across the land surfaces except for the west-central domain where slight dry biases are depicted in Minnesota, Wisconsin and Iowa. The wet biases that do exist are concentrated over the lake surfaces, eastern Pennsylvania, New Jersey, west of Lake Superior and northeast Lake Ontario. Similar to the HRM3 and WRFG, the MM5I shows increasing dry biases as the season progresses. These dry biases are shown over all of Minnesota, Iowa, Wisconsin, Michigan and the northern portions of Illinois, Indiana, Ohio and New York by August. Dry biases are also observed in the northern part of the domain. It appears that in August, the wet biases over the lake surfaces decrease in both spatial coverage and magnitude, with only slight overestimations remaining west of Lake Superior, western Lake Erie and just northeast of Lake Ontario.

Unlike spring, RCM biases for summer show both positive and negative values, with the positive values in the beginning of summer and the negative values in the latter part of the season (Table C.45). Bias values for summer range from -0.52mm for the MM5I in August to +1.19mm for the ECP2 in June. In June, the MM5I shows the lowest bias value followed by the CRCM and HRM3, the WRFG and ECP2. In July, the MM5I continues to show the lowest bias value, but is now followed by the HRM3 and WRFG, the CRCM, and ECP2. After showing the highest biases in the early part of summer, the ECP2 now shows the smallest bias value in August, followed by the CRCM, HRM3, WRFG and finally the MM5I that has the least amount of bias in early summer. Ranking the models in order, from best to worst, according to seasonal biases (with their respective bias values) yields the following order: WRFG (+0.01mm), HRM3 (+0.06mm), MM5I (-0.15mm), CRCM (+0.33mm) and ECP2 (+0.60mm).

5.3 Autumn

The CRCM (Figs. A.4.2.9.a, A.4.2.10.a, and A.4.2.11.a) in September illustrates dry biases over the land surfaces of the central, northwestern and southeastern domain while wet biases are shown over the lake surfaces. The greatest wet biases are shown over Lake Erie, Lake Ontario and northeast of Lake Ontario. Improvements are shown in October as the majority of the domain's land surfaces show little to no bias. However, slight dry biases are shown in the north-central area and southeast corner of the domain and a horizontal band of overestimations are also shown just west of northern Lake Superior. The lake surfaces continue to demonstrate wet biases; however, Lake Superior and northern Lake Michigan now show little to no bias. In November, Lake Superior and northern Lake Michigan continue to have little to no bias while the northeastern portion of the domain illustrates wet biases that were not present in the earlier part of autumn.

The ECP2 (Figs. A.4.2.9.b, A.4.2.10.b, and A.4.2.11.b) demonstrates warm biases in the western half of the domain with little to no biases shown over Lakes Superior, Michigan and Huron. However, overestimations are shown along the western shore of Lake Erie and the northeast corner of the domain. In October, the overestimations in the northeast corner of the domain become larger and also increase in magnitude northeast of Lake Ontario. However, the dry biases over the western domain have decreased in spatial extent and magnitude. Finally, in November, all of the dry biases are no longer present, as overestimations are shown across the eastern two-thirds of the domain and little to no biases are shown over parts of Lake Superior, Wisconsin, southern Minnesota, western Michigan and northern Illinois and Indiana. The largest of these wet biases are shown along the western shores of Lakes Erie and Ontario, northeast of Lake Ontario, west of northern Lake Superior and in portions of the northeastern domain.

The HRM3 (Figs. A.4.2.9.c, A.4.2.10.c, and A.4.2.11.c), MM5I (Figs. A.4.2.9.d, A.4.2.10.d, and A.4.2.11.d) and WRFG (Figs. A.4.2.9.e, A.4.2.10.e, and A.4.2.11.e) all show similar bias patterns across all autumn months with a few minor differences. In September, all three models show dry biases over most of the land surfaces, although the WRFG shows little to no biases over northern Ohio and western Pennsylvania and New York. The three models also depict wet biases over Lake Erie. However, the HRM3 shows slight wet biases over Lake Superior and the eastern and western shores of Lake Ontario, while the WRFG shows a slight wet bias over southern Lake Michigan. In October, the models continue to cover the majority of the domain with dry biases. However, the HRM3 shows little to no biases in the south-central domain and the WRFG shows little to no biases over land in the eastern part of the domain. The HRM3 now demonstrates a cool bias over southern Lake Michigan; however, the WRFG no longer depicts this bias. All three models also show dry biases over Lake Superior, with the WRFG showing the largest area of dry biases over the entire lake. In November, the HRM3 begins to deviate from the pattern of the MM5I and WRFG. While all three models show dry biases in the southern half of the domain and wet biases in the northern domain, the HRM3 shows its biases to be more localized in nature compared to the MM5I and WRFG. The MM5I and WRFG also show little no biases across the central part of the domain in Wisconsin and Michigan while the HRM3 continues to show slight dry biases over these states.

In autumn, bias values range from -0.88mm for the MM5I in September to +0.78mm for the ECP2 in November (Table C.45). In September and October, the CRCM has the lowest biases with values of -0.19mm and -0.02mm, respectively. However, in November, the WRFG shows the lowest bias value of +0.01mm. The MM5I shows the largest bias values of -0.88mm and -0.61mm in September and October, respectively, while the ECP2 shows the largest bias

value of +0.78mm in November. Ranking the models, from best to worst, according to seasonal biases of daily precipitation (with their respective bias values) yields the following order: CRCM (+0.01mm), ECP2 (+0.14mm), WRFG (-0.35mm), HRM3 (-0.39mm) and MM5I (-0.46mm).

5.4 Winter

The CRCM (Figs. A.4.2.1.a, A.4.2.2.a, and A.4.2.12.a) demonstrates faint dry biases over the Adirondack Mountains in New York, little to no biases in the western domain overall and wet biases shown in the eastern domain. In December, these wet biases are concentrated over the northeastern corner of the domain and over Lakes Erie and Ontario. However, in January, the wet biases reach further south into western Pennsylvania, Ohio, and southeast Lower Michigan. Slight wet biases are also shown from southwestern Iowa to southern Wisconsin. In February, a pattern similar to January is observed in the eastern domain, although the wet biases over the western domain have become more isolated.

The ECP2 (Figs. A.4.2.1.b, A.4.2.2.b, and A.4.2.12.b) shows wet biases over the entire domain, with the greatest values shown in the northeastern domain. However, a few notable exceptions can be seen. Northern Lake Superior consistently shows relatively lower wet biases compared to the surroundings in all winter months and the land surfaces downwind from Lake Ontario show little to no biases. However, it is suggested that this area of little to no bias is due to observed higher precipitation amounts from lake-effect snow rather than increased model skill over that location.

The HRM3 (Figs. A.4.2.1.c, A.4.2.2.c, and A.4.2.12.c) continues to show more isolated areas of higher biases compared to the relatively smoothed spatial patterns in other models. Similar to the CRCM, the HRM3 depicts wet biases over the northeastern domain with little to

no biases in the western domain. However, in December and January, Lakes Superior, and Huron depict dry biases. Dry biases are also shown near the Pennsylvania, New York, New Jersey border in December and January.

The MM5I (Figs. A.4.2.1.d, A.4.2.2.d, and A.4.2.12.d) shows varying patterns throughout winter. In December, the northern domain shows wet biases, with the greatest overestimations north of Lake Superior and east of Lake Huron. The southern half of the domain shows little to no bias from Iowa to Ohio and slight dry biases over eastern Pennsylvania, eastern New York and northern New Jersey. In January, wet biases are now shown across the central part of the domain in Wisconsin, Iowa and Michigan. The wet biases in the north have increased in magnitude and another region of higher wet biases has also emerged in the northeastern domain. The dry biases in the southeastern domain have decreased in spatial extent and are now only observed over New Jersey. In February, a pattern similar to January is illustrated, however, the dry bias in New Jersey is now gone and the wet biases over Iowa and southern Wisconsin no longer remain.

The WRFG (Figs. A.4.2.1.e, A.4.2.2.e, and A.4.2.12.e) shows a pattern similar to the HRM3 but spatially more consistent. In December, dry biases are shown over Lake Superior, Lake Huron, and southeastern Lake Michigan, parts of southern Lake Erie and near the Adirondack Mountains of New York. Dry biases are also observed south of Buffalo, New York where enhanced precipitation amounts are common due to lake-effect snow. Wet biases are observed in the northeast portion of the domain with the largest overestimations observed just east of Detroit, Michigan and northeast of Lake Ontario. In January, the dry biases formerly depicted in the southern half of the domain are no longer present, although dry biases are still shown over Lake Superior, Lake Huron, central and northeastern Lake Michigan and near the

Adirondack Mountains. In February, dry biases are no longer present, with most of the western half of the domain showing little to no biases. However, the overestimations over much of the eastern domain have increased in magnitude, especially along the New York-Canadian border.

In winter, the domain averaged bias values are almost all positive with the exception of the WRFG bias value of -0.04mm in December (Table C.45). Winter bias values range from -0.04mm for the WRFG in December to +1.30mm for the ECP2 in February. All RCMs, with the exception of the MM5I show their lowest bias values in December with bias values increasing as the season progresses. In all months, the ECP2 shows the largest biases while the WRFG shows the smallest biases. The WRFG is followed by the HRM3, CRCM, and MM5I in December and by the CRCM, HRM3 and MM5I in January and February. Therefore, ranking the models, from best to worst, according to their biases (with their respective seasonal bias values) yields the following order: WRFG (+0.20mm), CRCM (+0.46mm) and HRM3 (+0.46mm), MM5I (+0.70mm) and ECP2 (+1.18mm).

5.5 Summary

Model performance in simulating daily precipitation in the GLR varies by model and season. During the spring and winter seasons, the WRFG showed the lowest mean bias value, followed by the CRCM, HRM3, MM5I and ECP2. In summer, the WRFG continues to show the lowest bias value, now followed by the HRM3, MM5I, CRCM and ECP2 (note the CRCM's decreased level of skill during the summer months). However, in autumn, the CRCM and ECP2 both show improvements as the CRCM shows the lowest mean bias value, followed by the ECP2, WRFG, HRM3 and MM5I. Overall, the WRFG produced the lowest bias values in all seasons but autumn while the ECP2 produced the highest bias values in all seasons but autumn.

Wet biases dominate the region for all RCMs from January through June and are mostly concentrated in the eastern half of the region. In most cases, the largest wet biases were observed just east of Detroit along the northwest shores of Lake Erie and north of Lake Ontario. Of all the models, the ECP2 consistently demonstrates the largest wet biases. However, between July and October dry biases are produced by all RCMs, with the greatest dry biases shown in September. These dry biases begin to appear in the southwestern portion of the domain and increase in spatial extent, covering most of the domain by September.

6. Statistics and Annual Cycle of Daily Accumulated Precipitation

The seasonal pattern of daily precipitation from NARR in the GLR is similar to that of the NE. The lowest precipitation is observed in February, followed by a gradual increase into June. Precipitation in July levels off through September with a slight decrease observed in August. From September to February, precipitation decreases but does show a short period of constant precipitation from October to November. The CRCM and WRFG show the most similarity in overall shape compared to the NARR precipitation curve. From January to July, the CRCM best matches the NARR precipitation curve but does consistently overestimate precipitation. However, from August to October, the WRFG is the only model to simulate the slight rise in precipitation during September before decreasing again in October. All models, including the CRCM and WRFG show an increase in precipitation during November before falling in December whereas NARR shows no increase in precipitation during that time.

Overall, all models overestimate precipitation from December to June, while they underestimate precipitation in September. Like the NE, the ECP2 shows the most frequent and largest deviations from the NARR precipitation pattern.

Chapter V – Conclusions

a. Summary

This study was conducted to achieve the following goals: (1) To fill the gaps within the literature by assessing the skill of leading RCMs in their ability of simulating mean surface-air temperatures and daily accumulated precipitation in the CONUS, and specifically the GLR, and (2) To provide quantitative estimates of surface temperature and precipitation biases and their spatial and temporal variations, for the leading RCMs, for future use in climate impact studies over the GLR.

In particular, the study attempts to answer the following research questions: (1) How well do RCM simulations, driven by NCEP reanalysis, describe the current temperature and precipitation patterns of the CONUS (and subsequent sub-regions: NE, SE, NW, SW) and the GLR?, and (2) Which, if any, RCM(s) consistently outperform(s) the others in representing the current temperature and precipitation patterns of the CONUS (and subsequent sub-regions: NE, SE, NW, SW) and the GLR?

Simulations from five NARCCAP RCMs (CRCM, ECP2, HRM3, MM5I, and WRFG) for the period of 1981-2000 were validated against NARR data from the same period. The results revealed that the skill of these RCMs in simulating surface temperature and precipitation varied spatially and temporally. However, some overall trends common to all model simulations were observed over the CONUS and GLR and are summarized below.

1. Contiguous United States

1.1 Mean Surface-Air Temperature

The spatial distribution and seasonal variability of the surface-air temperature are well simulated by all five models with only small differences among the models. The ECP2 consistently outperforms the others with the highest spatial correlation values in all seasons, while CRCM shows relatively poor performance in spring, summer and autumn, but matches the high performance of the ECP2 in winter. In addition to demonstrating the lowest-level of overall spatial accuracy, the CRCM also shows the largest overall biases. The HRM3, however, has the lowest biases in all seasons except winter when the lowest bias is given by the WRFG.

Annual mean biases for the CONUS range from -2.34K for the CRCM to +0.99K for the HRM3. By and large, the western CONUS demonstrates larger biases where topography is more complex. With the exceptions of the Rocky, Cascade and Sierra-Nevada Mountains where positive biases are frequently observed, the biases observed in the western CONUS are generally negative, with the CRCM and MM5I showing the greatest negative biases. The positive biases over the three major high mountain ranges could be a result of terrain smoothing and model resolution that tend to lower the mountain peaks within the model. In contrast, warm biases are most frequently exhibited in the north central region of the CONUS, especially during the winter season suggesting the models do not correctly simulate the southern migration of cold arctic air from central Canada. However, the HRM3 consistently demonstrates warm biases in all seasons across the majority of the domain. The south central region of the CONUS consistently exhibits the least amount of bias with little to no biases shown throughout much of the year.

1.2 Daily Accumulated Precipitation

Precipitation patterns proved much more difficult to simulate compared to the spatial distribution of temperature. Overall, the CRCM depicts the greatest spatial correlation with that of NARR, showing the highest correlation values in spring, summer and winter, while the HRM3 shows the lowest spatial accuracy with the lowest correlation values in spring, summer and winter. All RCMs collectively show the least amount of skill in the NW where simulations exhibit highly localized areas of heavy or light precipitation rather than the spatially smooth patterns observed from NARR, suggesting model parameterization schemes to be very sensitive to changes in elevation. The RCMs also show a tendency to underestimate the rain shadow effect of the Cascade Mountains with excess precipitation simulated on the leeward side and too little simulated on the windward side of the mountains. Poor terrain resolution and terrain smoothing, spatial interpolation, and inadequate cloud and precipitation parameterization are possible reasons for the underestimation of the rain shadow effect in this region.

Overall, the models show greater skill in simulating winter season precipitation and the least skill in simulating summer season precipitation as summer precipitation is more locally-driven and convective in nature across much of the domain. While the HRM3 demonstrates the lowest skill in accurately simulating the spatial pattern of precipitation, it shows the lowest domain averaged biases in all seasons. The largest overall biases are exhibited by the MM5I and ECP2. The variation of biases across the regions appears to have some consistency among the models. Most wet biases are shown in the western CONUS with a few exceptions from July to October. However, most of the dry biases are concentrated in the SE between November and March and/or the central CONUS between April and October suggesting the models do not correctly simulate the cool season influx of moisture from the Gulf of Mexico and Atlantic

Ocean in the SE or the large amount of precipitable water available within the atmosphere resulting from available soil moisture and the evapotranspiration of crops in the central CONUS during the growing season.

2. Great Lakes Region

2.1 Mean Surface-Air Temperature

Like the CONUS, model performance over the GLR varies spatially and temporally for all models; however, model simulations for the GLR demonstrate a wider spread within the seasonal variations. The ECP2 and WRFG show the highest spatial correlations in spring and summer, with the HRM3 having the same high correlation value in spring. While the WRFG continues to show the highest correlation value in autumn, the CRCM shows increased skill in simulating the spatial pattern of temperatures as it shares the same high correlation value as the WRFG. The CRCM also shows the highest correlation value in winter; however, WRFG skill declines while MM5I skill improves, resulting in the MM5I and CRCM both showing the highest correlation values in winter. Overall, all models show their highest correlation values in autumn and winter and their lowest correlation values in summer, with the exception of the WRFG which shows its worst performance in winter.

Annual mean biases for the GLR range from -1.56K for the MM5I to +2.04K for the HRM3, which is similar to the CONUS range (-2.43K to +0.99K), but more positively defined and with the MM5I having the largest overall negative biases rather than the CRCM. In general, the ECP2 shows the least amount of domain-averaged bias in spring, autumn and winter, and the HRM3 having the lowest bias value in summer. However, in spring and winter the HRM3 has the largest biases. In summer and autumn, the MM5I shows the largest mean biases. All models

demonstrate highly localized and isolated areas of bias along the coastlines of the Great Lakes during the warm season between April and August. All models also show warm biases over the lake surfaces between March and October and cool biases between November and February. The exception to these cool biases is the HRM3, which demonstrates warm biases across much of the domain during these months. In addition to the HRM3 showing widespread warm biases, the WRFG also exhibits widespread warm biases that are primarily observed from February to April.

During the warmer months of the year, specifically from April to October, the models collectively demonstrate warm biases over the lake surfaces and cool biases over the adjacent land surfaces. However, during the cooler months of the year, specifically from November to January, the models collectively simulate cool biases over the lake surfaces with little to no bias or slightly warm biases over the adjacent land surfaces. In both instances, these biases lead to a smaller temperature gradient across the lake boundaries and potentially reduce the effect of the lakes.

2.2 Daily Accumulated Precipitation

Similar to the CONUS, decreased accuracy in simulating precipitation patterns compared to temperature patterns are shown in the GLR, with each of the four seasons having a different model with the highest correlation value. The highest correlation values for each season are observed from the ECP2, MM5I, WRFG and CRCM for spring, summer, autumn and winter, respectively. However, the ECP2 is consistently within the top two within all seasons while the HRM3 consistently shows low spatial correlations having the lowest values in spring, summer and winter. While the ECP2 consistently shows higher spatial correlations, it produces the

highest bias values in all seasons but autumn. The WRFG produces the lowest bias values in all seasons but autumn when the lowest bias is produced by CRCM while the highest biases are given by MM5I.

Between January and June all RCMs simulate wet biases, most noticeably in the eastern half of the domain with the largest wet biases occurring just east of Detroit along the northwest shores of Lake Erie and north of Lake Ontario. Dry biases are simulated by all RCMs between July and October that are concentrated in the southwestern portion of the domain but spread north and east.

b. Limitations and Future Research

This study provides detailed analyses of the spatial and temporal distribution of mean surface-air temperature and daily accumulated precipitation from NARR and the NCEP-driven simulations of five NARCCAP RCMs (CRCM, ECP2, HRM3, MM5I and WRFG). The spatial and temporal distribution of biases between each RCM and NARR of both variables are presented. While these standard variables do attest to overall model skill, a more holistic understanding of RCM performance over the CONUS and GLR can be achieved through the validation of additional surface and upper-level variables.

A major limitation of the study is the use of reanalysis data, NARR, as a basis for the RCM evaluations. As an objectively analyzed gridded dataset that blends operational weather forecast model output with observational data through data assimilation, NARR data in general provide a good representation of the state of the atmosphere. However, studies have identified errors in the NARR data which can be relatively large, especially over areas of complex terrain such as the Western U.S. (Bukovsky and Karoly 2007; West et al. 2007). Future research may

utilize a more observation-based dataset, such as the United States Historical Climate Network (Karl et al. 1990), to provide a more accurate quantitative evaluation of RCMs. Additionally, because the NARR data were up-scaled from 32-km and the NARCCAP data were re-gridded to a 0.5° latitude by 0.5° longitude common grid spacing, further uncertainty may have been introduced within the analyses. While the re-gridding of the data was necessary in order to perform the analyses and ultimately could not be avoided, the uncertainties that may have been introduced is noted and offered as a precautionary measure when interpreting the results.

Because this study evaluates the differences between NCEP-driven RCM simulations and reanalysis, the results presented discuss the biases that exist solely within the RCMs. To better understand the total bias that exists within the model simulations, comparisons between the NCEP-driven and GCM-driven simulations would also prove beneficial, as this analysis would capture the biases that exist due to the driving GCMs. Combining both comparative analyses would then provide a better understand of the total bias and therefore provide valuable information for future climate and stakeholder research.

APPENDICES

APPENDIX A SPATIAL PLOTS

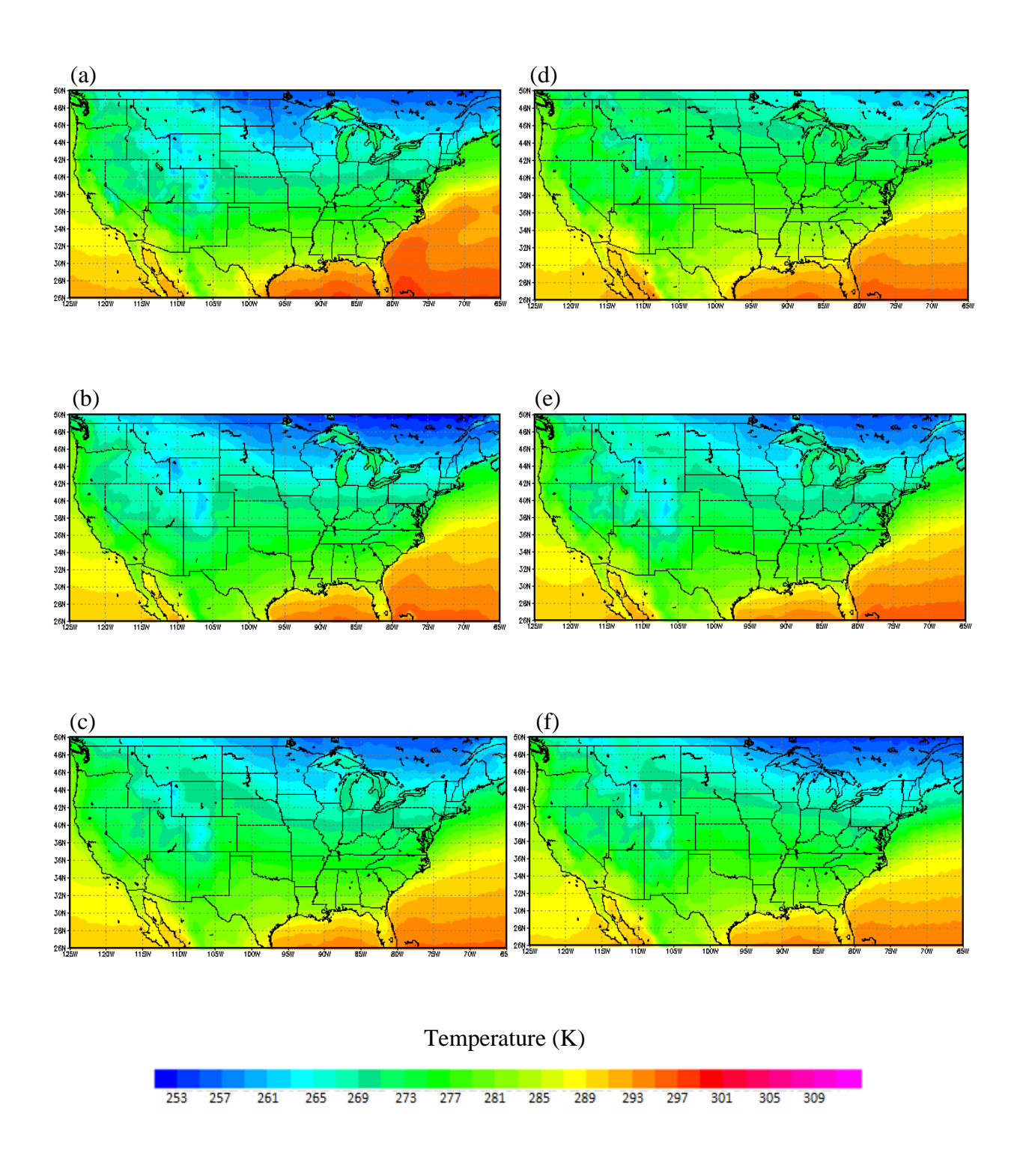


Fig. A.1.1.1 Mean January surface-air temperatures from (a) NARR, (b) CRCM, (c) ECP2, (d) HRM3, (e) MM5I, and (f) WRFG for the CONUS domain.

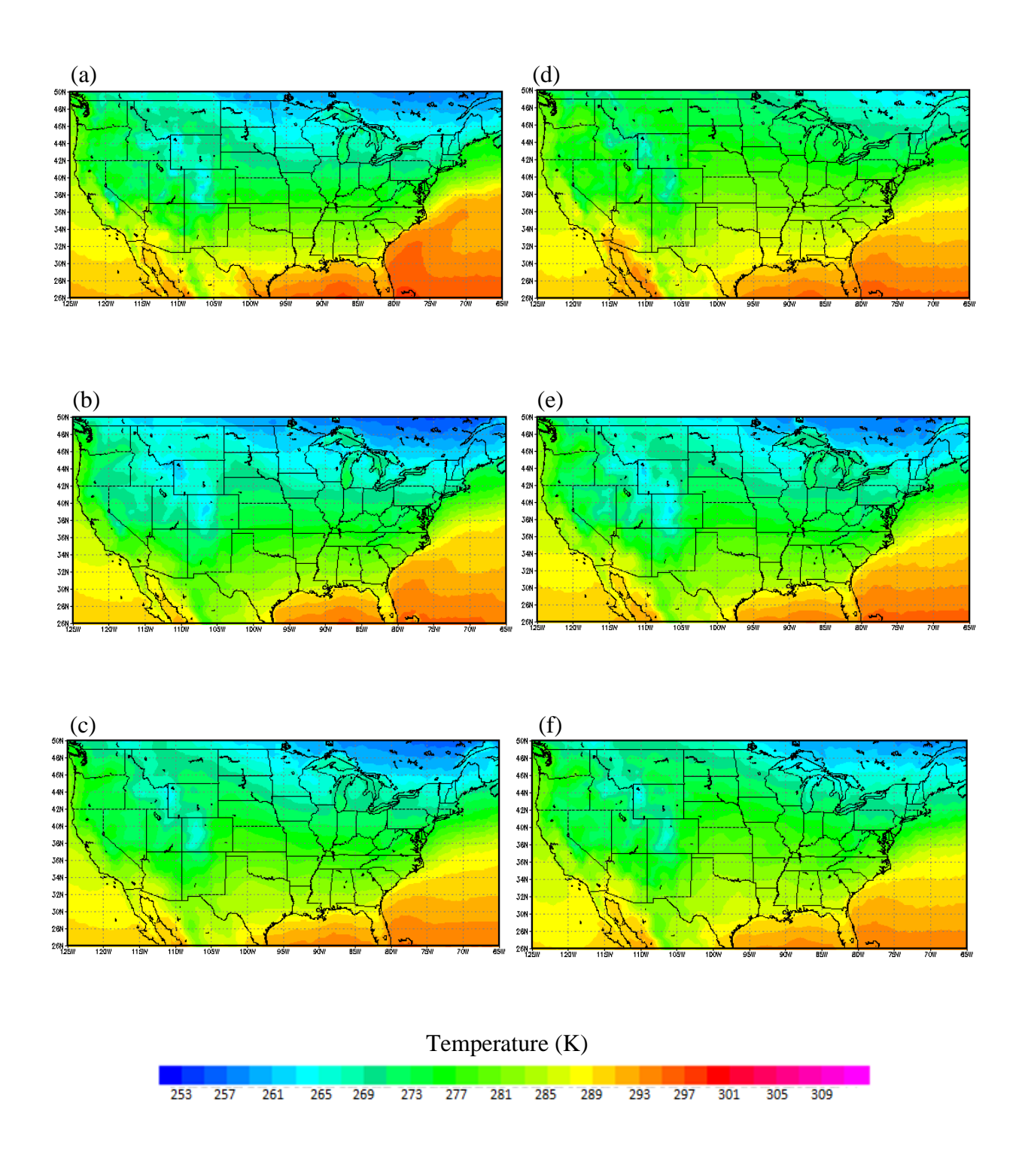


Fig. A.1.1.2. Mean February surface-air temperatures from (a) NARR, (b) CRCM, (c) ECP2, (d) HRM3, (e) MM5I, and (f) WRFG for the CONUS domain.

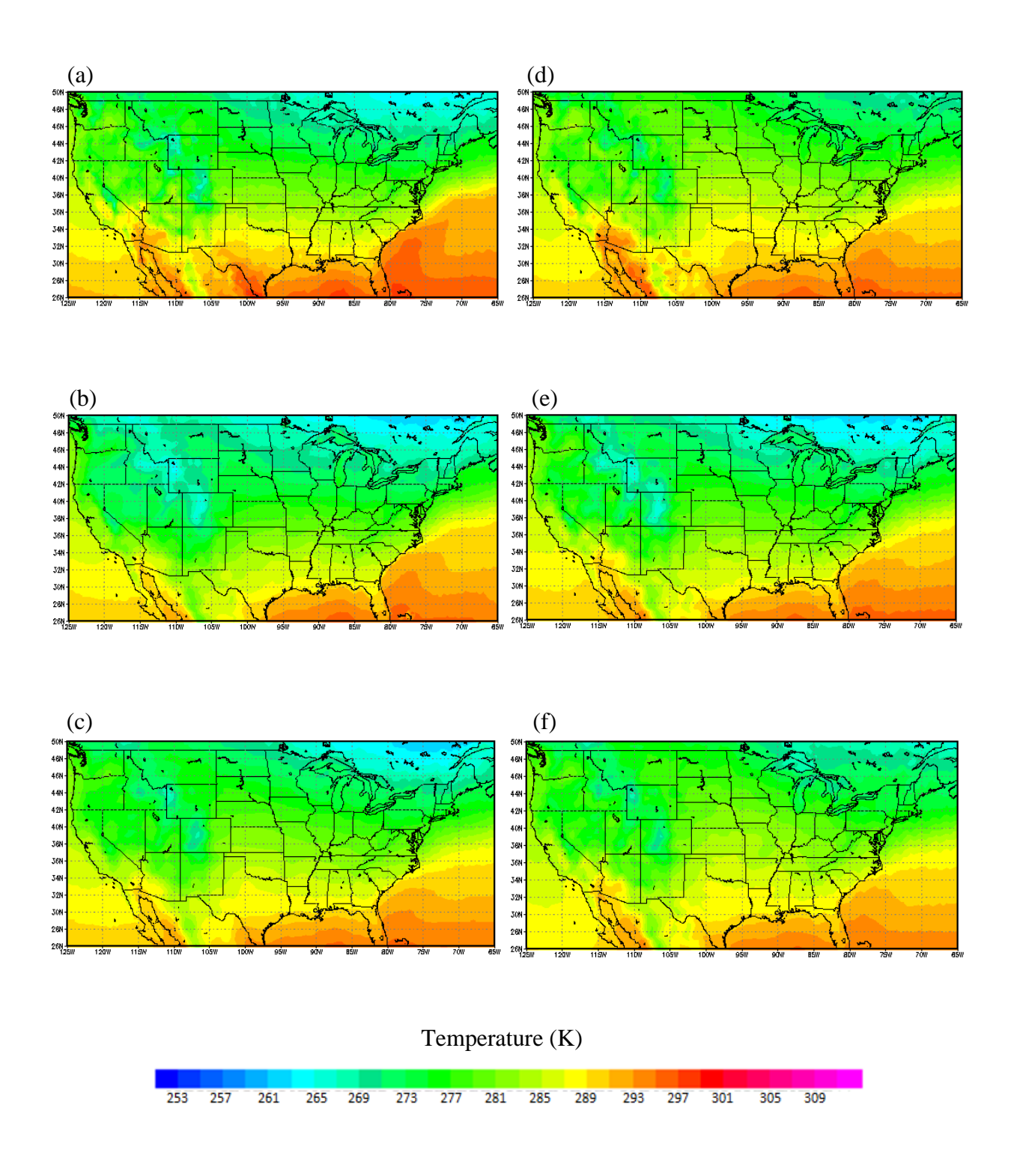


Fig. A.1.1.3. Mean March surface-air temperatures from (a) NARR, (b) CRCM, (c) ECP2, (d) HRM3, (e) MM5I, and (f) WRFG for the CONUS domain.

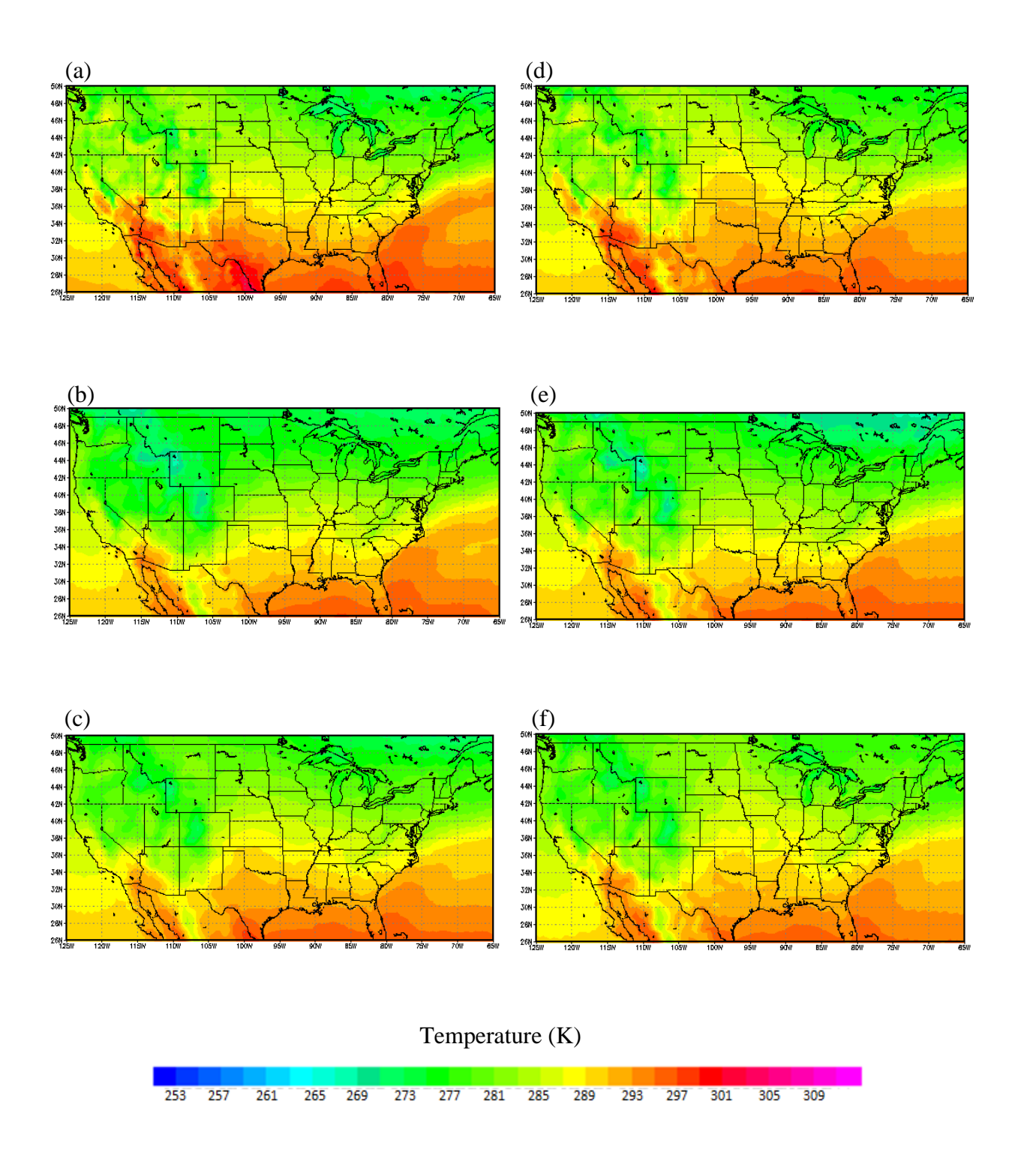


Fig. A.1.1.4. Mean April surface-air temperatures from (a) NARR, (b) CRCM, (c) ECP2, (d) HRM3, (e) MM5I, and (f) WRFG for the CONUS domain.

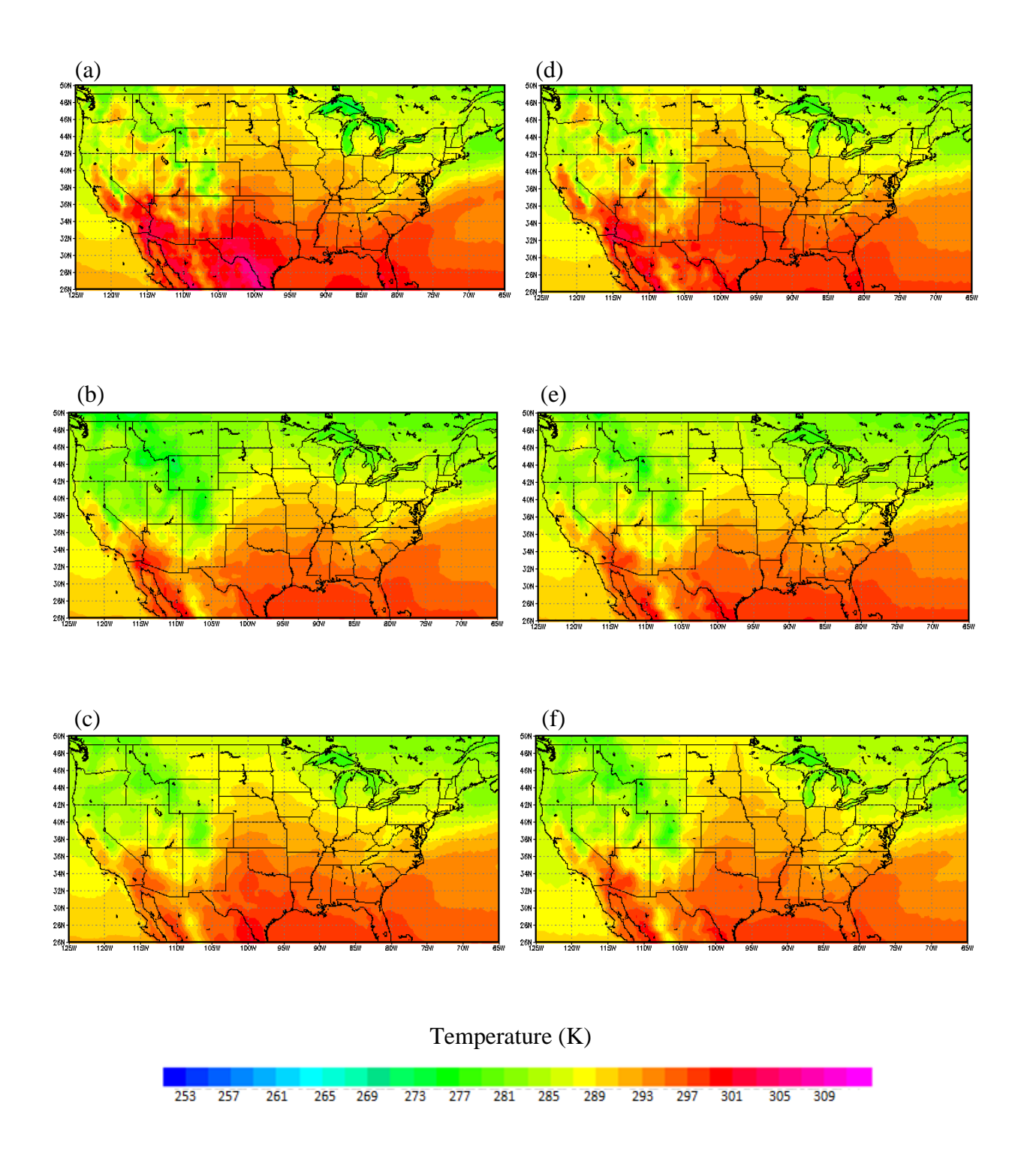


Fig. A.1.1.5. Mean May surface-air temperatures from (a) NARR, (b) CRCM, (c) ECP2, (d) HRM3, (e) MM5I, and (f) WRFG for the CONUS domain.

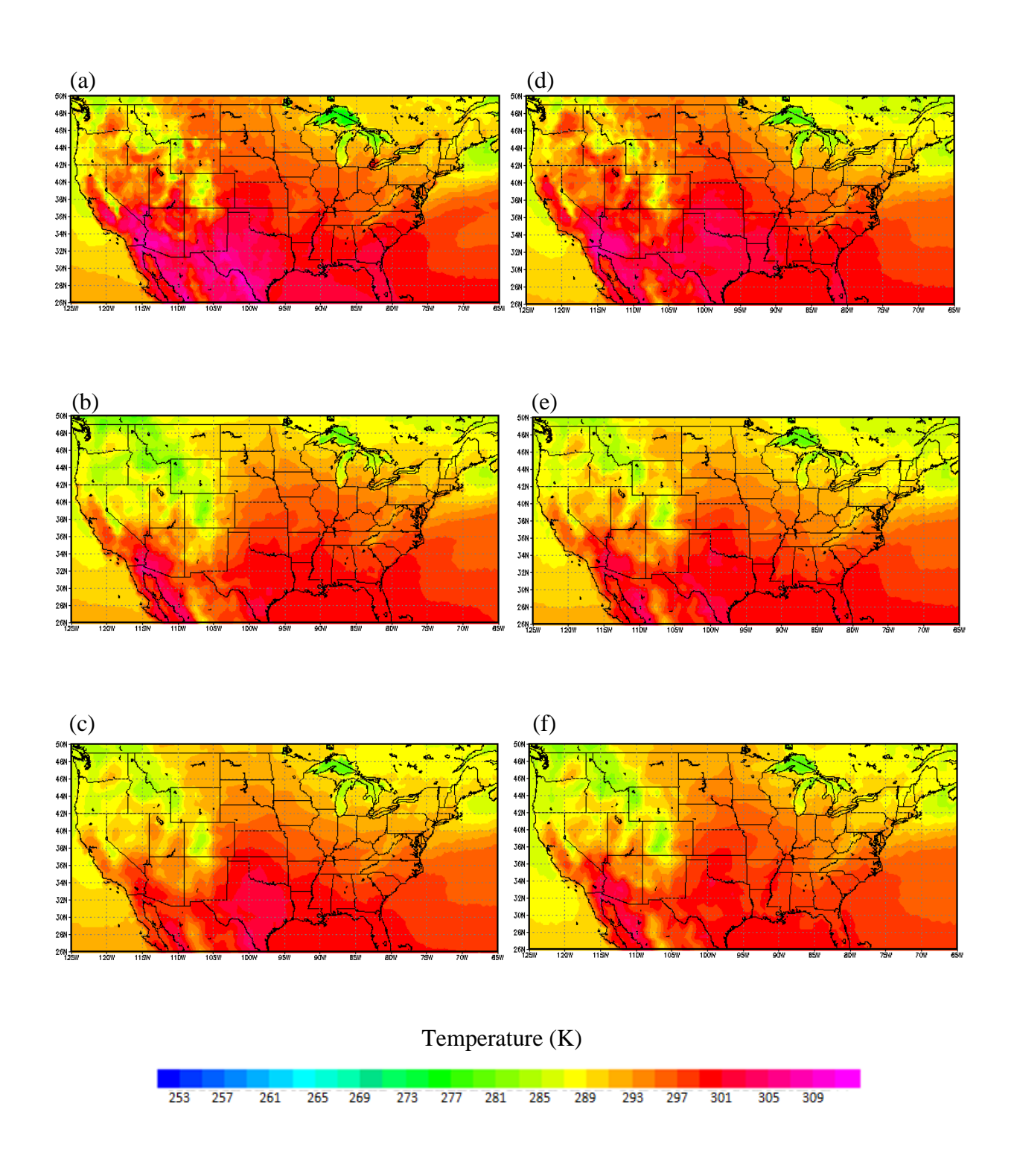


Fig. A.1.1.6. Mean June surface-air temperatures from (a) NARR, (b) CRCM, (c) ECP2, (d) HRM3, (e) MM5I, and (f) WRFG for the CONUS domain.

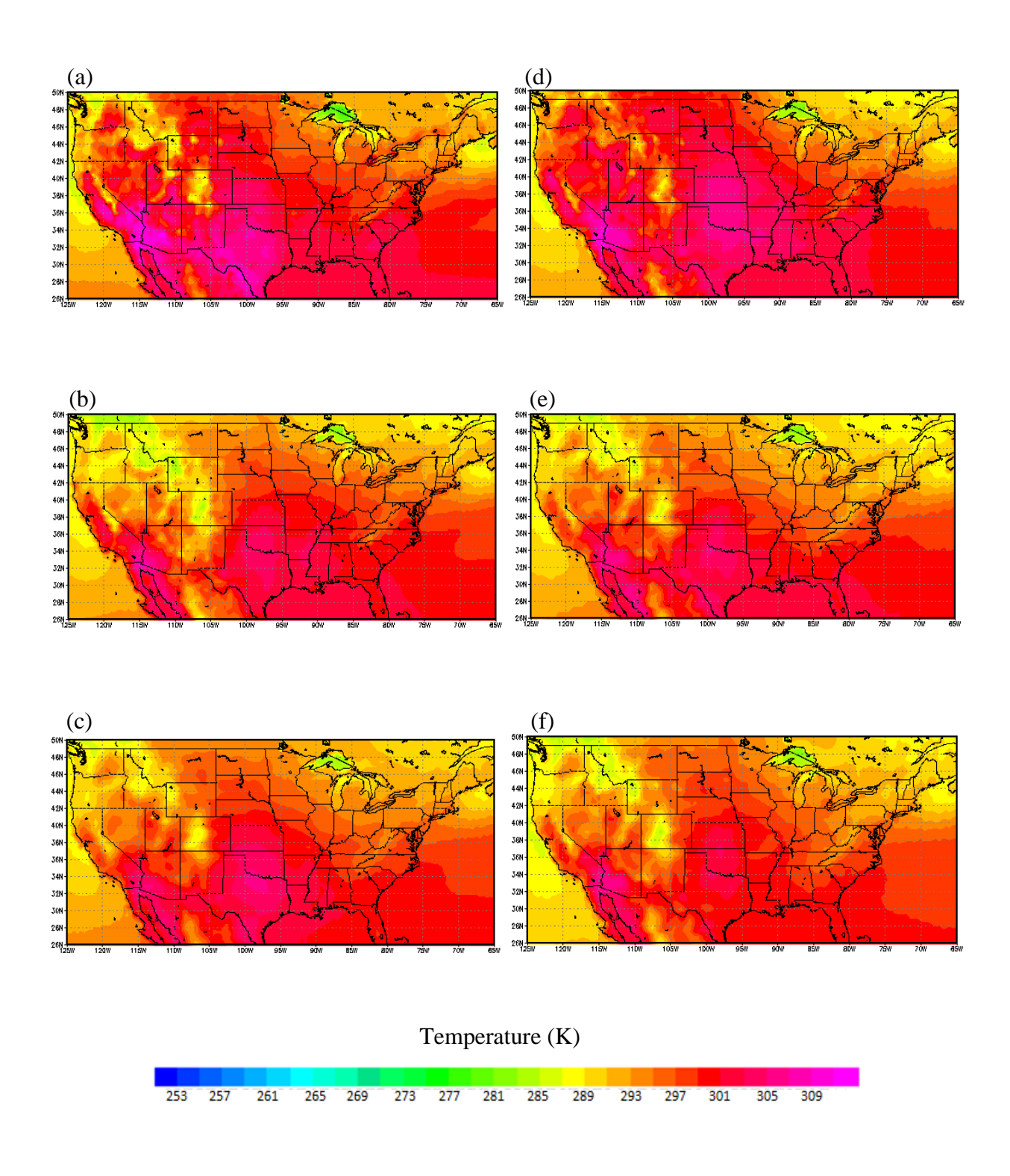


Fig. A.1.1.7. Mean July surface-air temperatures from (a) NARR, (b) CRCM, (c) ECP2, (d) HRM3, (e) MM5I, and (f) WRFG for the CONUS domain.

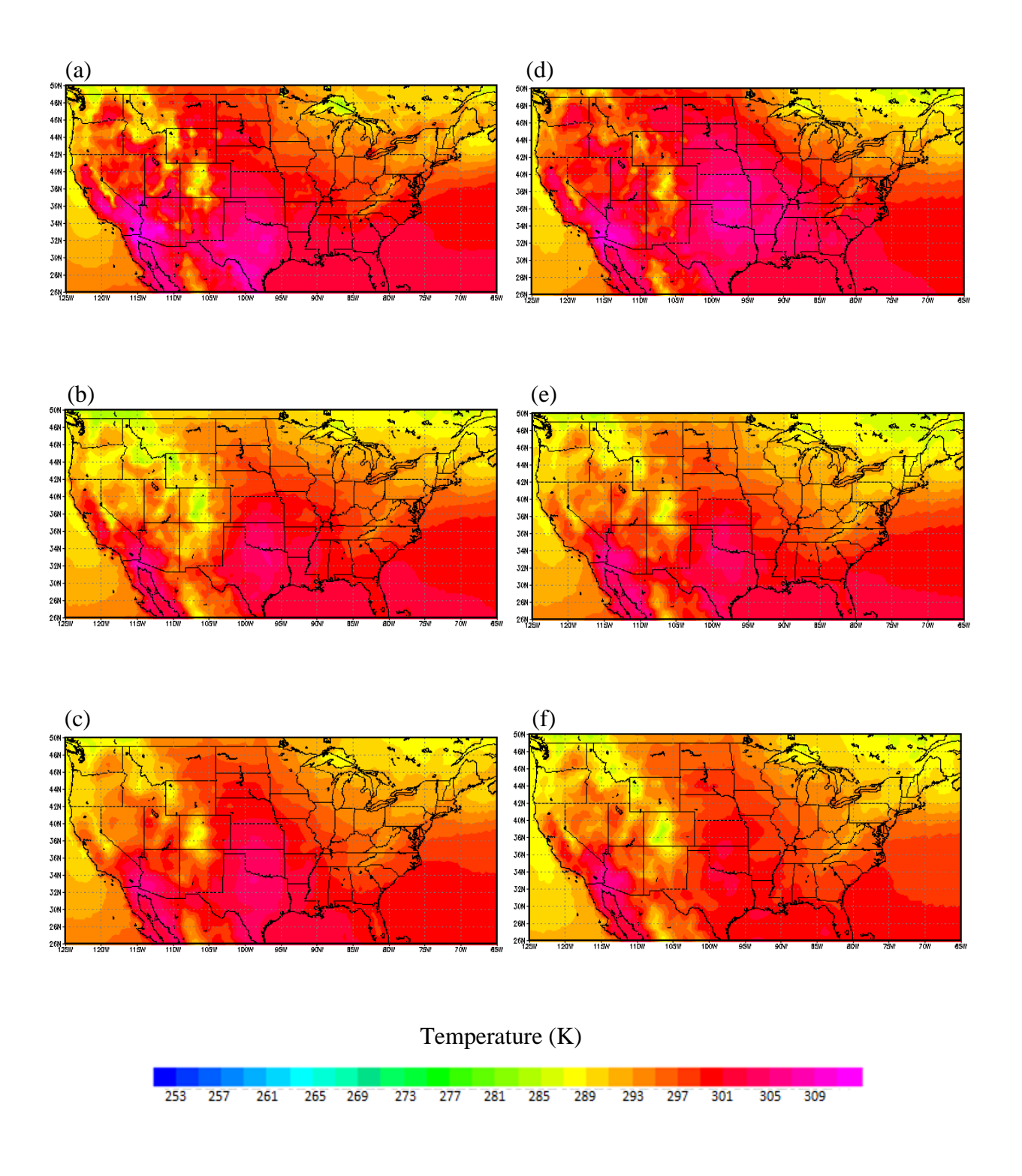


Fig. A.1.1.8. Mean August surface-air temperatures from (a) NARR, (b) CRCM, (c) ECP2, (d) HRM3, (e) MM5I, and (f) WRFG for the CONUS domain.

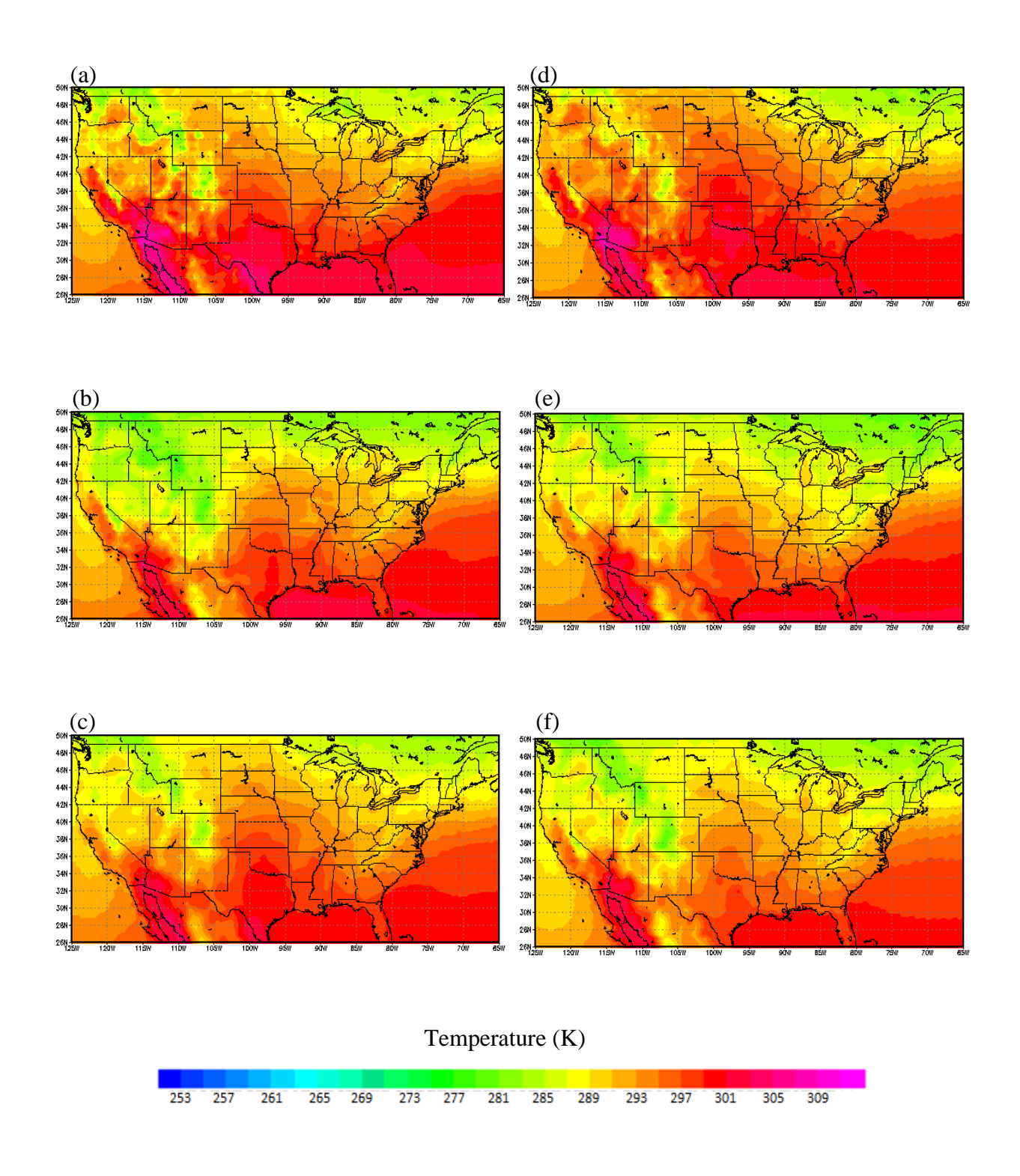


Fig. A.1.1.9. Mean September surface-air temperatures from (a) NARR, (b) CRCM, (c) ECP2, (d) HRM3, (e) MM5I, and (f) WRFG for the CONUS domain.

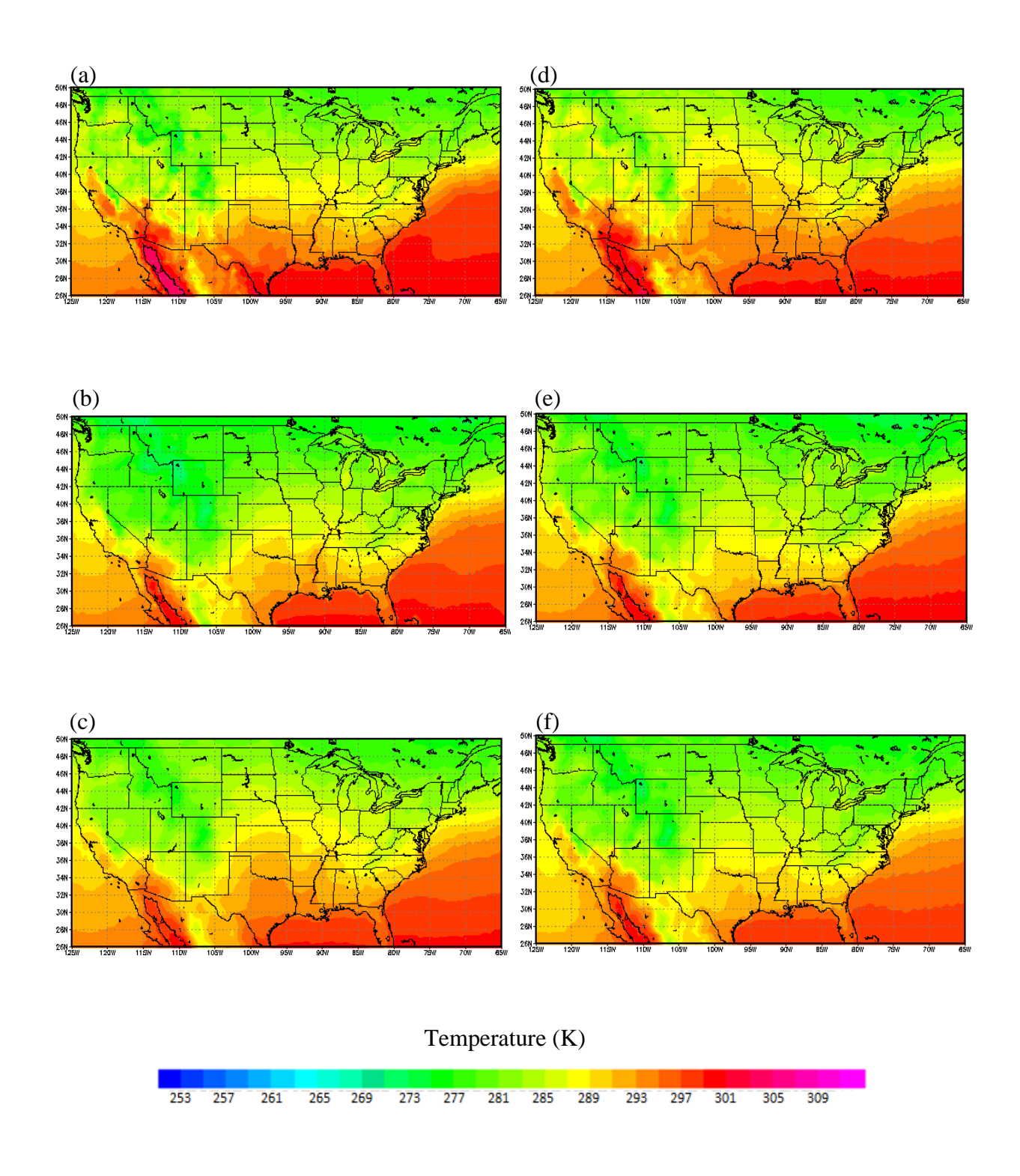


Fig. A.1.1.10. Mean October surface-air temperatures from (a) NARR, (b) CRCM, (c) ECP2, (d) HRM3, (e) MM5I, and (f) WRFG for the CONUS domain.

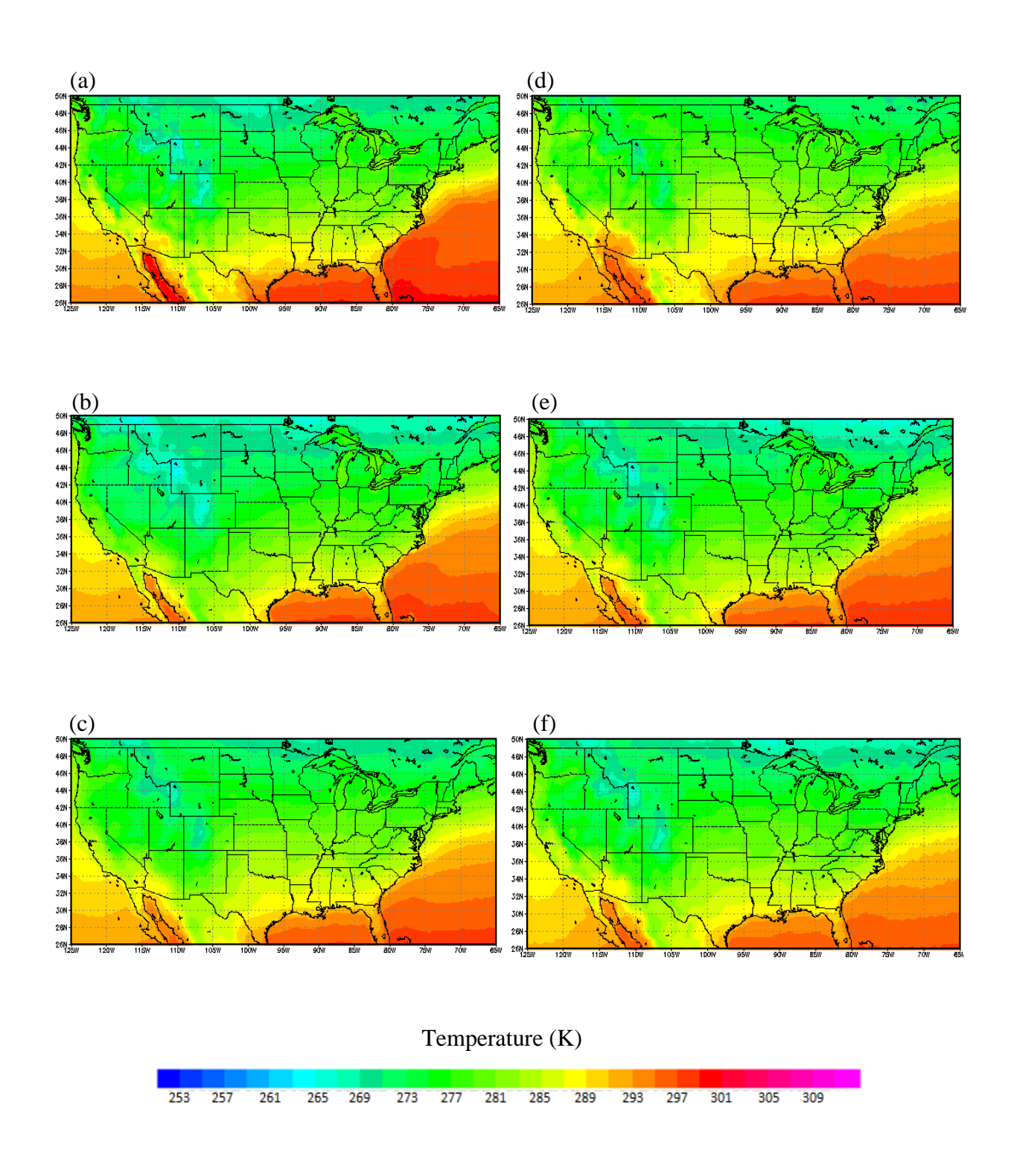


Fig. A.1.1.11. Mean November surface-air temperatures from (a) NARR, (b) CRCM, (c) ECP2, (d) HRM3, (e) MM5I, and (f) WRFG for the CONUS domain.

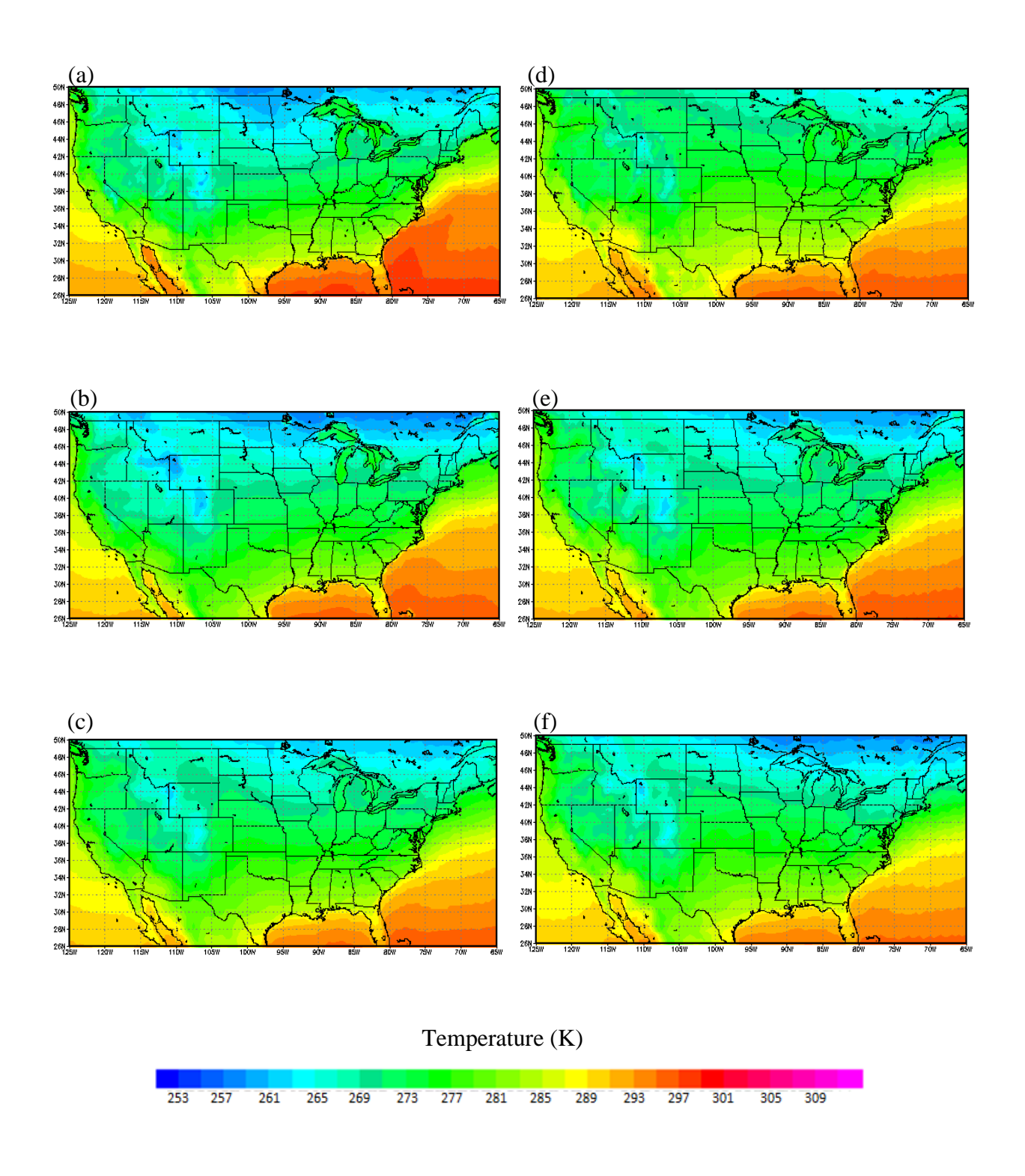


Fig. A.1.1.12. Mean December surface-air temperatures from (a) NARR, (b) CRCM, (c) ECP2, (d) HRM3, (e) MM5I, and (f) WRFG for the CONUS domain.

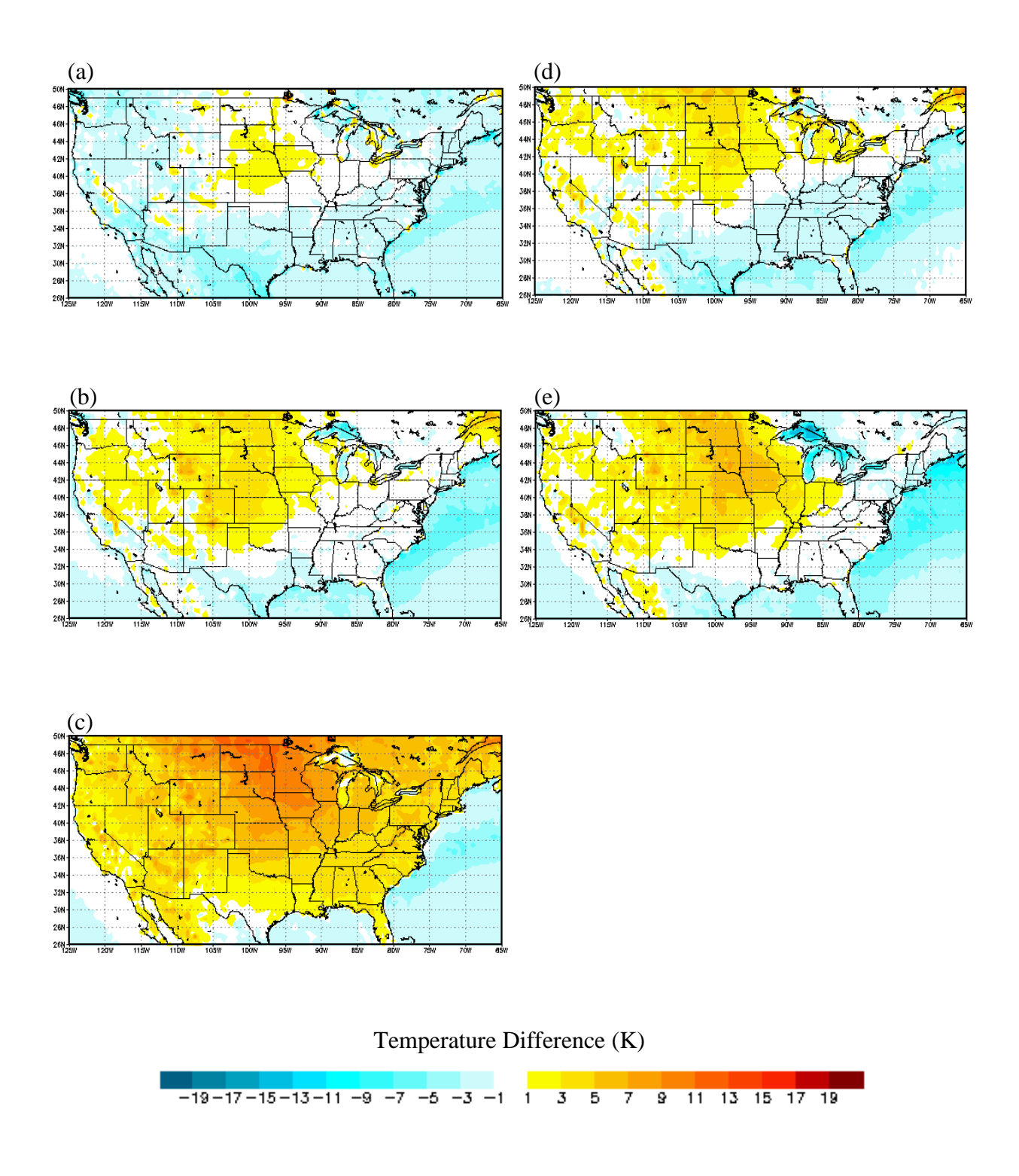


Fig. A.1.2.1. January mean surface-air temperature differences between (a) CRCM, (b) ECP2, (c) HRM3, (d) MM5I, (e) WRFG, and NARR for the CONUS domain.

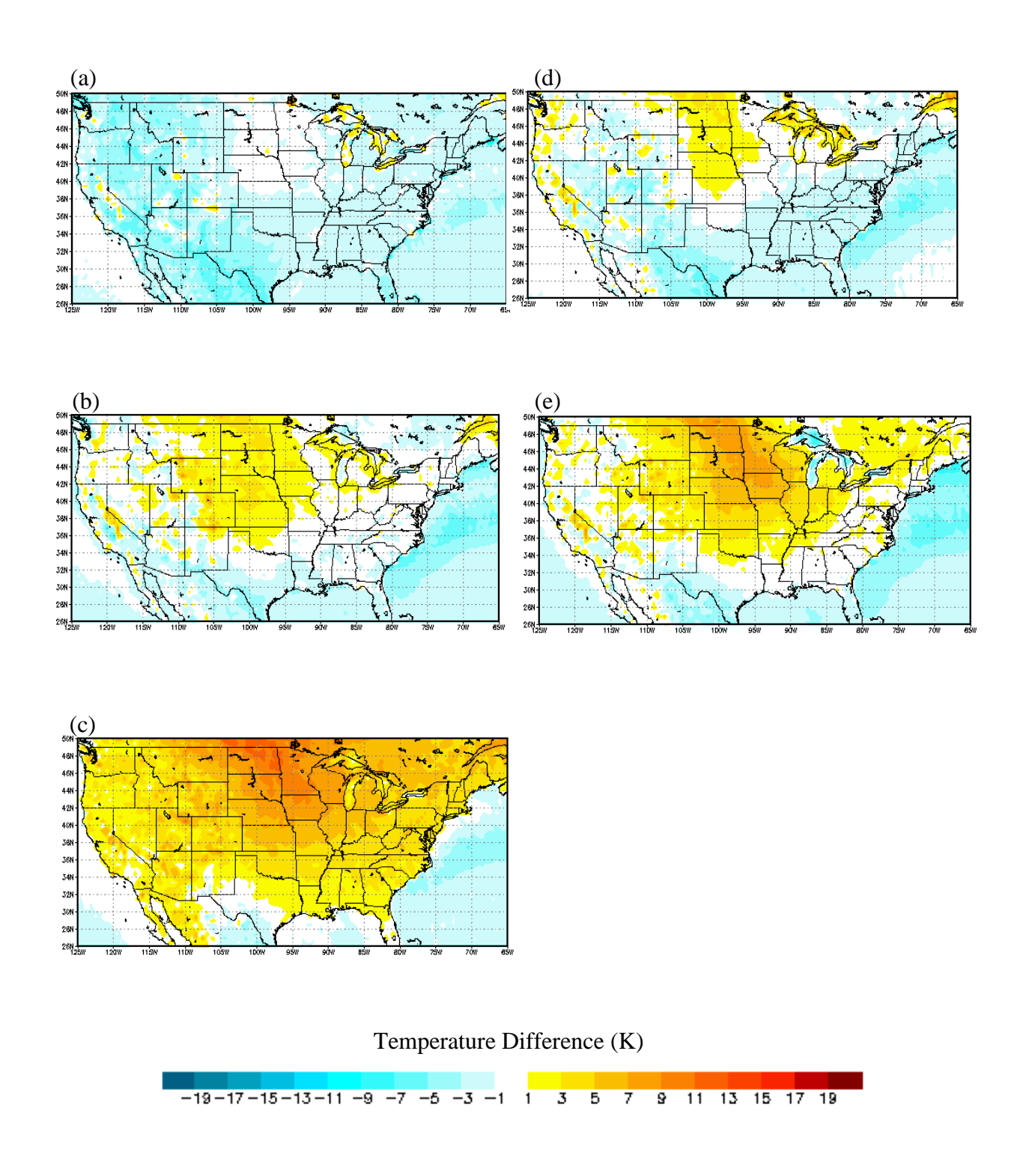


Fig. A.1.2.2. February mean surface-air temperature differences between (a) CRCM, (b) ECP2, (c) HRM3, (d) MM5I, (e) WRFG, and NARR for the CONUS domain.

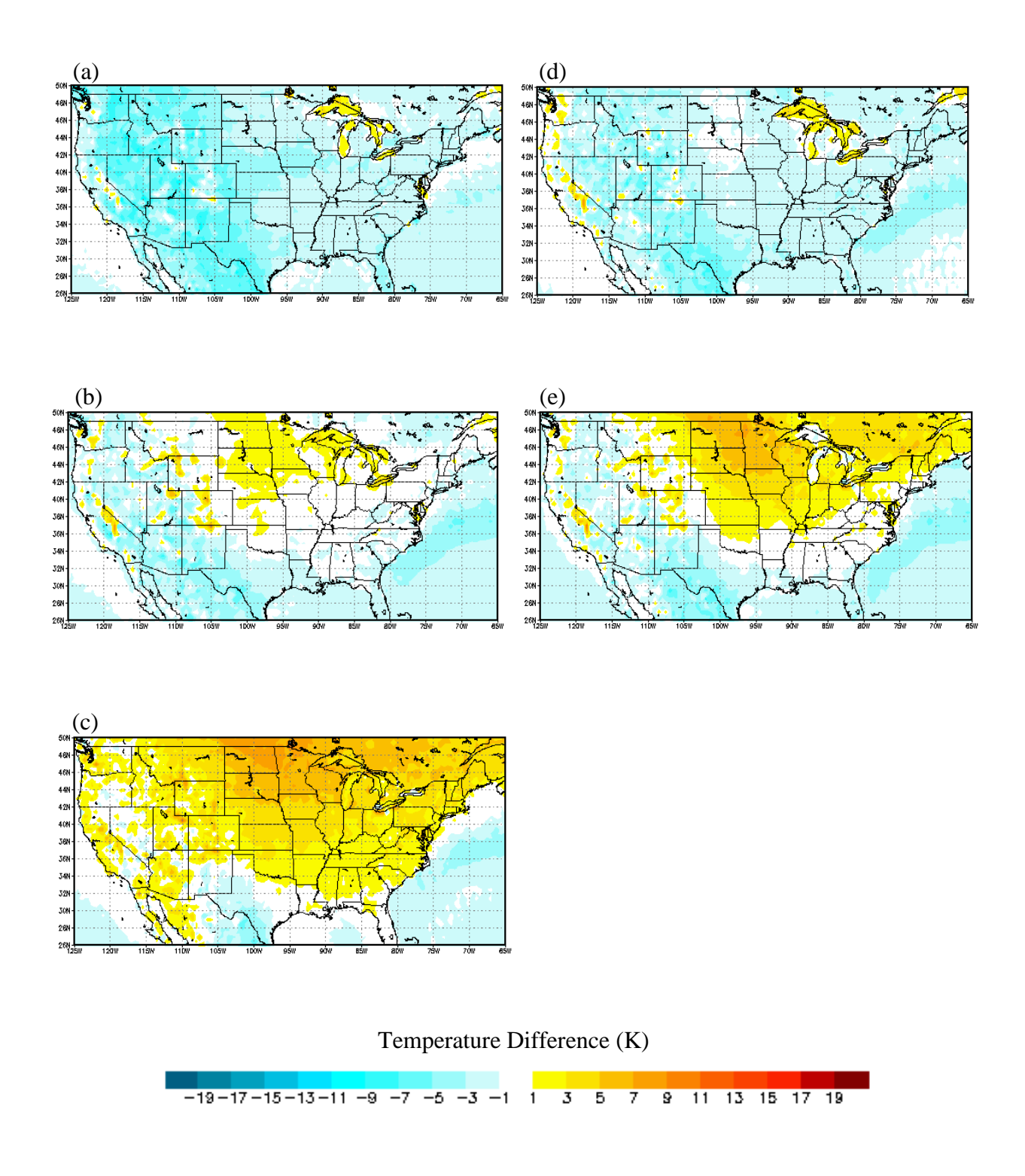


Fig. A.1.2.3. March mean surface-air temperature differences between (a) CRCM, (b) ECP2, (c) HRM3, (d) MM5I, (e) WRFG, and NARR for the CONUS domain.

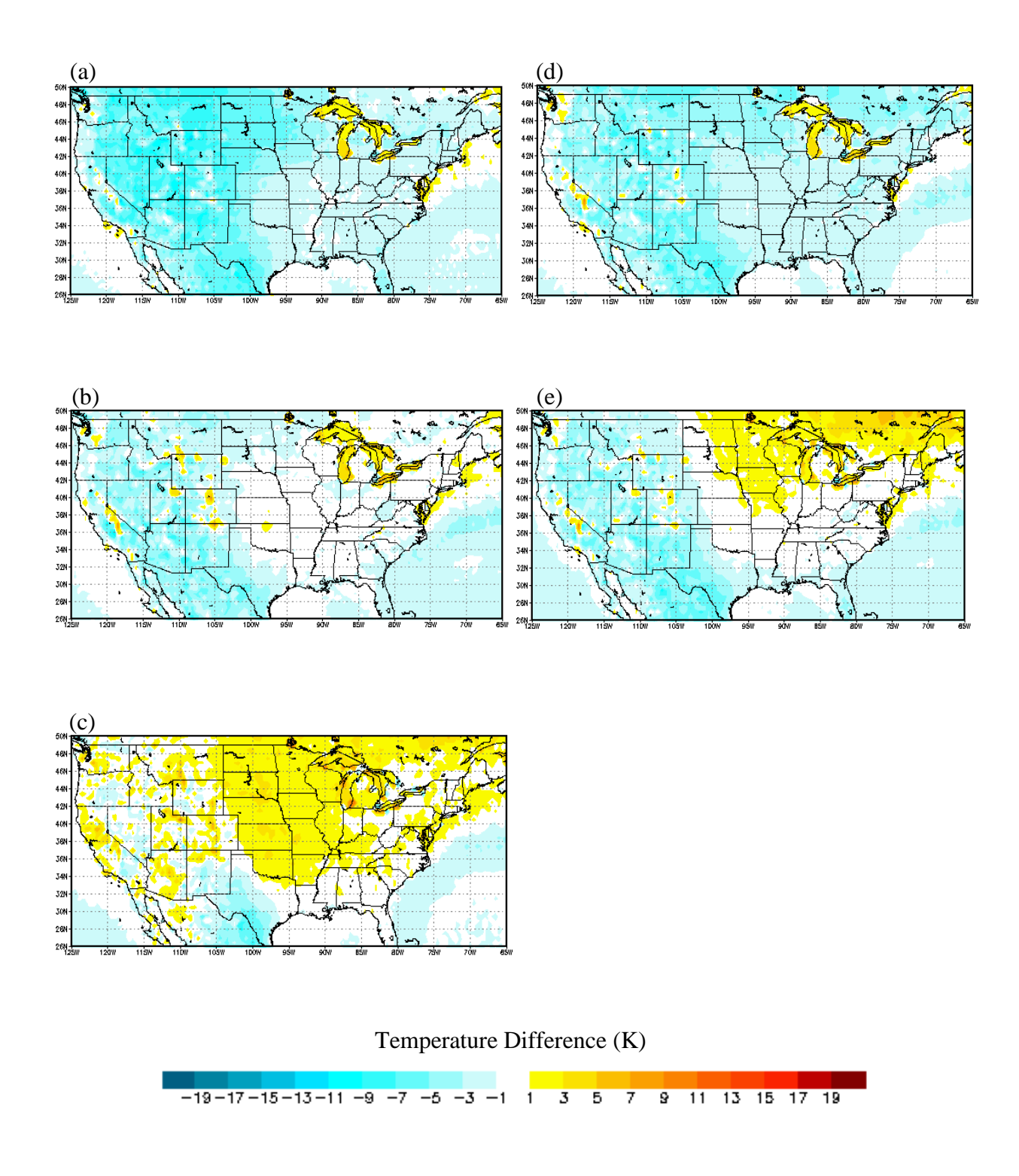


Fig. A.1.2.4. April mean surface-air temperature differences between (a) CRCM, (b) ECP2, (c) HRM3, (d) MM5I, (e) WRFG, and NARR for the CONUS domain.

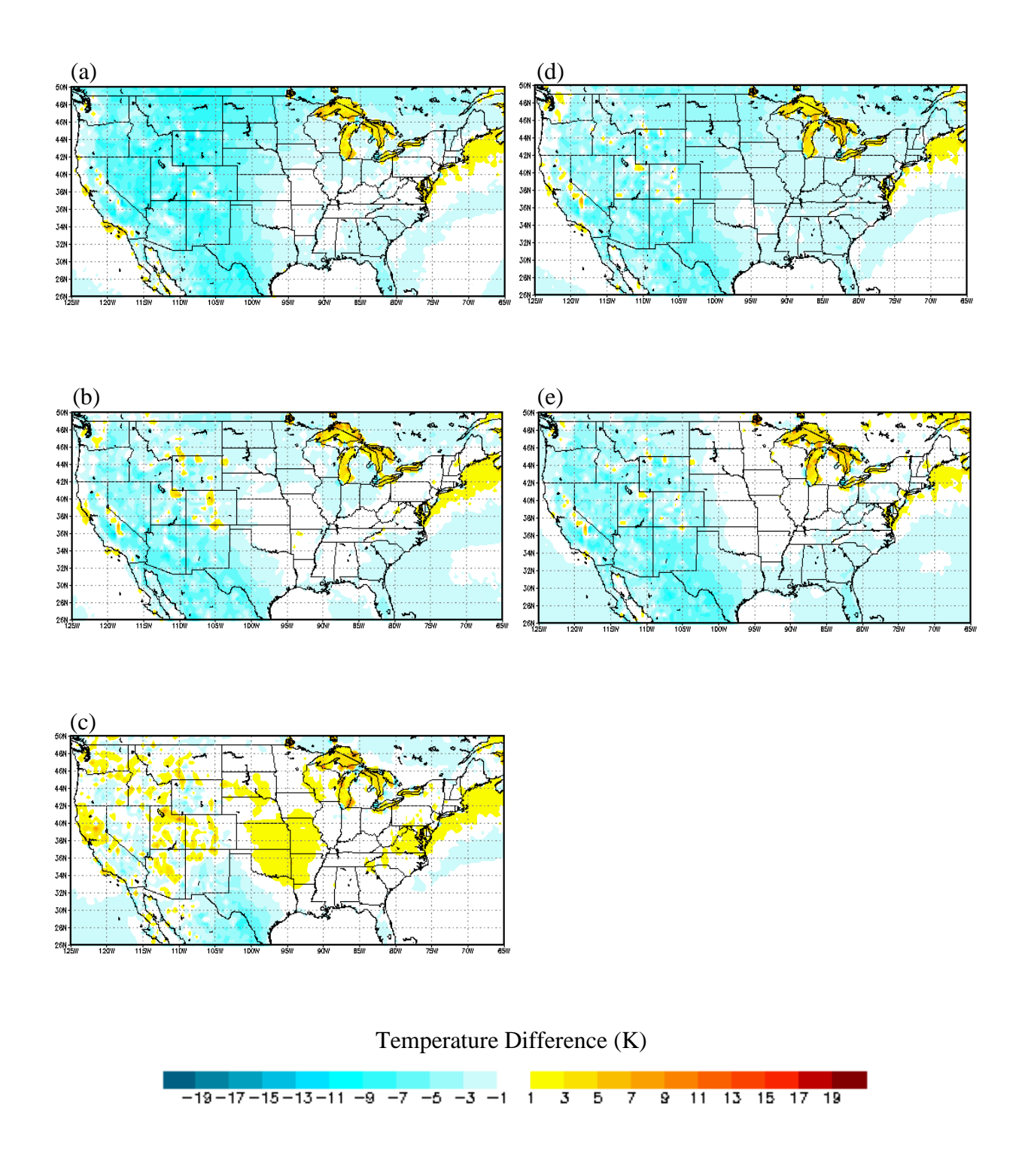


Fig. A.1.2.5. May mean surface-air temperature differences between (a) CRCM, (b) ECP2, (c) HRM3, (d) MM5I, (e) WRFG, and NARR for the CONUS domain.

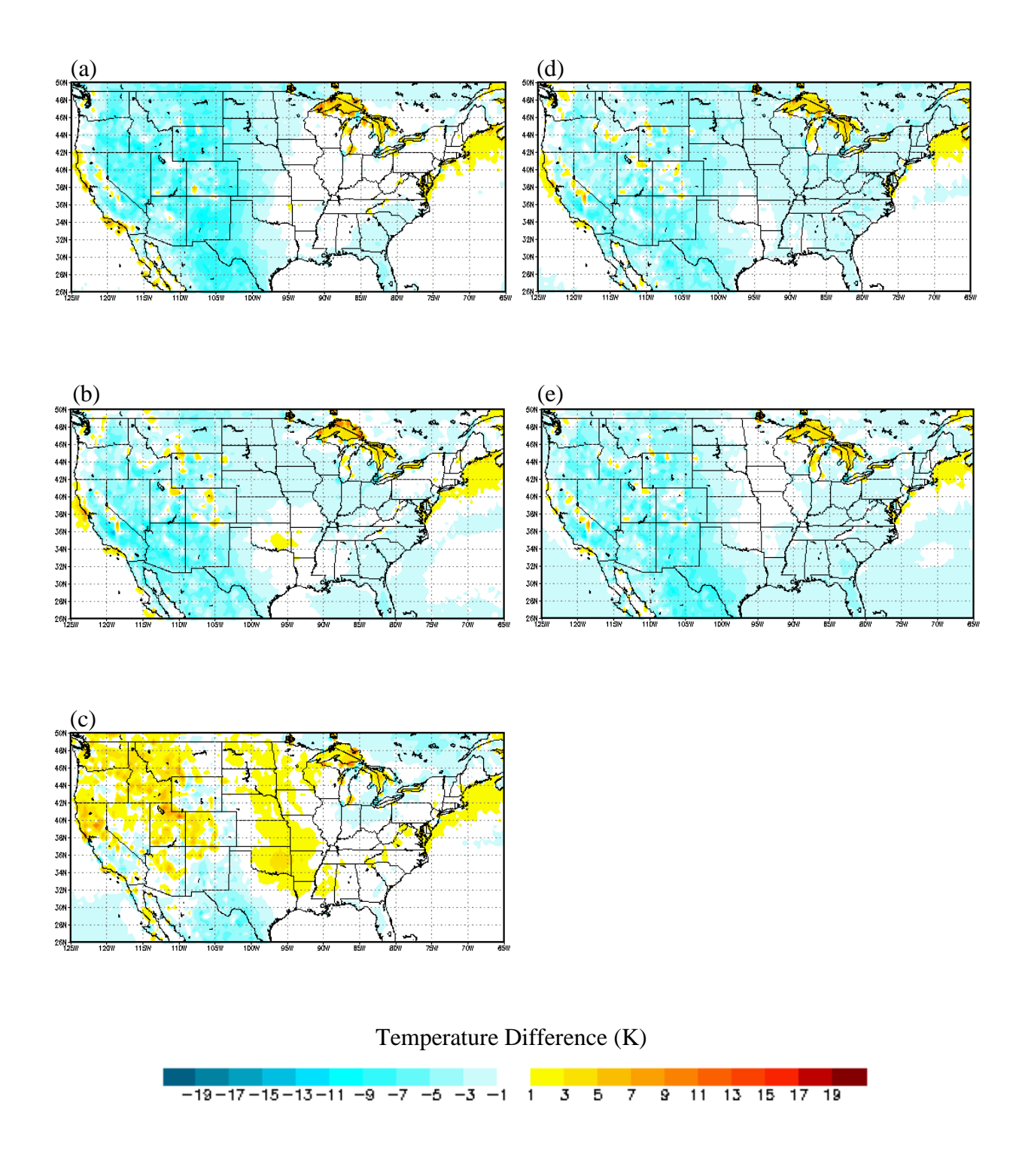


Fig. A.1.2.6. June mean surface-air temperature differences between (a) CRCM, (b) ECP2, (c) HRM3, (d) MM5I, (e) WRFG, and NARR for the CONUS domain.

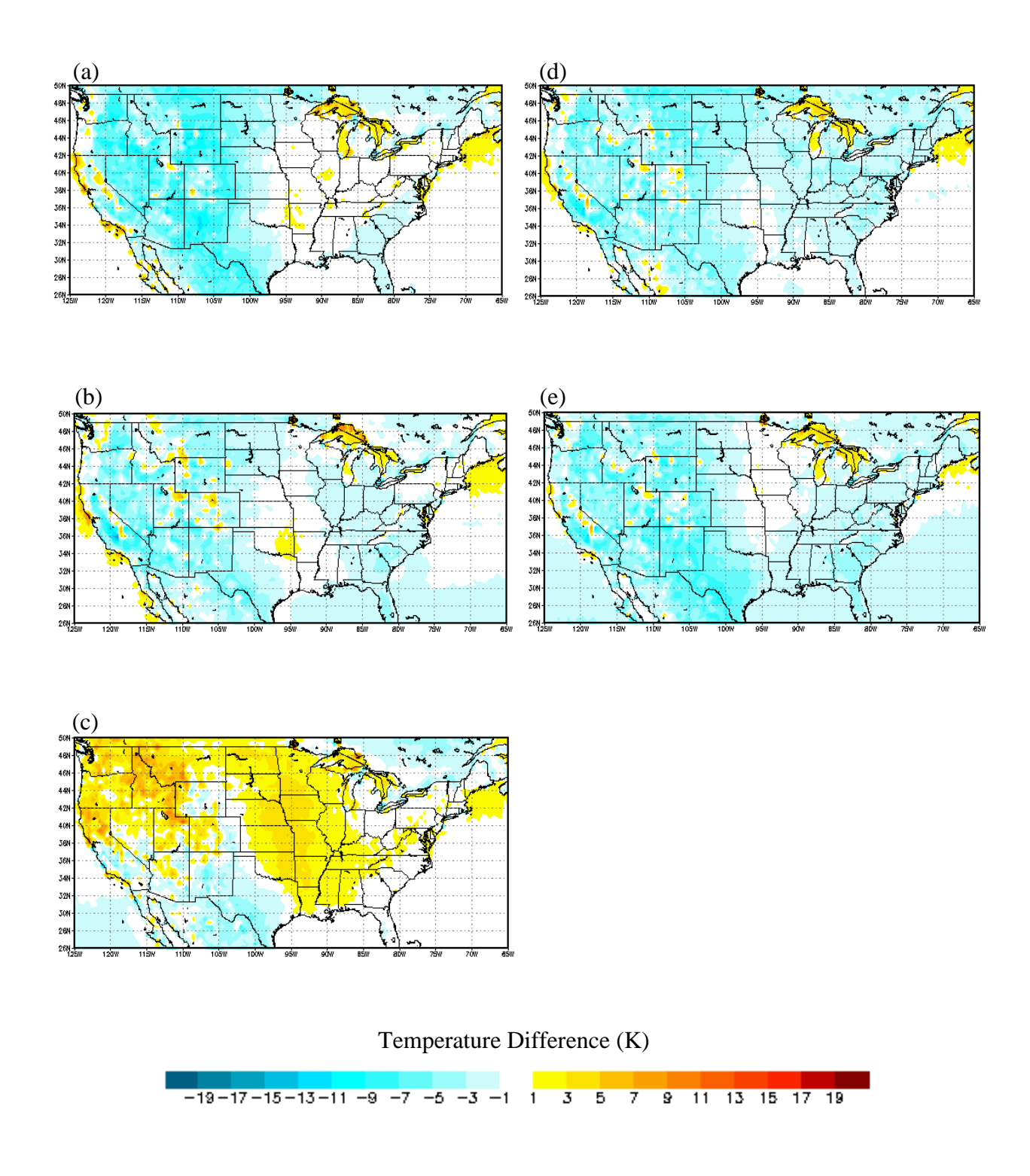


Fig. A.1.2.7. July mean surface-air temperature differences between (a) CRCM, (b) ECP2, (c) HRM3, (d) MM5I, (e) WRFG, and NARR for the CONUS domain.

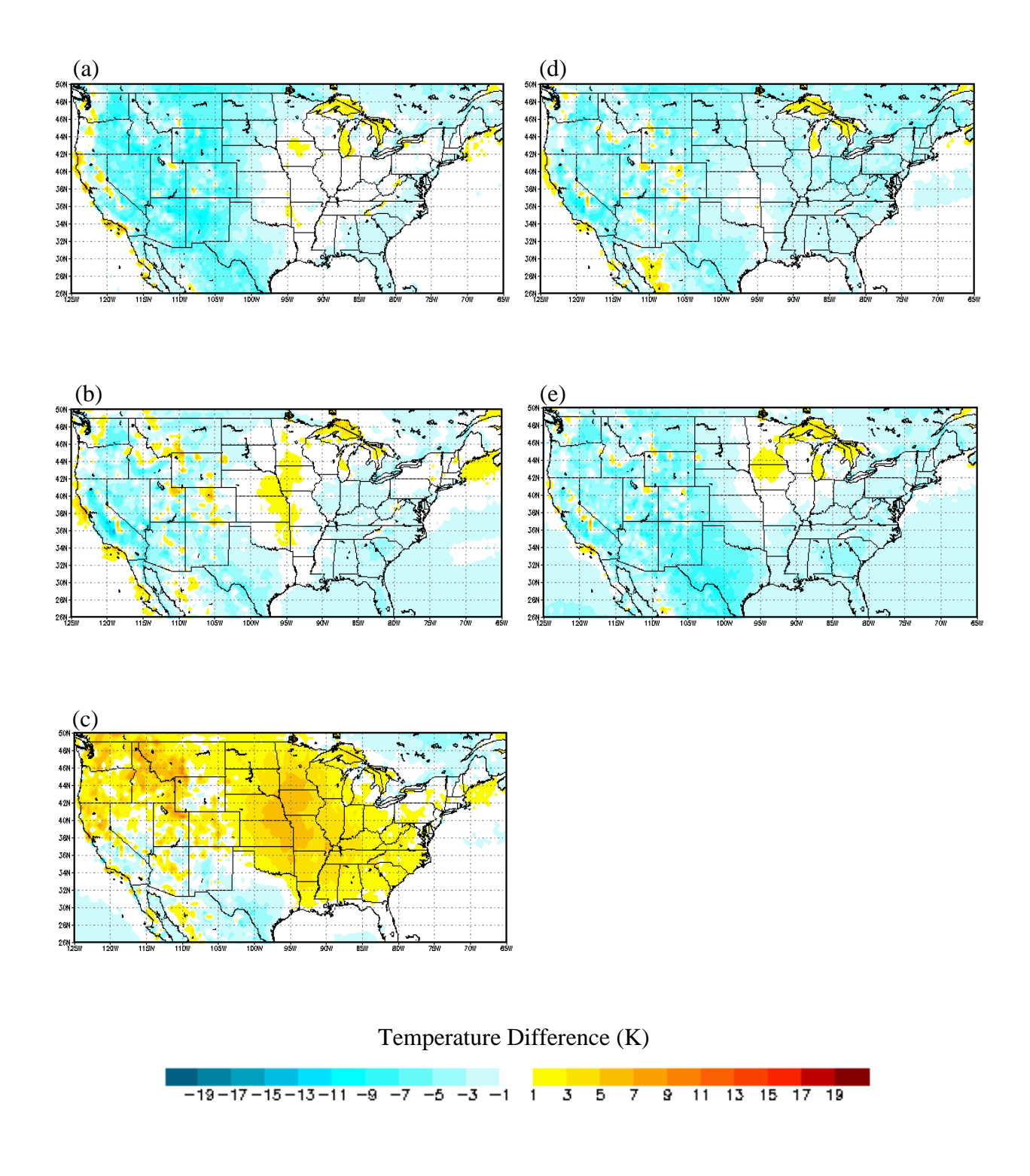


Fig. A.1.2.8. August mean surface-air temperature differences between (a) CRCM, (b) ECP2, (c) HRM3, (d) MM5I, (e) WRFG, and NARR for the CONUS domain.

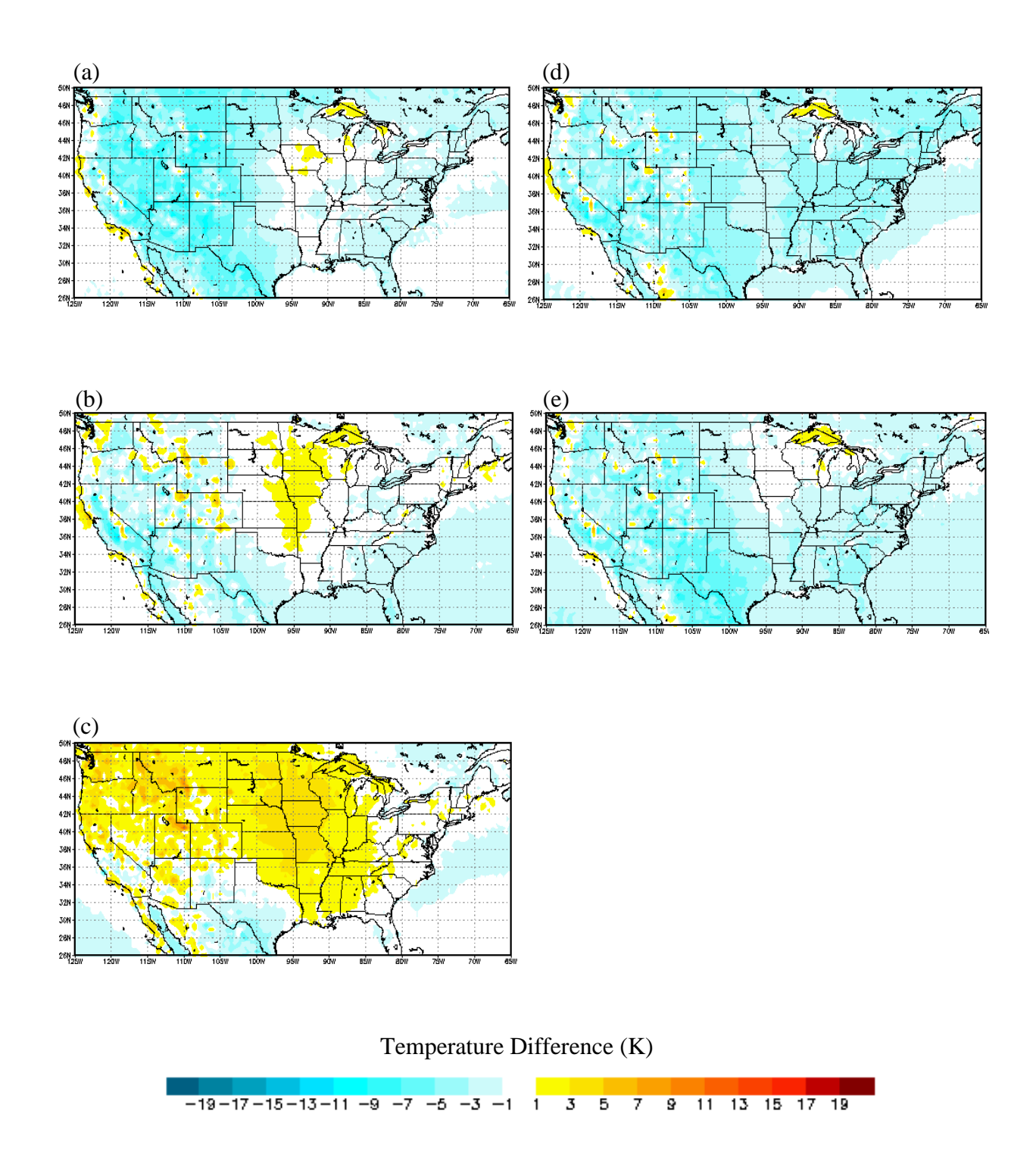


Fig. A.1.2.9. September mean surface-air temperature differences between (a) CRCM, (b) ECP2, (c) HRM3, (d) MM5I, (e) WRFG, and NARR for the CONUS domain.

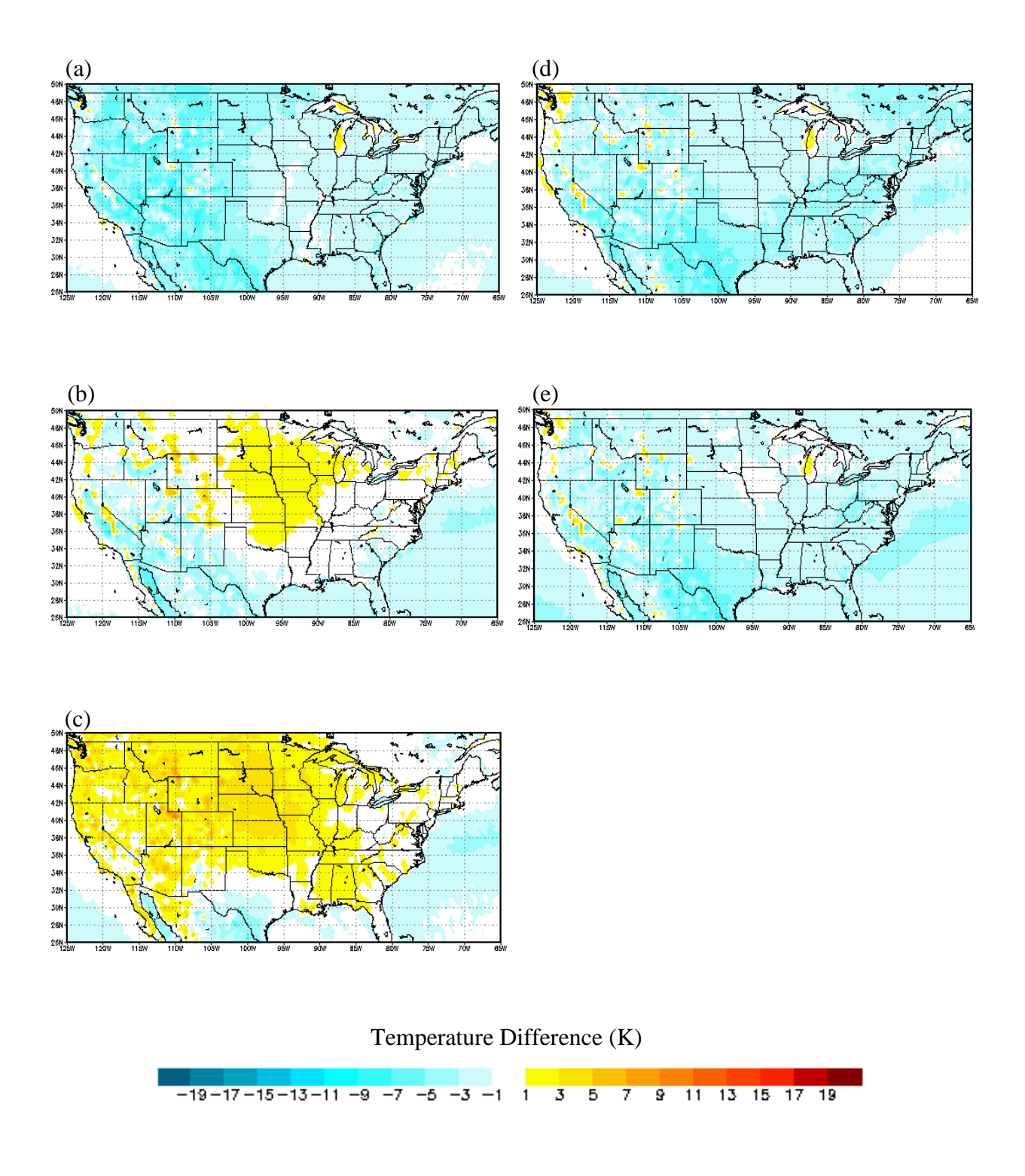


Fig. A.1.2.10. October mean surface-air temperature differences between (a) CRCM, (b) ECP2, (c) HRM3, (d) MM5I, (e) WRFG, and NARR for the CONUS domain.

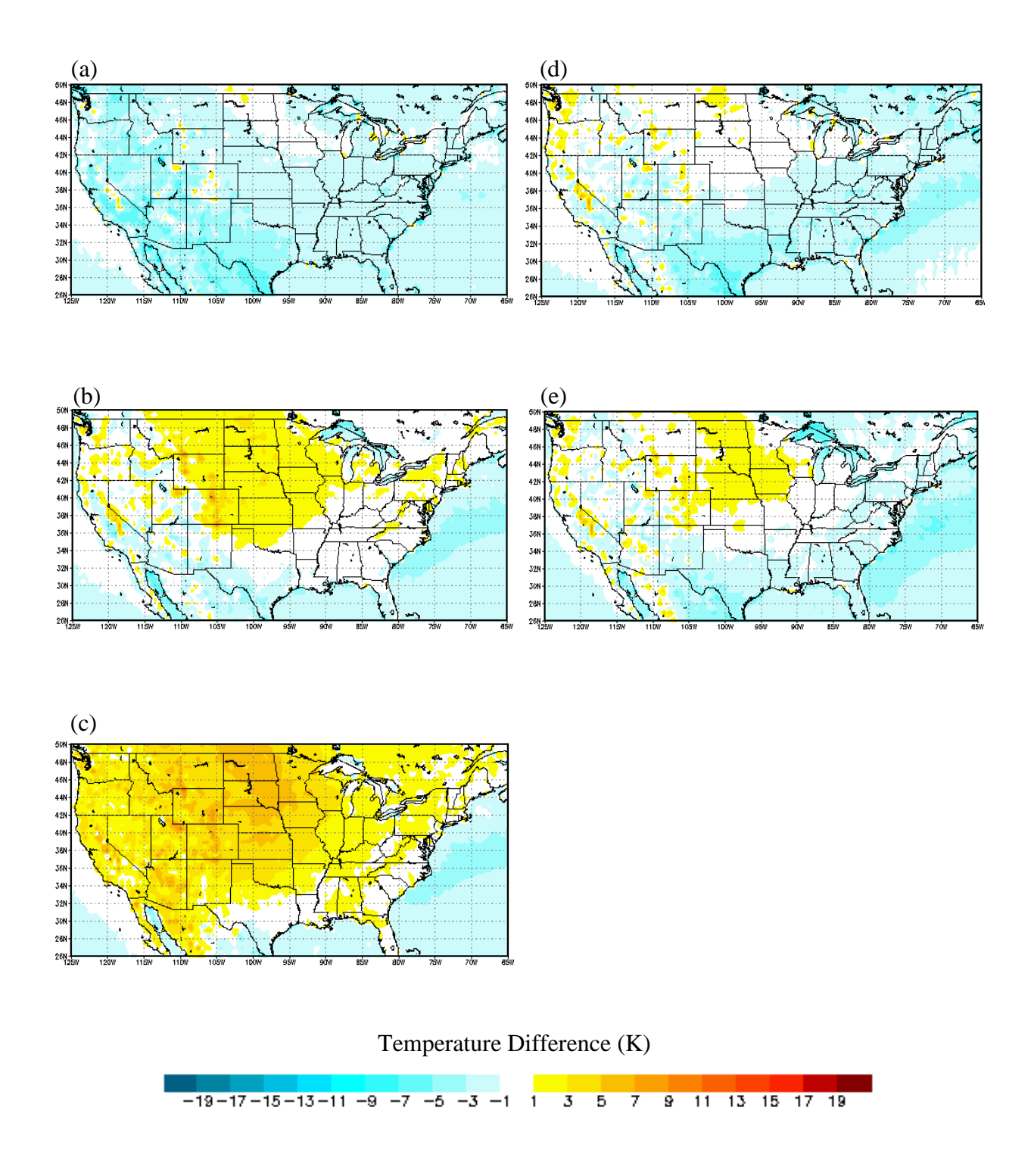


Fig. A.1.2.11. November mean surface-air temperature differences between (a) CRCM, (b) ECP2, (c) HRM3, (d) MM5I, (e) WRFG, and NARR for the CONUS domain.

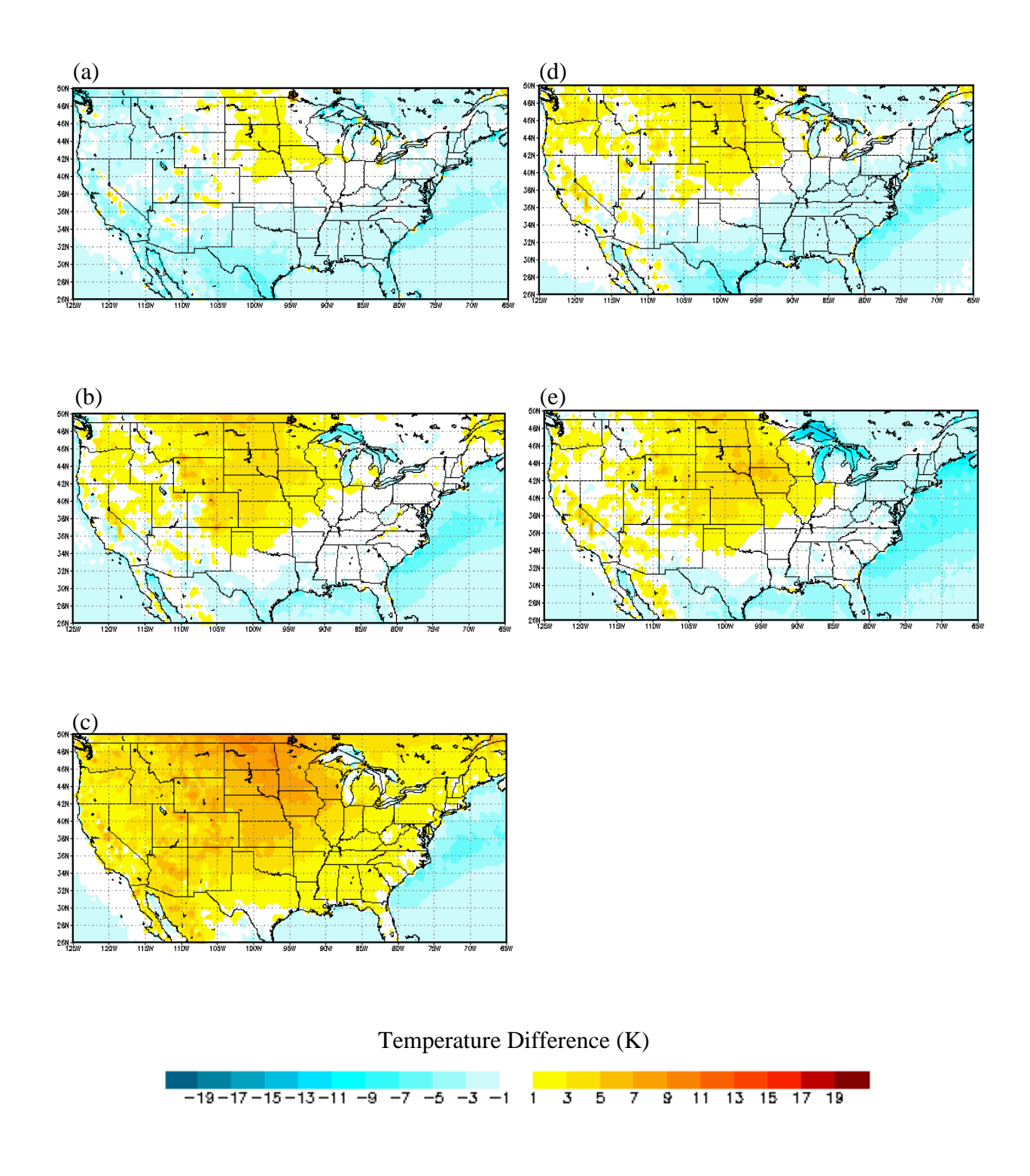


Fig. A.1.2.12. December mean surface-air temperature differences between (a) CRCM, (b) ECP2, (c) HRM3, (d) MM5I, (e) WRFG, and NARR for the CONUS domain.

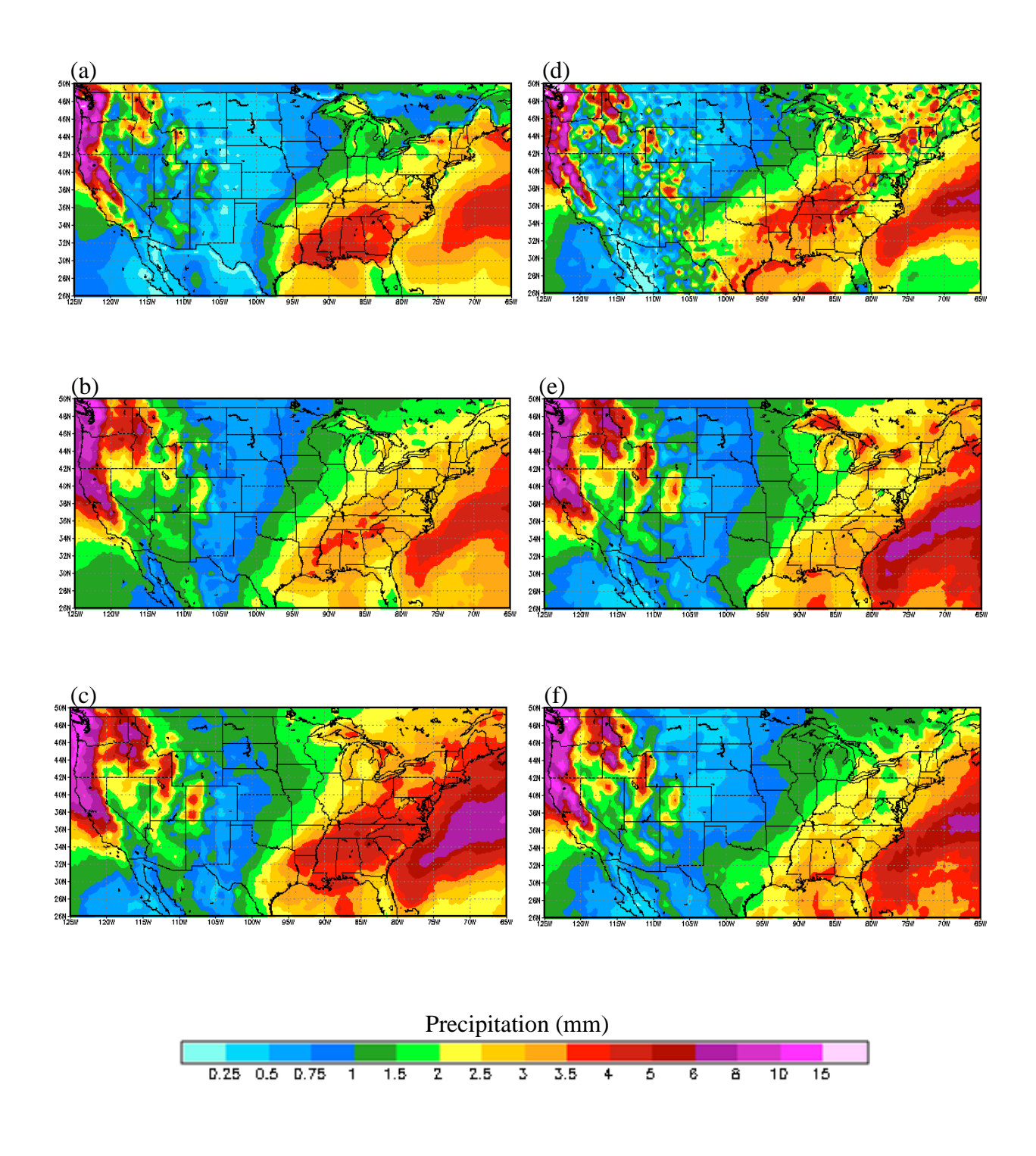


Fig. A.2.1.1. January daily accumulated precipitation from (a) NARR, (b) CRCM, (c) ECP2, (d) HRM3, (e) MM5I, and (f) WRFG for the CONUS domain.

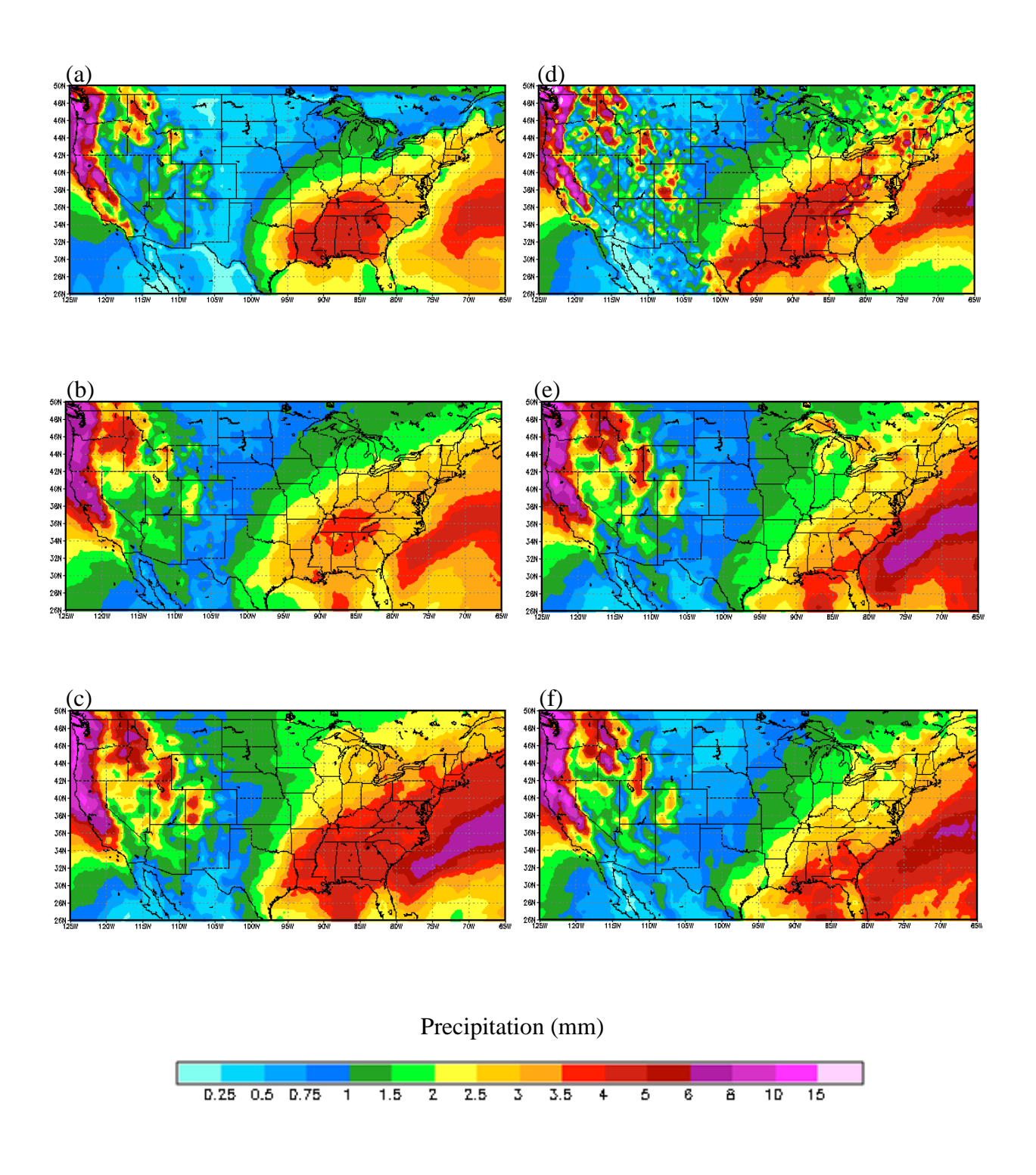


Fig. A.2.1.2. February daily accumulated precipitation from (a) NARR, (b) CRCM, (c) ECP2, (d) HRM3, (e) MM5I, and (f) WRFG for the CONUS domain.

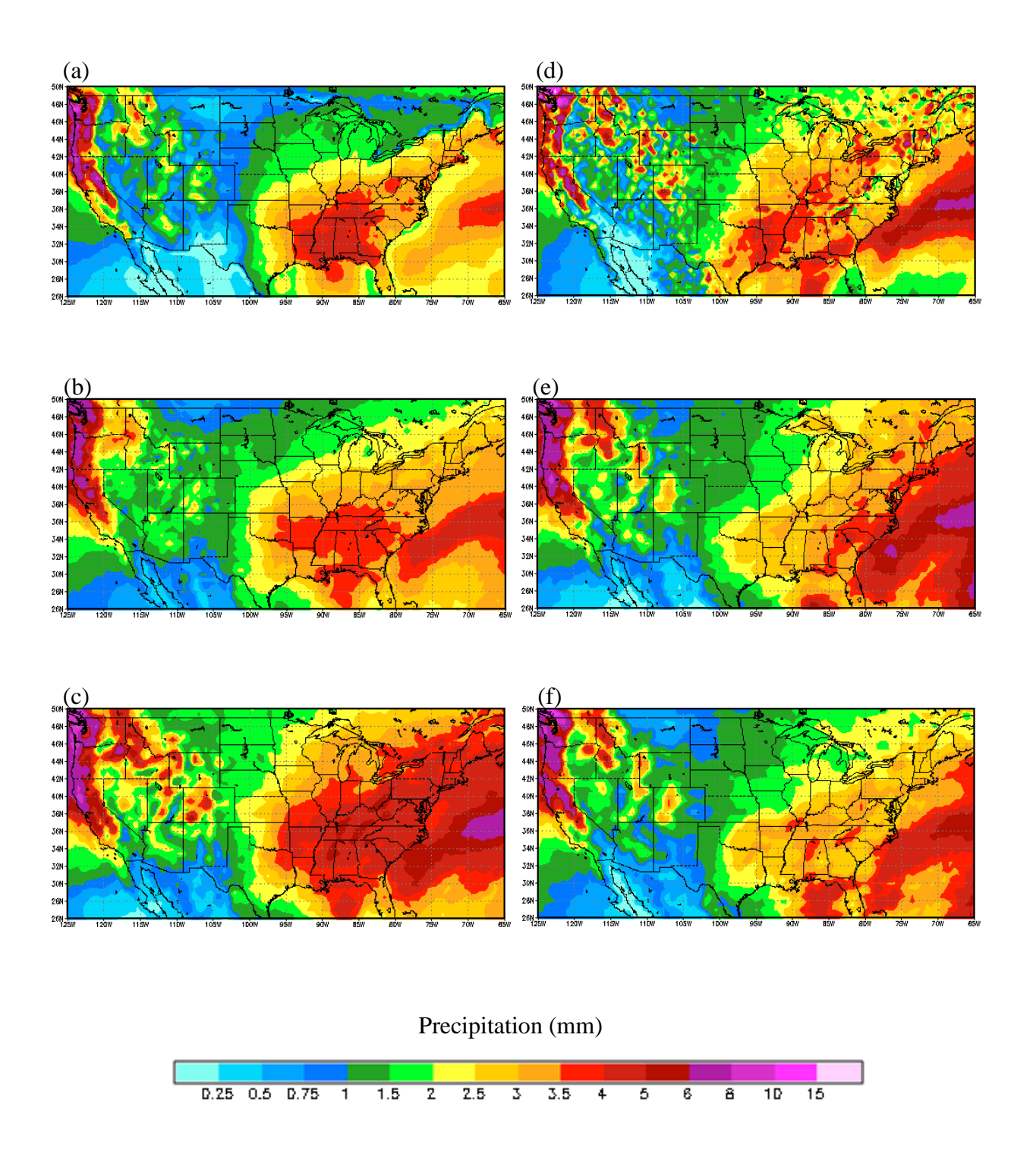


Fig. A.2.1.3. March daily accumulated precipitation from (a) NARR, (b) CRCM, (c) ECP2, (d) HRM3, (e) MM5I, and (f) WRFG for the CONUS domain.

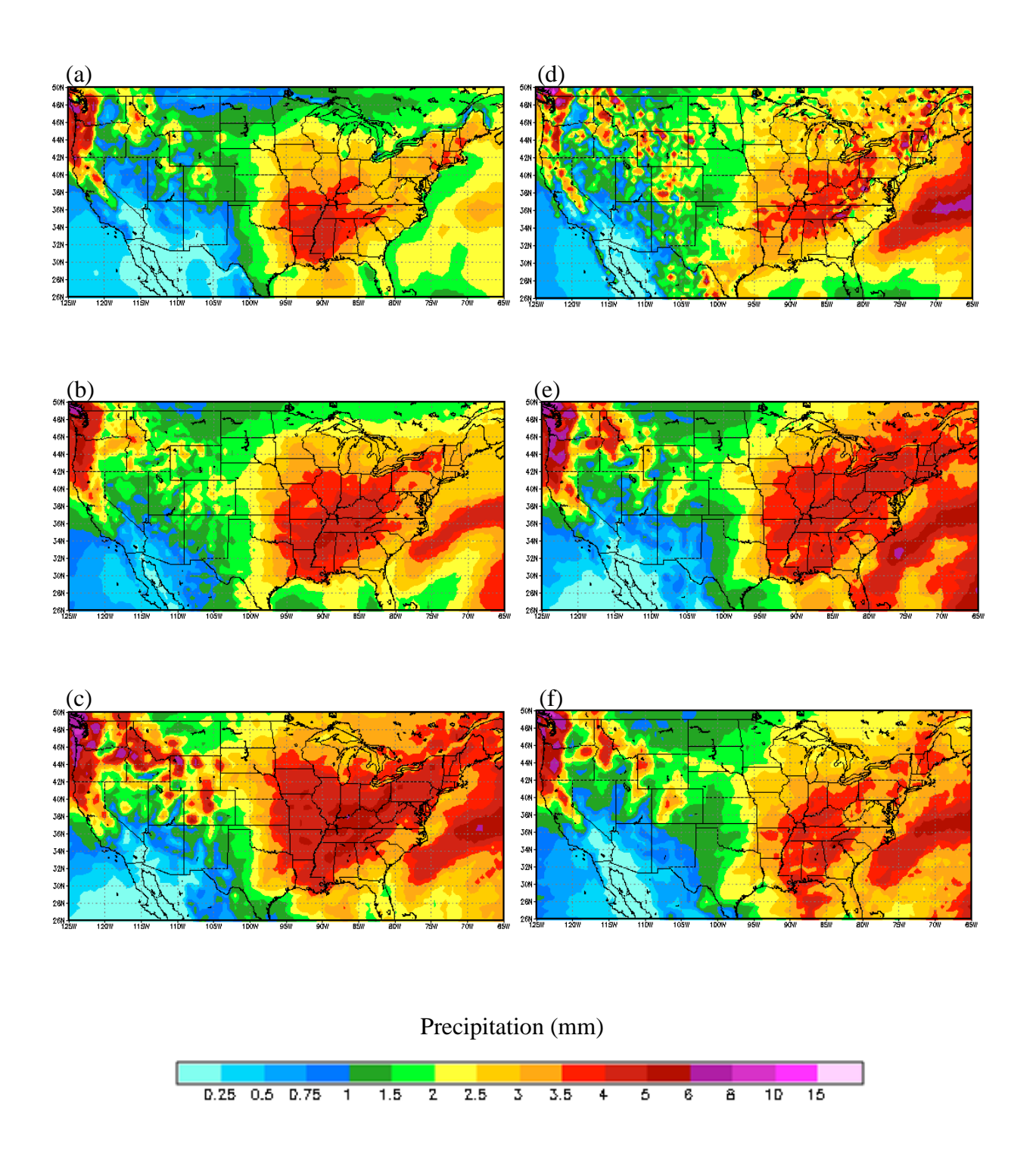


Fig. A.2.1.4. April daily accumulated precipitation from (a) NARR, (b) CRCM, (c) ECP2, (d) HRM3, (e) MM5I, and (f) WRFG for the CONUS domain.

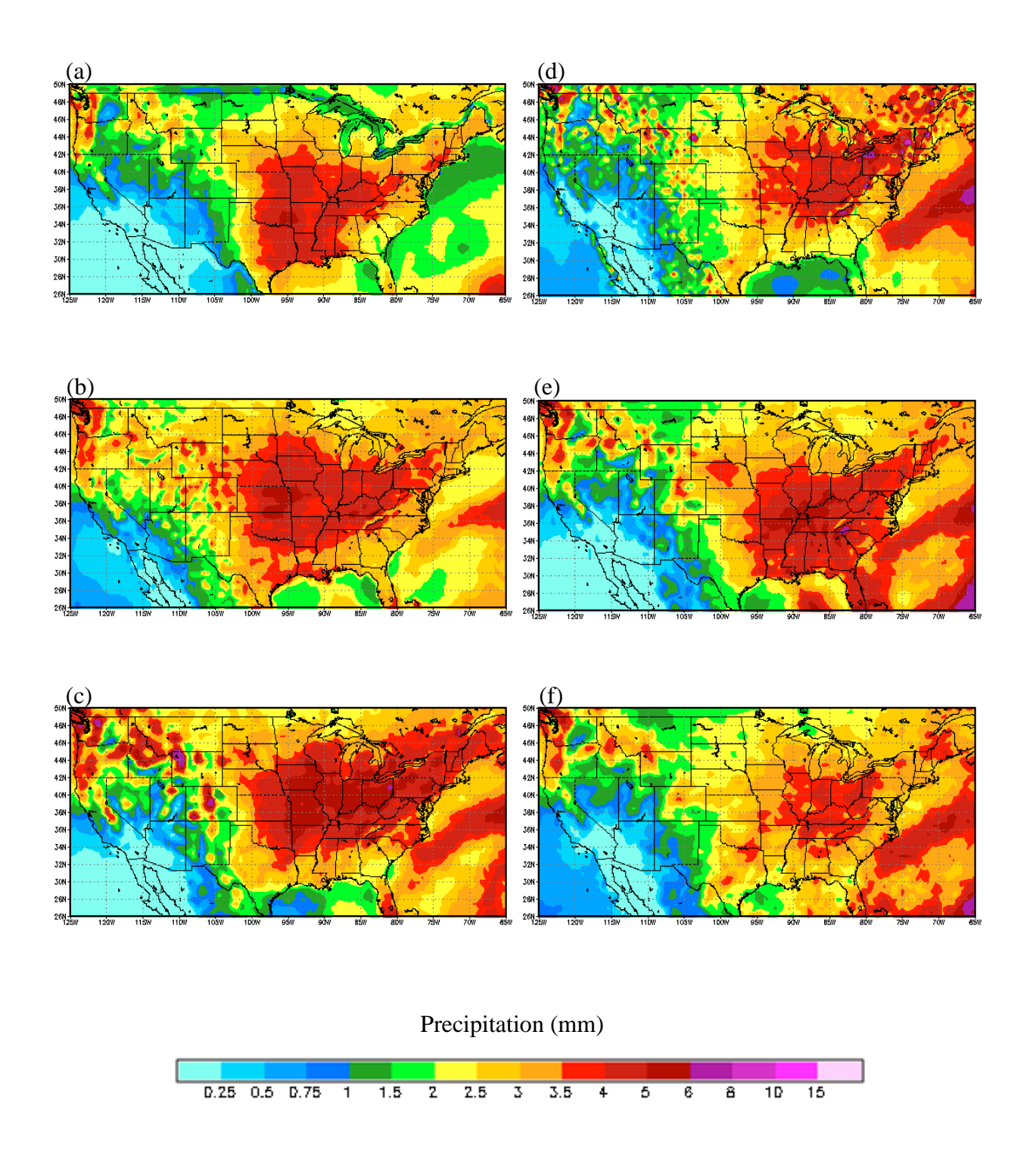


Fig. A.2.1.5. May daily accumulated precipitation from (a) NARR, (b) CRCM, (c) ECP2, (d) HRM3, (e) MM5I, and (f) WRFG for the CONUS domain.

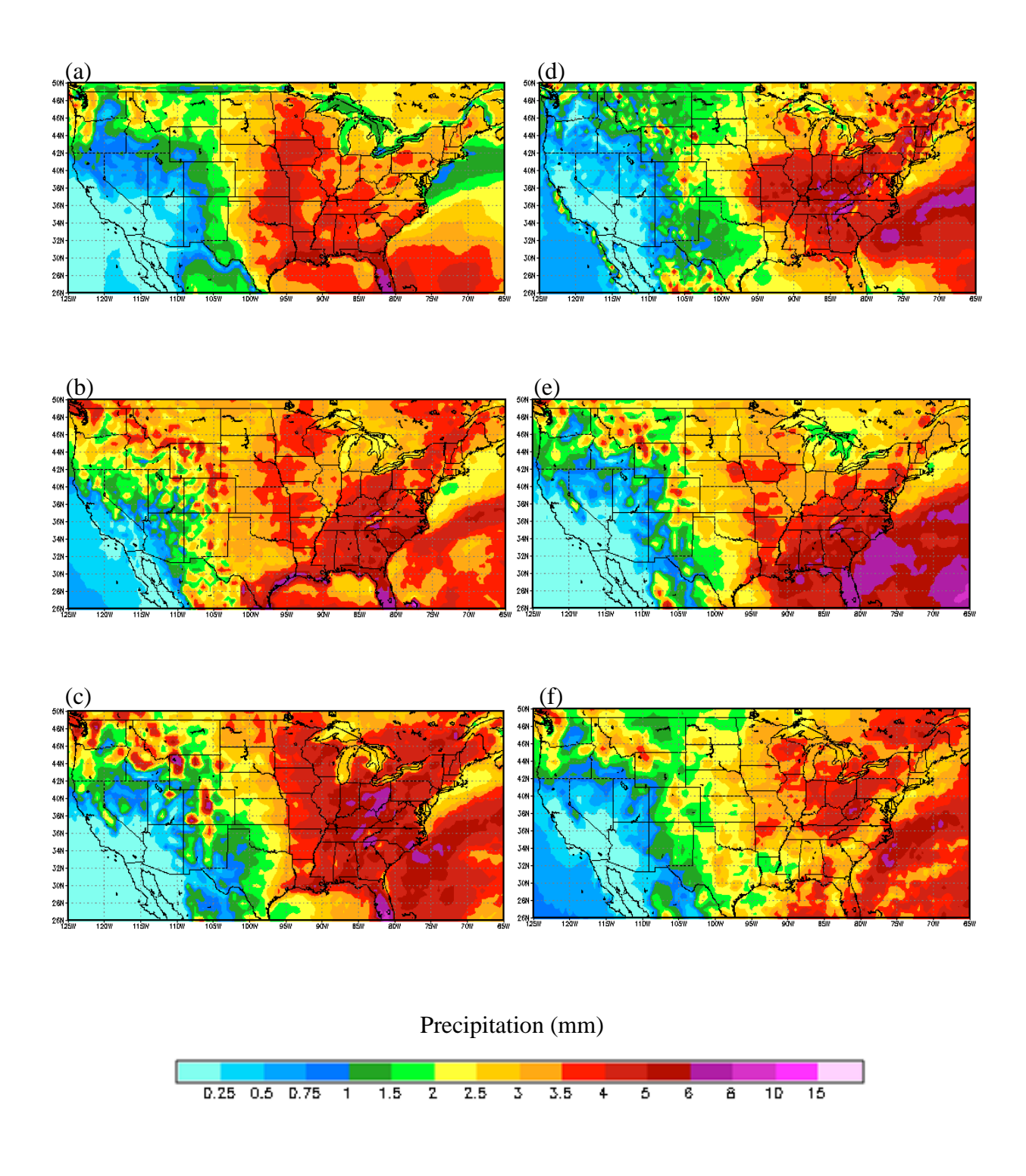


Fig. A.2.1.6. June daily accumulated precipitation from (a) NARR, (b) CRCM, (c) ECP2, (d) HRM3, (e) MM5I, and (f) WRFG for the CONUS domain.

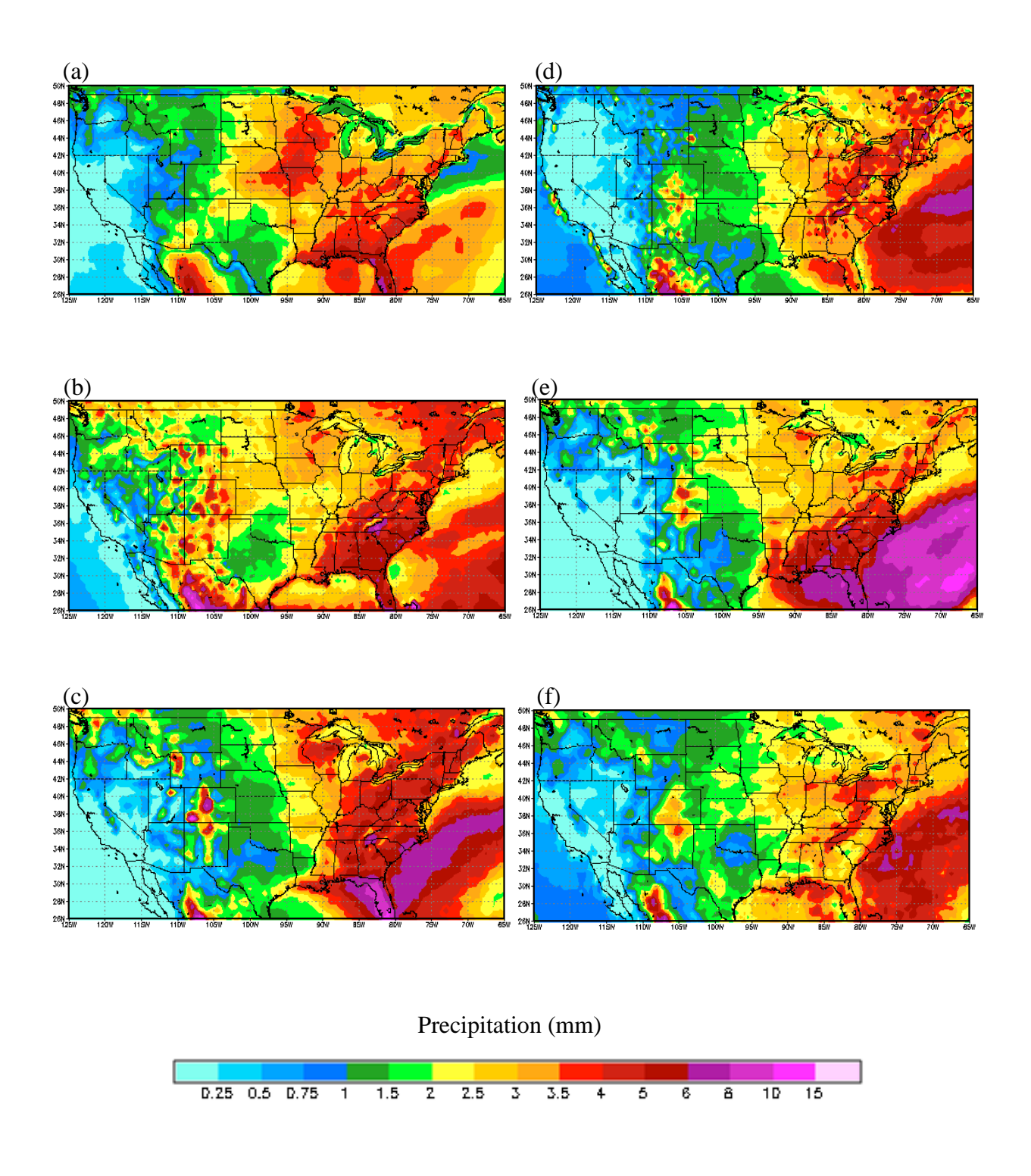


Fig. A.2.1.7. July daily accumulated precipitation from (a) NARR, (b) CRCM, (c) ECP2, (d) HRM3, (e) MM5I, and (f) WRFG for the CONUS domain.

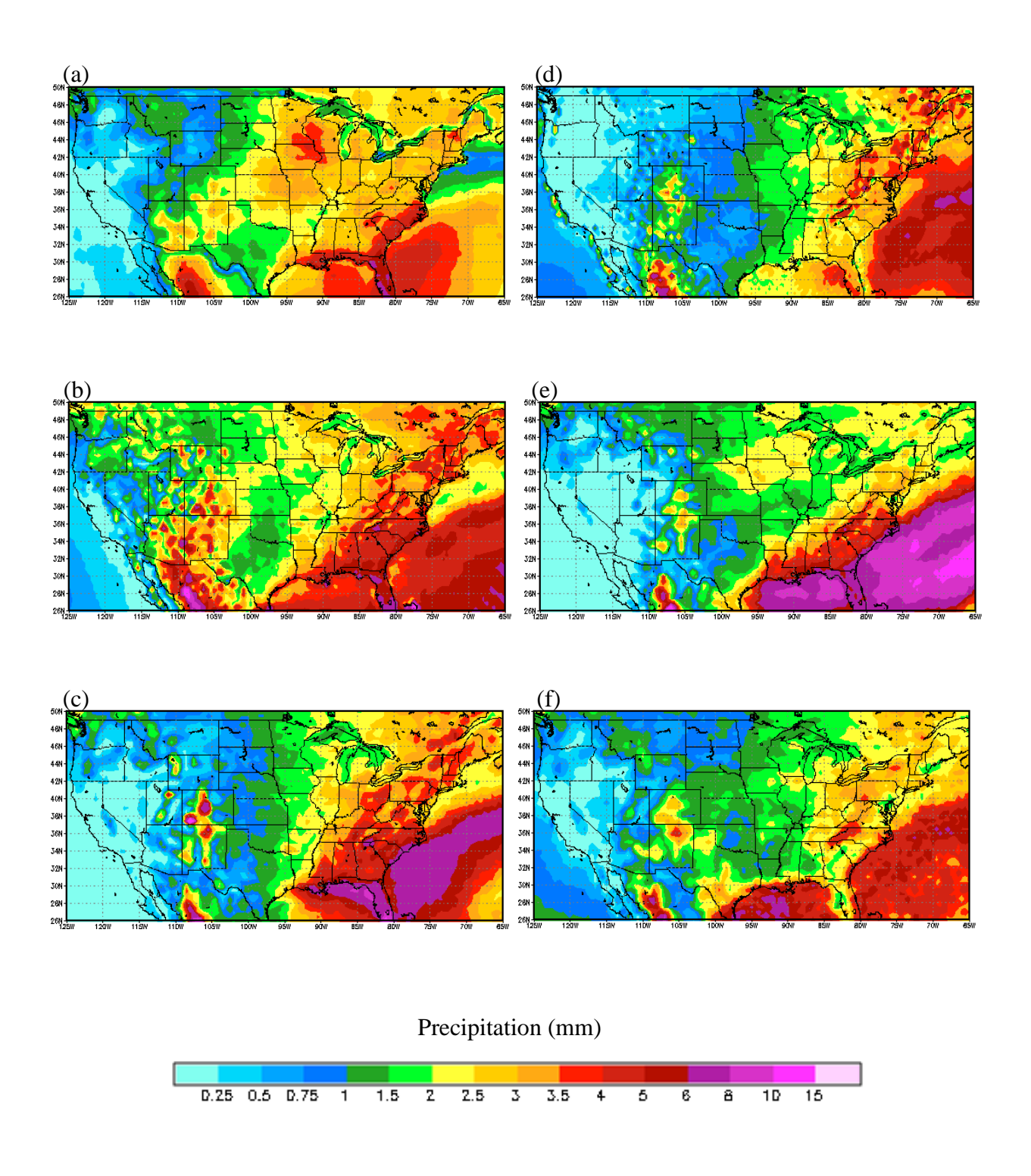


Fig. A.2.1.8. August daily accumulated precipitation from (a) NARR, (b) CRCM, (c) ECP2, (d) HRM3, (e) MM5I, and (f) WRFG for the CONUS domain.

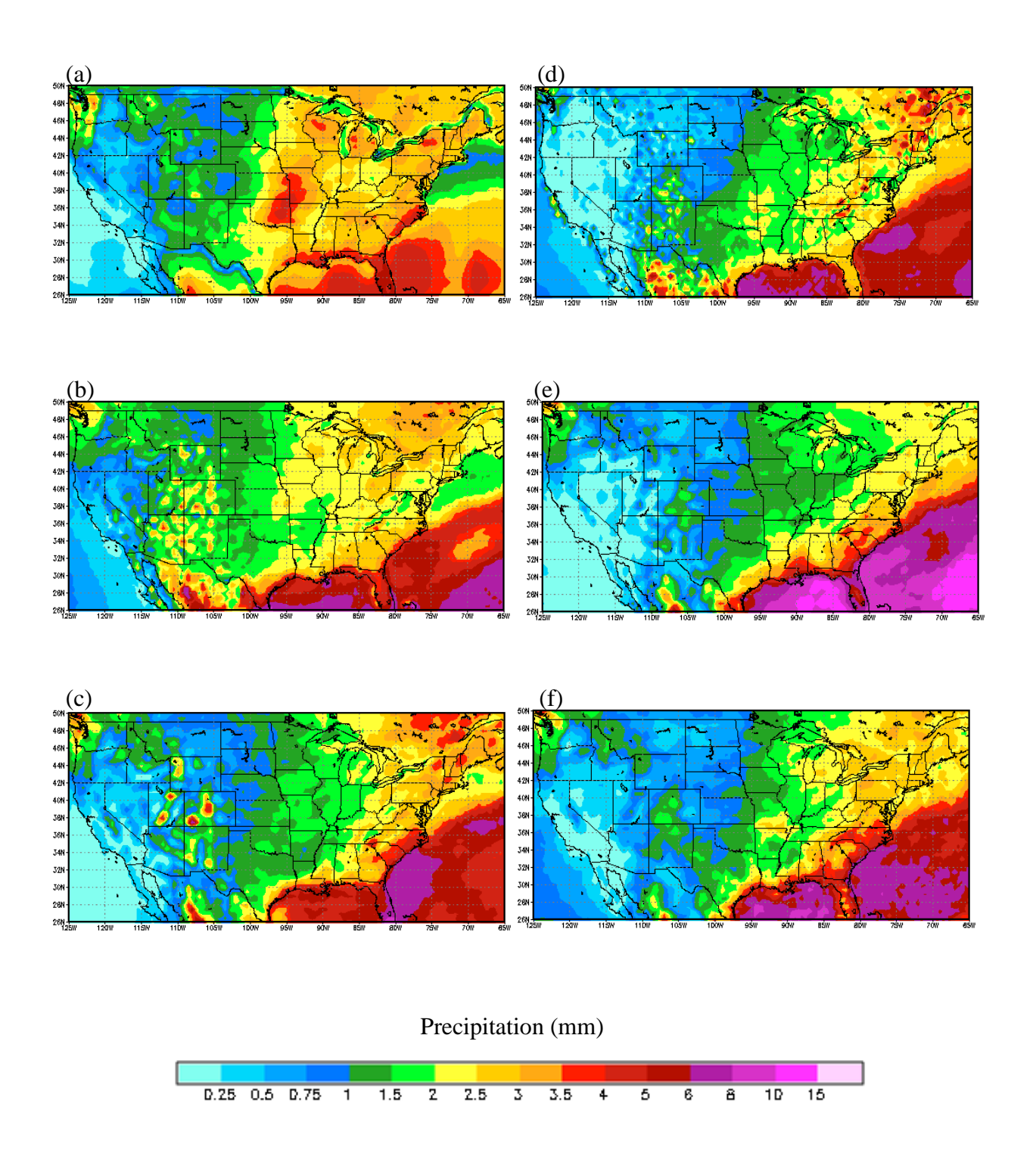


Fig. A.2.1.9. September daily accumulated precipitation from (a) NARR, (b) CRCM, (c) ECP2, (d) HRM3, (e) MM5I, and (f) WRFG for the CONUS domain.

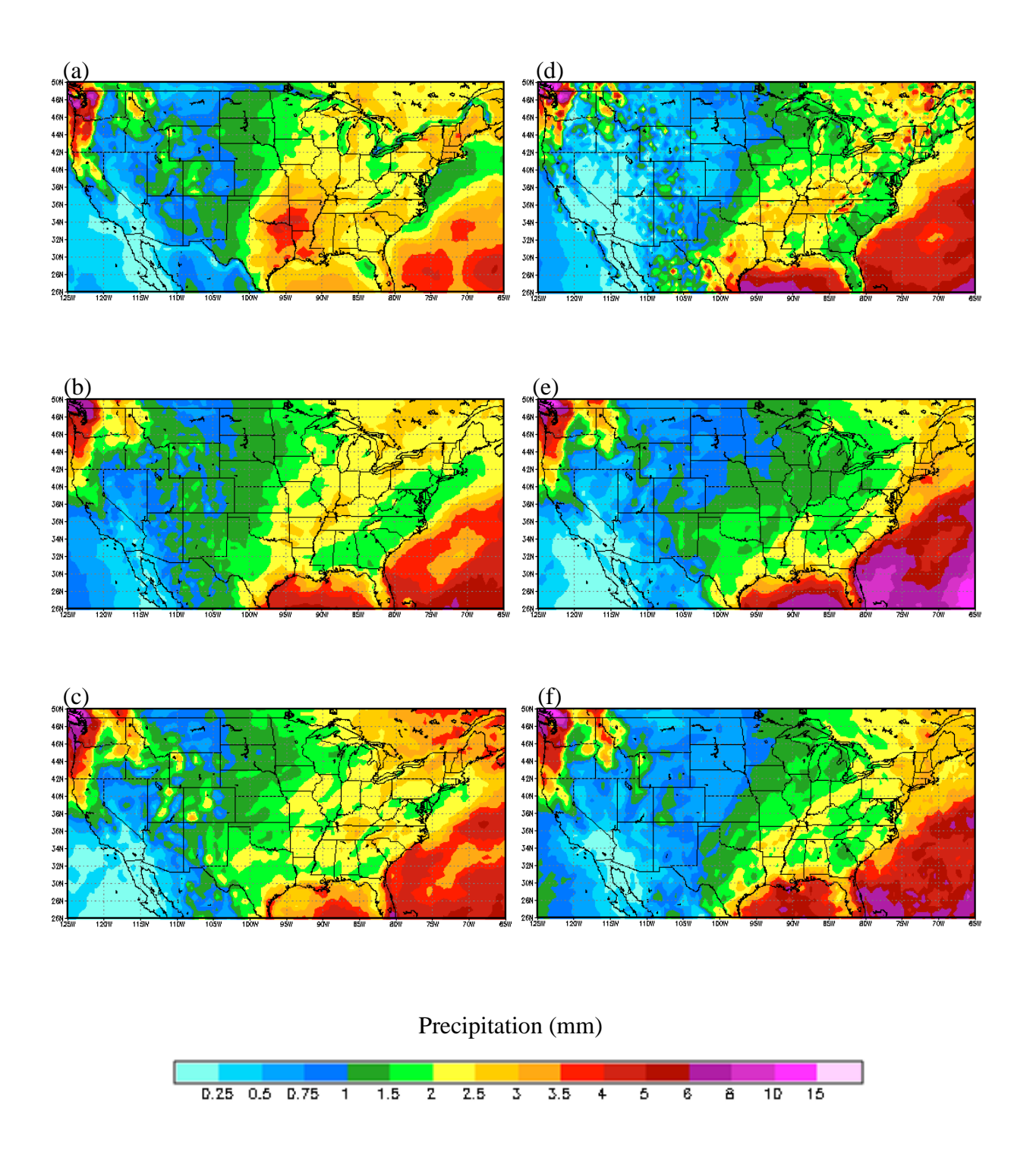


Fig. A.2.1.10. October daily accumulated precipitation from (a) NARR, (b) CRCM, (c) ECP2, (d) HRM3, (e) MM5I, and (f) WRFG for the CONUS domain.

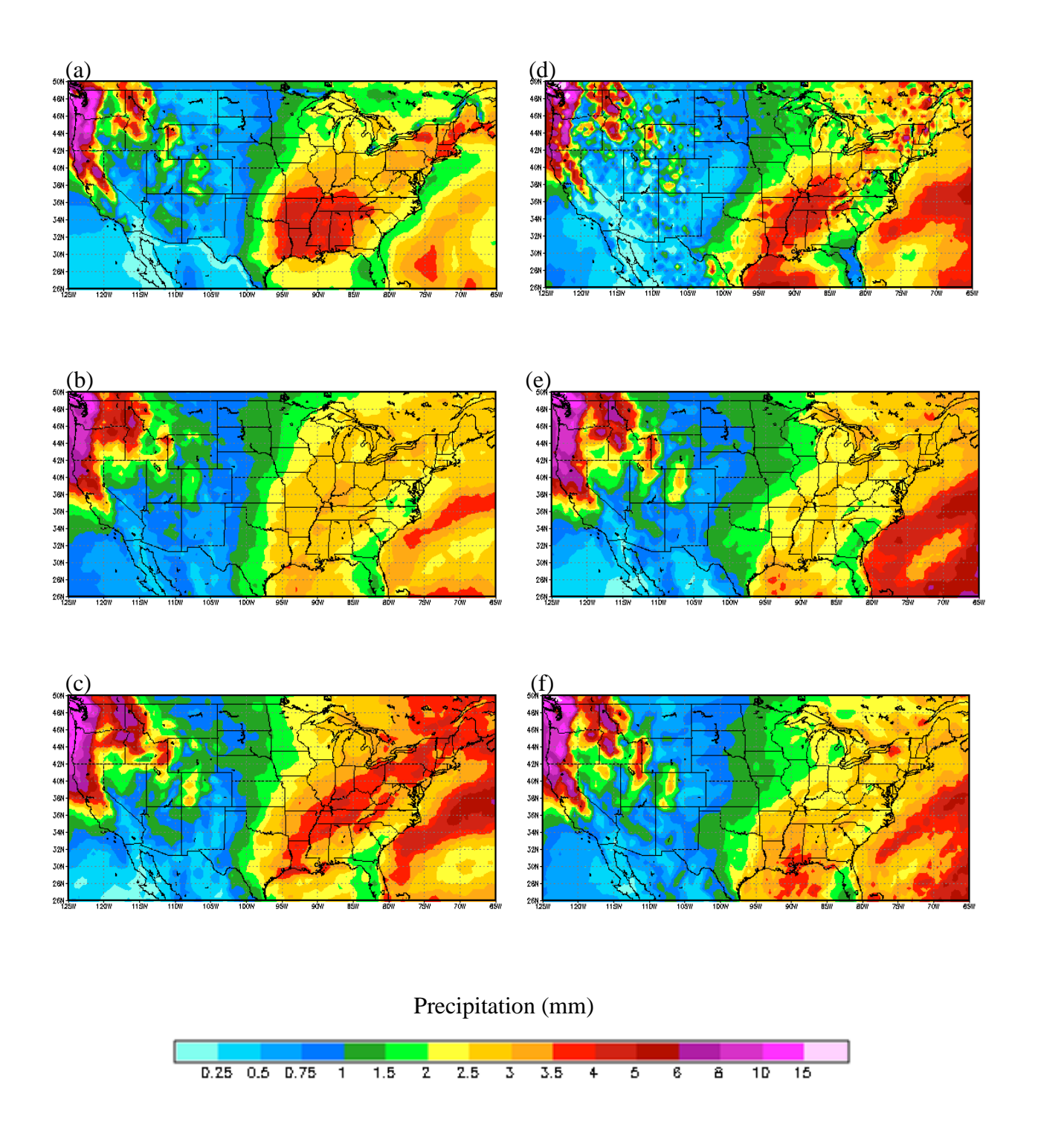


Fig. A.2.1.11. November daily accumulated precipitation from (a) NARR, (b) CRCM, (c) ECP2, (d) HRM3, (e) MM5I, and (f) WRFG for the CONUS domain.

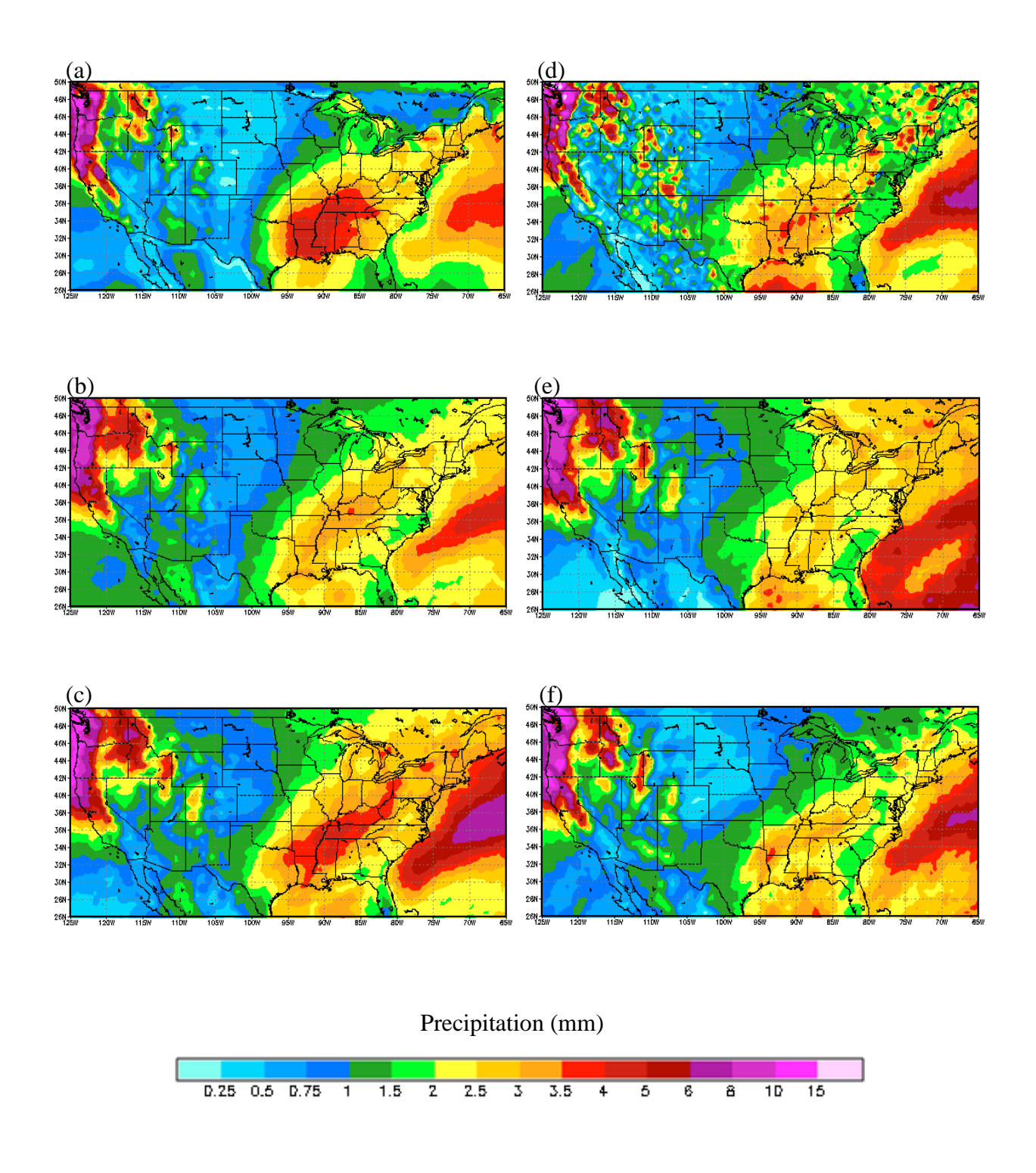


Fig. A.2.1.12. December daily accumulated precipitation from (a) NARR, (b) CRCM, (c) ECP2, (d) HRM3, (e) MM5I, and (f) WRFG for the CONUS domain.

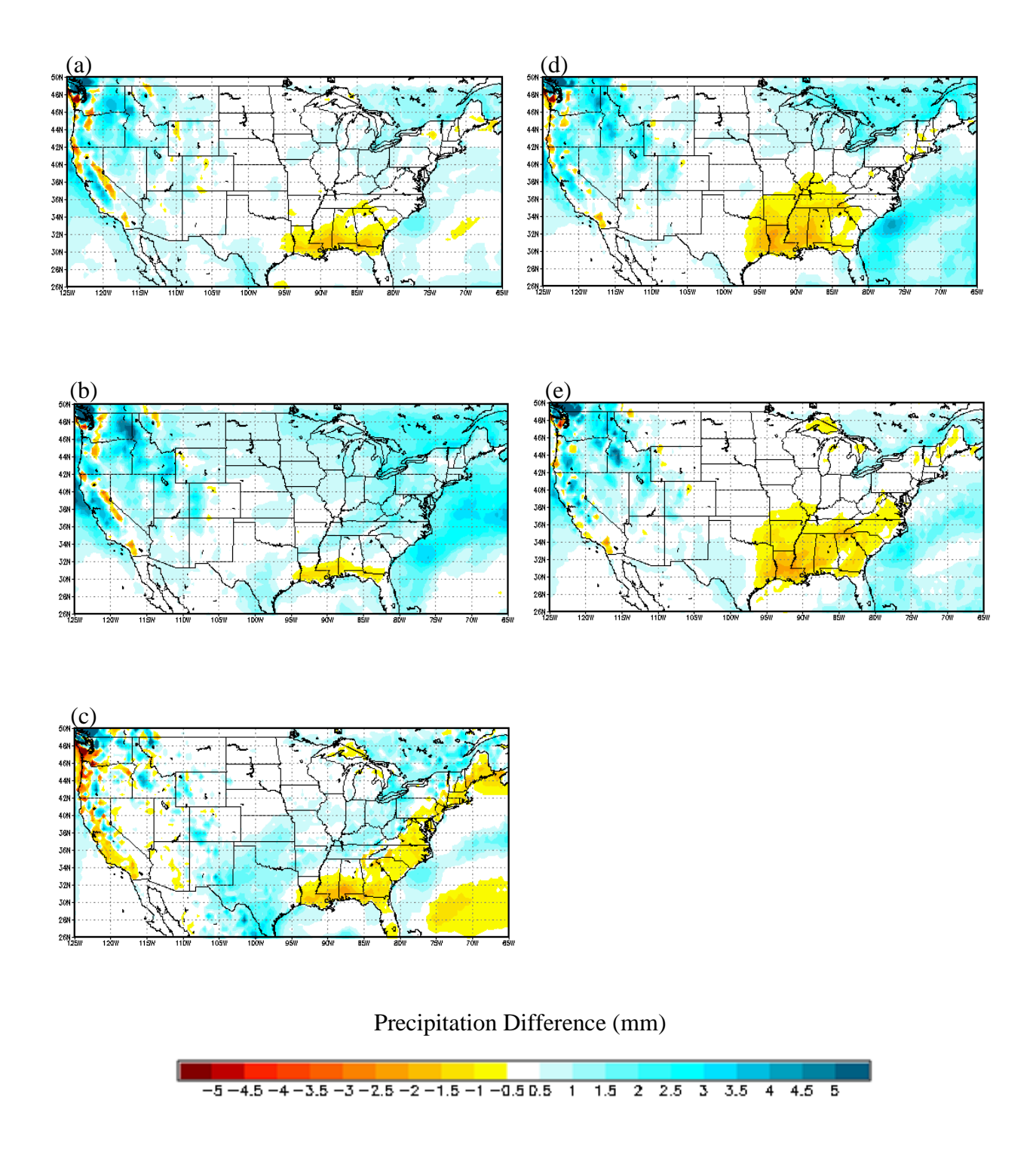


Fig. A.2.2.1. January daily accumulated precipitation differences between (a) CRCM, (b) ECP2, (c) HRM3, (d) MM5I, and (e) WRFG, and NARR for the CONUS domain.

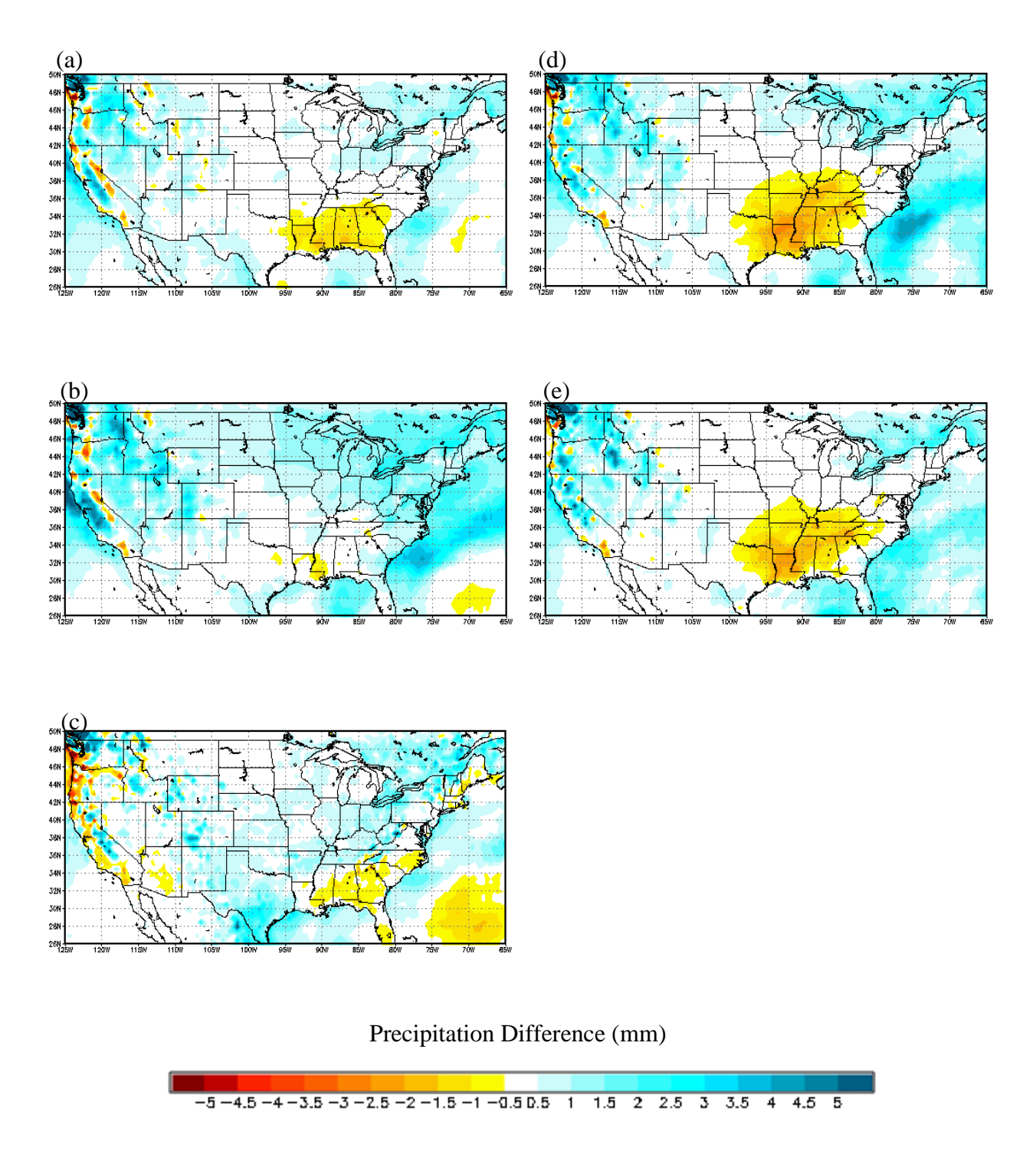


Fig. A.2.2.2. February daily accumulated precipitation differences between (a) CRCM, (b) ECP2, (c) HRM3, (d) MM5I, and (e) WRFG, and NARR for the CONUS domain.

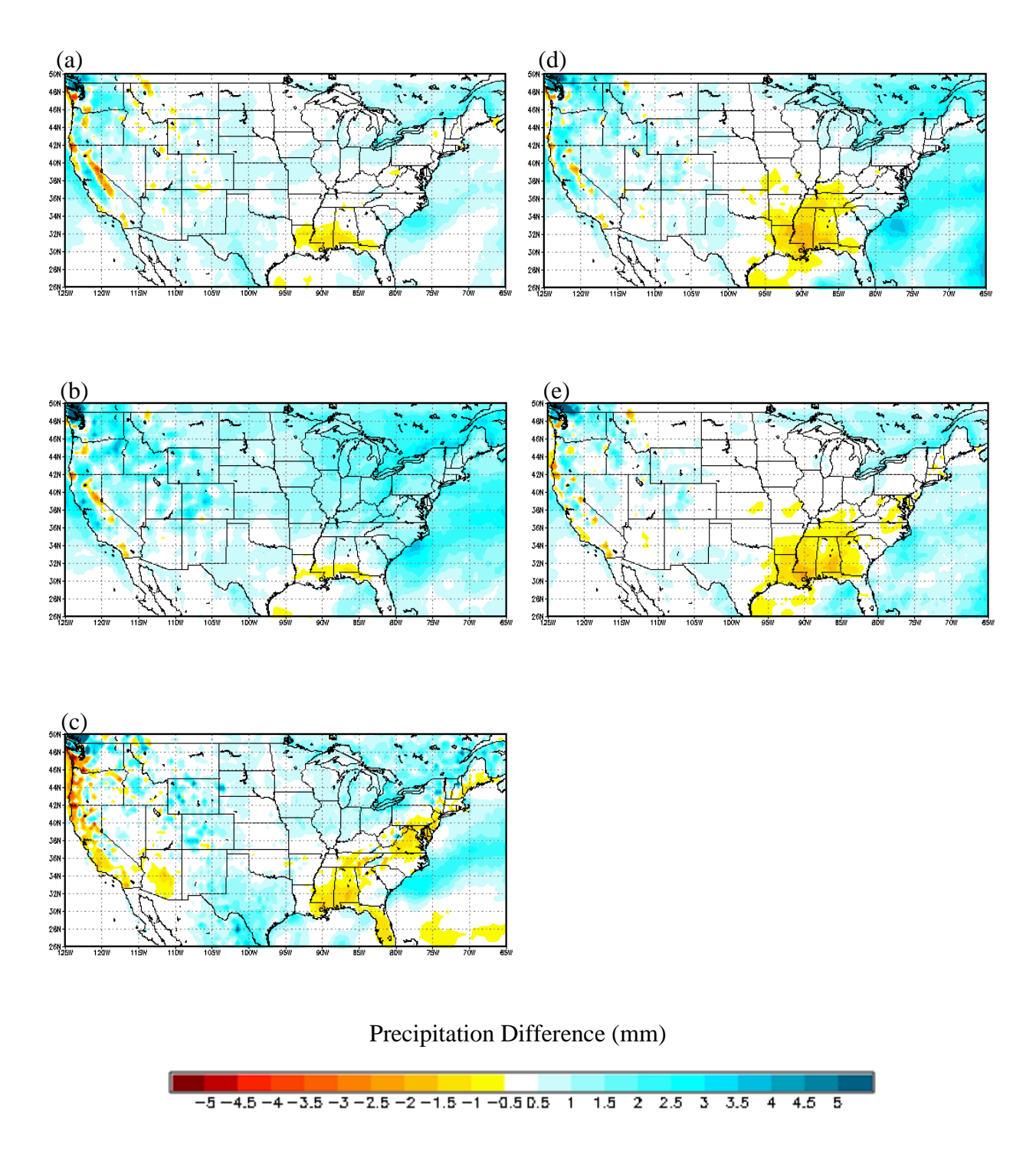


Fig. A.2.2.3. March daily accumulated precipitation differences between (a) CRCM, (b) ECP2, (c) HRM3, (d) MM5I, and (e) WRFG, and NARR for the CONUS domain.

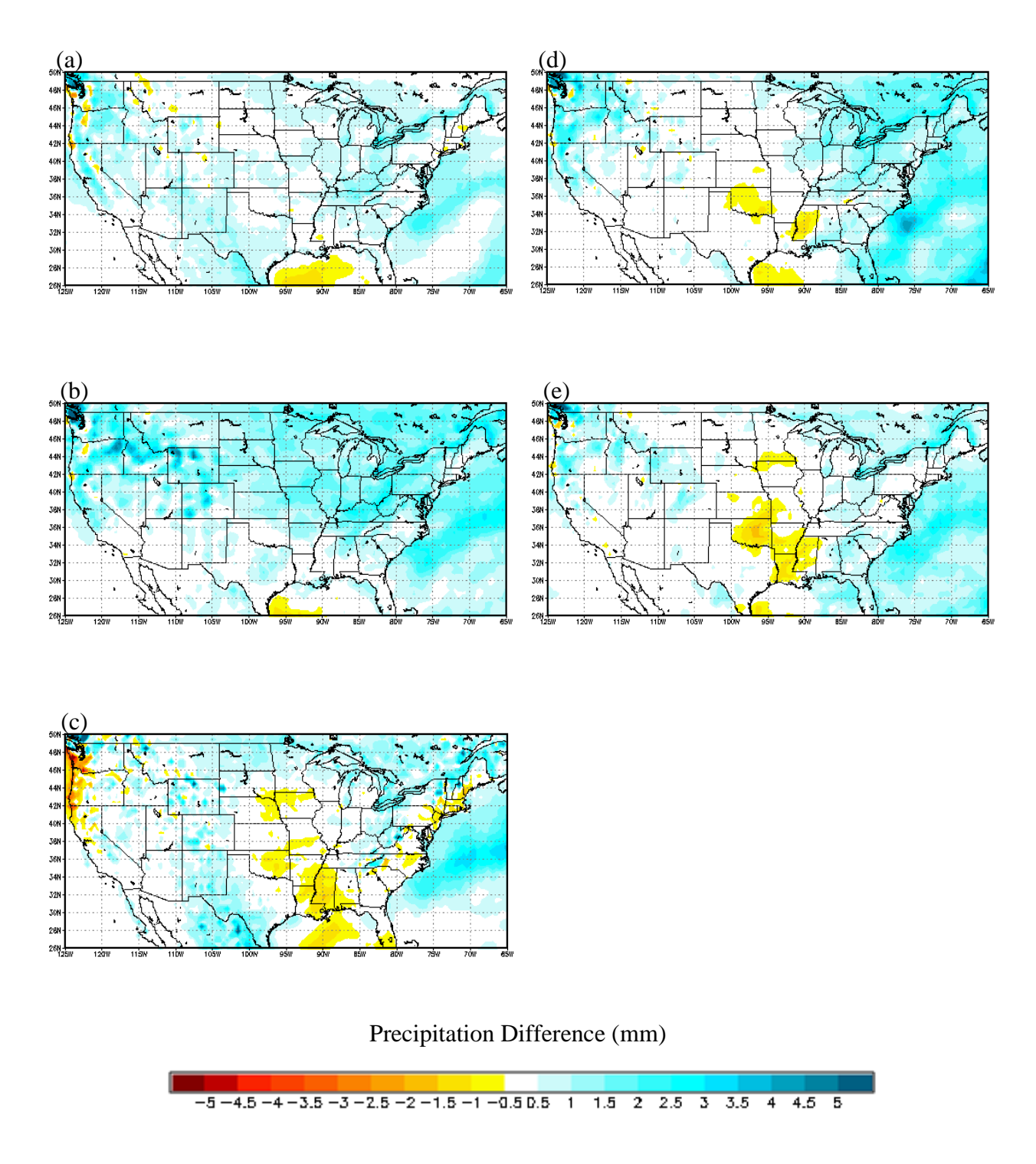


Fig. A.2.2.4. April daily accumulated precipitation differences between (a) CRCM, (b) ECP2, (c) HRM3, (d) MM5I, and (e) WRFG, and NARR for the CONUS domain.

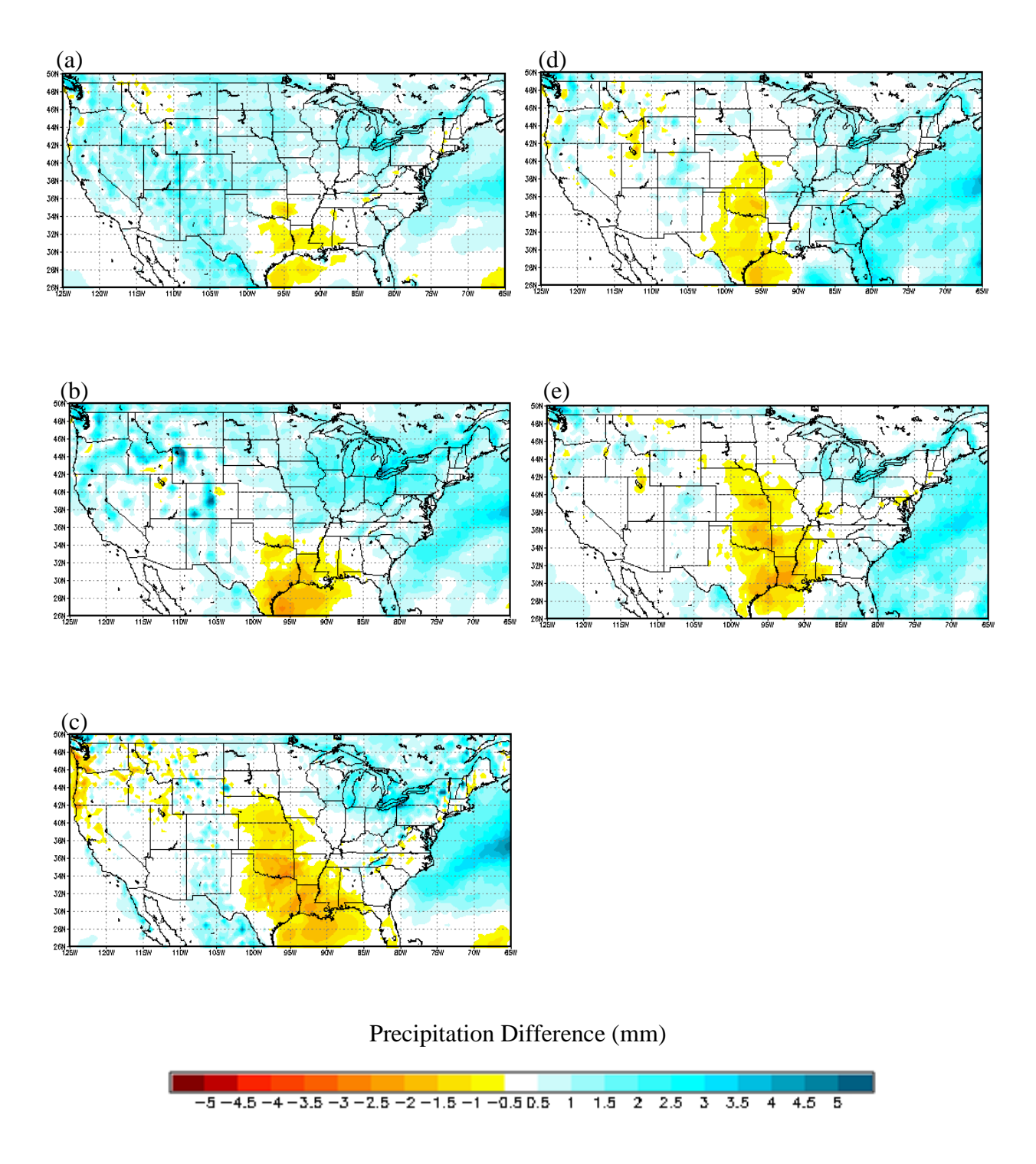


Fig. A.2.2.5. May daily accumulated precipitation differences between (a) CRCM, (b) ECP2, (c) HRM3, (d) MM5I, and (e) WRFG, and NARR for the CONUS domain.

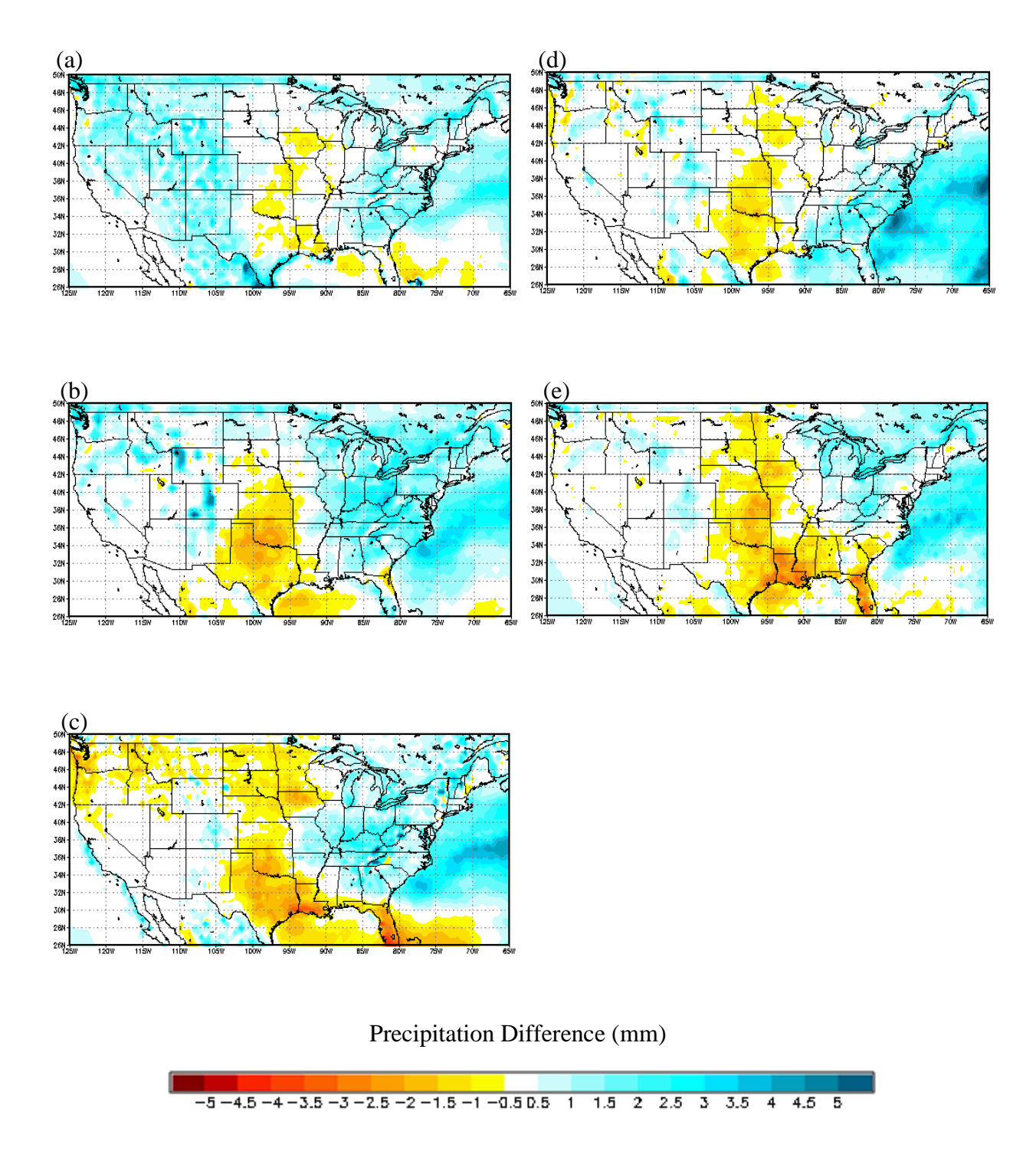


Fig. A.2.2.6. June daily accumulated precipitation differences between (a) CRCM, (b) ECP2, (c) HRM3, (d) MM5I, and (e) WRFG, and NARR for the CONUS domain.

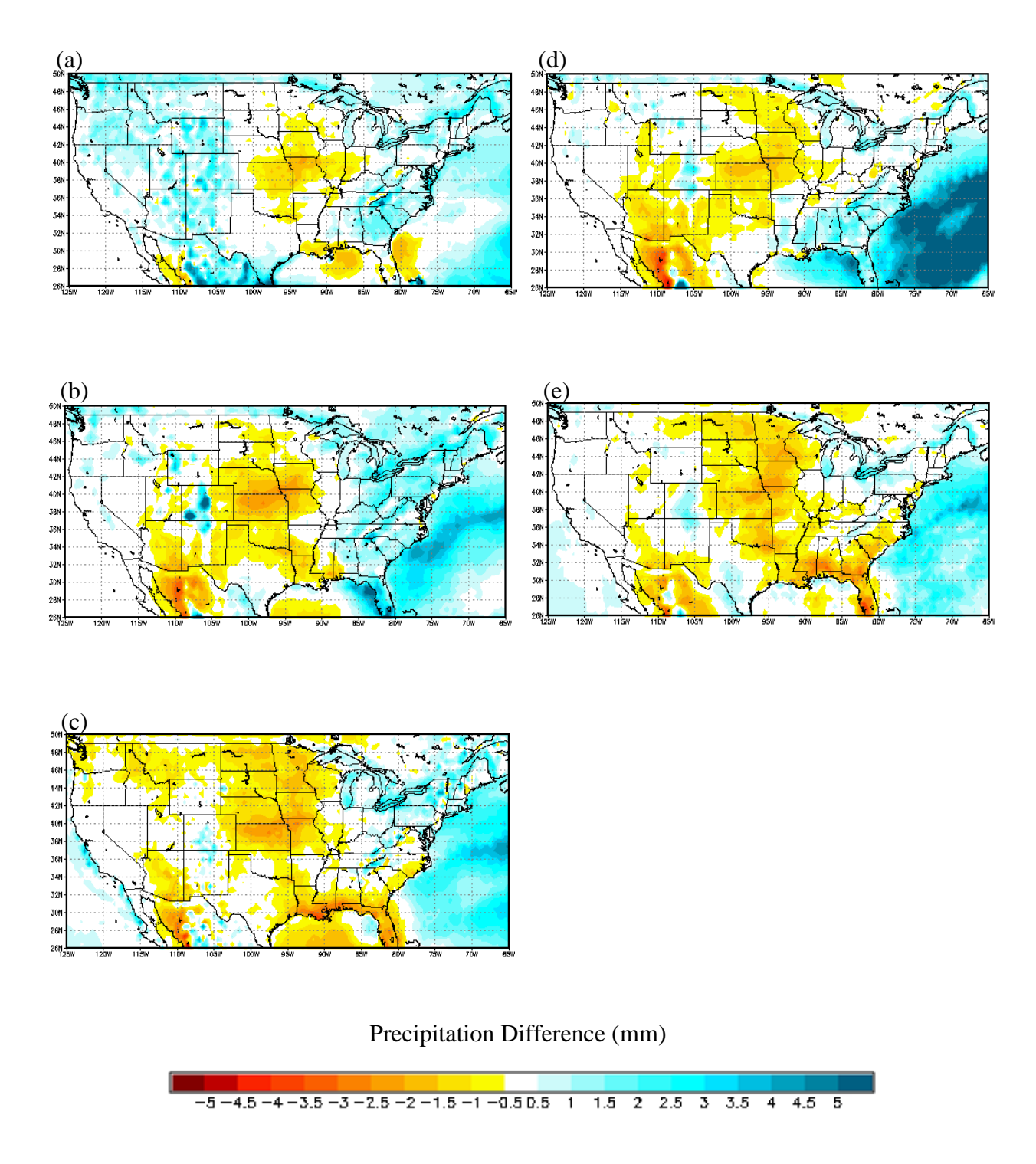


Fig. A.2.2.7. July daily accumulated precipitation differences between (a) CRCM, (b) ECP2, (c) HRM3, (d) MM5I, and (e) WRFG, and NARR for the CONUS domain.

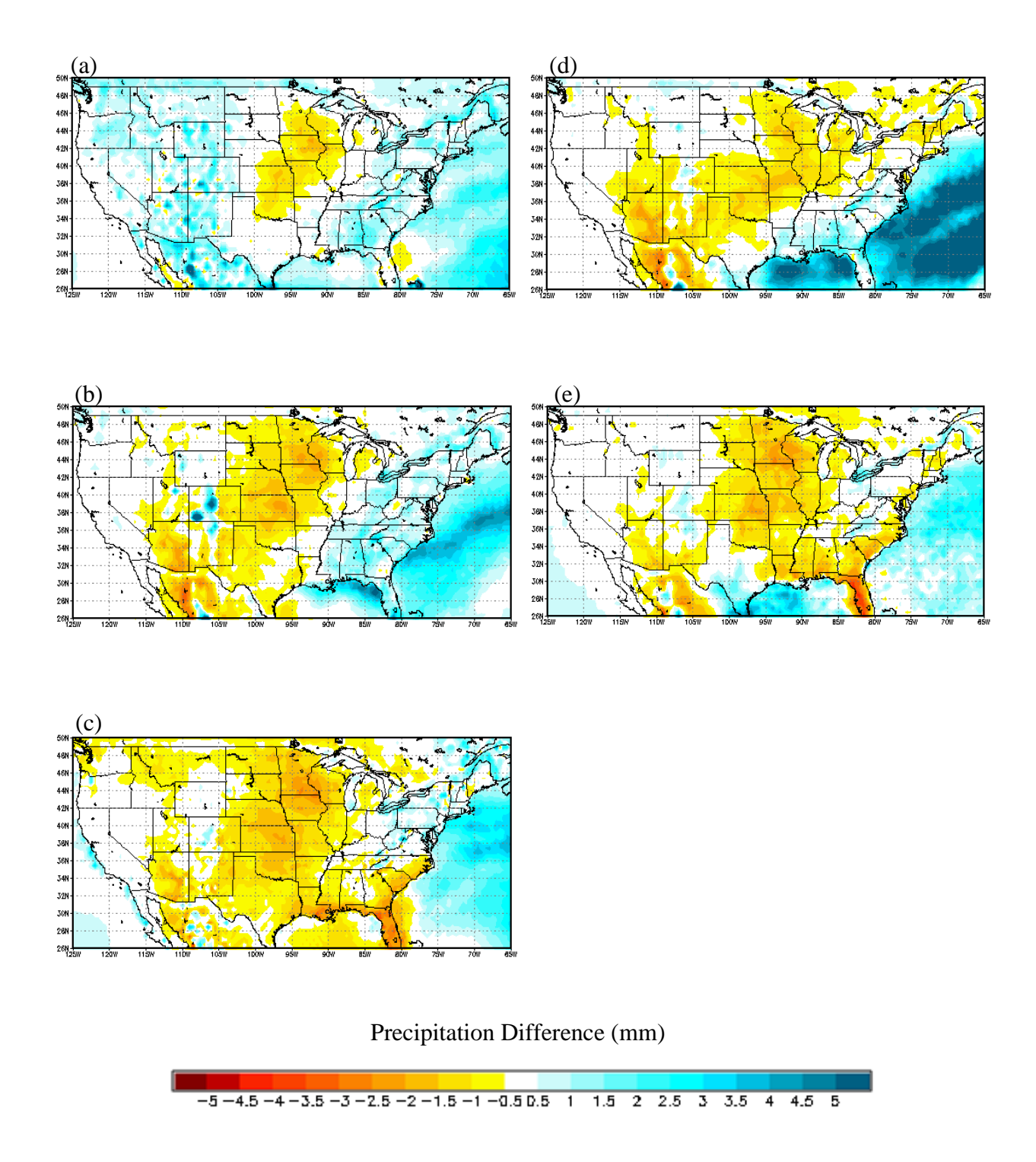


Fig. A.2.2.8. August daily accumulated precipitation differences between (a) CRCM, (b) ECP2, (c) HRM3, (d) MM5I, and (e) WRFG, and NARR for the CONUS domain.

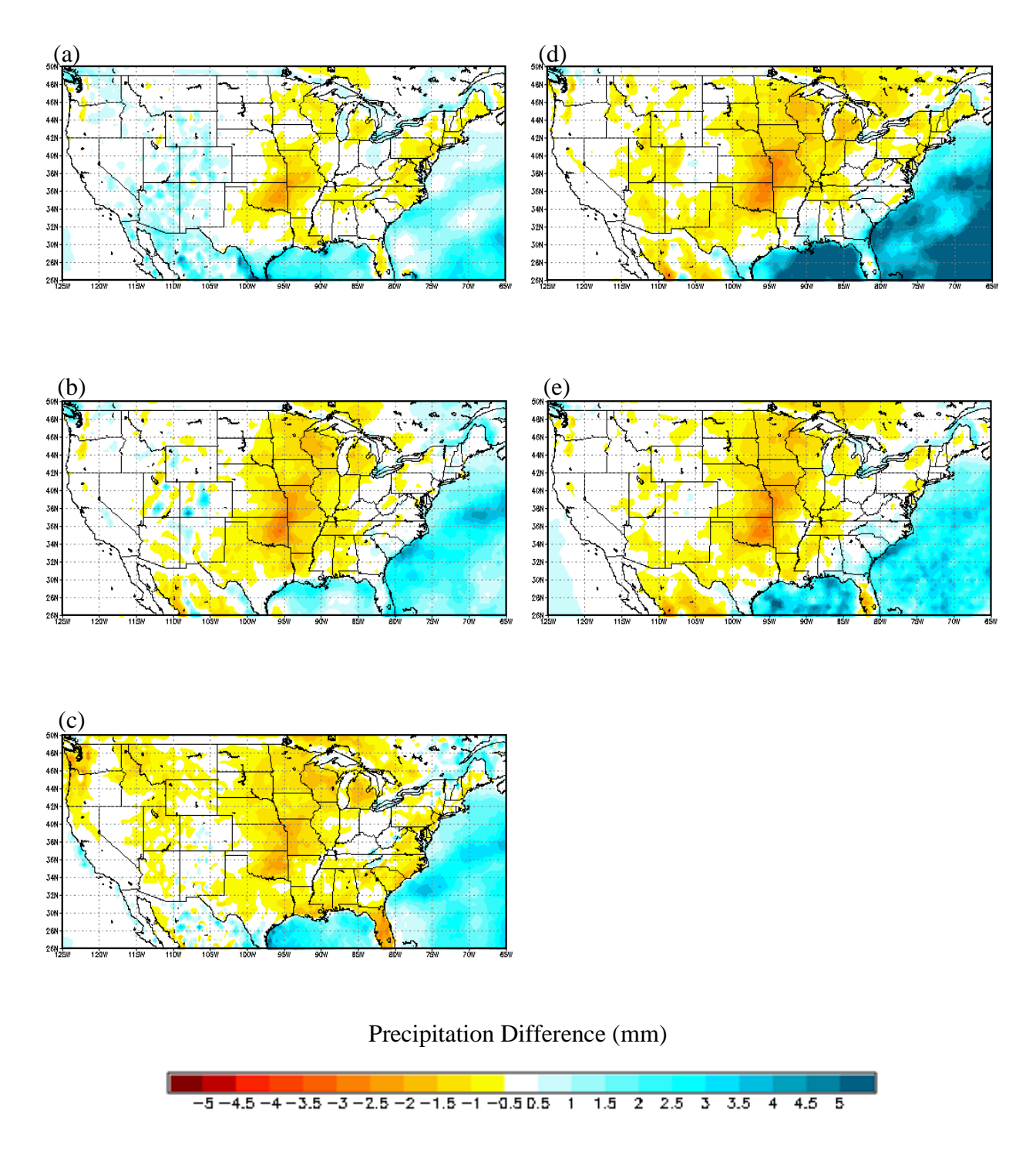


Fig. A.2.2.9. September daily accumulated precipitation differences between (a) CRCM, (b) ECP2, (c) HRM3, (d) MM5I, and (e) WRFG, and NARR for the CONUS domain.

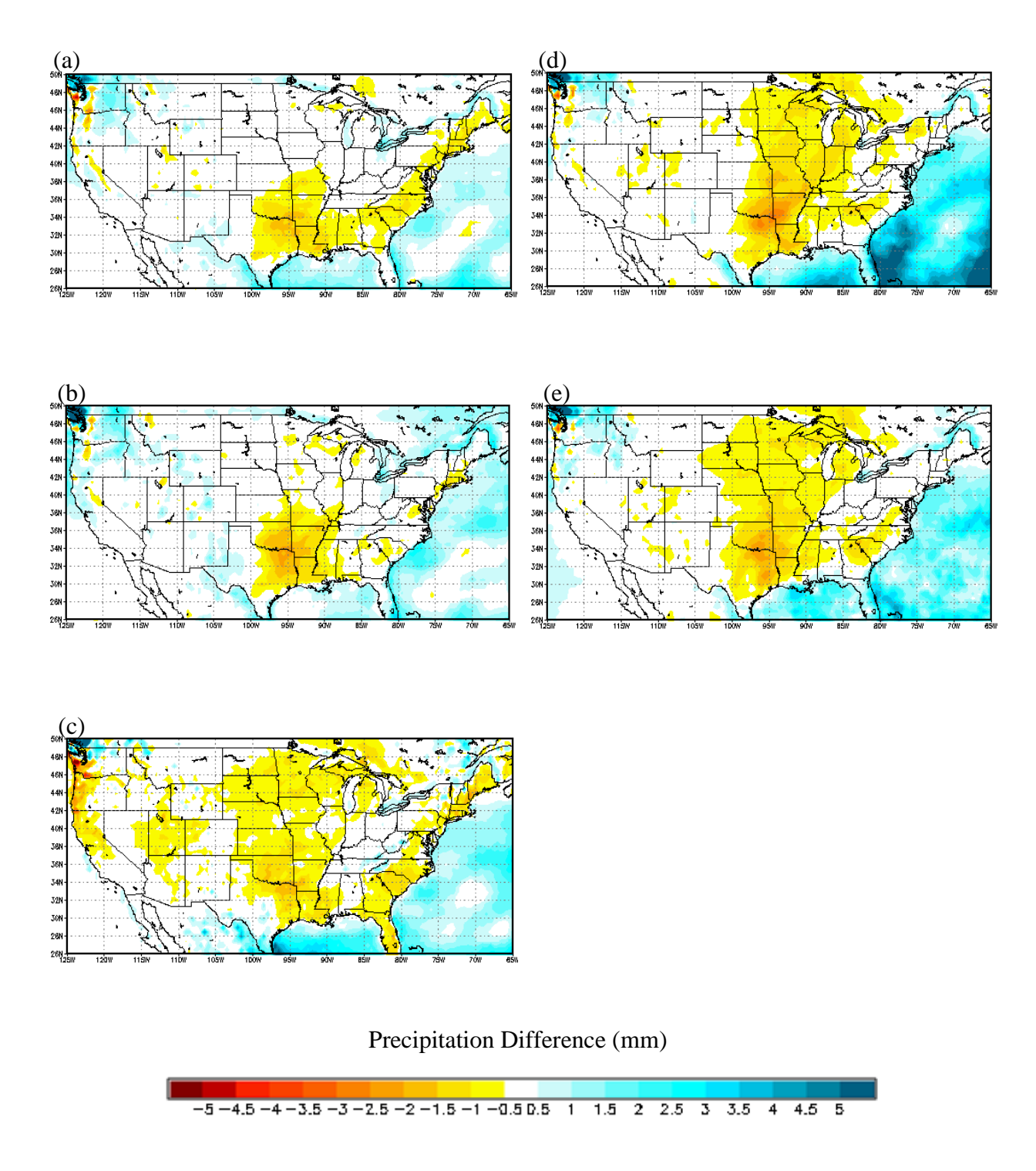


Fig. A.2.2.10. October daily accumulated precipitation differences between (a) CRCM, (b) ECP2, (c) HRM3, (d) MM5I, and (e) WRFG, and NARR for the CONUS domain.

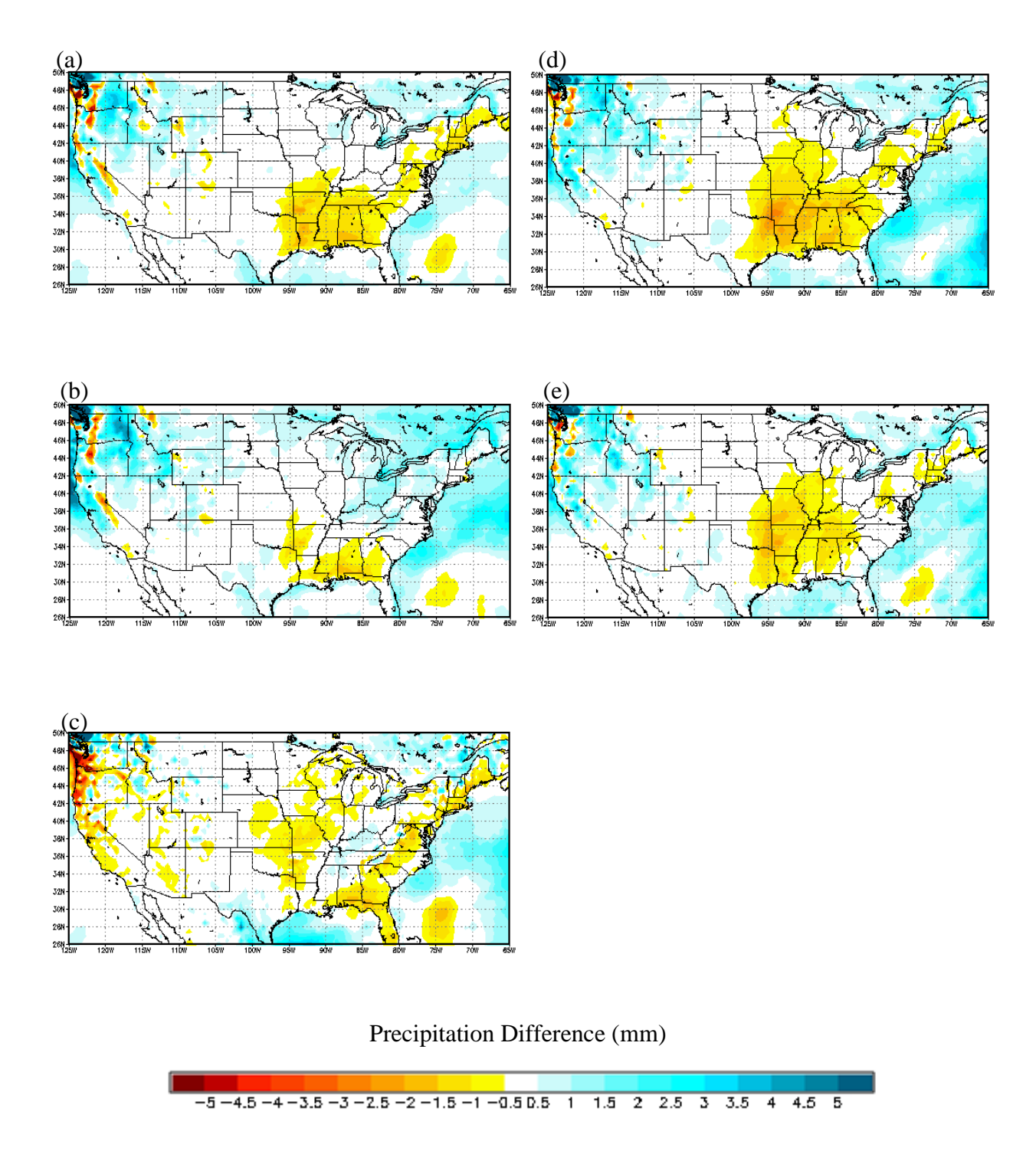


Fig. A.2.2.11. November daily accumulated precipitation differences between (a) CRCM, (b) ECP2, (c) HRM3, (d) MM5I, and (e) WRFG, and NARR for the CONUS domain.

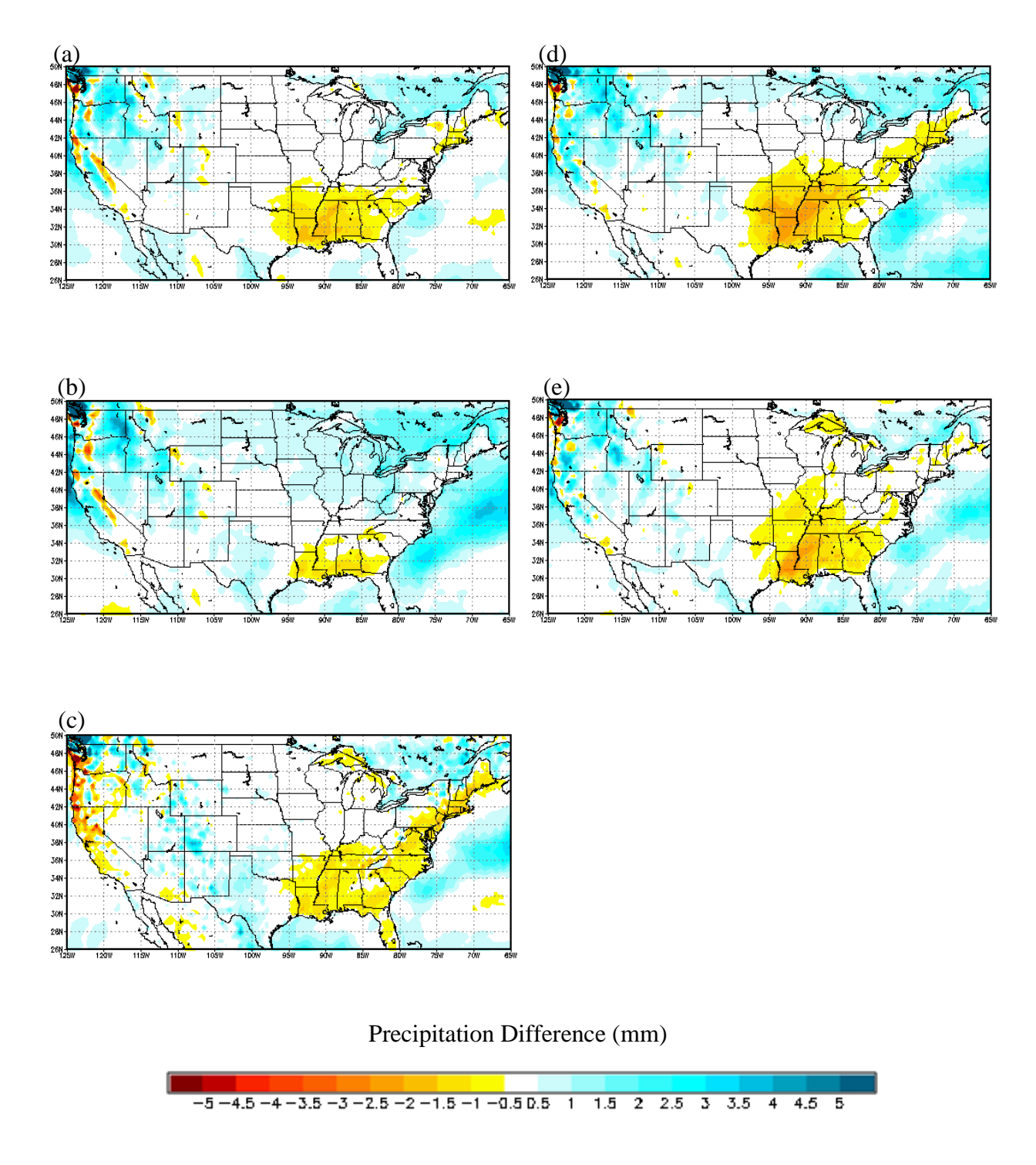


Fig. A.2.2.12. December daily accumulated precipitation differences between (a) CRCM, (b) ECP2, (c) HRM3, (d) MM5I, and (e) WRFG, and NARR for the CONUS domain.

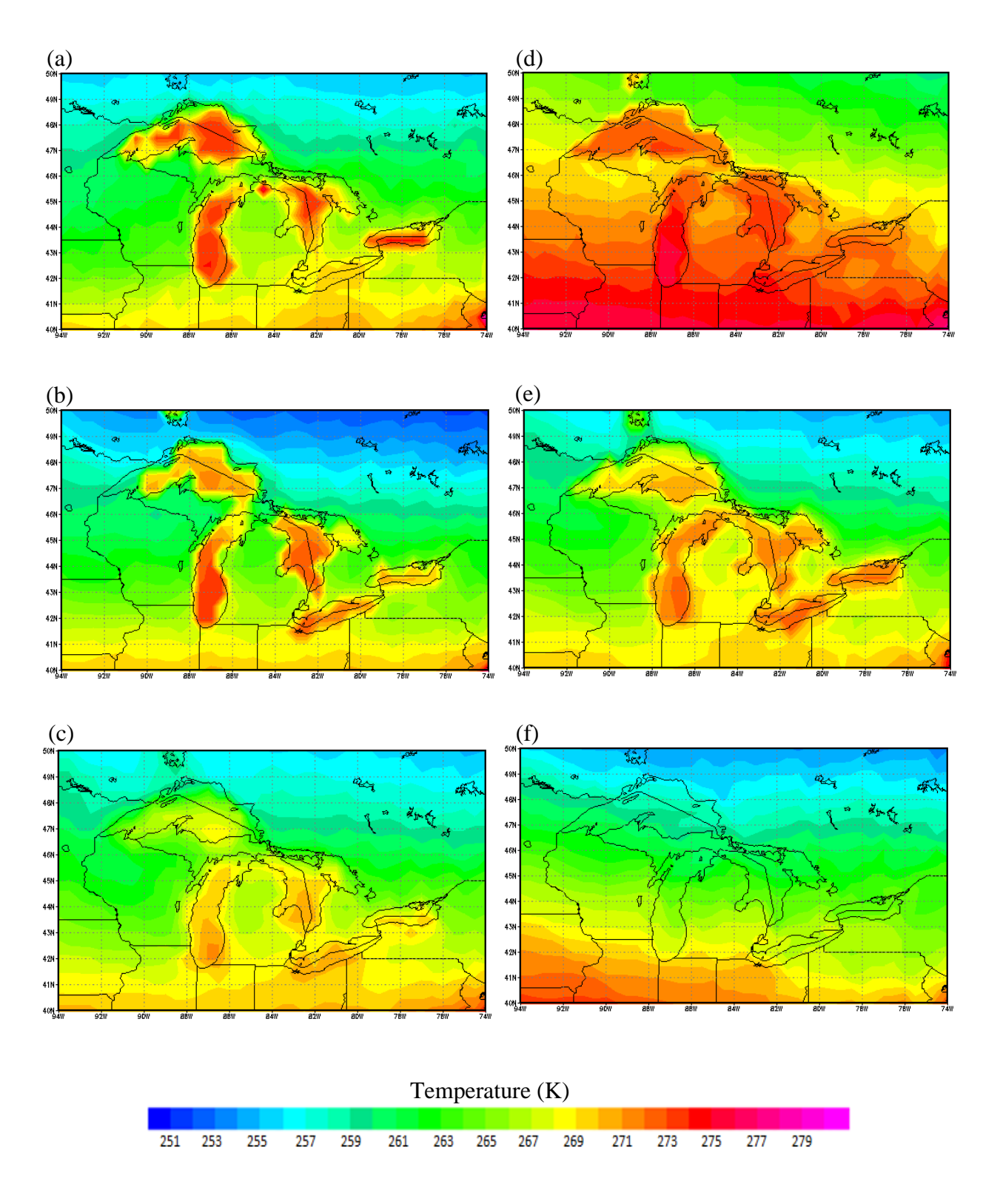


Fig. A.3.1.1. Mean January surface-air temperatures from (a) NARR, (b) CRCM, (c) ECP2, (d) HRM3, (e) MM5I, and (f) WRFG for the GLR domain.

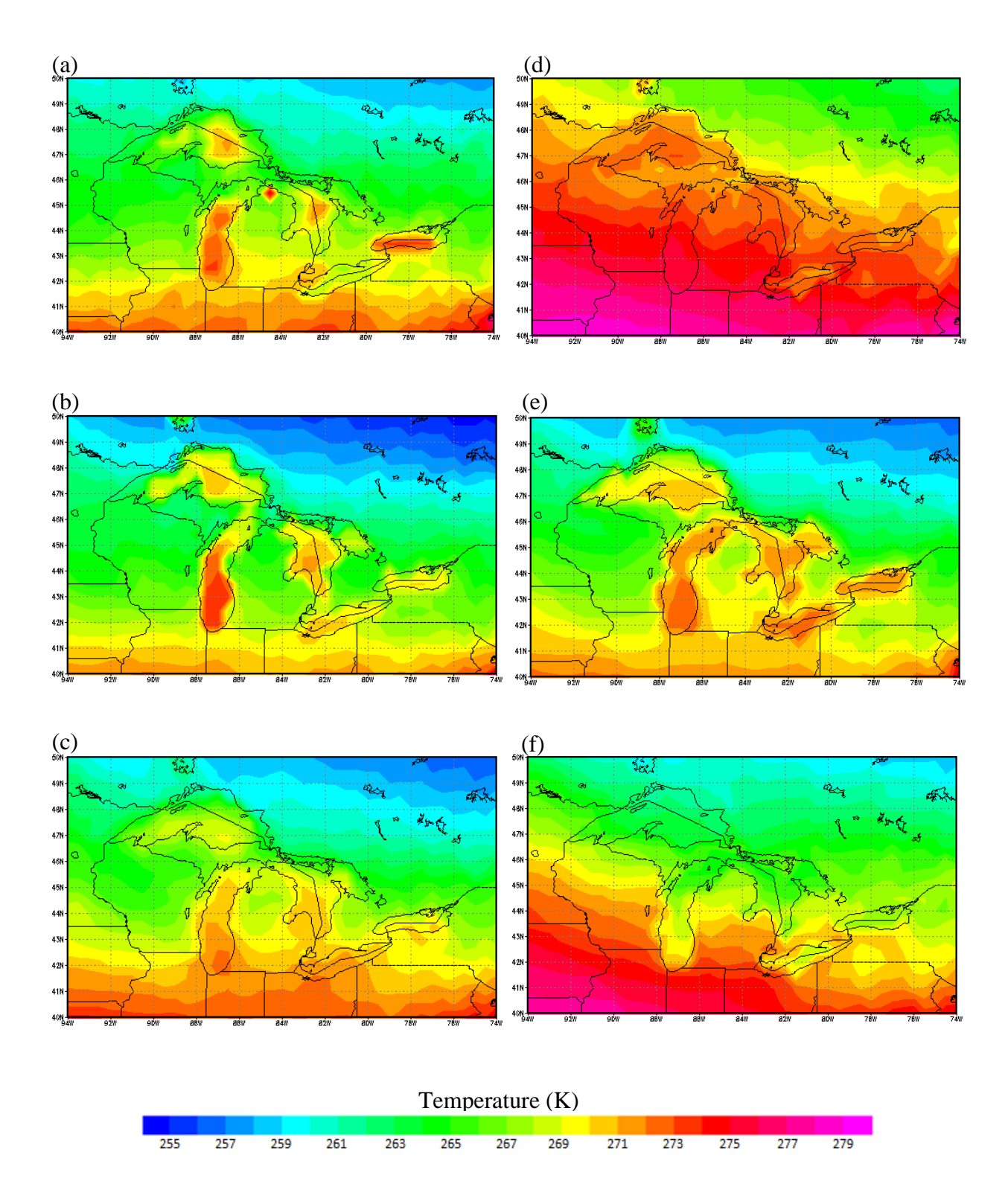


Fig. A.3.1.2. Mean February surface-air temperatures from (a) NARR, (b) CRCM, (c) ECP2, (d) HRM3, (e) MM5I, and (f) WRFG for the GLR domain.

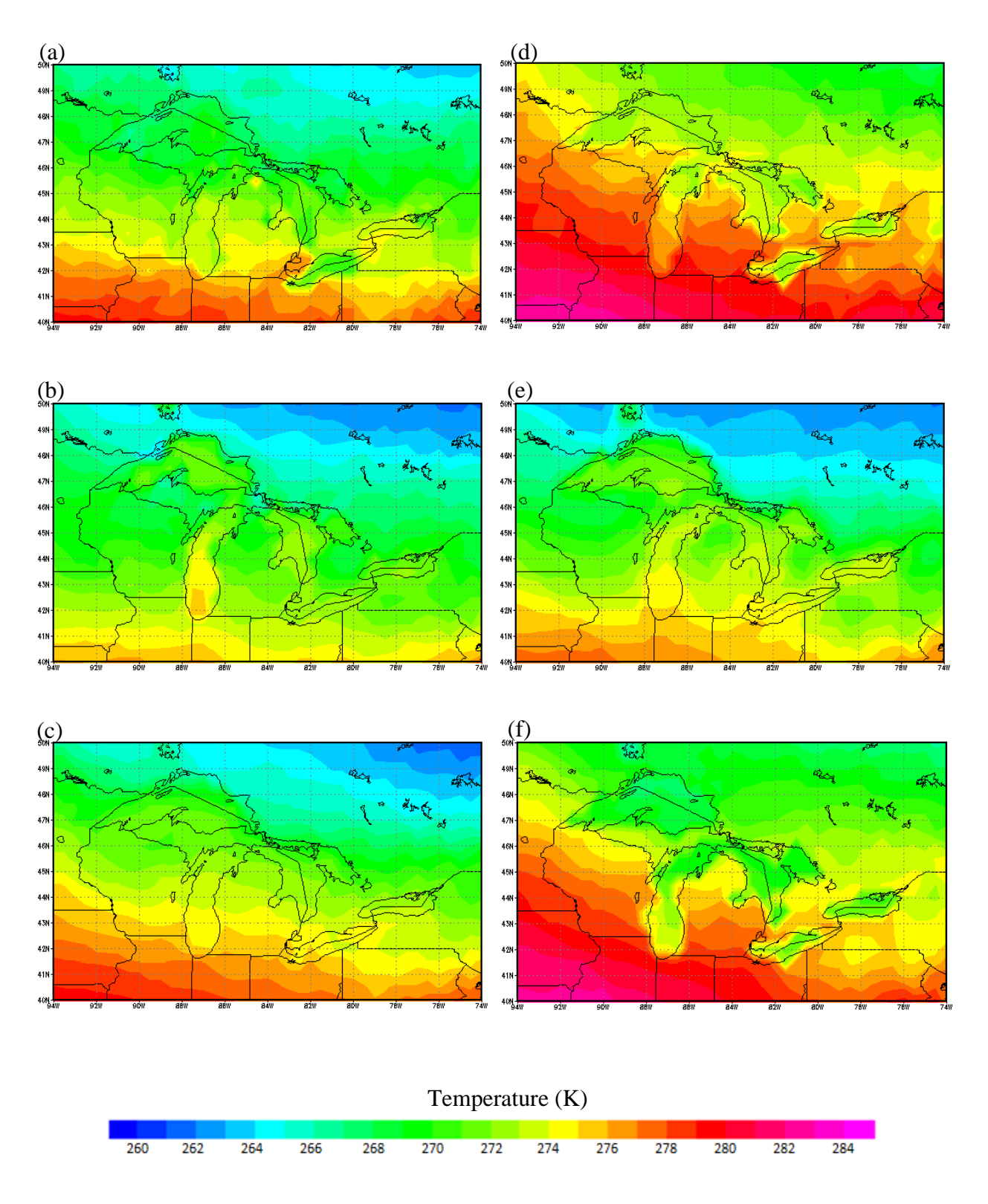


Fig. A.3.1.3. Mean March surface-air temperatures from (a) NARR, (b) CRCM, (c) ECP2, (d) HRM3, (e) MM5I, and (f) WRFG for the GLR domain.

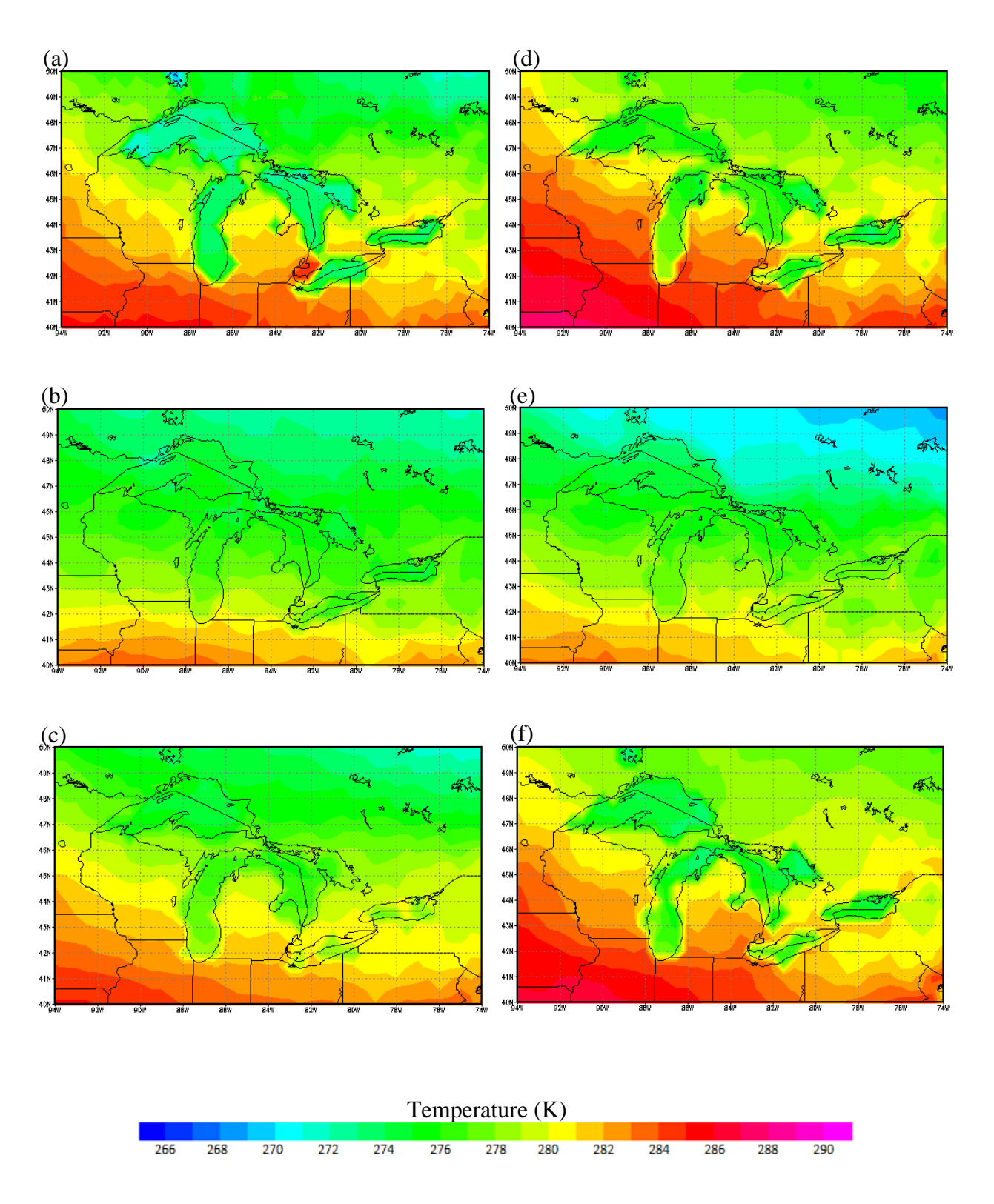


Fig. A.3.1.4. Mean April surface-air temperatures from (a) NARR, (b) CRCM, (c) ECP2, (d) HRM3, (e) MM5I, and (f) WRFG for the GLR domain.

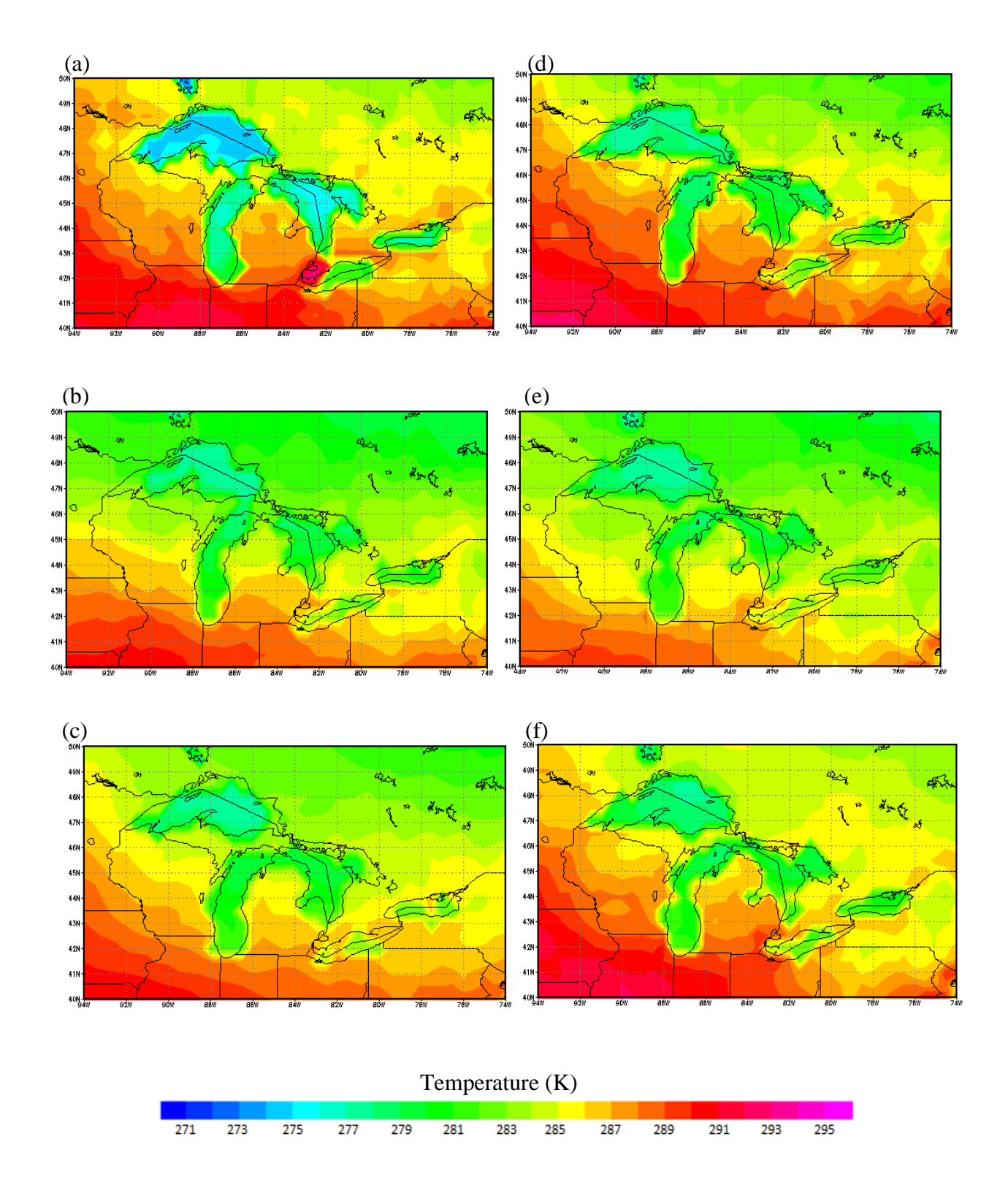


Fig. A.3.1.5. Mean May surface-air temperatures from (a) NARR, (b) CRCM, (c) ECP2, (d) HRM3, (e) MM5I, and (f) WRFG for the GLR domain.

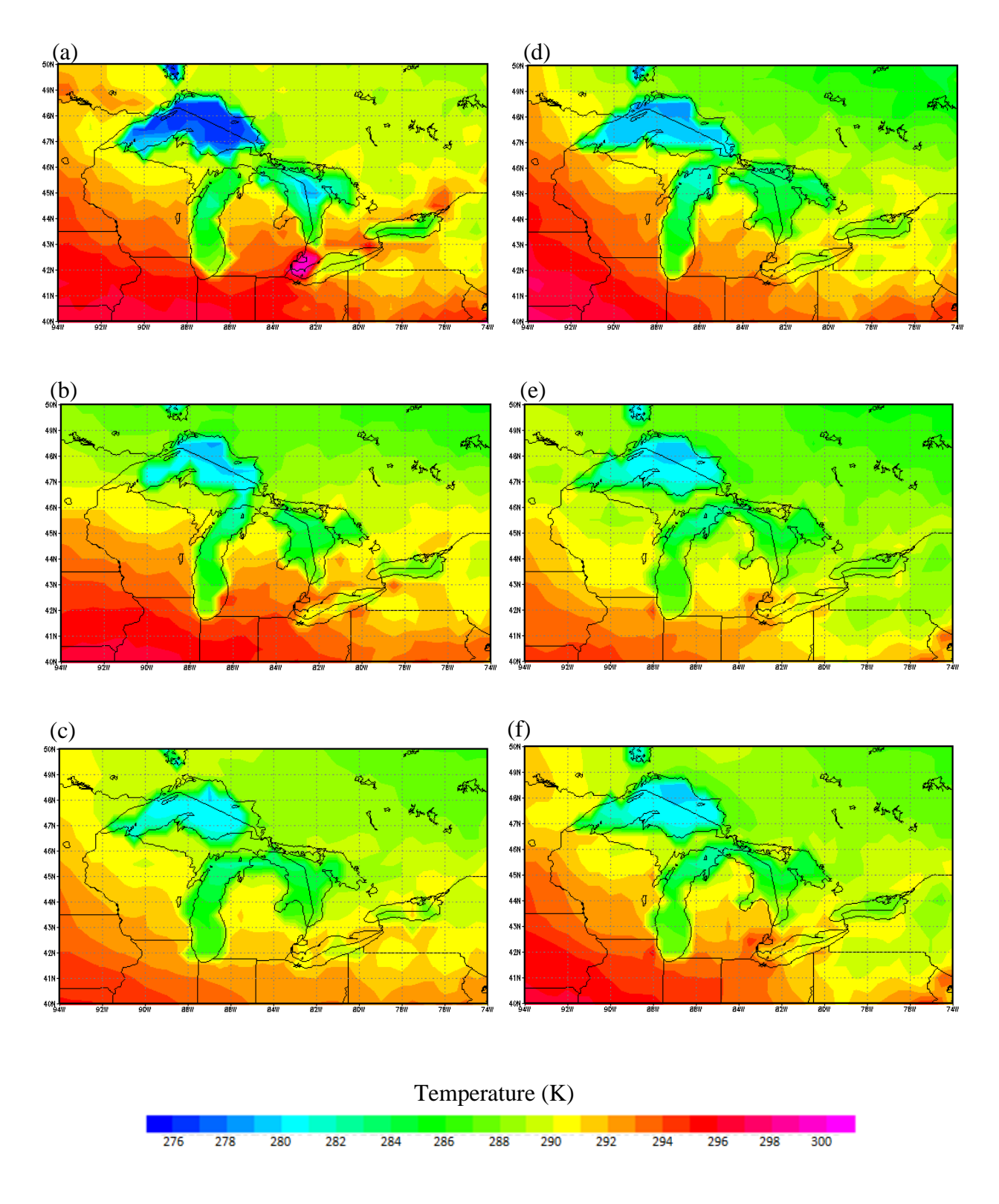


Fig. A.3.1.6. Mean June surface-air temperatures from (a) NARR, (b) CRCM, (c) ECP2, (d) HRM3, (e) MM5I, and (f) WRFG for the GLR domain.

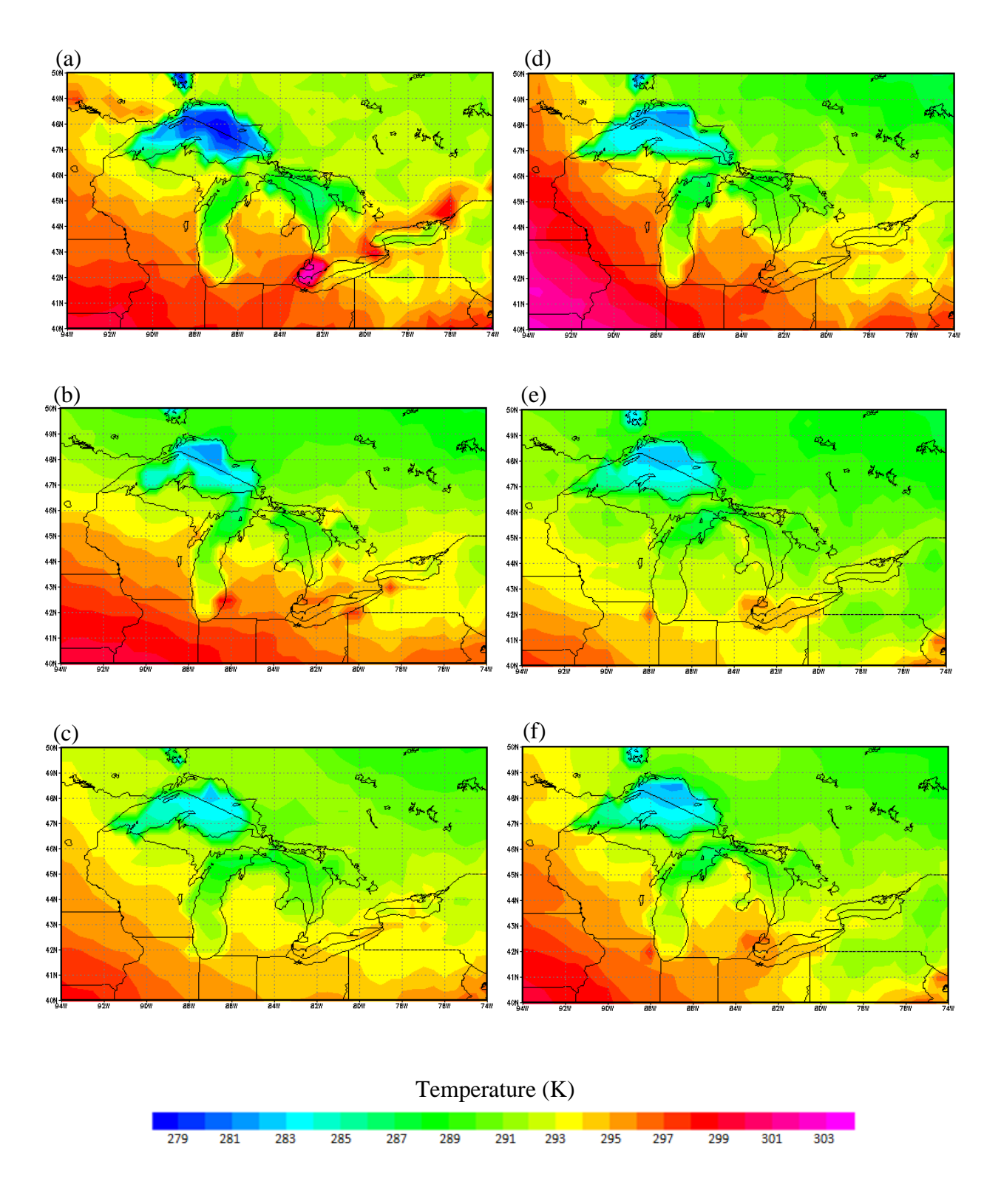


Fig. A.3.1.7. Mean July surface-air temperatures from (a) NARR, (b) CRCM, (c) ECP2, (d) HRM3, (e) MM5I, and (f) WRFG for the GLR domain.

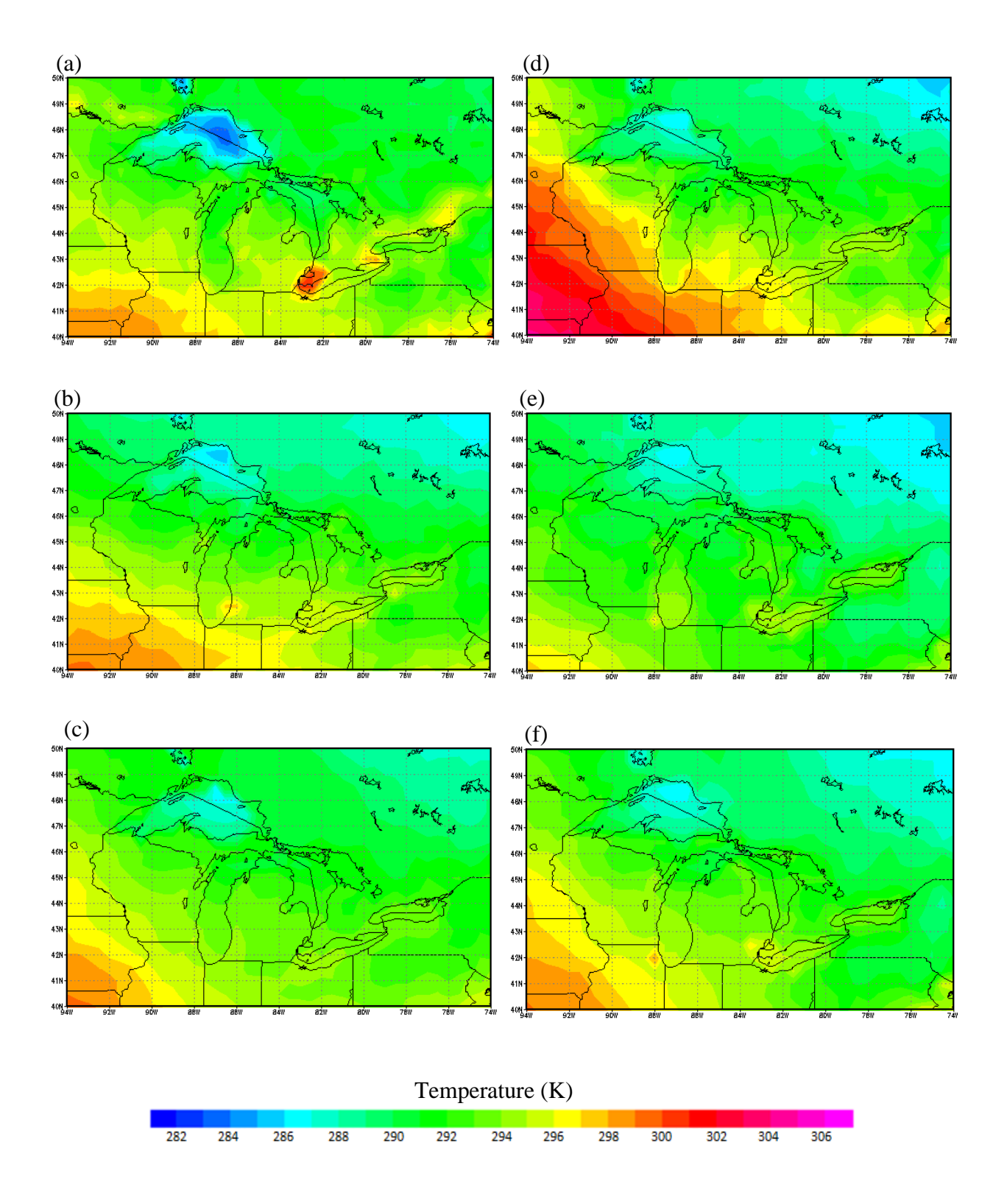


Fig. A.3.1.8. Mean August surface-air temperatures from (a) NARR, (b) CRCM, (c) ECP2, (d) HRM3, (e) MM5I, and (f) WRFG for the GLR domain.

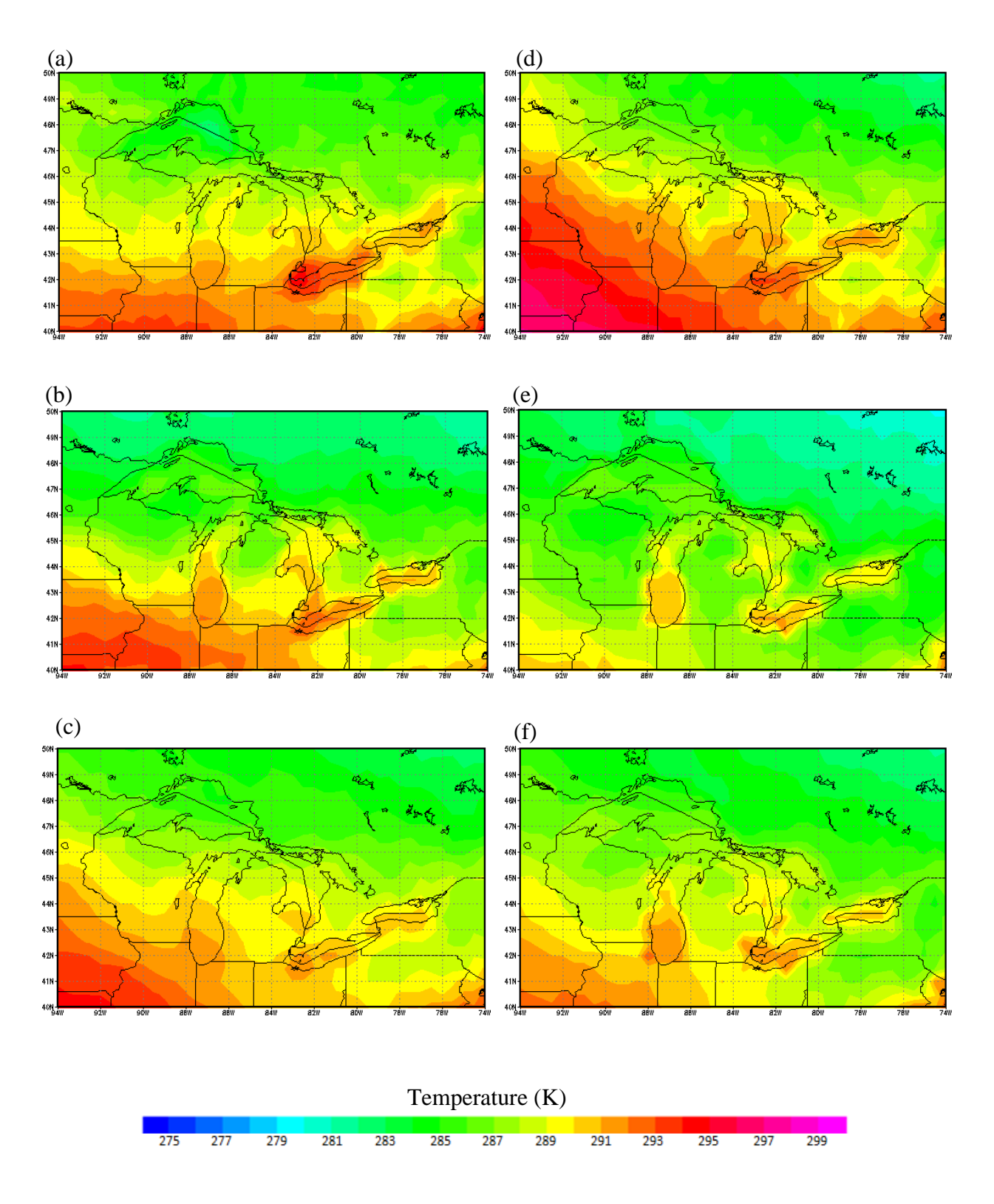


Fig. A.3.1.9. Mean September surface-air temperatures from (a) NARR, (b) CRCM, (c) ECP2, (d) HRM3, (e) MM5I, and (f) WRFG for the GLR domain.

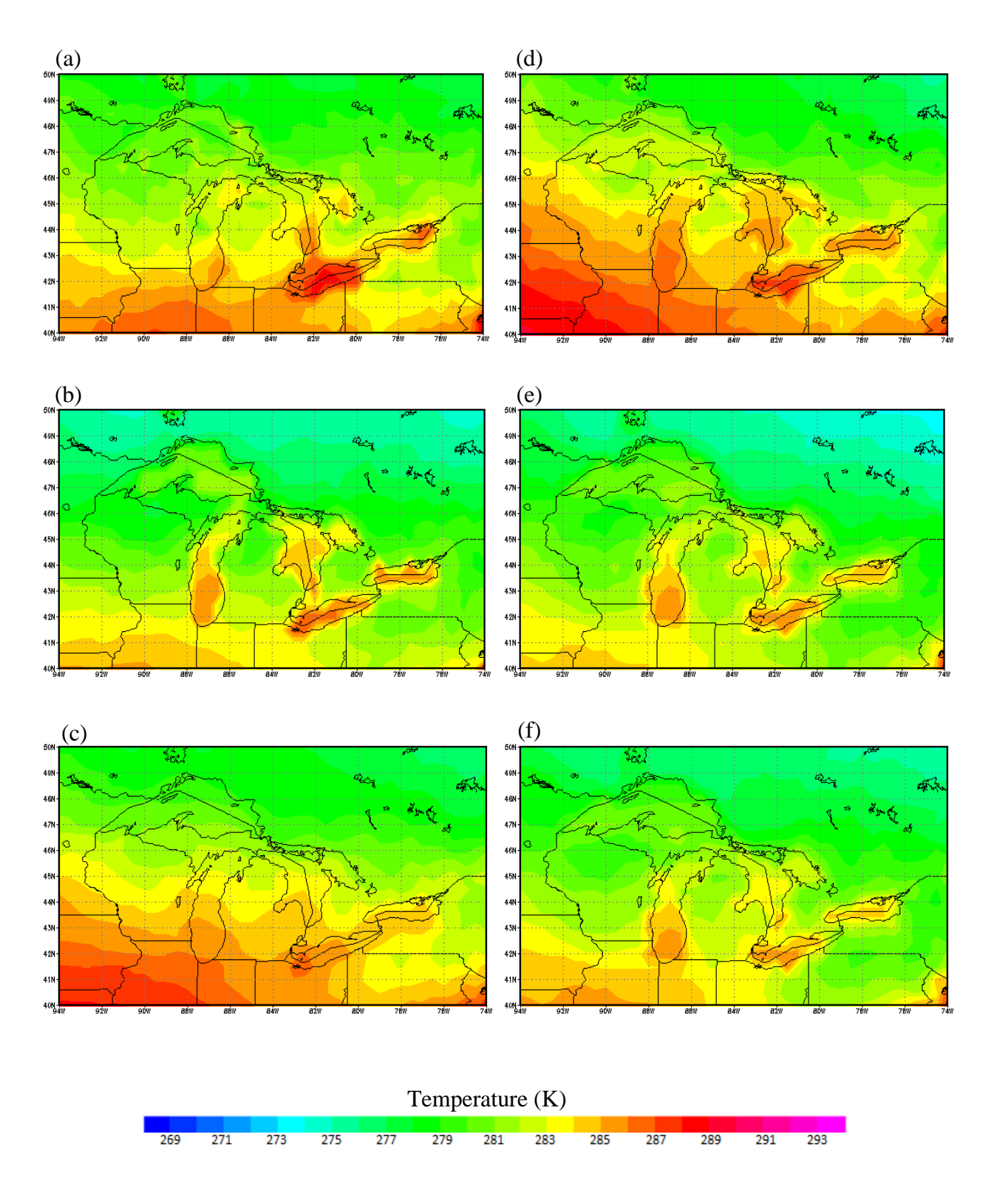


Fig. A.3.1.10. Mean October surface-air temperatures from (a) NARR, (b) CRCM, (c) ECP2, (d) HRM3, (e) MM5I, and (f) WRFG for the GLR domain.

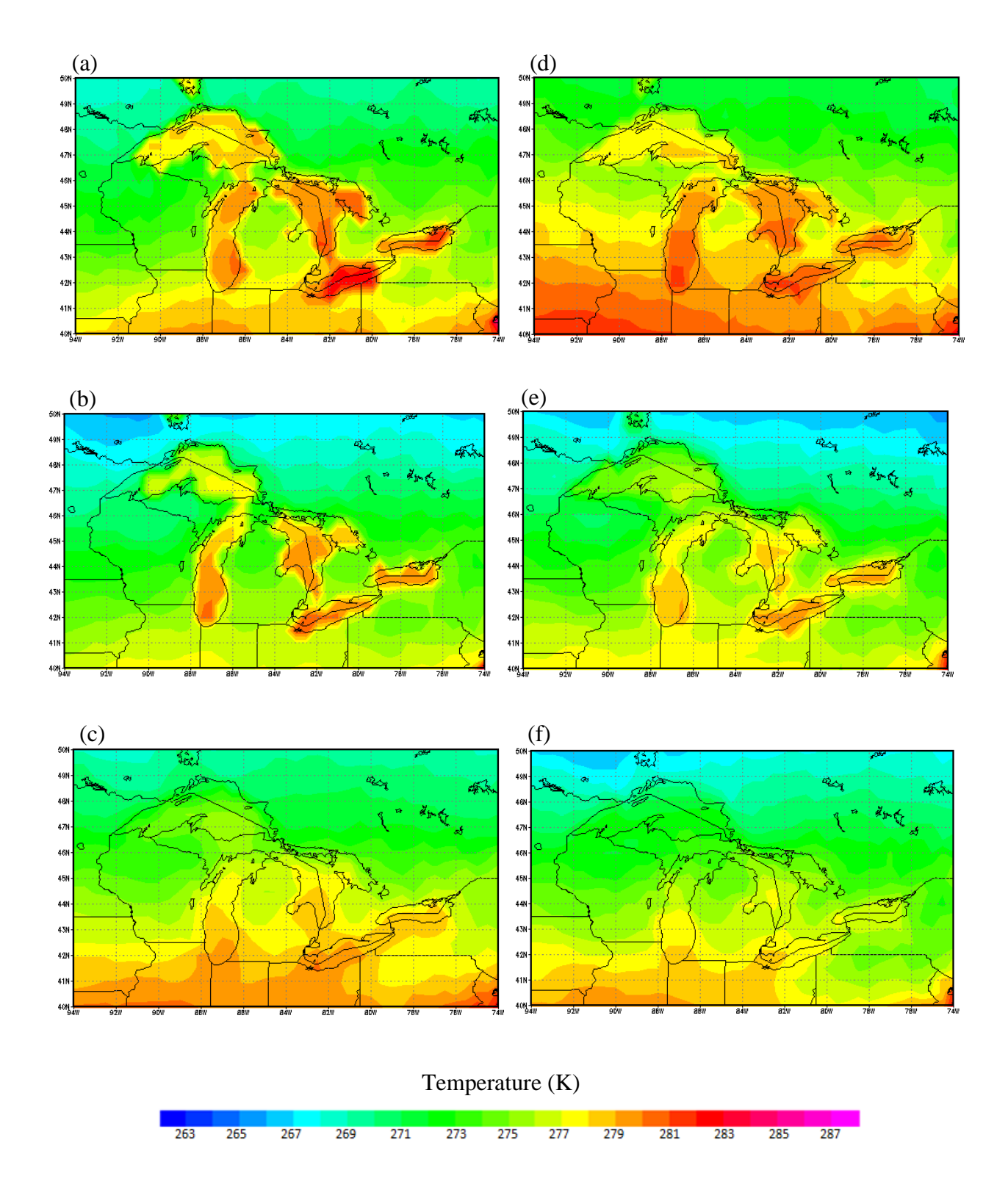


Fig. A.3.1.11. Mean November surface-air temperatures from (a) NARR, (b) CRCM, (c) ECP2, (d) HRM3, (e) MM5I, and (f) WRFG for the GLR domain.

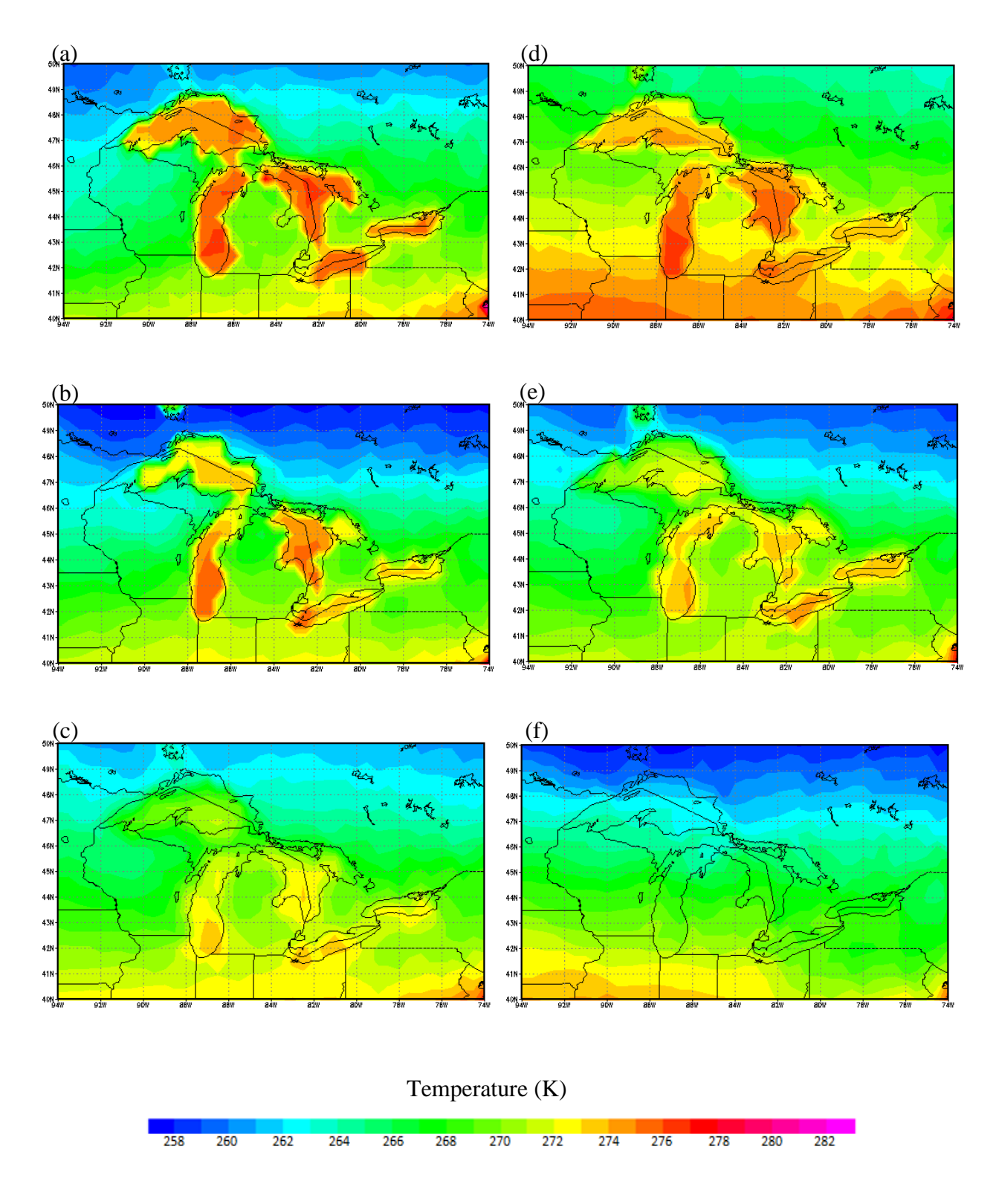


Fig. A.3.1.12. Mean December surface-air temperatures from (a) NARR, (b) CRCM, (c) ECP2, (d) HRM3, (e) MM5I, and (f) WRFG for the GLR domain.

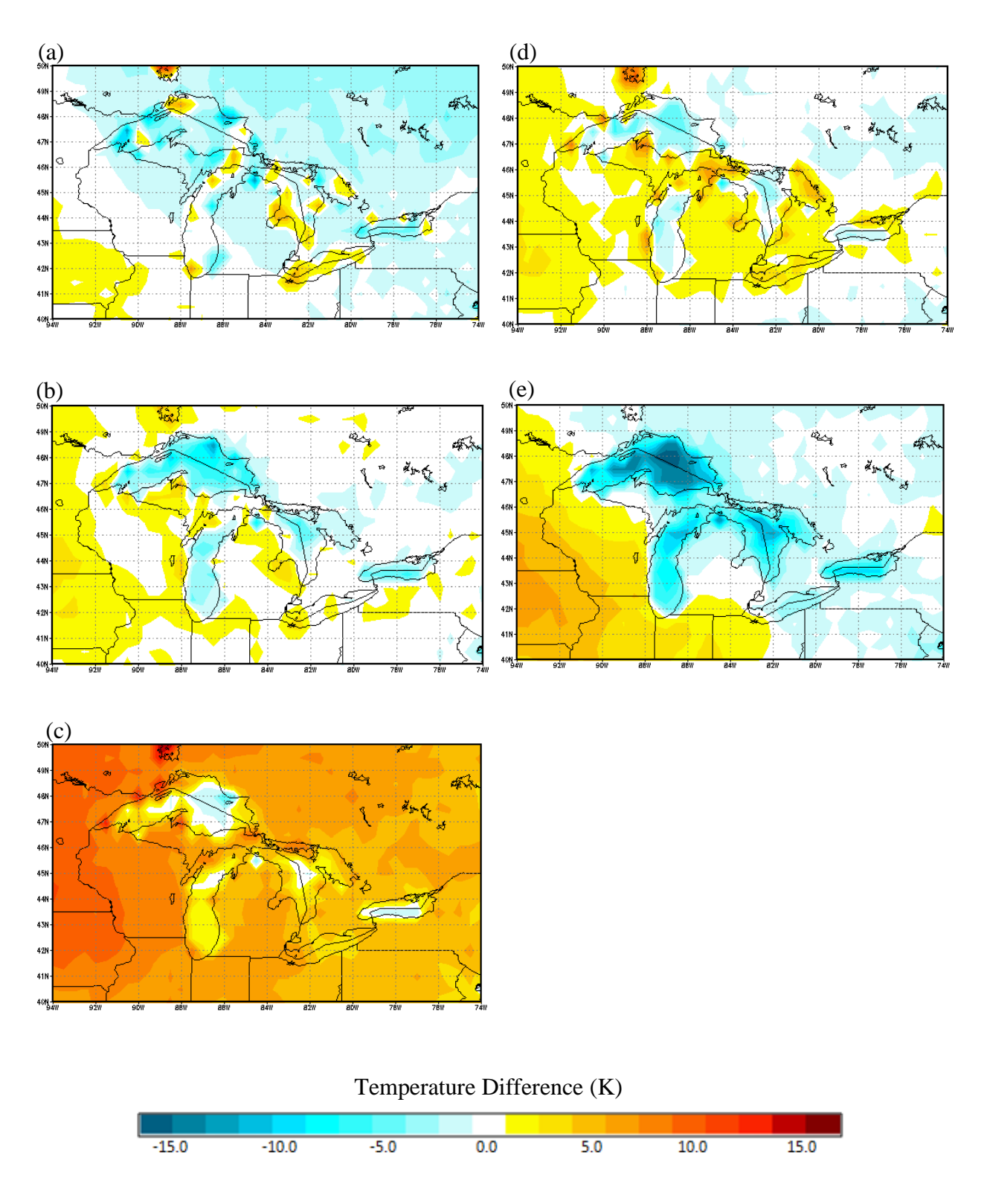


Fig. A.3.2.1. January mean surface-air temperature differences between (a) CRCM, (b) ECP2, (c) HRM3, (d) MM5I, (e) WRFG, and NARR for the GLR domain.

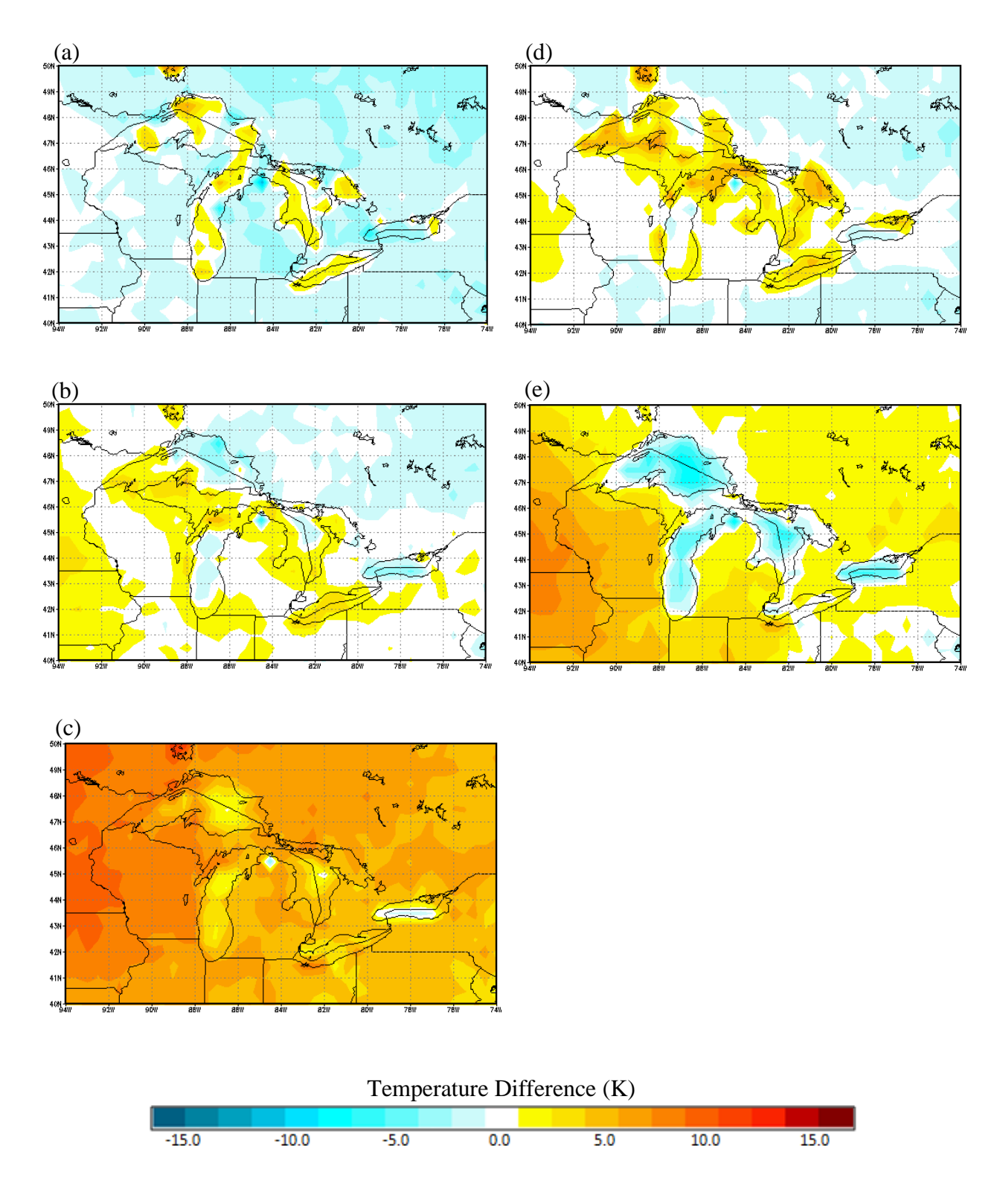


Fig. A.3.2.2. February mean surface-air temperature differences between (a) CRCM, (b) ECP2, (c) HRM3, (d) MM5I, (e) WRFG, and NARR for the GLR domain.

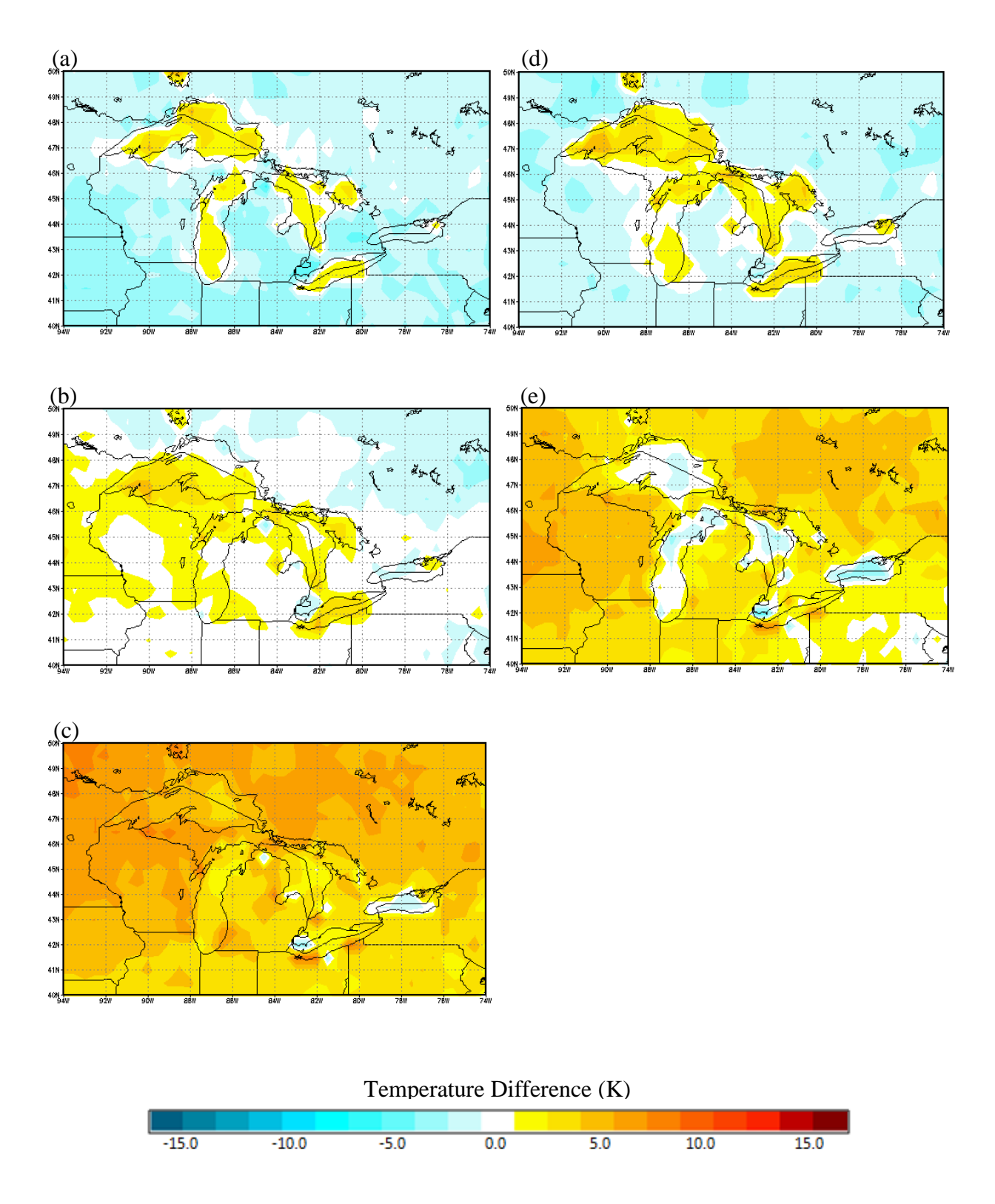


Fig. A.3.2.3. March mean surface-air temperature differences between (a) CRCM, (b) ECP2, (c) HRM3, (d) MM5I, (e) WRFG, and NARR for the GLR domain.

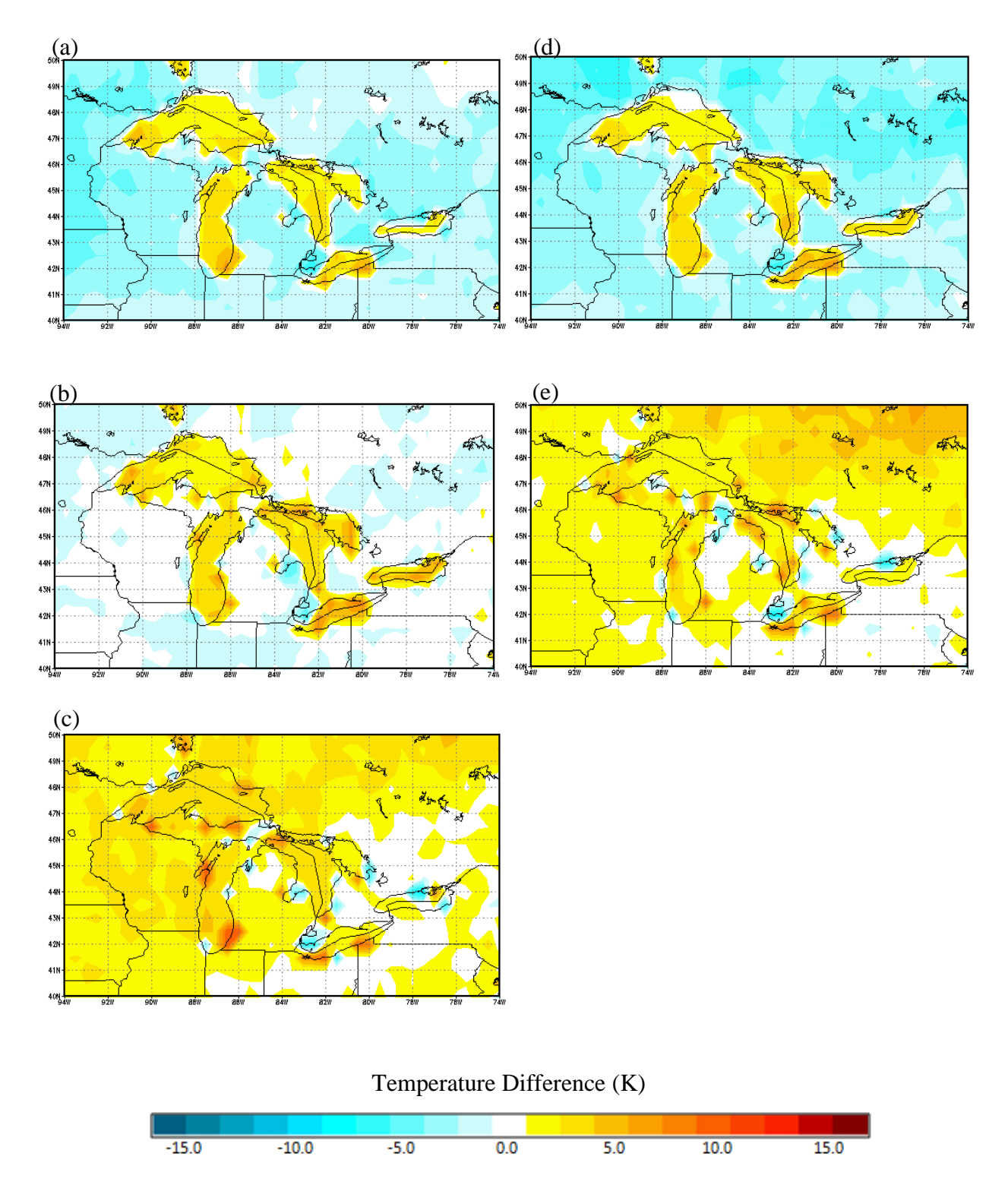


Fig. A.3.2.4. April mean surface-air temperature differences between (a) CRCM, (b) ECP2, (c) HRM3, (d) MM5I, (e) WRFG, and NARR for the GLR domain.

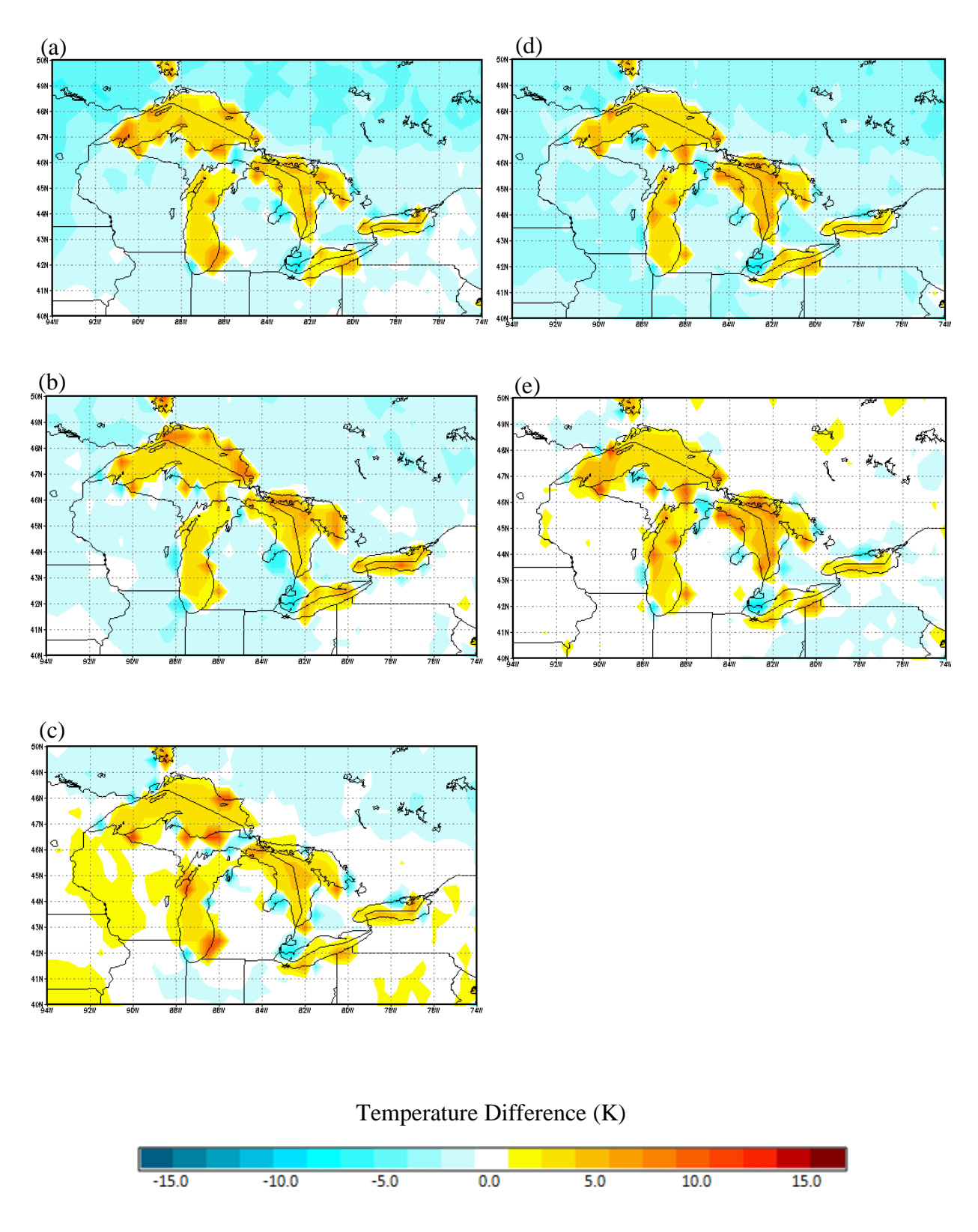


Fig. A.3.2.5. May mean surface-air temperature differences between (a) CRCM, (b) ECP2, (c) HRM3, (d) MM5I, (e) WRFG, and NARR for the GLR domain.

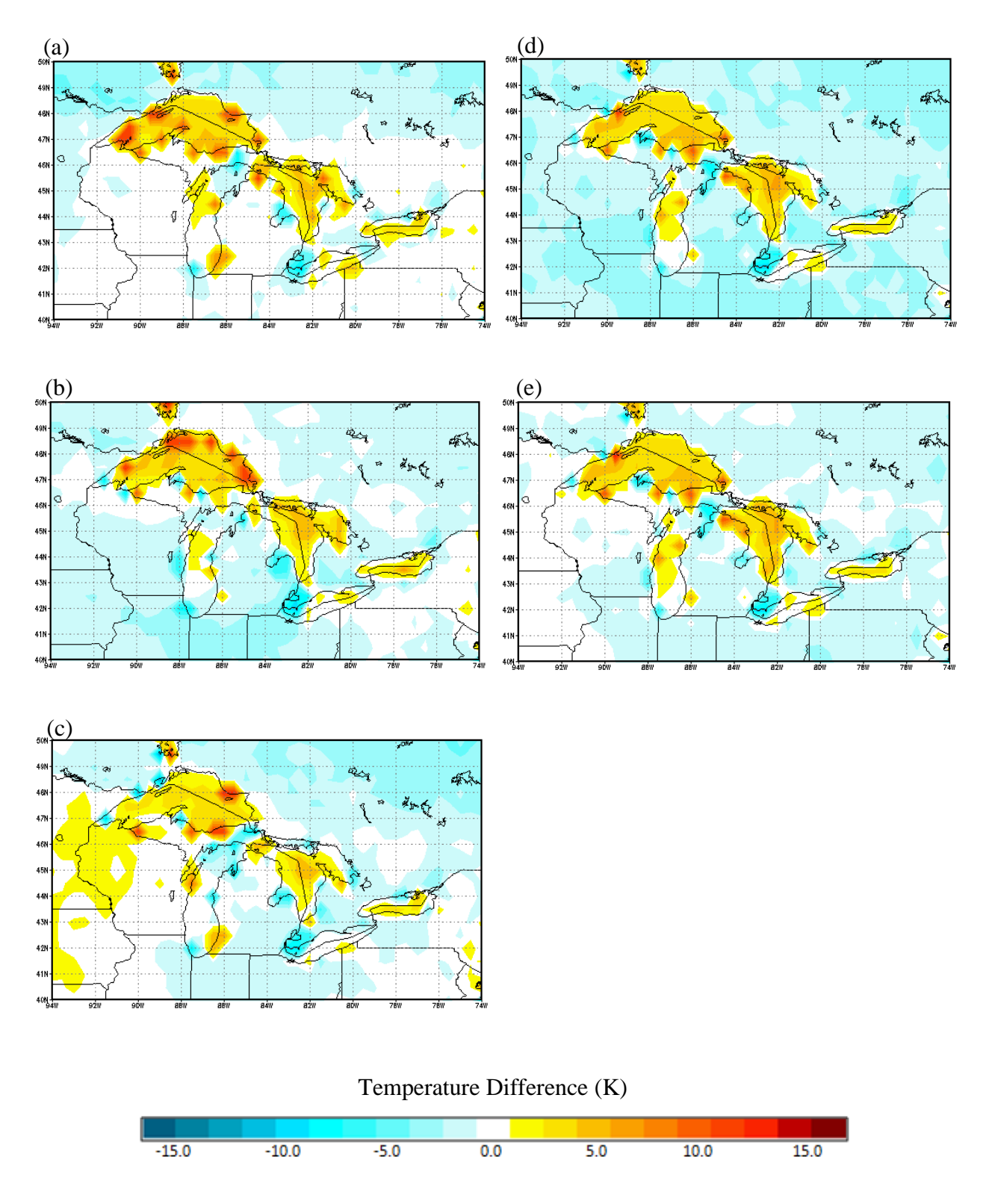


Fig. A.3.2.6. June mean surface-air temperature differences between (a) CRCM, (b) ECP2, (c) HRM3, (d) MM5I, (e) WRFG, and NARR for the GLR domain.

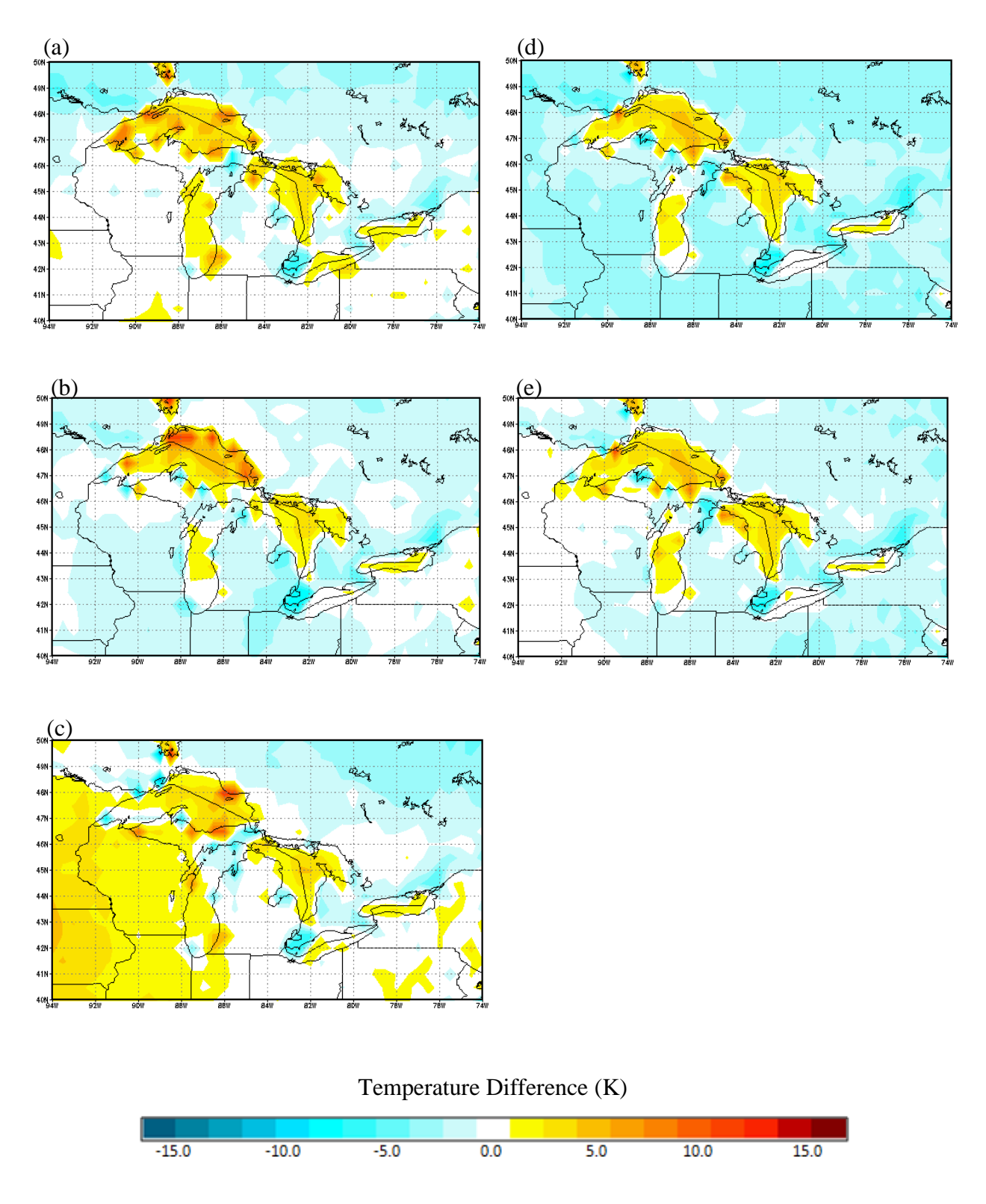


Fig. A.3.2.7. July mean surface-air temperature differences between (a) CRCM, (b) ECP2, (c) HRM3, (d) MM5I, (e) WRFG, and NARR for the GLR domain.

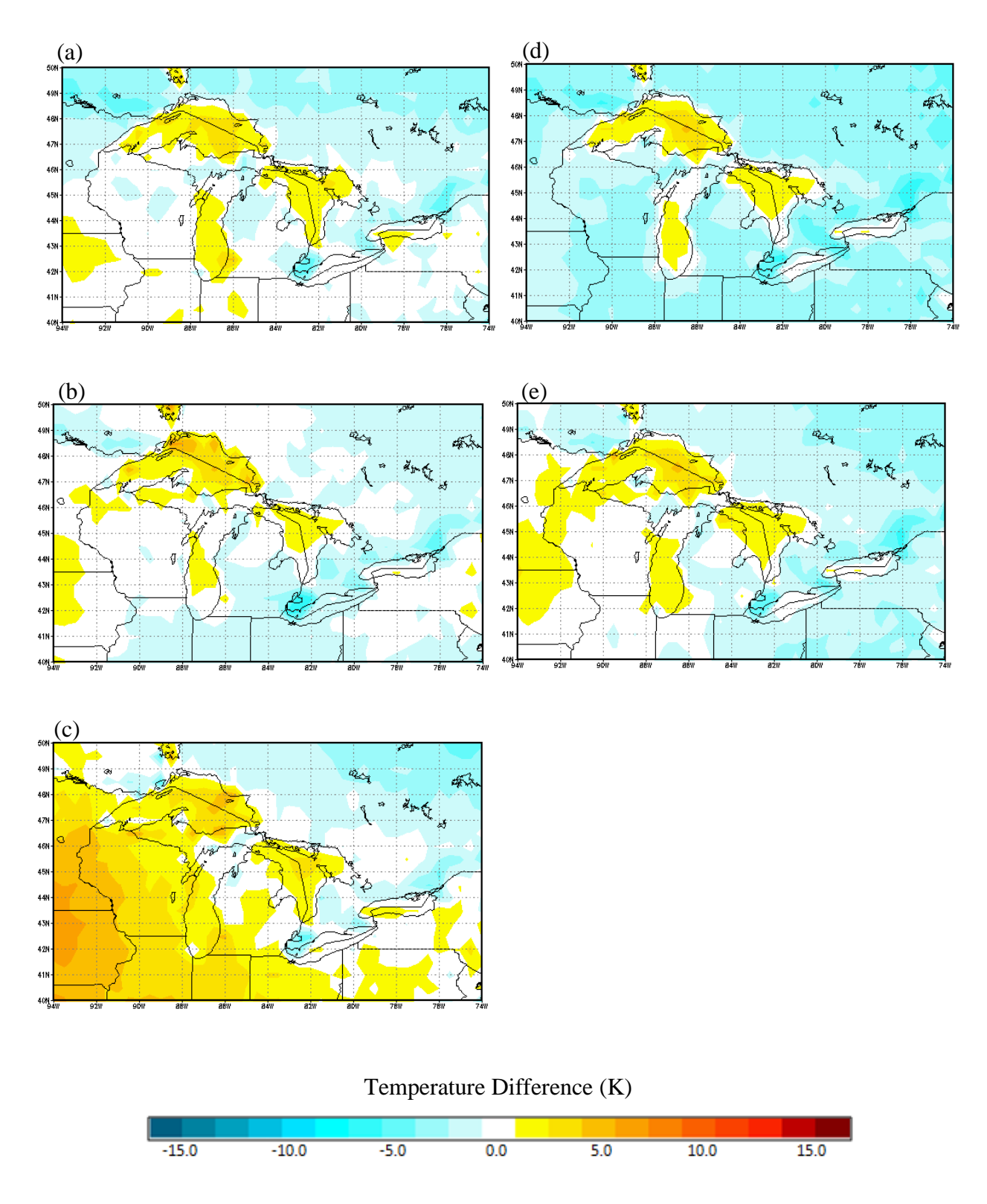


Fig. A.3.2.8. August mean surface-air temperature differences between (a) CRCM, (b) ECP2, (c) HRM3, (d) MM5I, (e) WRFG, and NARR for the GLR domain.

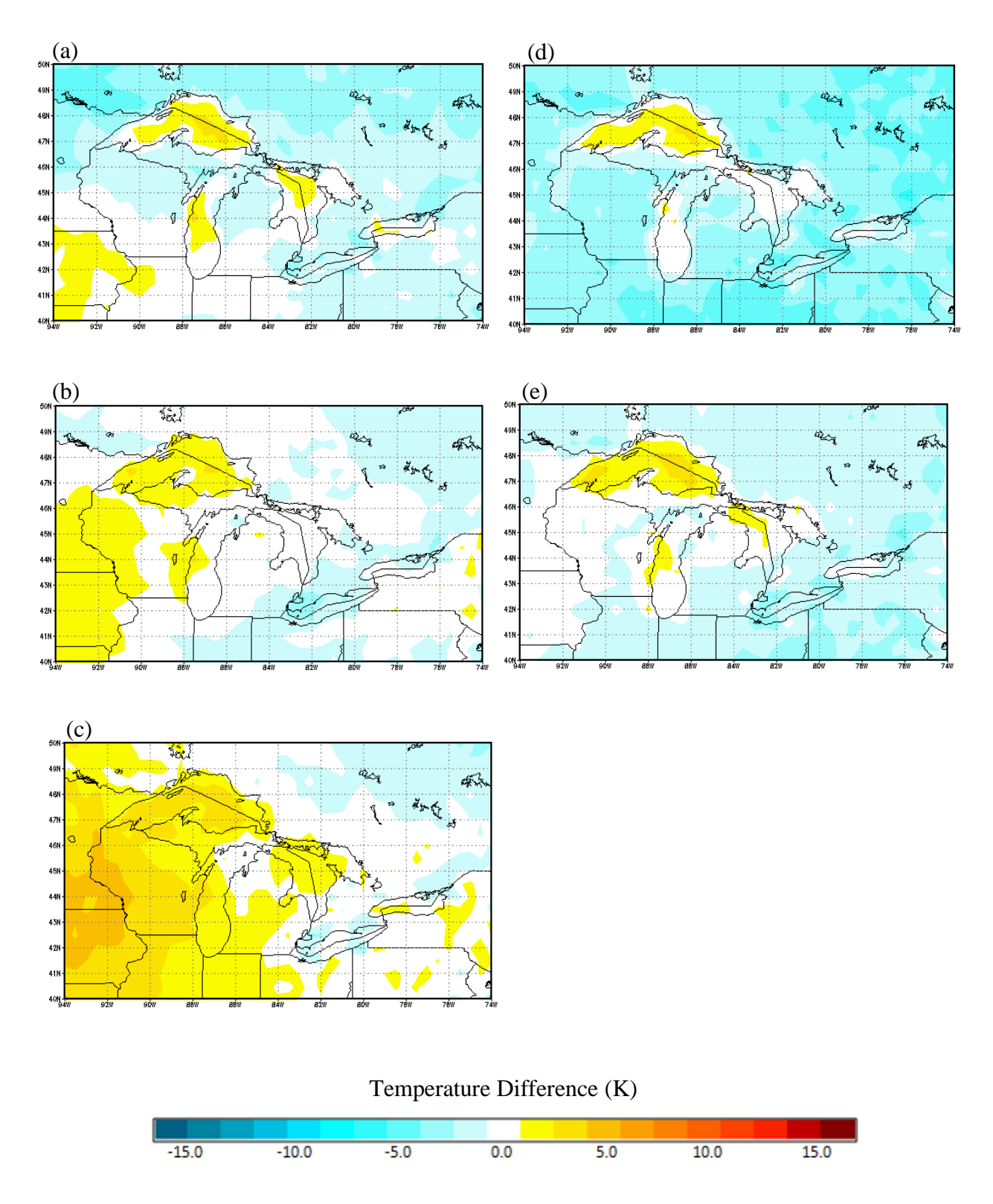


Fig. A.3.2.9. September mean surface-air temperature differences between (a) CRCM, (b) ECP2, (c) HRM3, (d) MM5I, (e) WRFG, and NARR for the GLR domain.

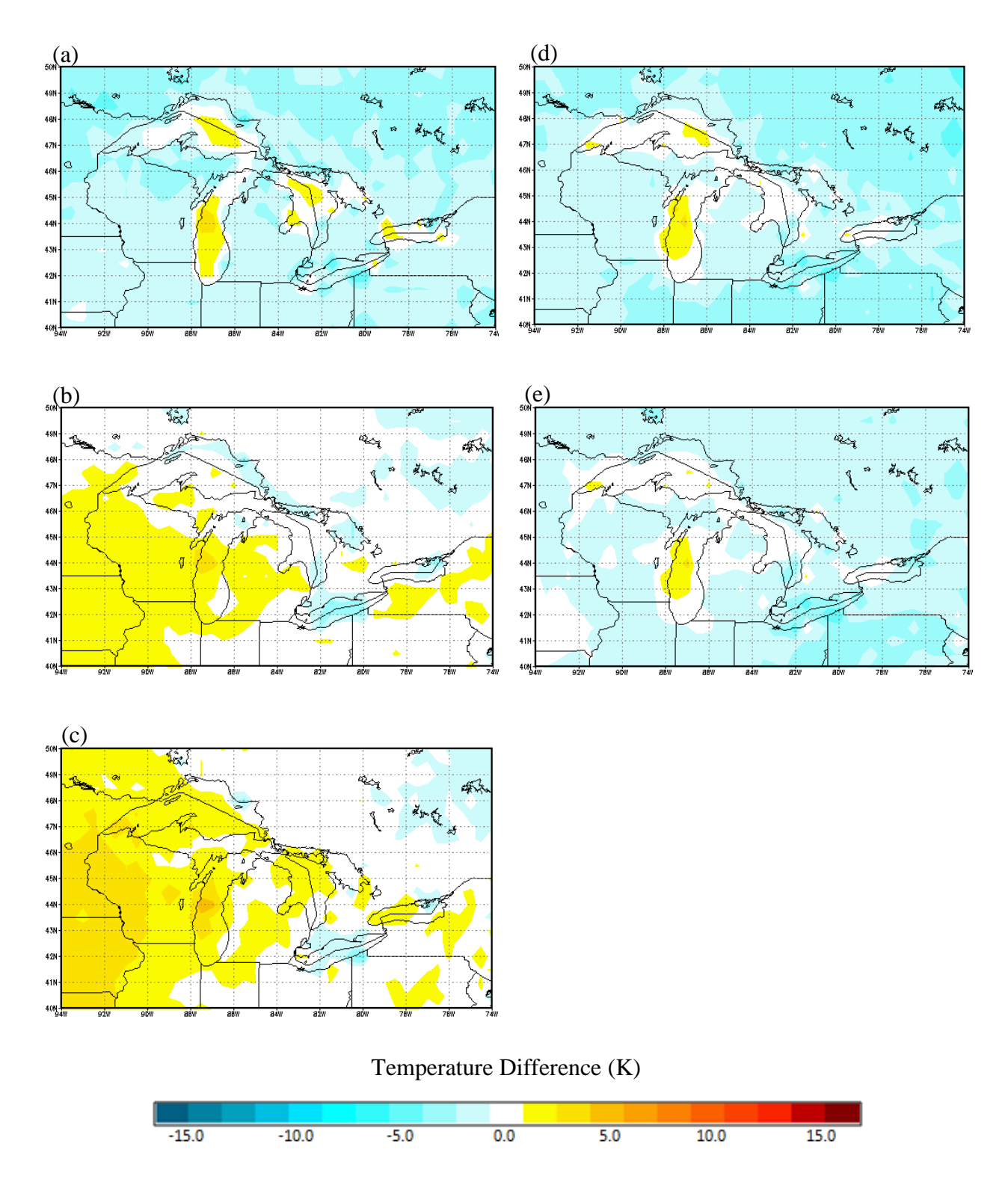


Fig. A.3.2.10. October mean surface-air temperature differences between (a) CRCM, (b) ECP2, (c) HRM3, (d) MM5I, (e) WRFG, and NARR for the GLR domain.

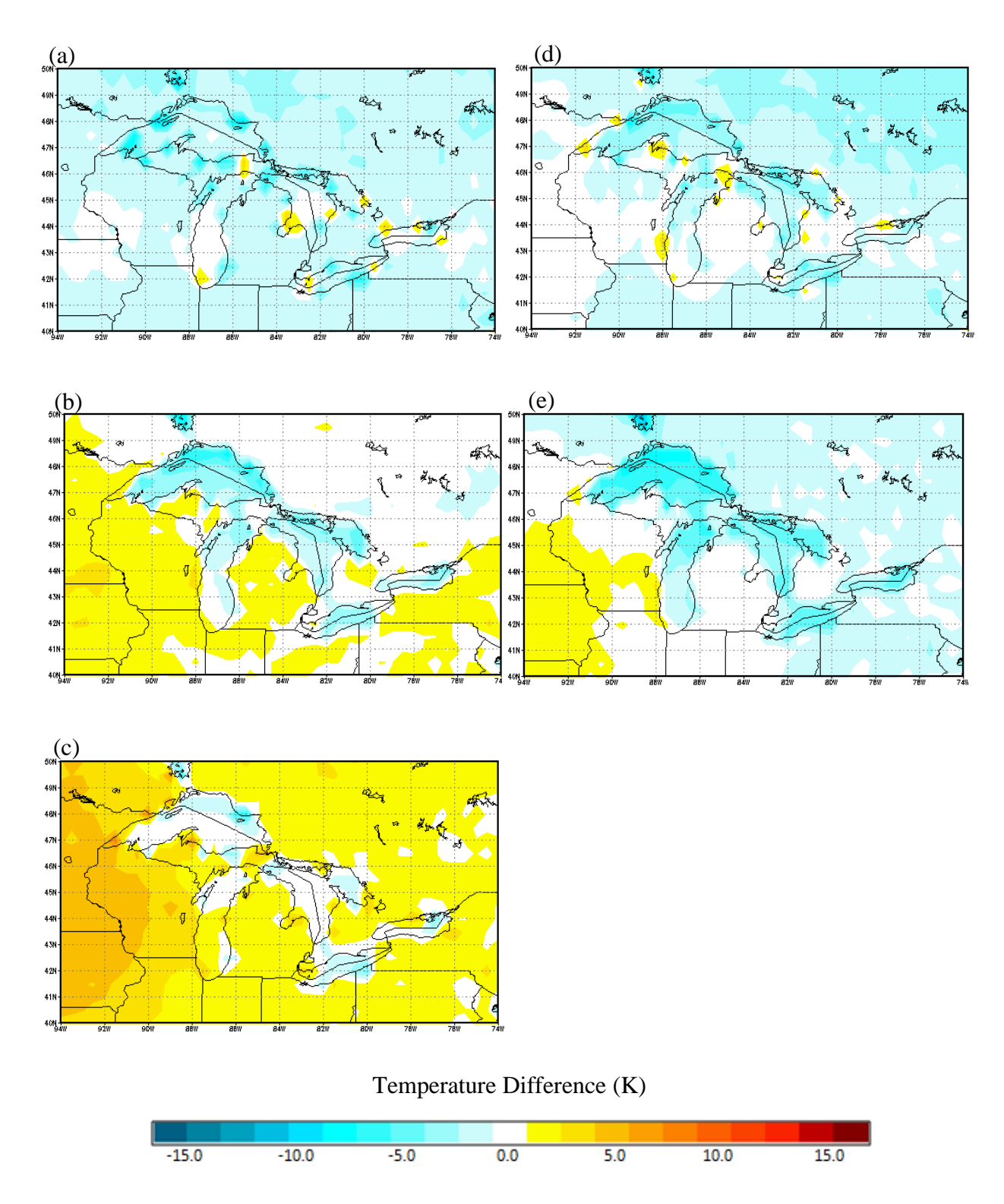


Fig. A.3.2.11. November mean surface-air temperature differences between (a) CRCM, (b) ECP2, (c) HRM3, (d) MM5I, (e) WRFG, and NARR for the GLR domain.

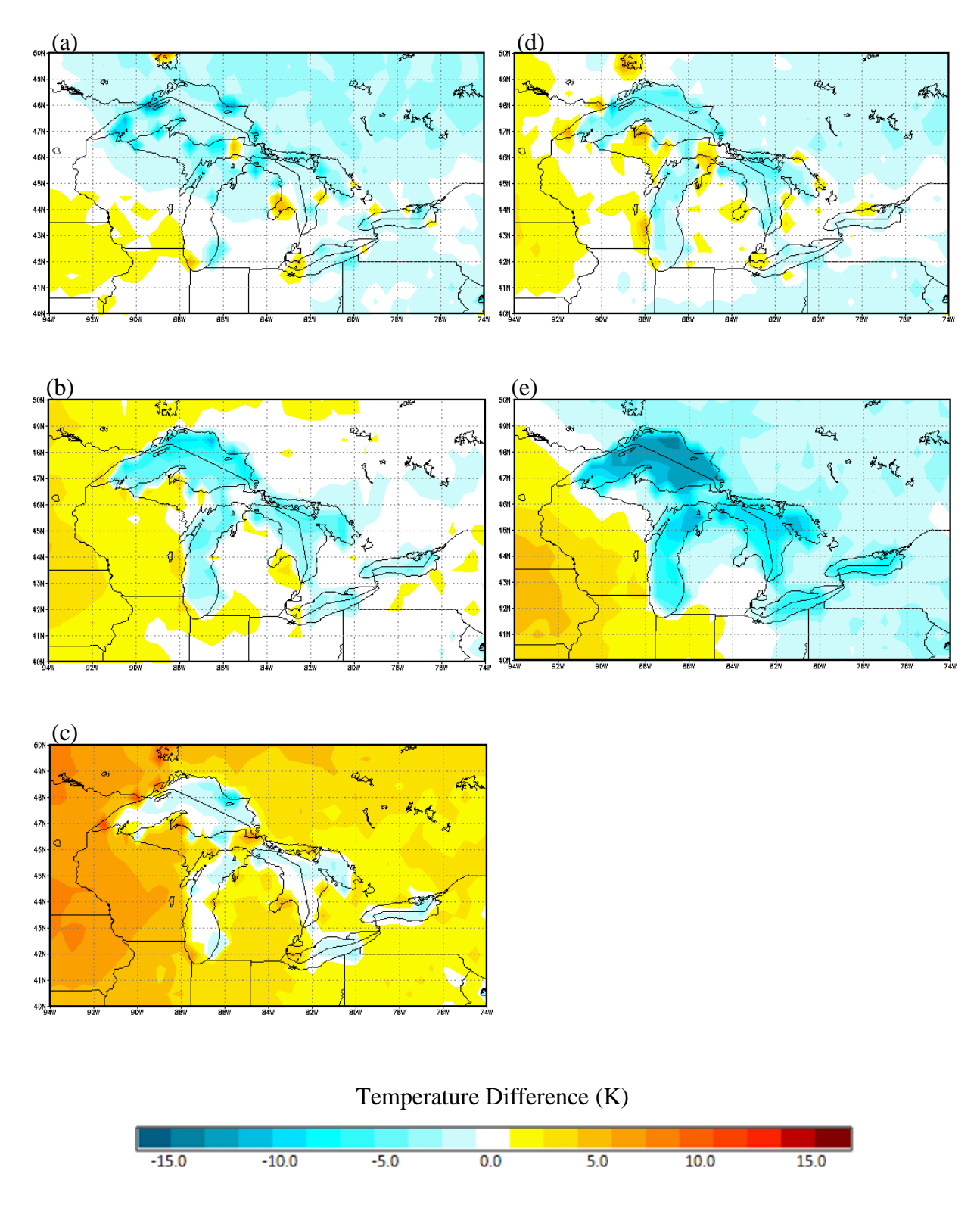


Fig. A.3.2.12. December mean surface-air temperature differences between (a) CRCM, (b) ECP2, (c) HRM3, (d) MM5I, (e) WRFG, and NARR for the GLR domain.

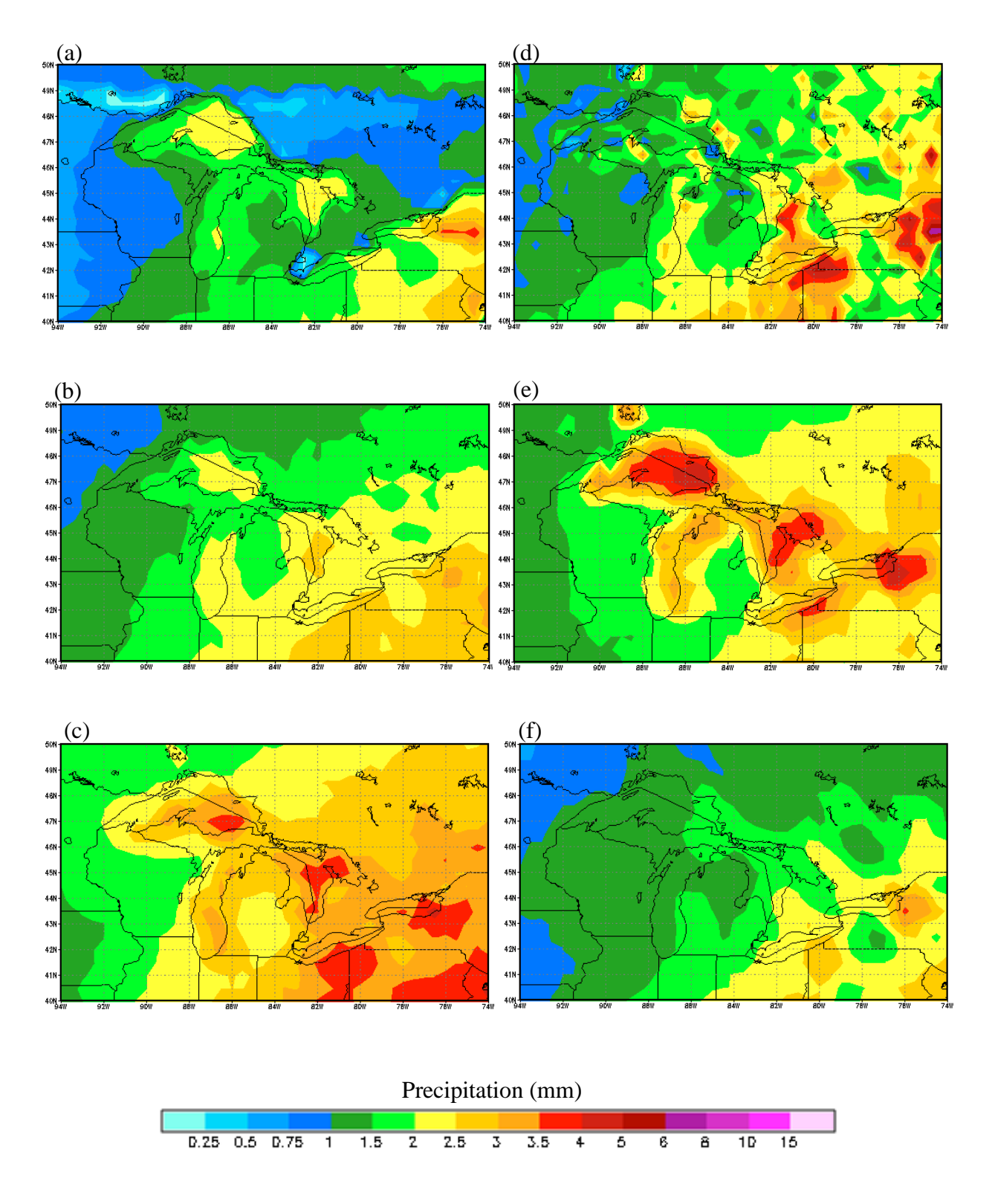


Fig. A.4.1.1. January daily accumulated precipitation from (a) NARR, (b) CRCM, (c) ECP2, (d) HRM3, (e) MM5I, and (f) WRFG for the GLR domain.

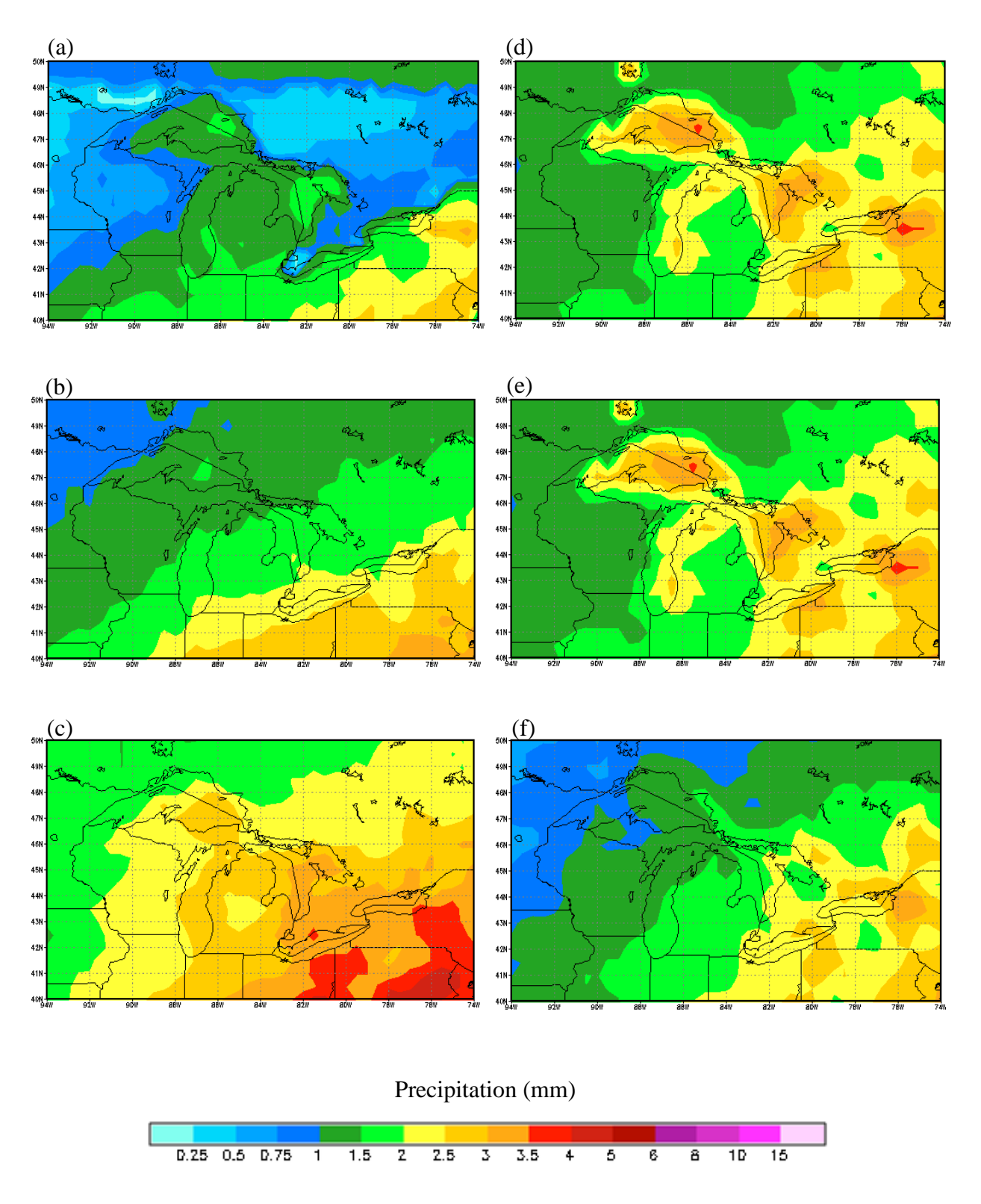


Fig. A.4.1.2. February daily accumulated precipitation from (a) NARR, (b) CRCM, (c) ECP2, (d) HRM3, (e) MM5I, and (f) WRFG for the GLR domain.

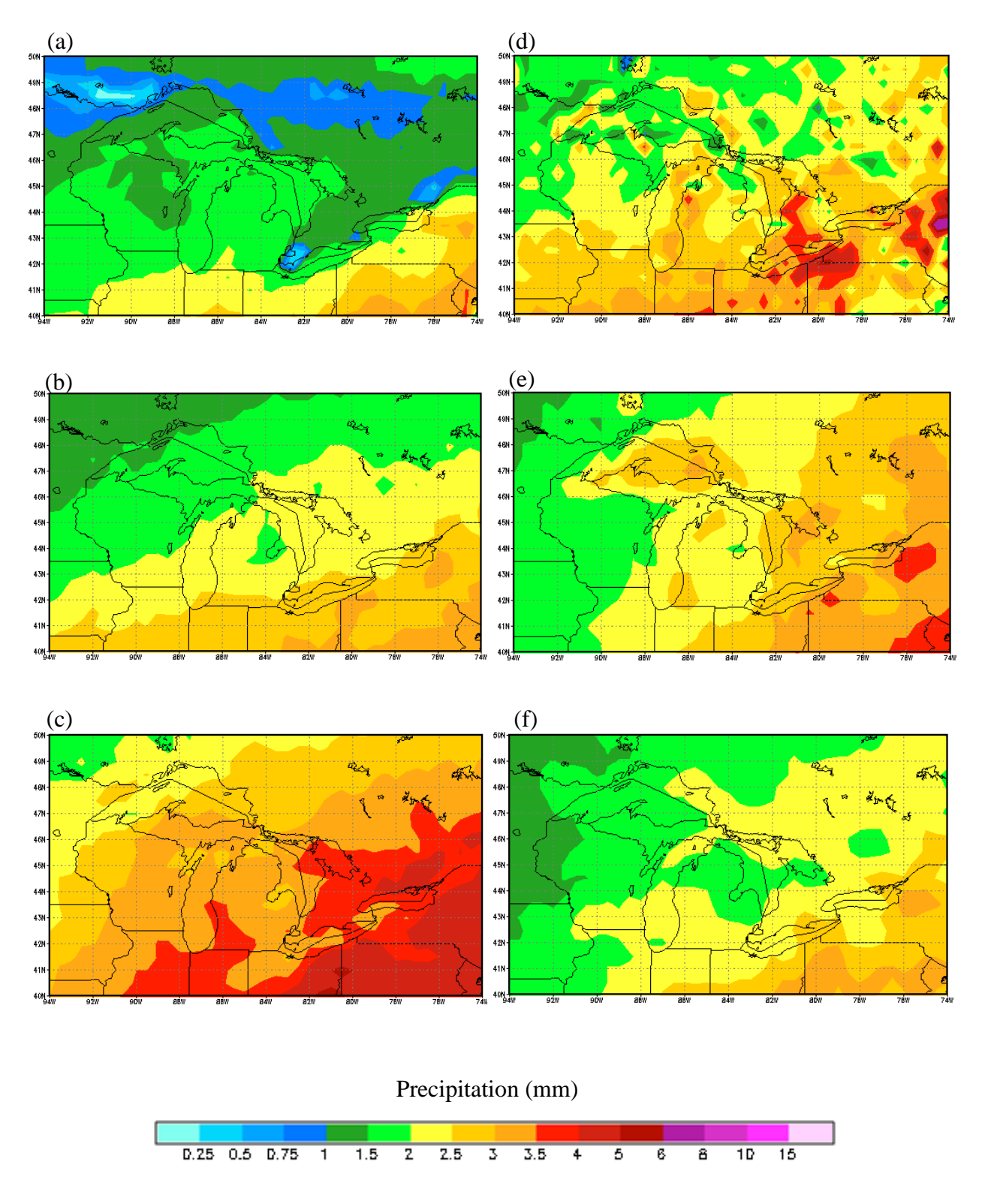


Fig. A.4.1.3. March daily accumulated precipitation from (a) NARR, (b) CRCM, (c) ECP2, (d) HRM3, (e) MM5I, and (f) WRFG for the GLR domain.

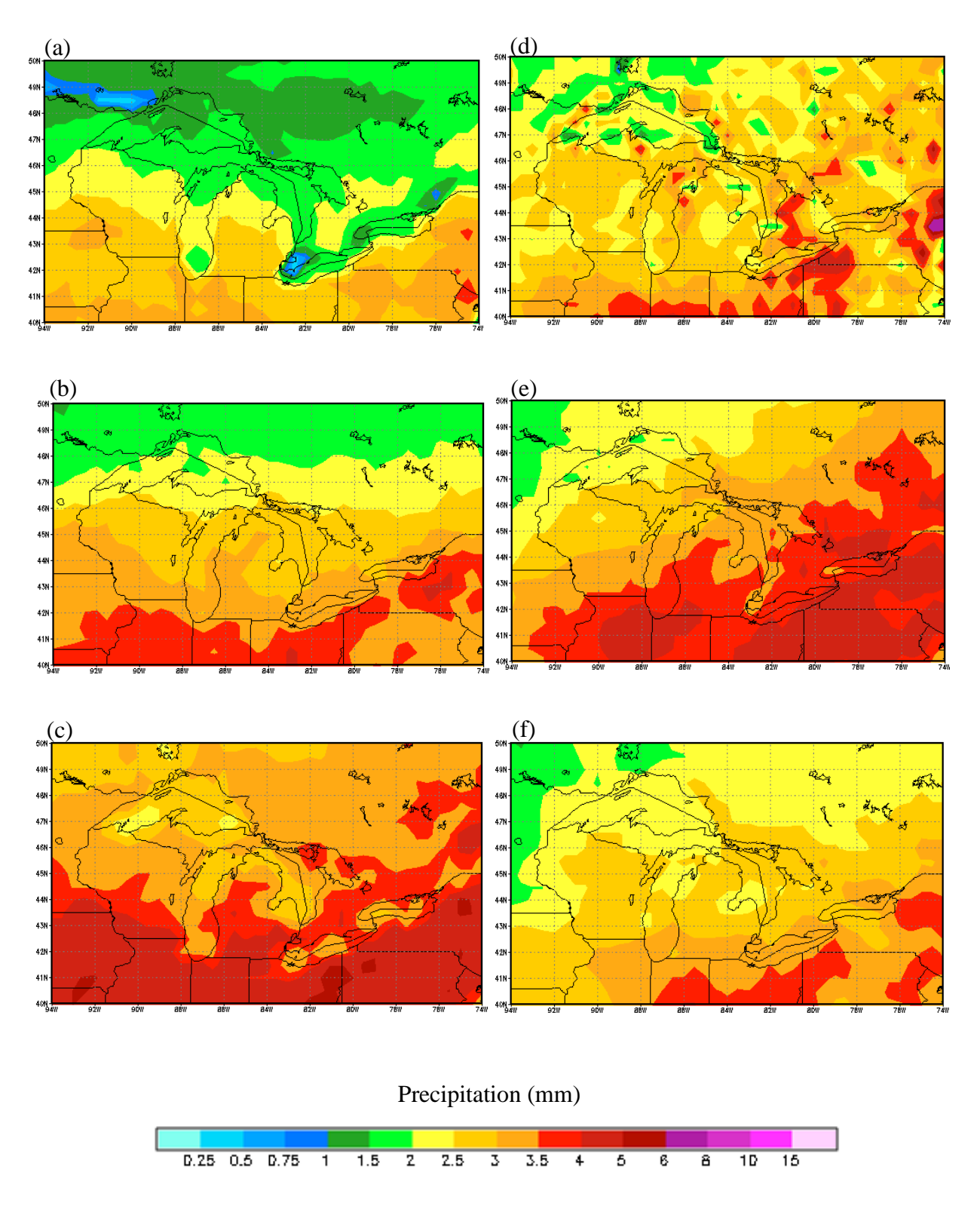


Fig. A.4.1.4. April daily accumulated precipitation from (a) NARR, (b) CRCM, (c) ECP2, (d) HRM3, (e) MM5I, and (f) WRFG for the GLR domain.

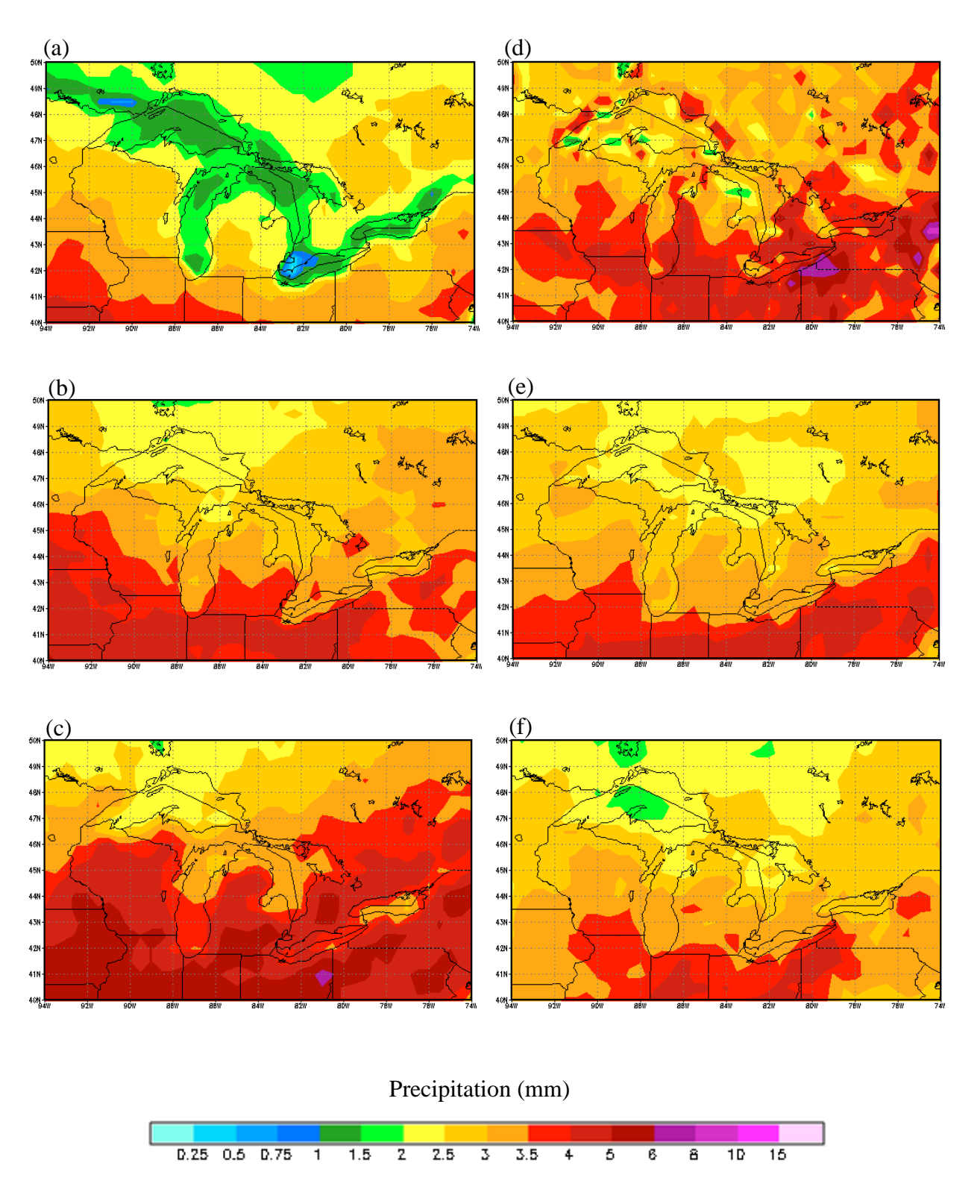


Fig. A.4.1.5. May daily accumulated precipitation from (a) NARR, (b) CRCM, (c) ECP2, (d) HRM3, (e) MM5I, and (f) WRFG for the GLR domain.

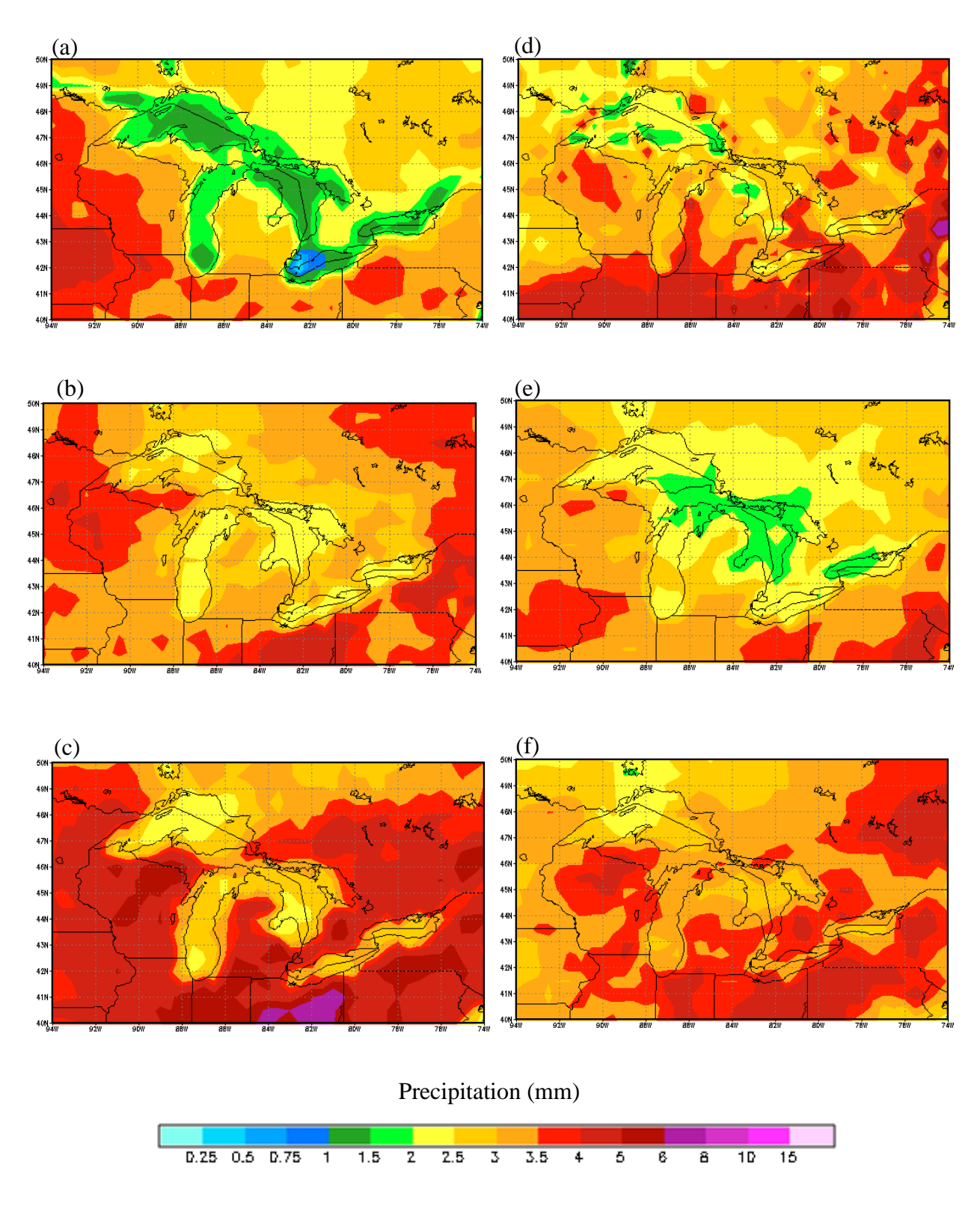


Fig. A.4.1.6. June daily accumulated precipitation from (a) NARR, (b) CRCM, (c) ECP2, (d) HRM3, (e) MM5I, and (f) WRFG for the GLR domain.

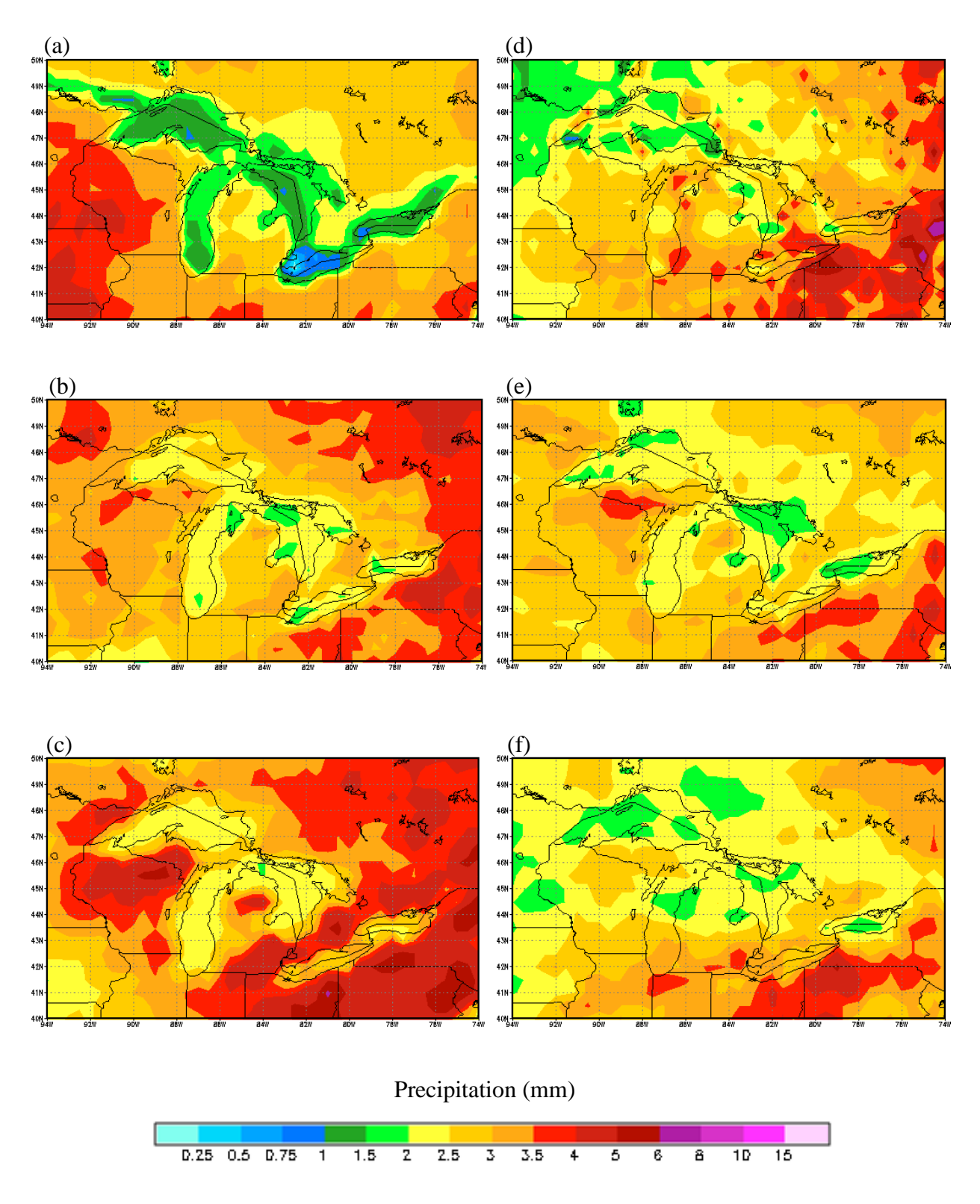


Fig. A.4.1.7. July daily accumulated precipitation from (a) NARR, (b) CRCM, (c) ECP2, (d) HRM3, (e) MM5I, and (f) WRFG for the GLR domain.

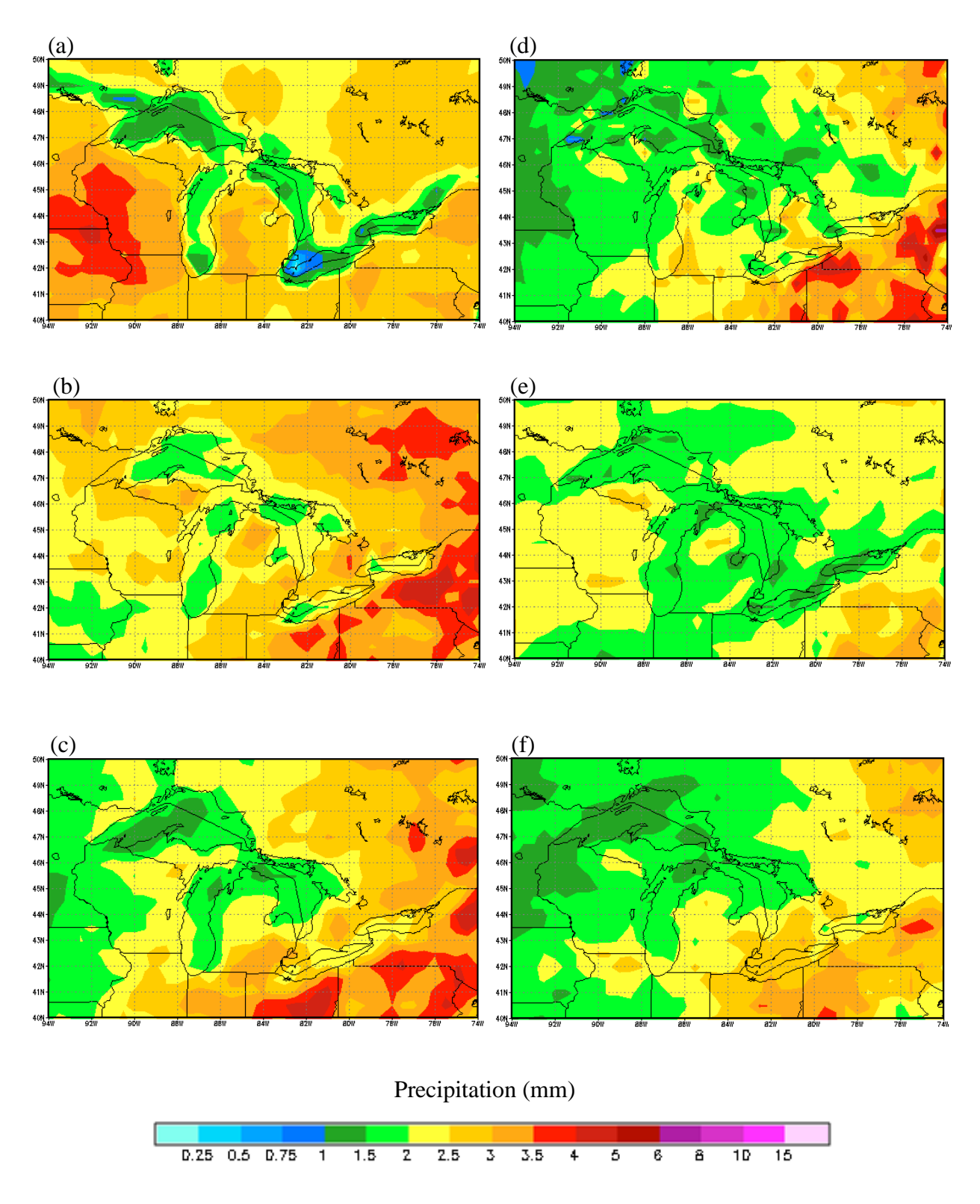


Fig. A.4.1.8. August daily accumulated precipitation from (a) NARR, (b) CRCM, (c) ECP2, (d) HRM3, (e) MM5I, and (f) WRFG for the GLR domain.

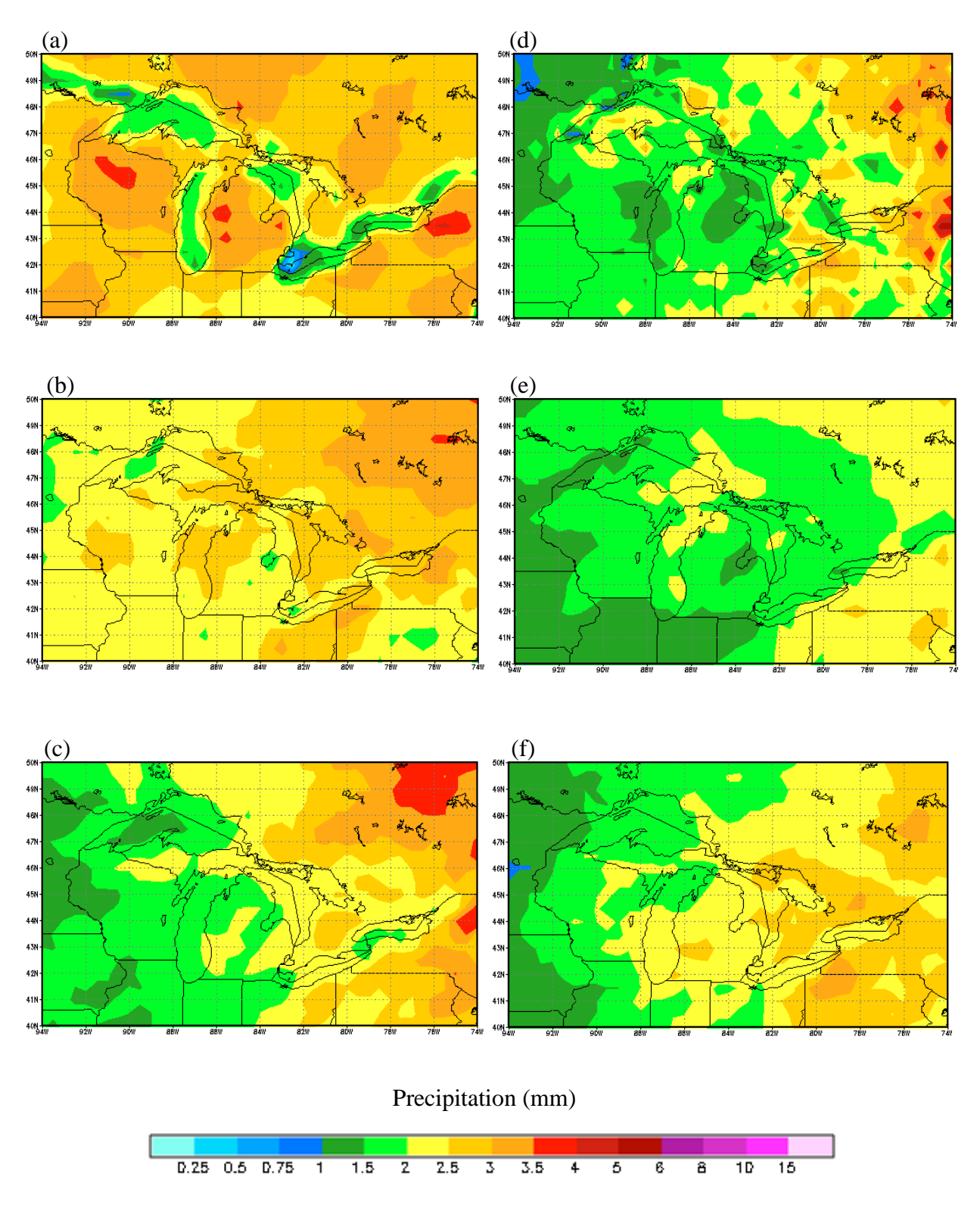


Fig. A.4.1.9. September daily accumulated precipitation from (a) NARR, (b) CRCM, (c) ECP2, (d) HRM3, (e) MM5I, and (f) WRFG for the GLR domain.

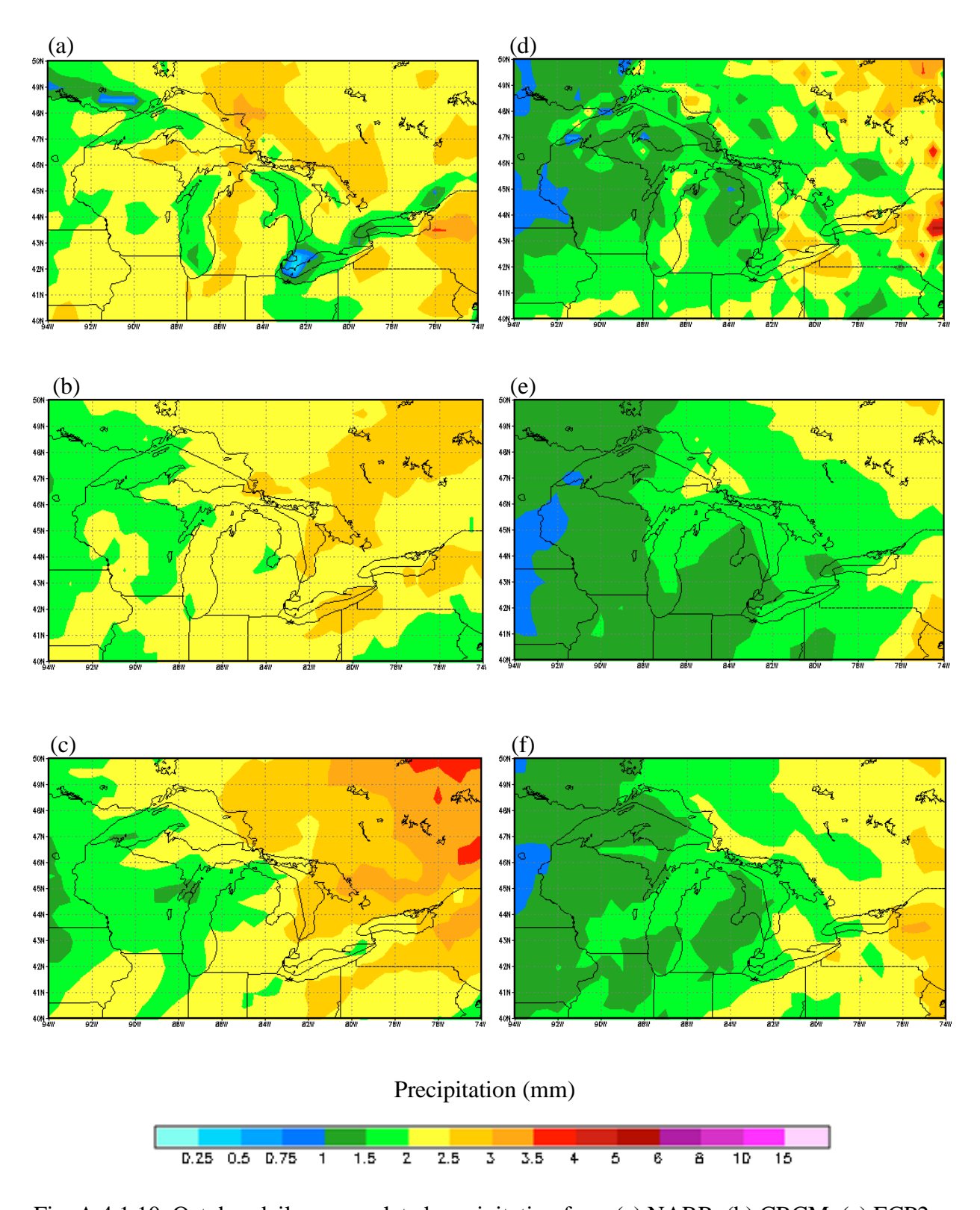


Fig. A.4.1.10. October daily accumulated precipitation from (a) NARR, (b) CRCM, (c) ECP2, (d) HRM3, (e) MM5I, and (f) WRFG for the GLR domain.

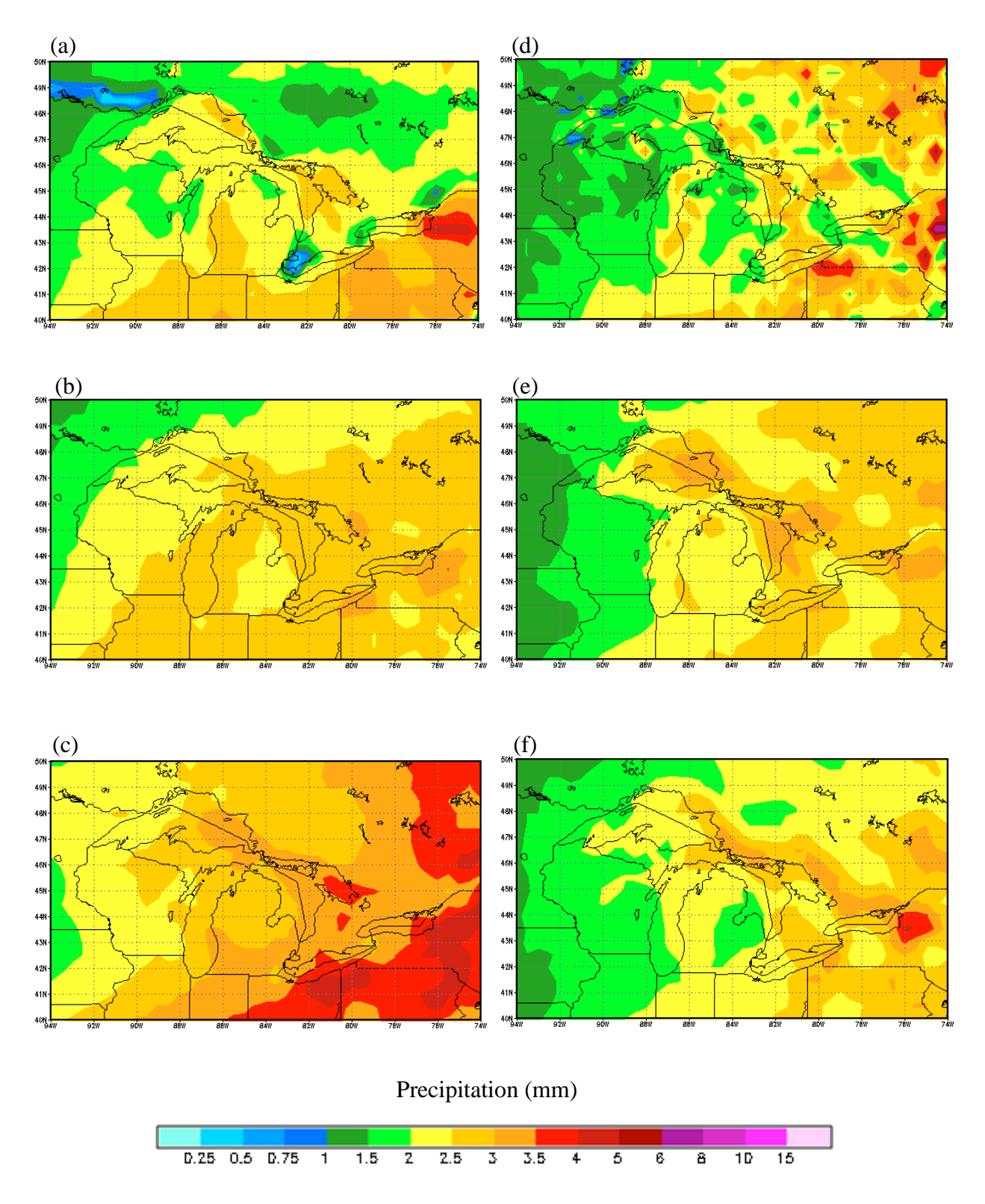


Fig. A.4.1.11. November daily accumulated precipitation from (a) NARR, (b) CRCM, (c) ECP2, (d) HRM3, (e) MM5I, and (f) WRFG for the GLR domain.

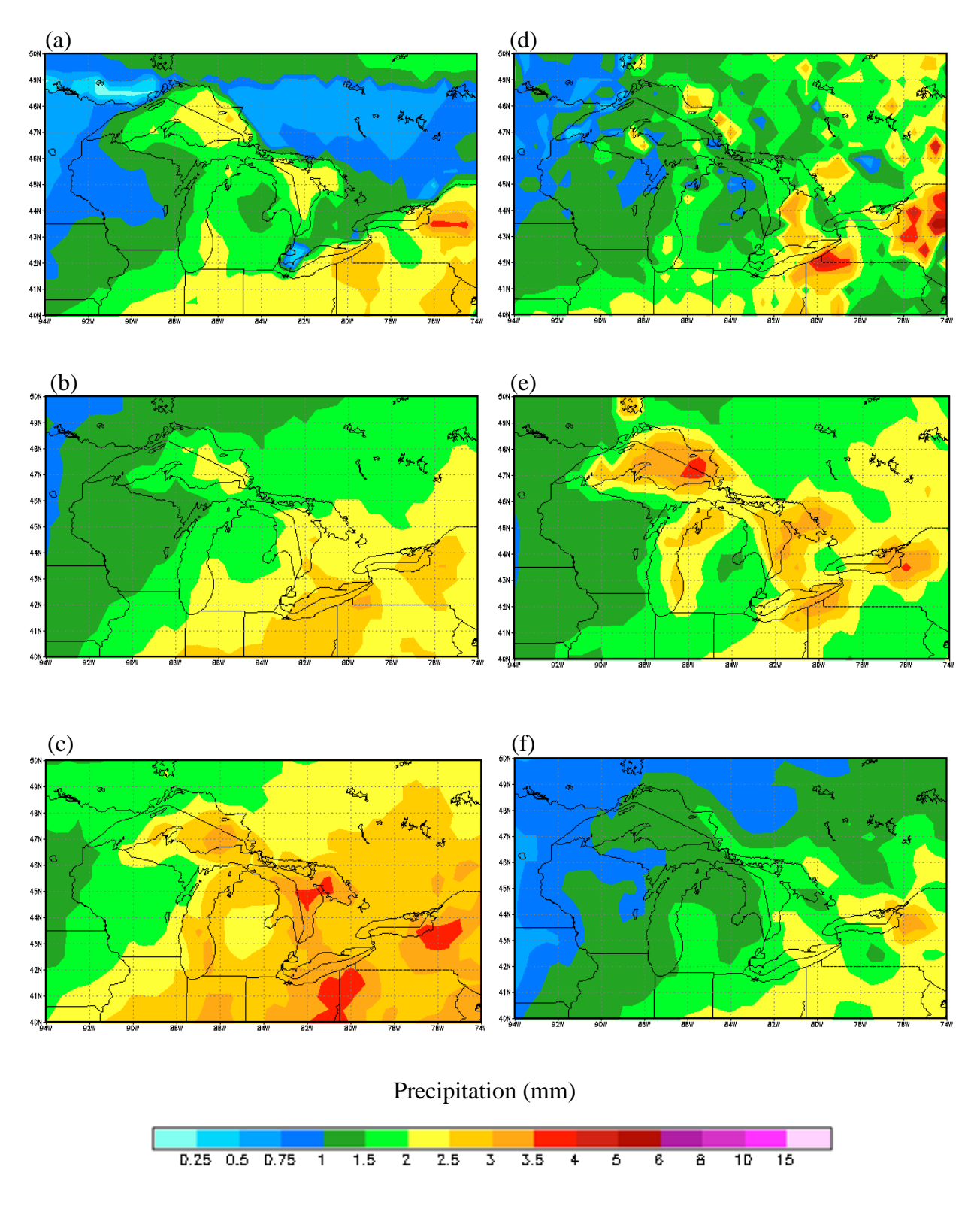


Fig. A.4.1.12. December daily accumulated precipitation from (a) NARR, (b) CRCM, (c) ECP2, (d) HRM3, (e) MM5I, and (f) WRFG for the GLR domain.

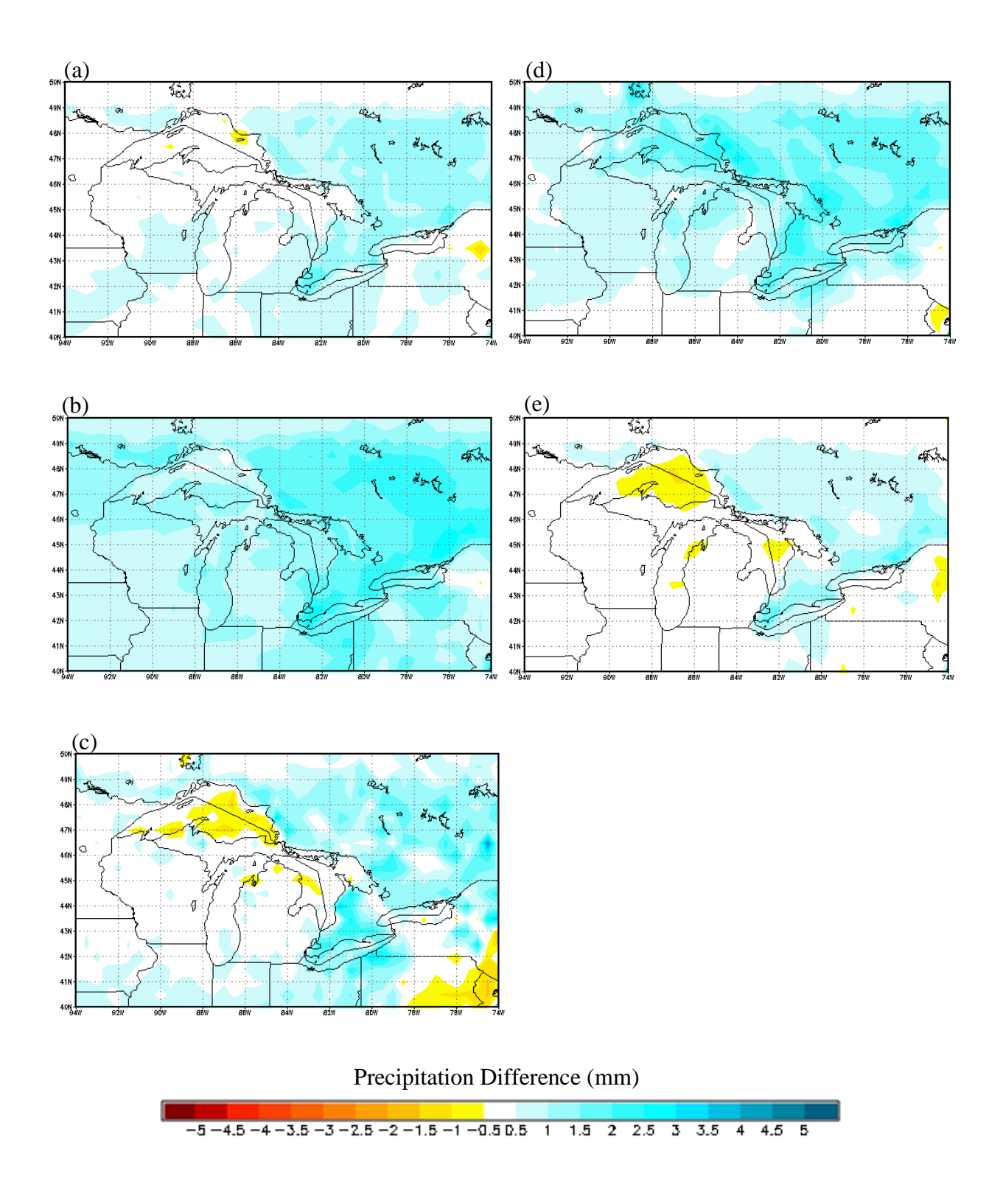


Fig. A.4.2.1. January daily accumulated precipitation differences between (a) CRCM, (b) ECP2, (c) HRM3, (d) MM5I, and (e) WRFG, and NARR for the GLR domain.

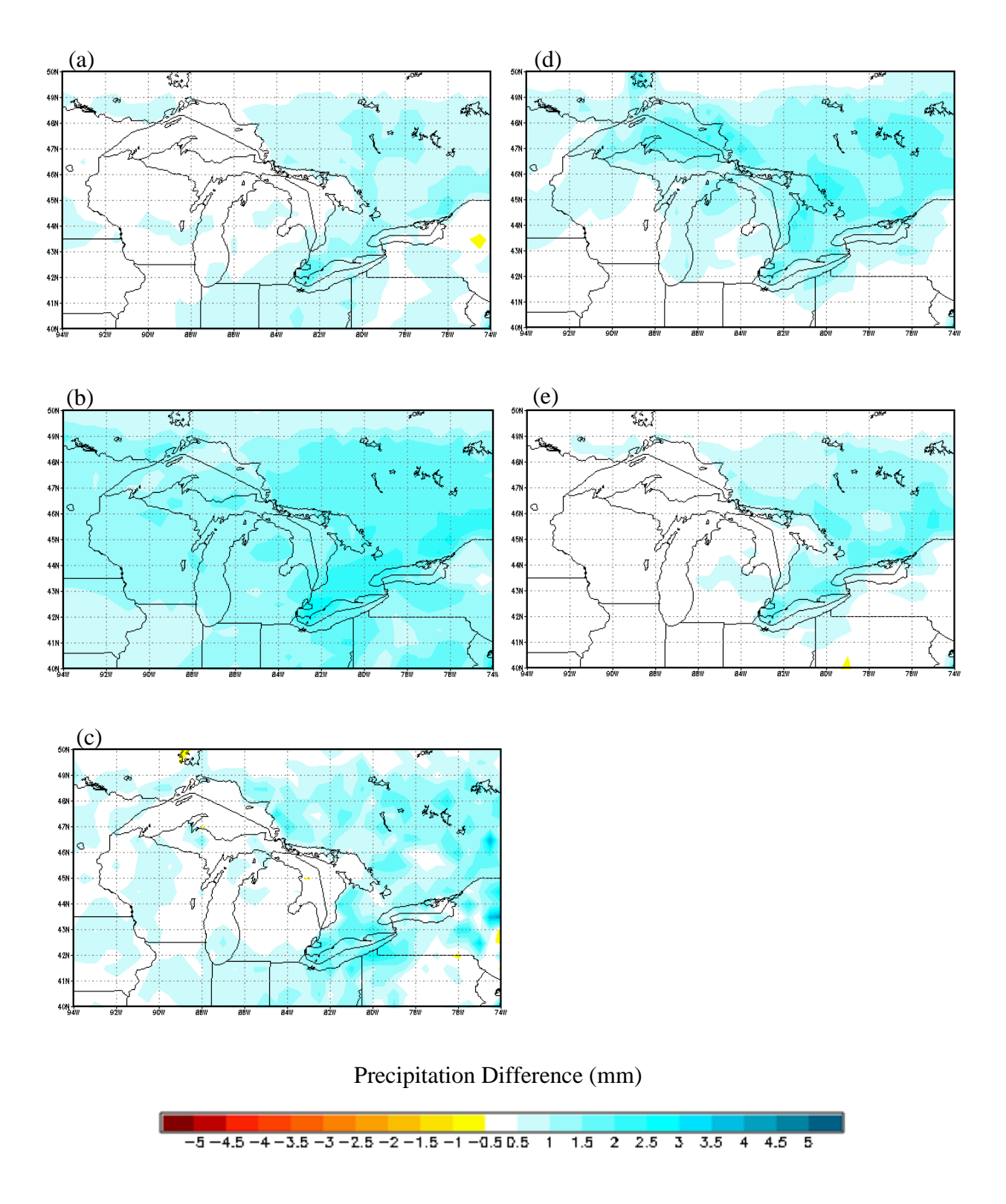


Fig. A.4.2.2. February daily accumulated precipitation differences between (a) CRCM, (b) ECP2, (c) HRM3, (d) MM5I, and (e) WRFG, and NARR for the GLR domain.

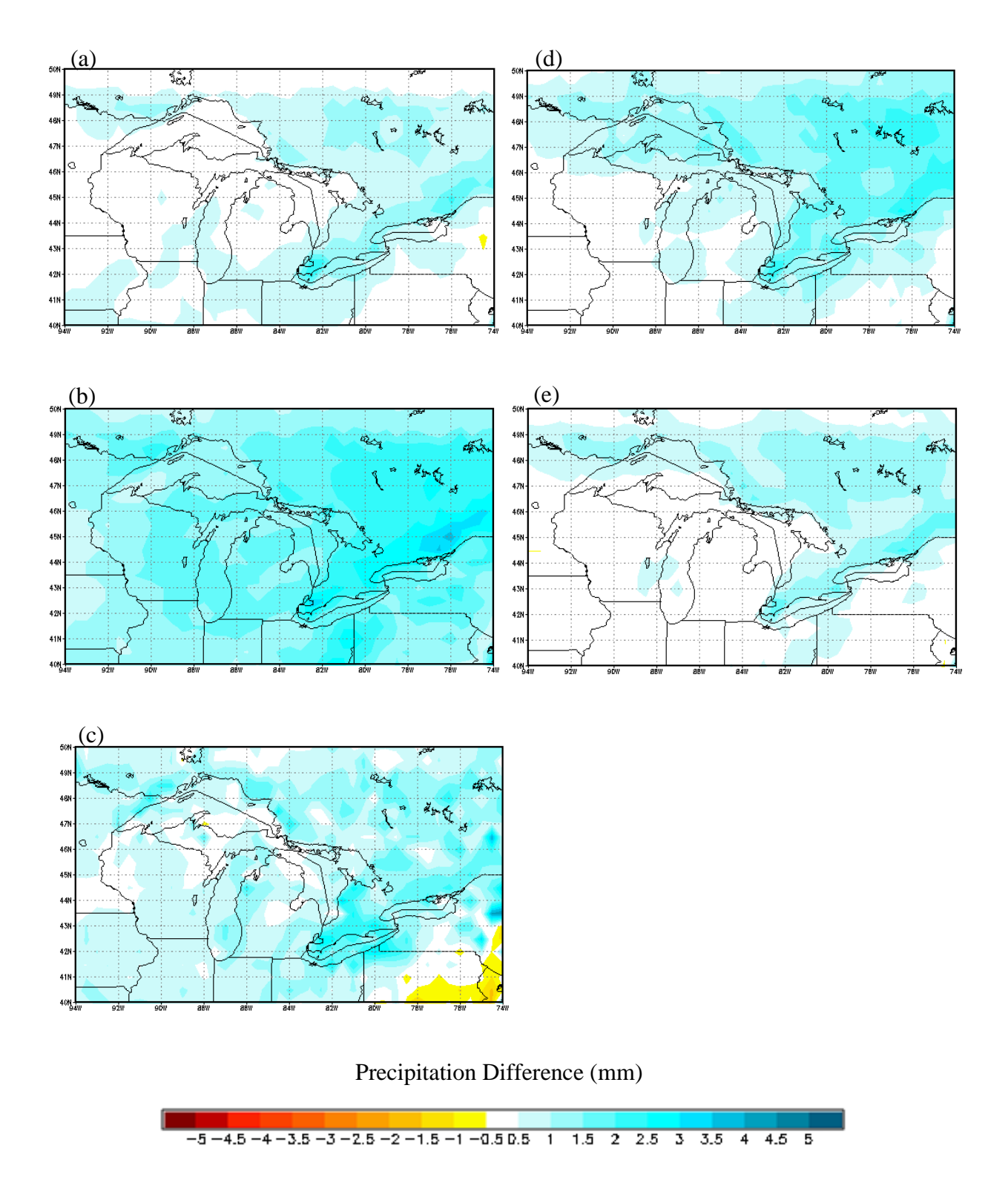


Fig. A.4.2.3. March daily accumulated precipitation differences between (a) CRCM, (b) ECP2, (c) HRM3, (d) MM5I, and (e) WRFG, and NARR for the GLR domain.

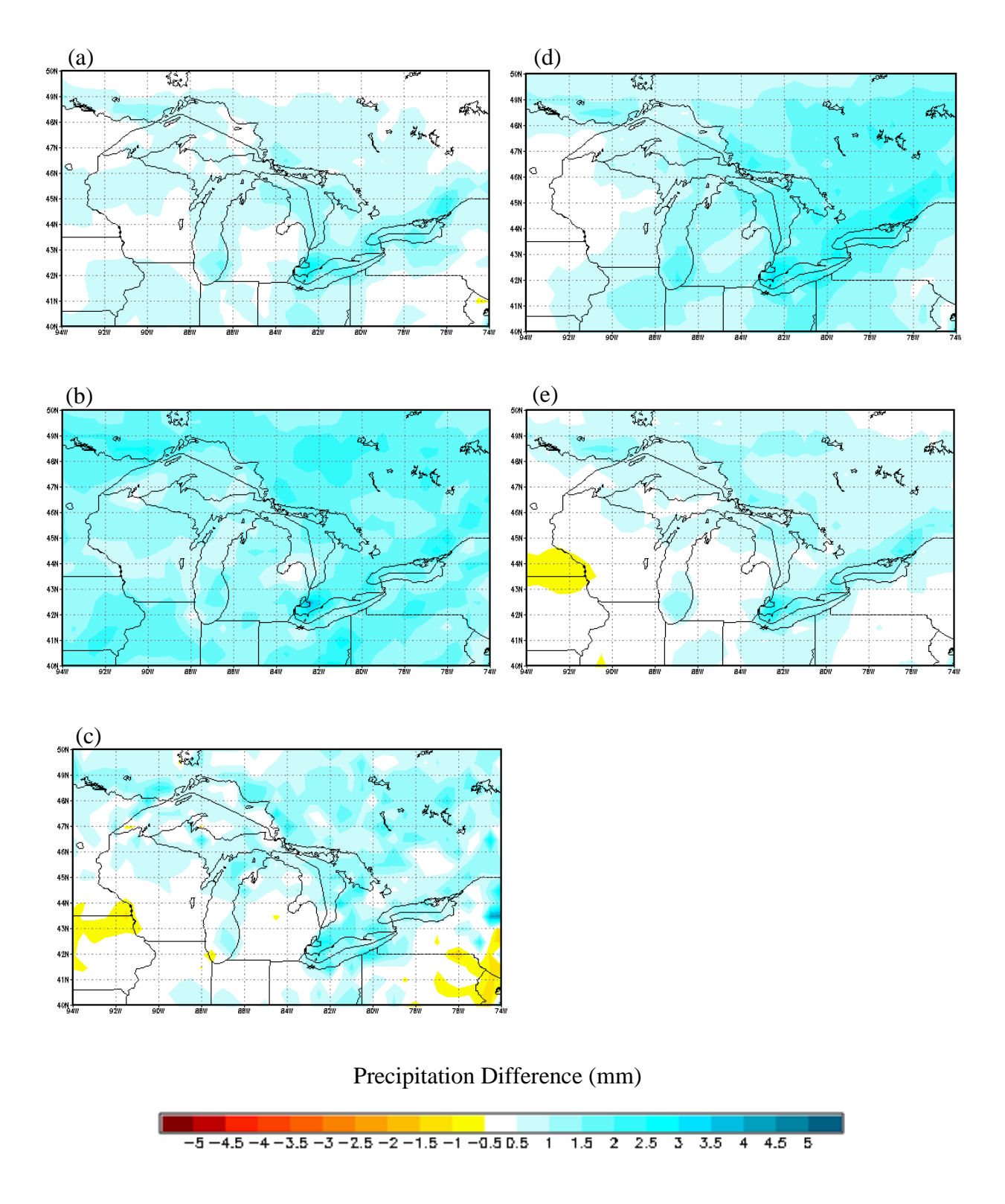


Fig. A.4.2.4. April daily accumulated precipitation differences between (a) CRCM, (b) ECP2, (c) HRM3, (d) MM5I, and (e) WRFG, and NARR for the GLR domain.

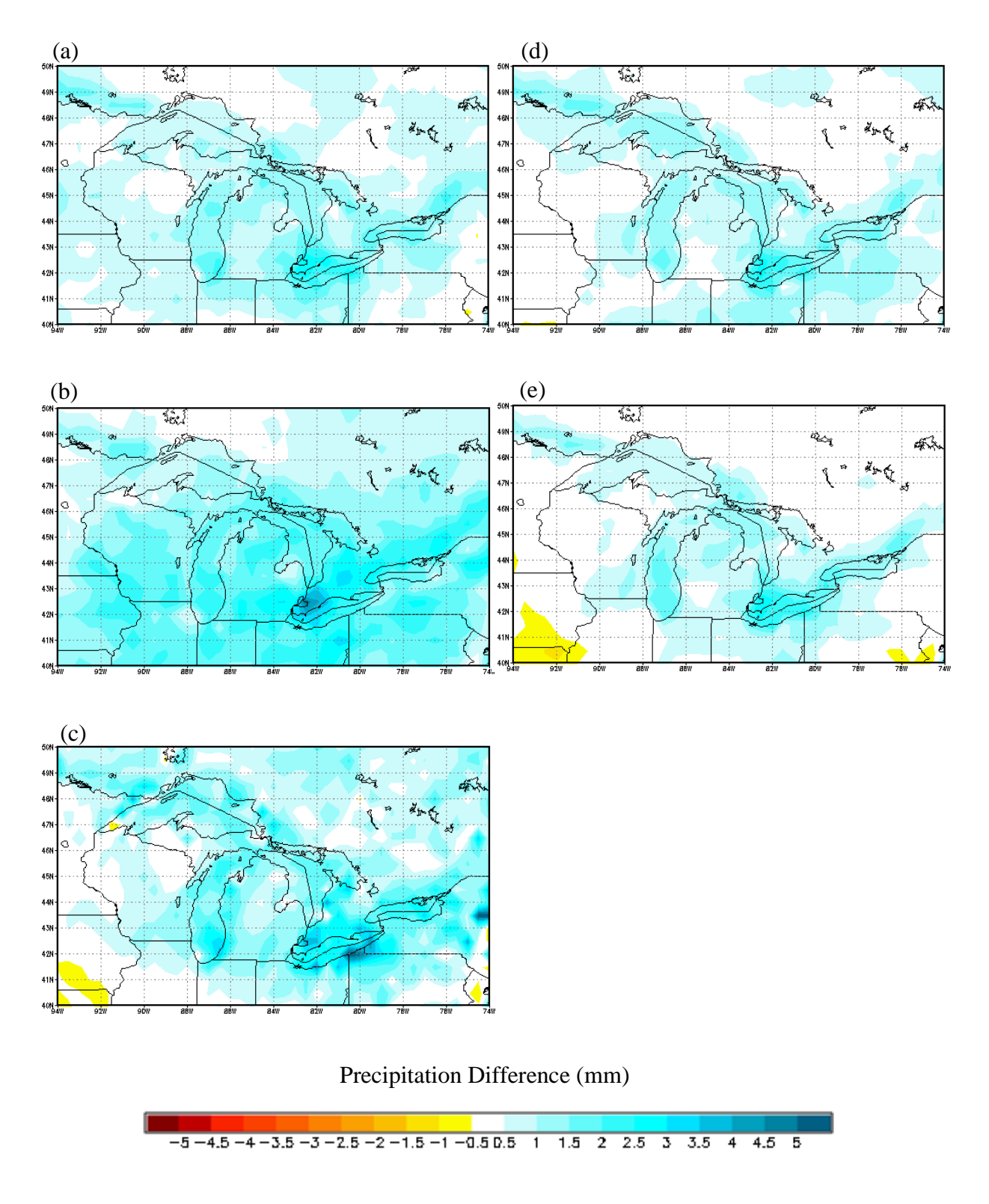


Fig. A.4.2.5. May daily accumulated precipitation differences between (a) CRCM, (b) ECP2, (c) HRM3, (d) MM5I, and (e) WRFG, and NARR for the GLR domain.

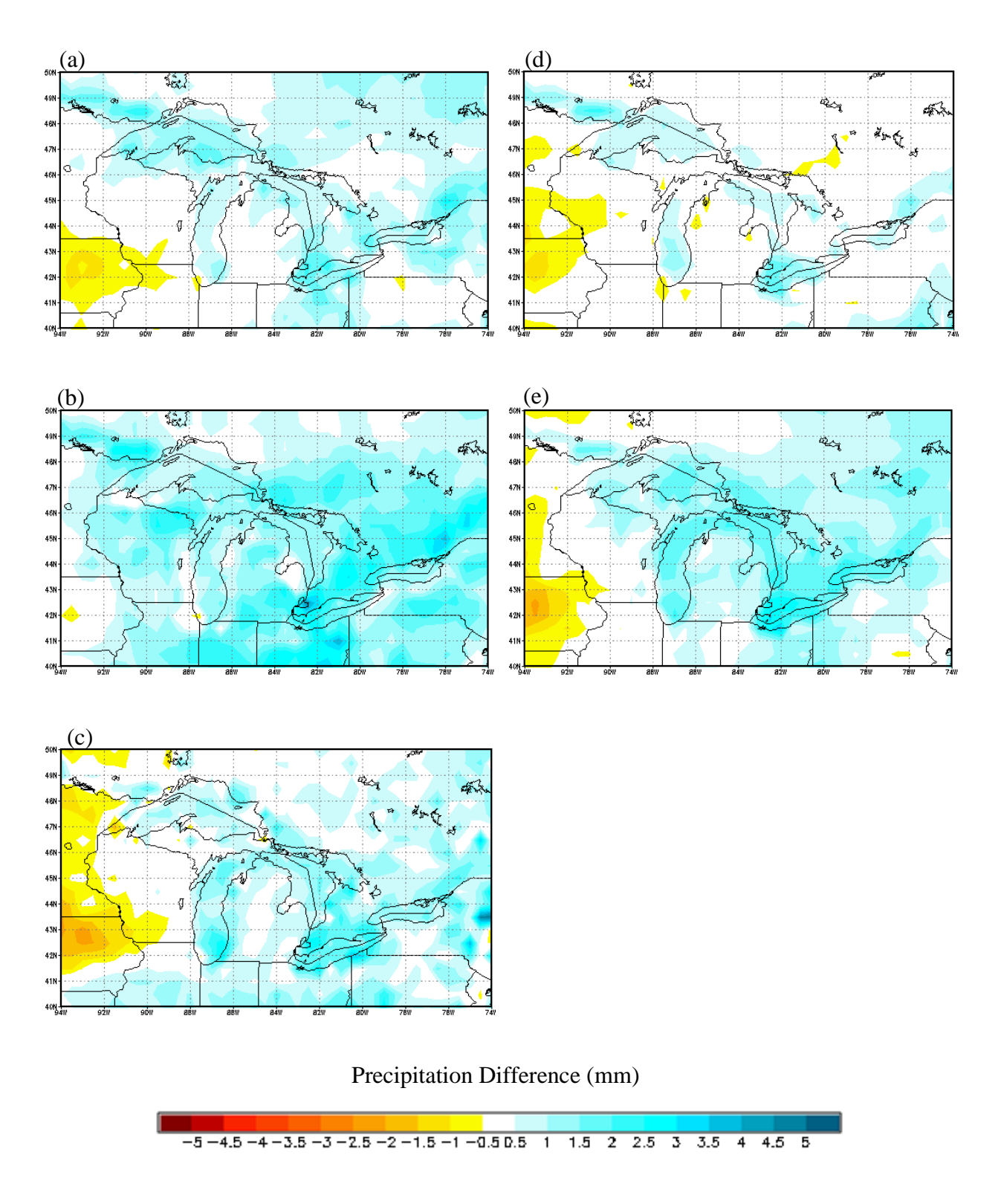


Fig. A.4.2.6. June daily accumulated precipitation differences between (a) CRCM, (b) ECP2, (c) HRM3, (d) MM5I, and (e) WRFG, and NARR for the GLR domain.

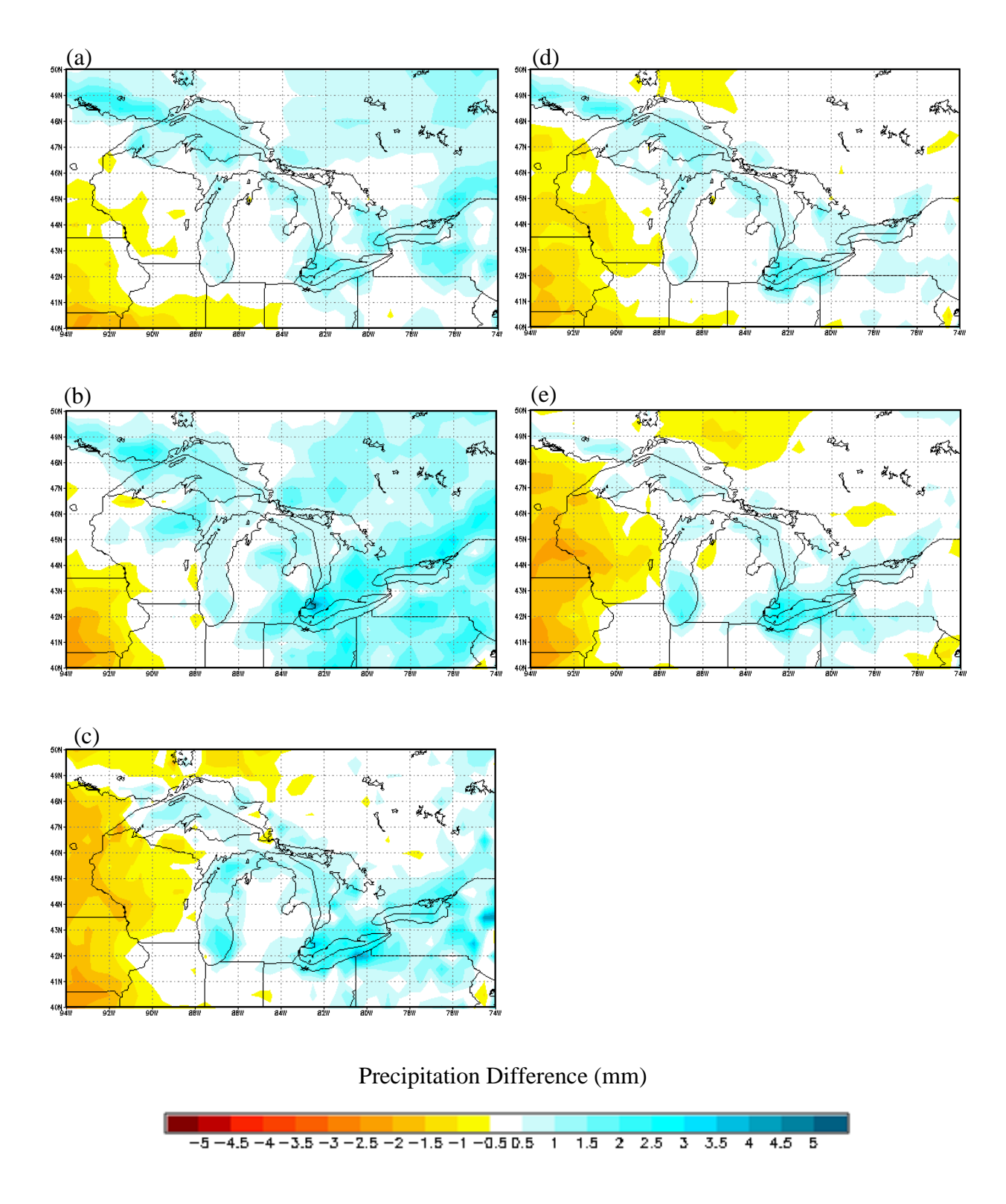


Fig. A.4.2.7. July daily accumulated precipitation differences between (a) CRCM, (b) ECP2, (c) HRM3, (d) MM5I, and (e) WRFG, and NARR for the GLR domain.

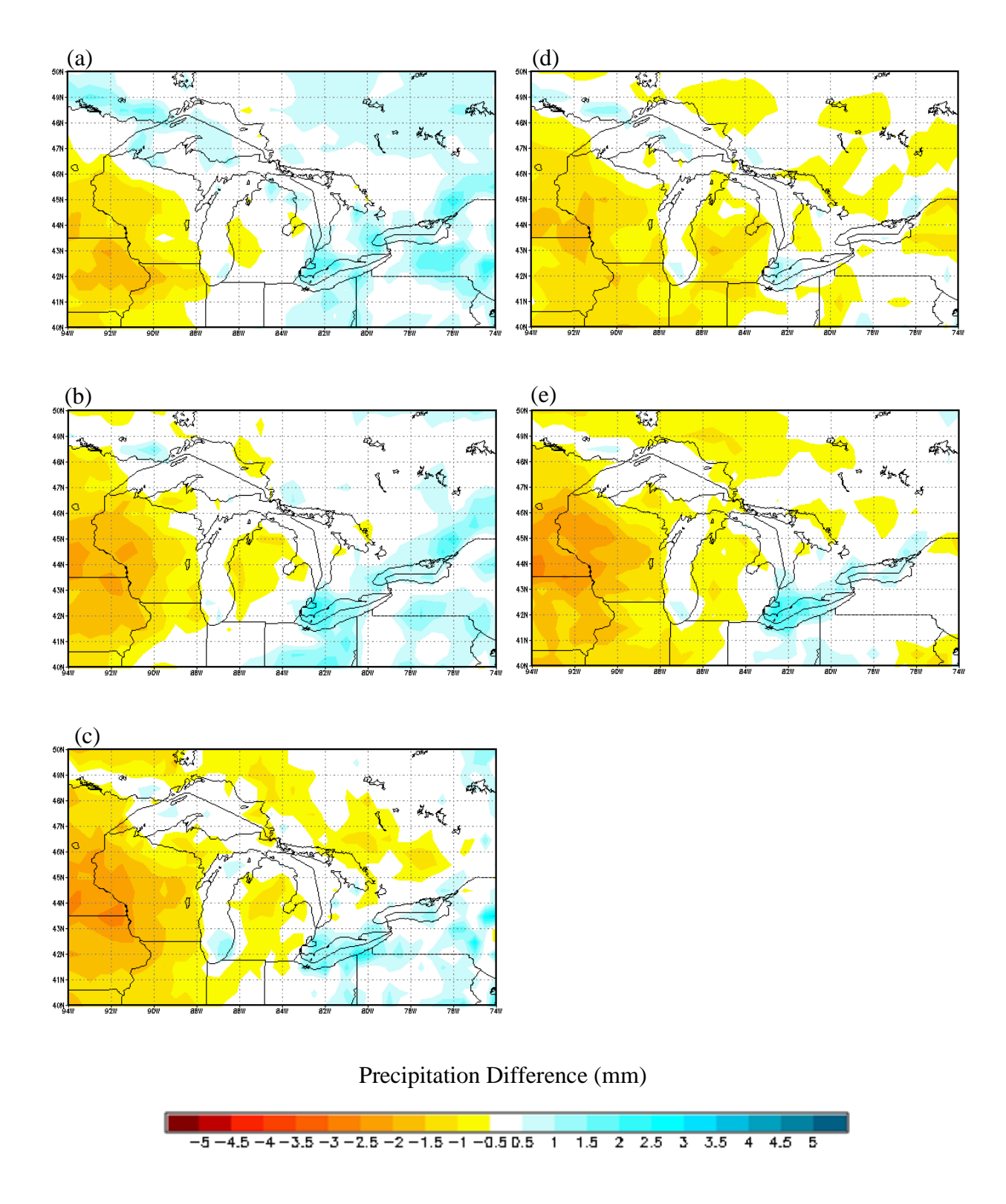


Fig. A.4.2.8. August daily accumulated precipitation differences between (a) CRCM, (b) ECP2, (c) HRM3, (d) MM5I, and (e) WRFG, and NARR for the GLR domain.

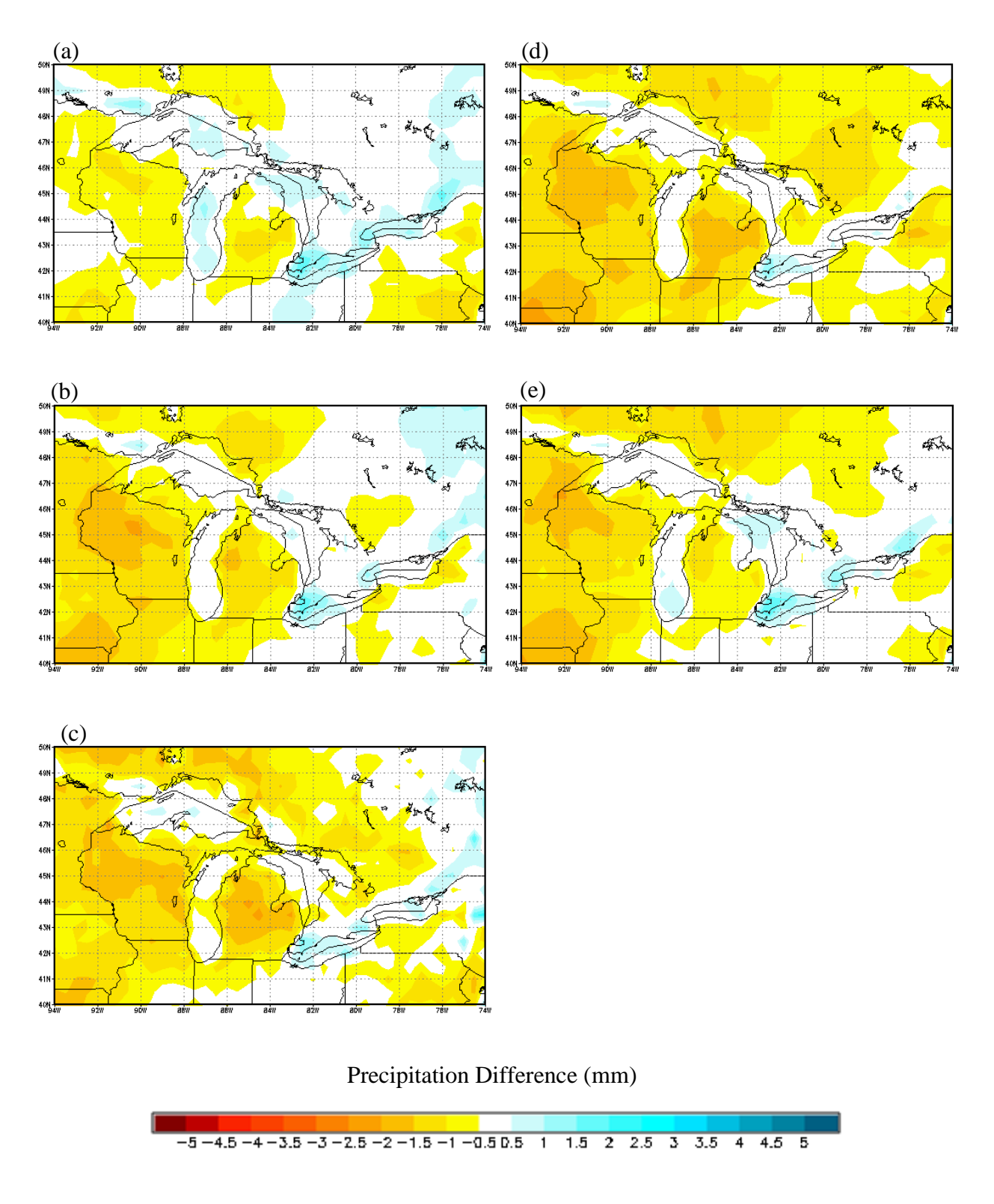


Fig. A.4.2.9. September daily accumulated precipitation differences between (a) CRCM, (b) ECP2, (c) HRM3, (d) MM5I, and (e) WRFG, and NARR for the GLR domain.

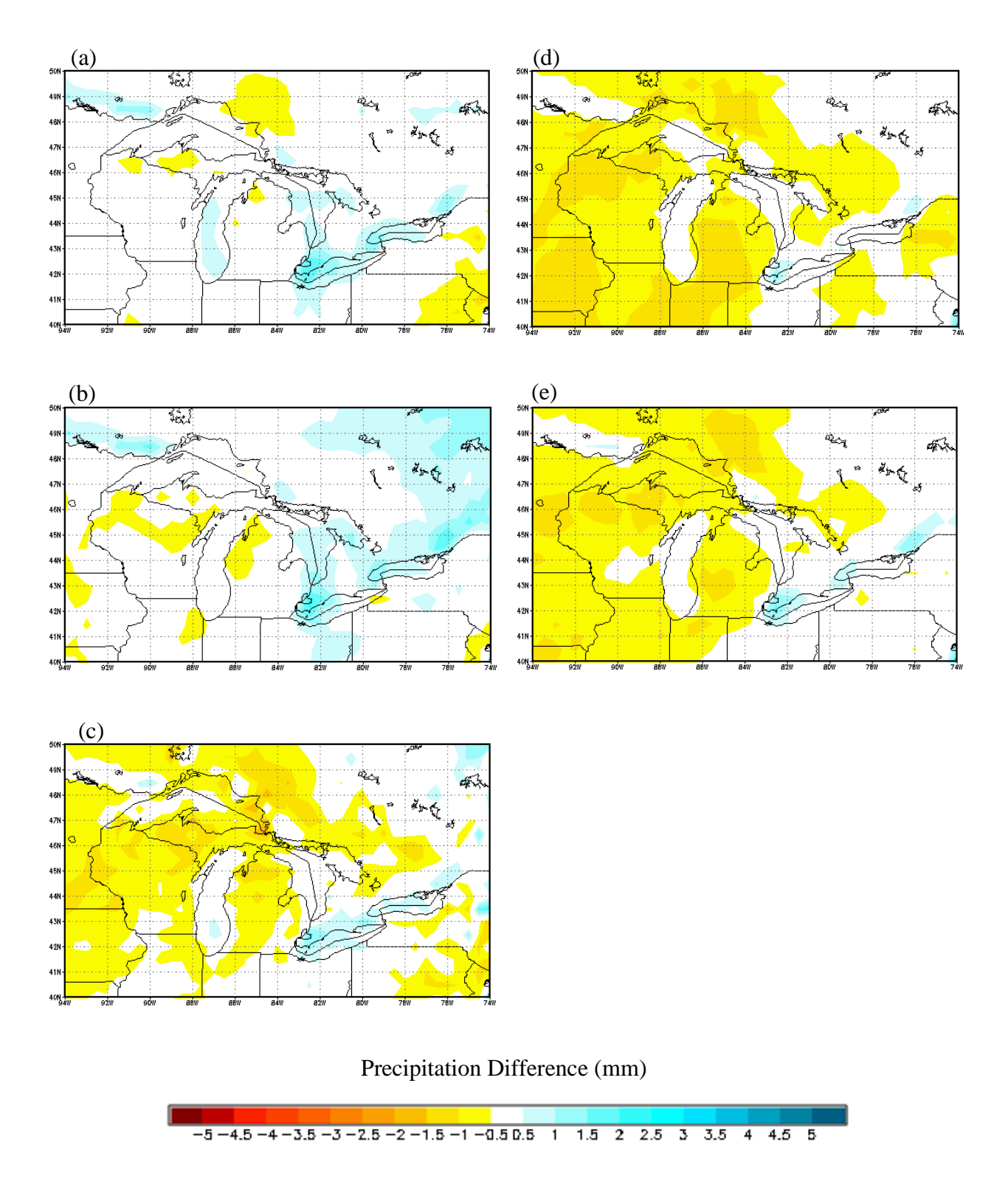


Fig. A.4.2.10. October daily accumulated precipitation differences between (a) CRCM, (b) ECP2, (c) HRM3, (d) MM5I, and (e) WRFG, and NARR for the GLR domain.

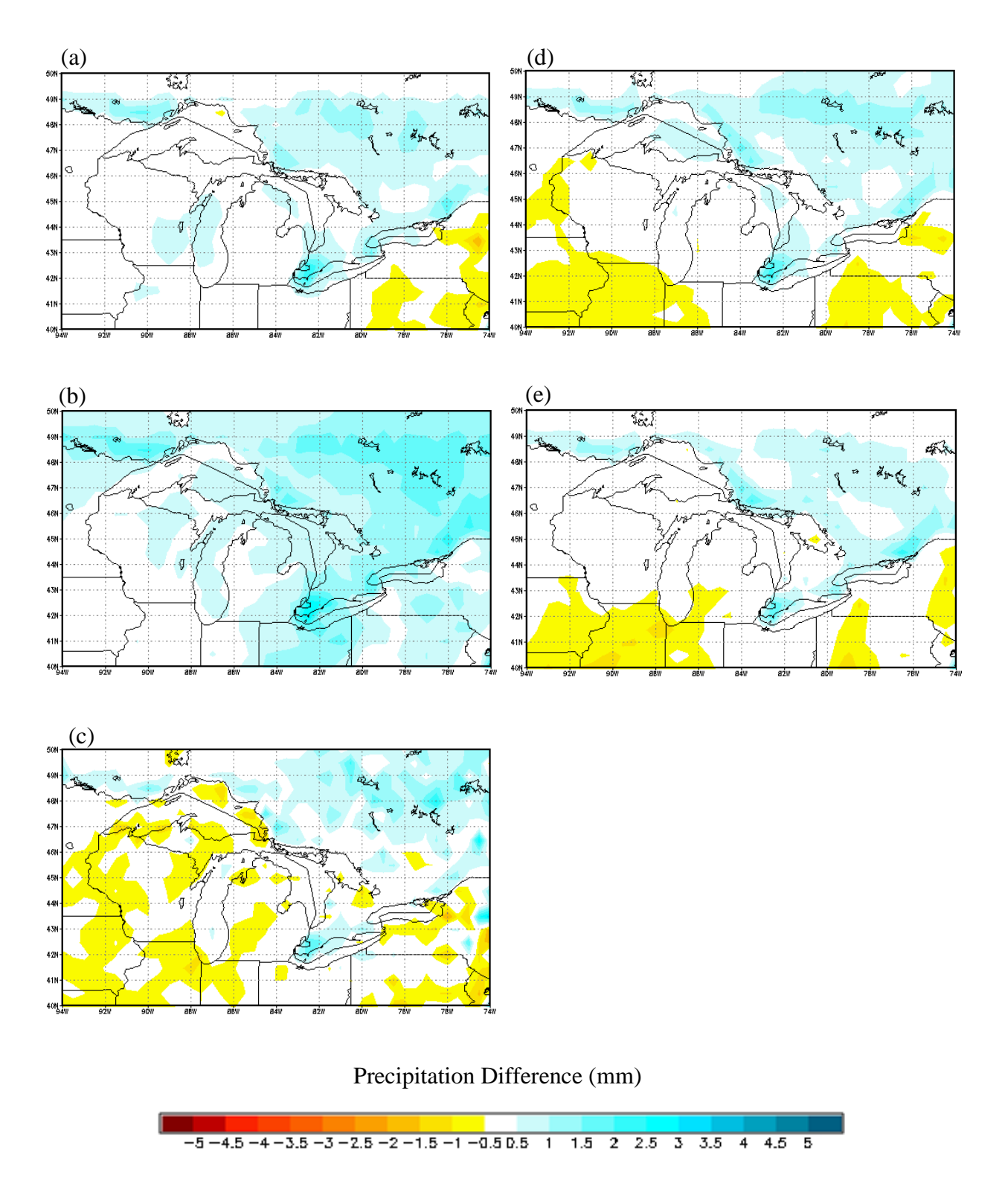


Fig. A.4.2.11. November daily accumulated precipitation differences between (a) CRCM, (b) ECP2, (c) HRM3, (d) MM5I, and (e) WRFG, and NARR for the GLR domain.

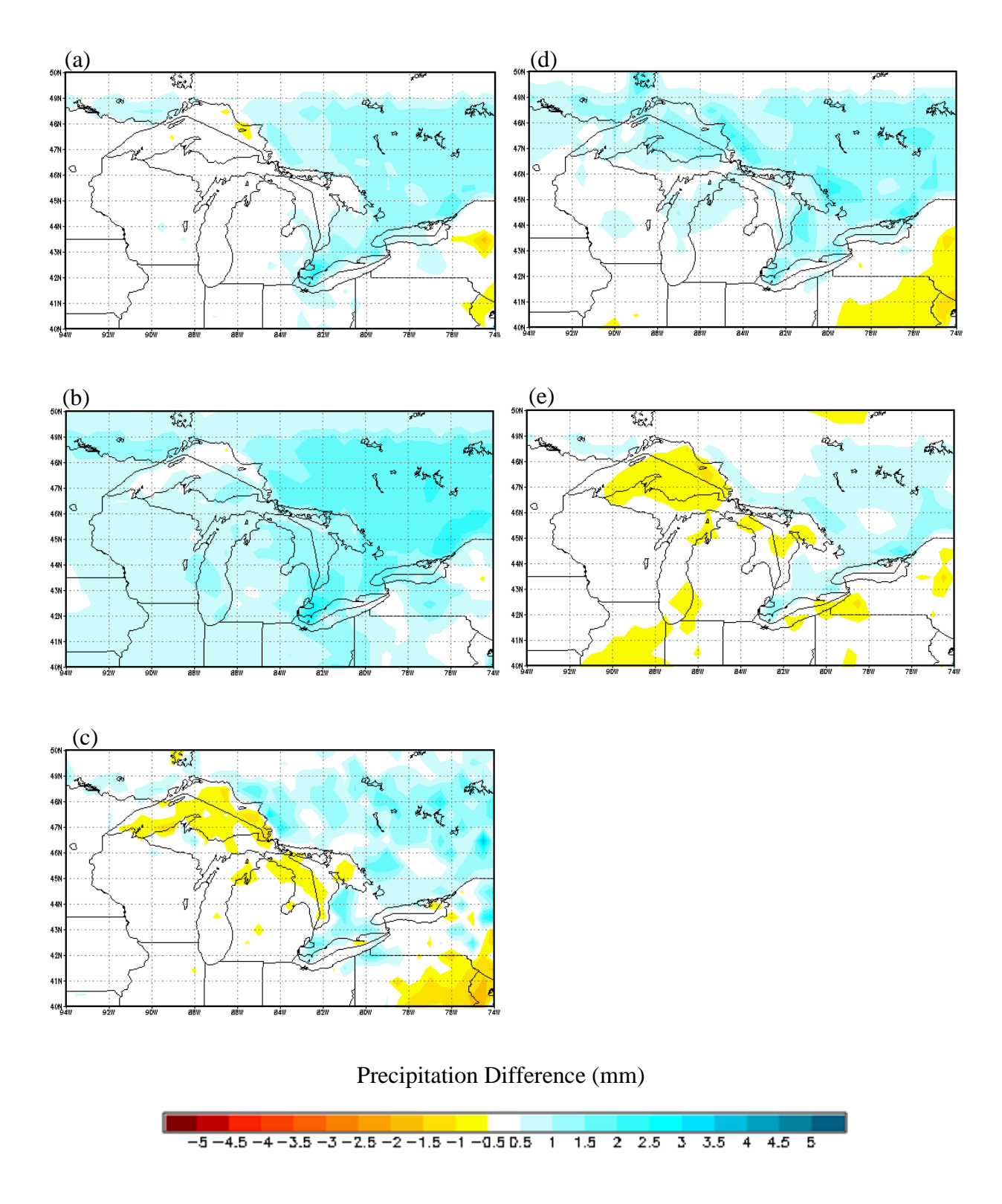


Fig. A.4.2.12. December daily accumulated precipitation differences between (a) CRCM, (b) ECP2, (c) HRM3, (d) MM5I, and (e) WRFG, and NARR for the GLR domain.

APPENDIX B ANNUAL CYCLES

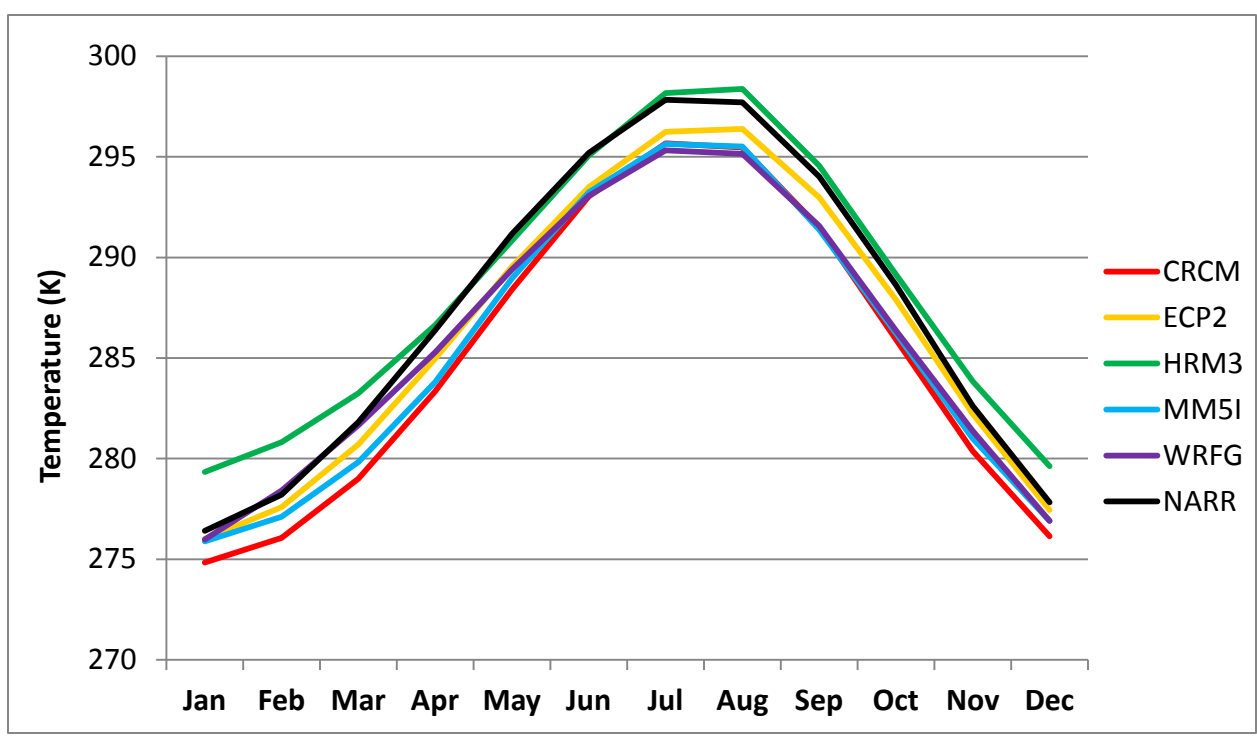


Fig. B.1. Monthly mean surface-air temperatures for the CONUS domain.

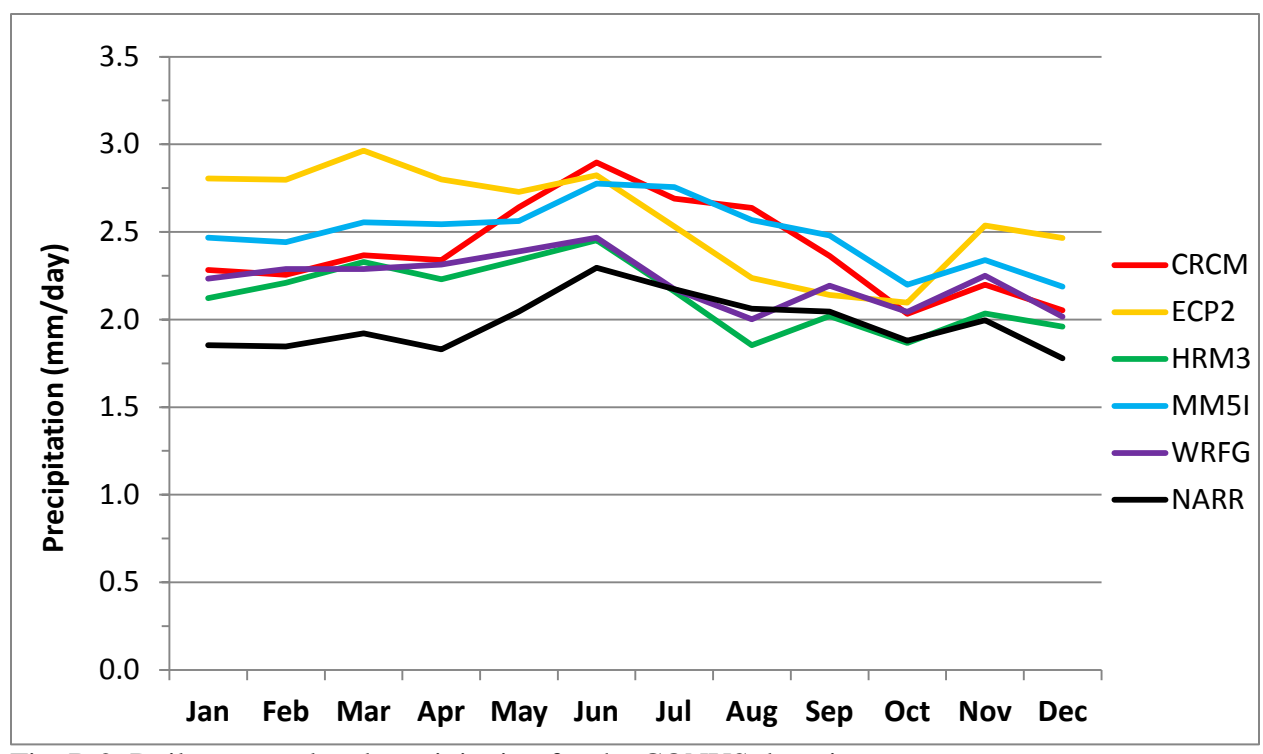


Fig. B.2. Daily accumulated precipitation for the CONUS domain.

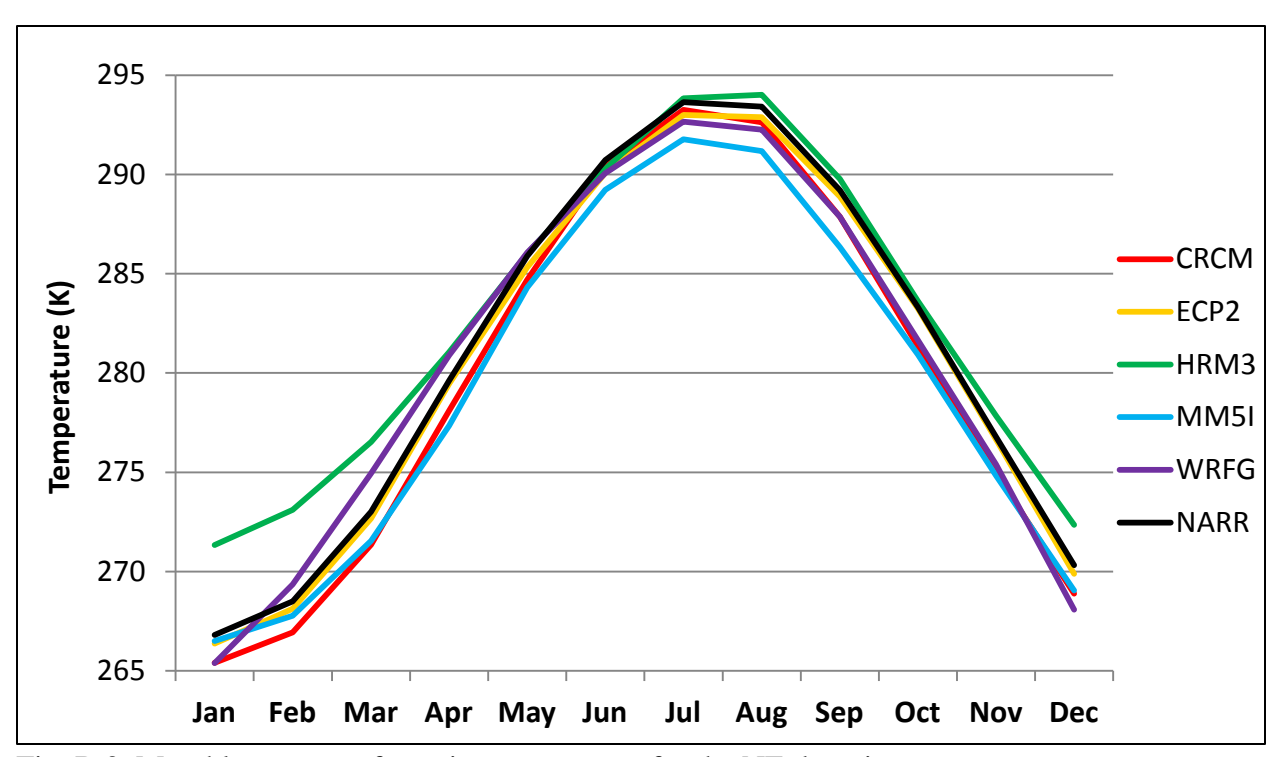


Fig. B.3. Monthly mean surface-air temperatures for the NE domain.

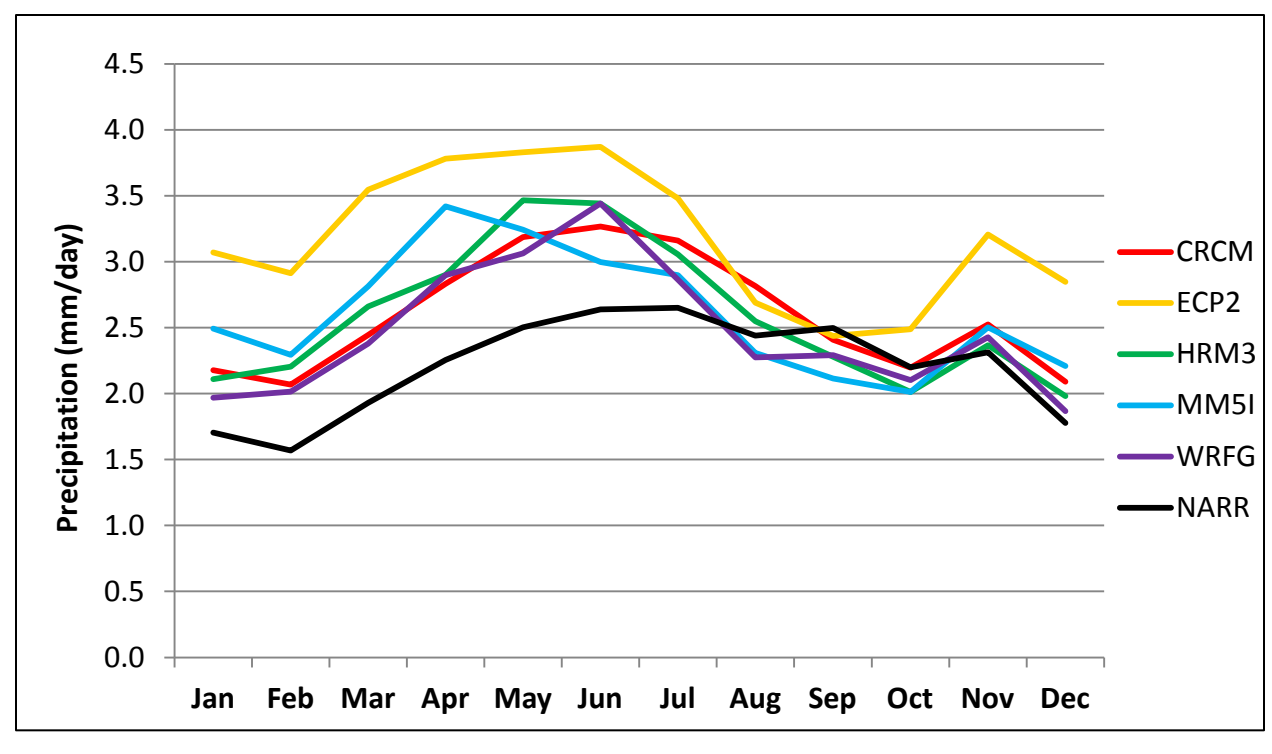


Fig. B.4. Daily accumulated precipitation for the NE domain.

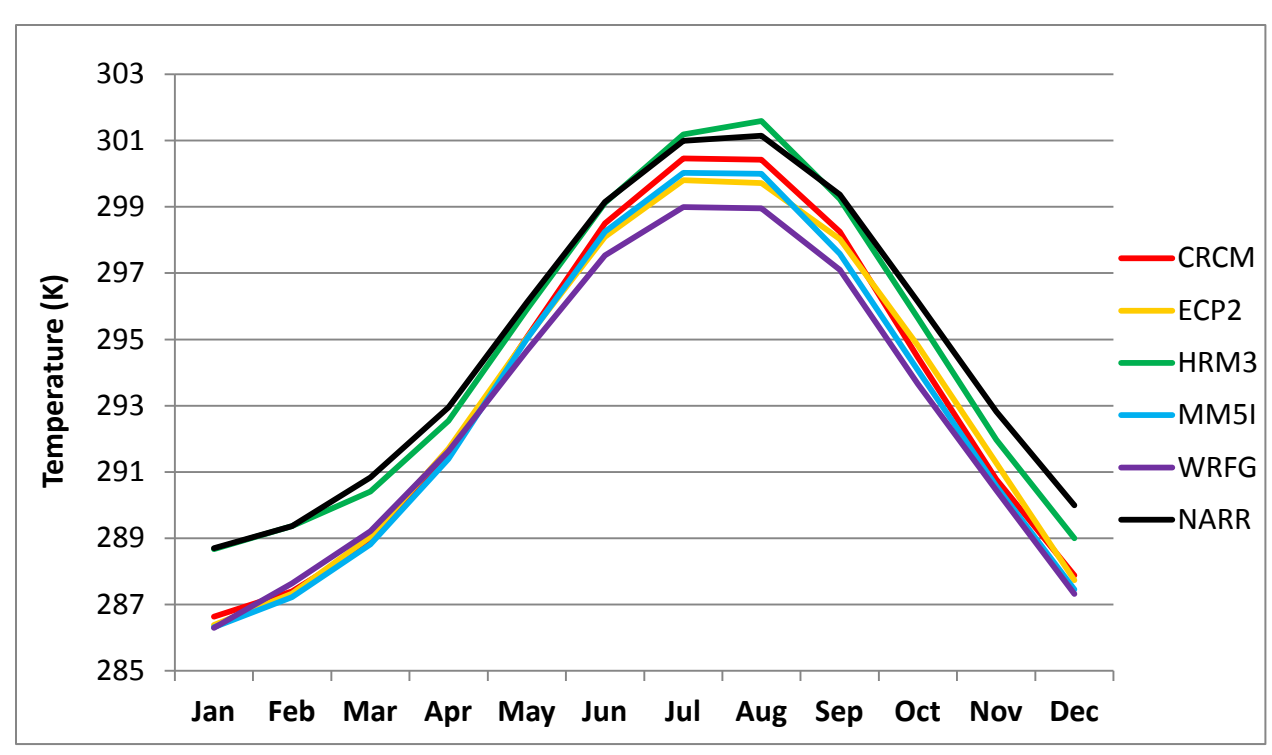


Fig. B.5. Monthly mean surface-air temperatures for the SE domain.

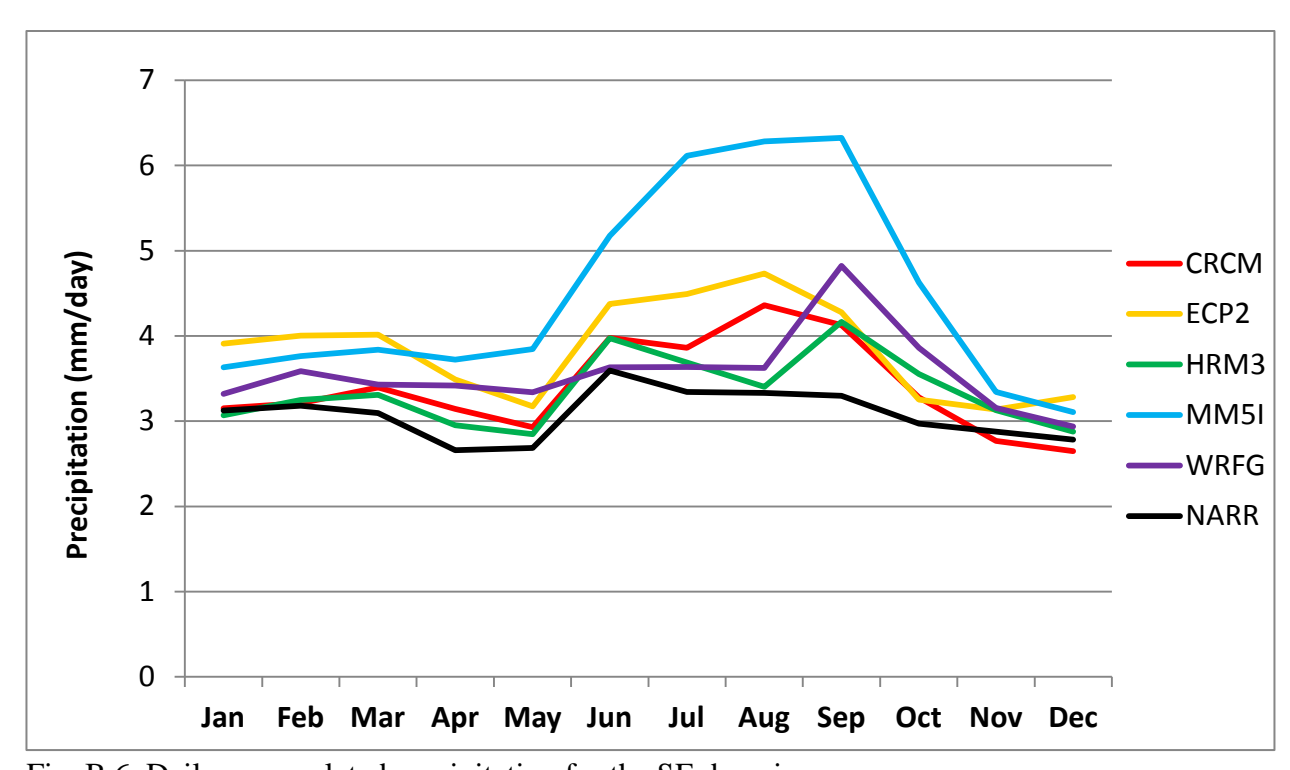


Fig. B.6. Daily accumulated precipitation for the SE domain.

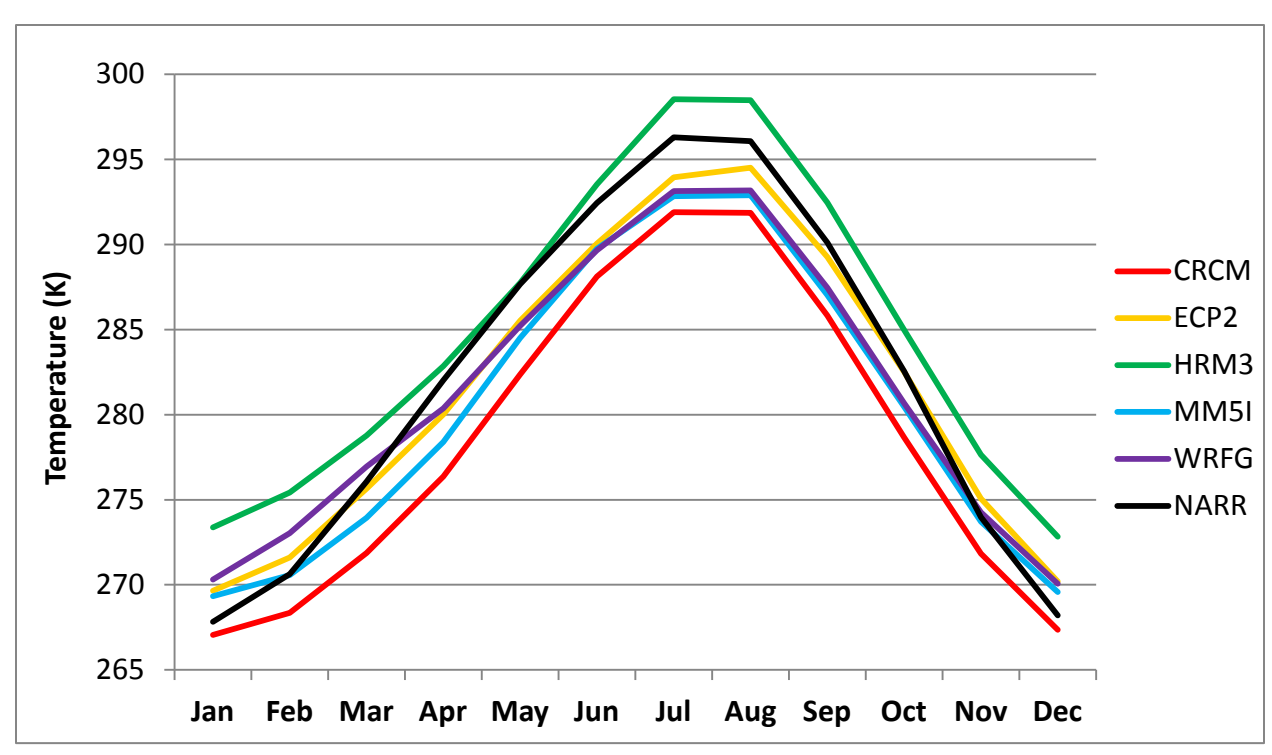


Fig. B.7. Monthly mean surface-air temperatures for the NW domain.

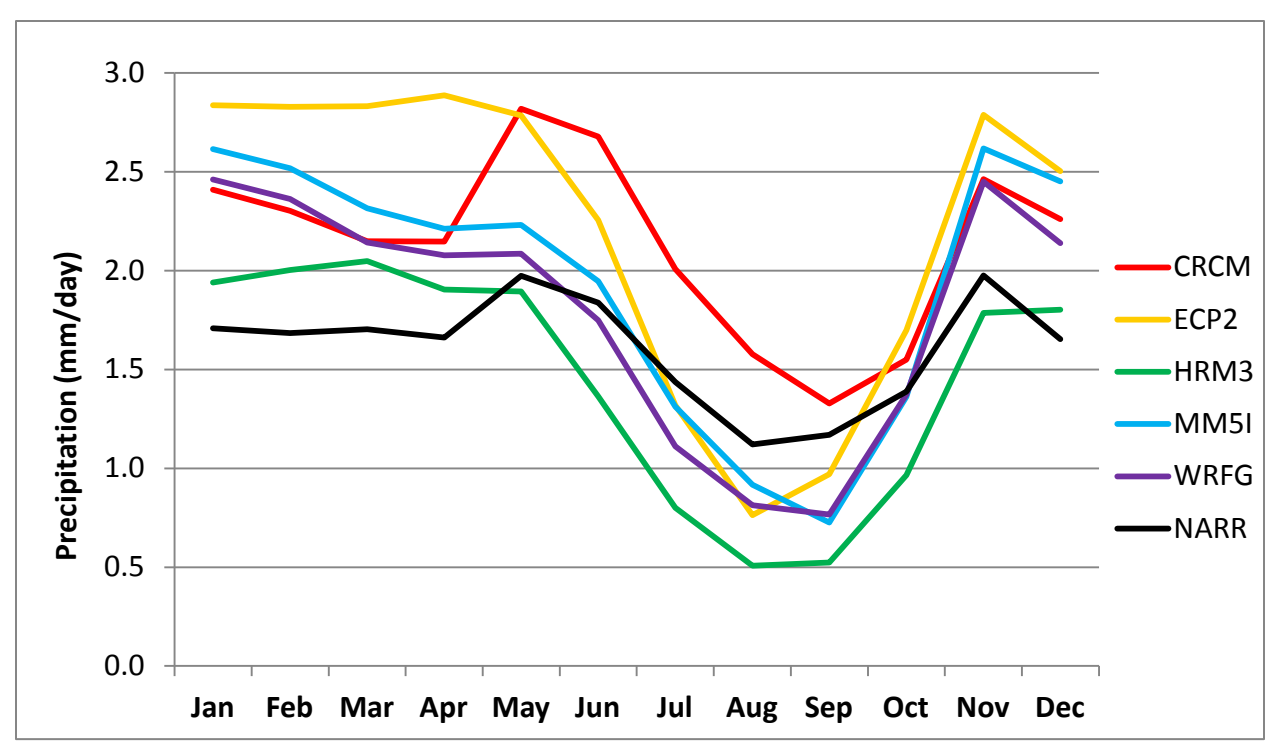


Fig. B.8. Daily accumulated precipitation for the NW domain.

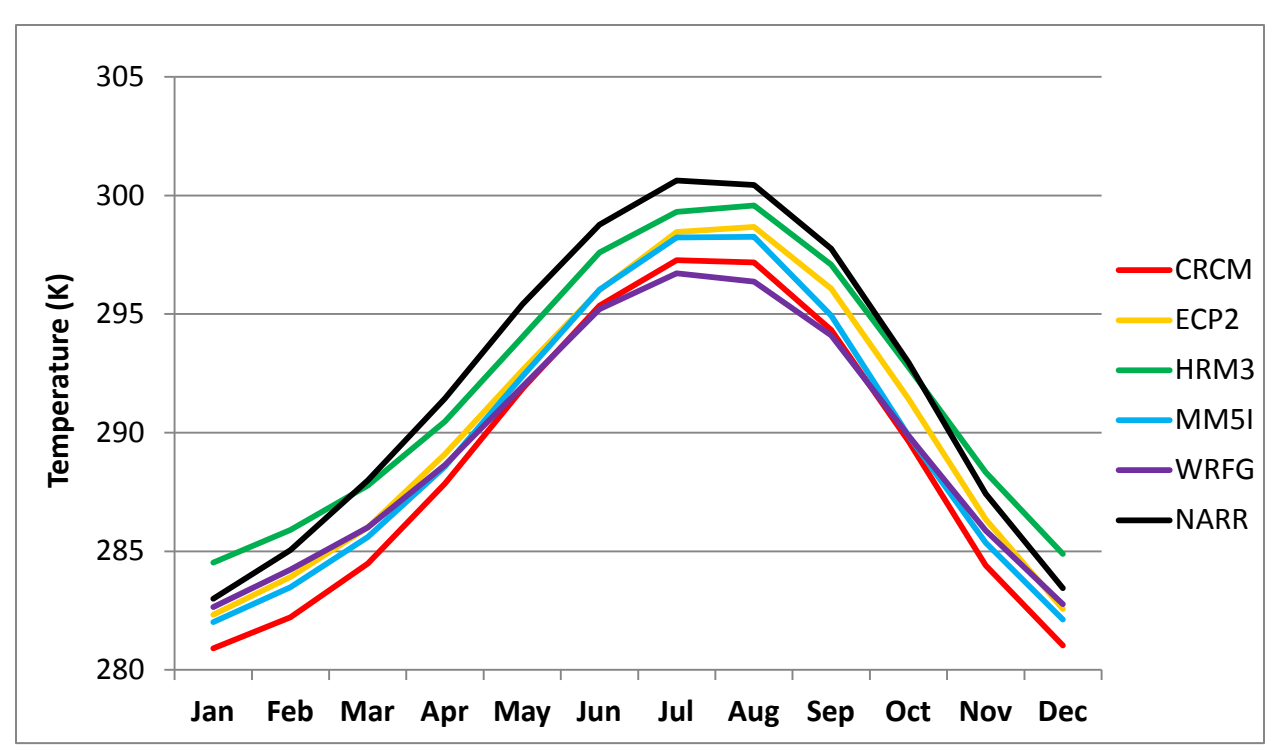


Fig. B.9. Monthly mean surface-air temperatures for the SW domain.

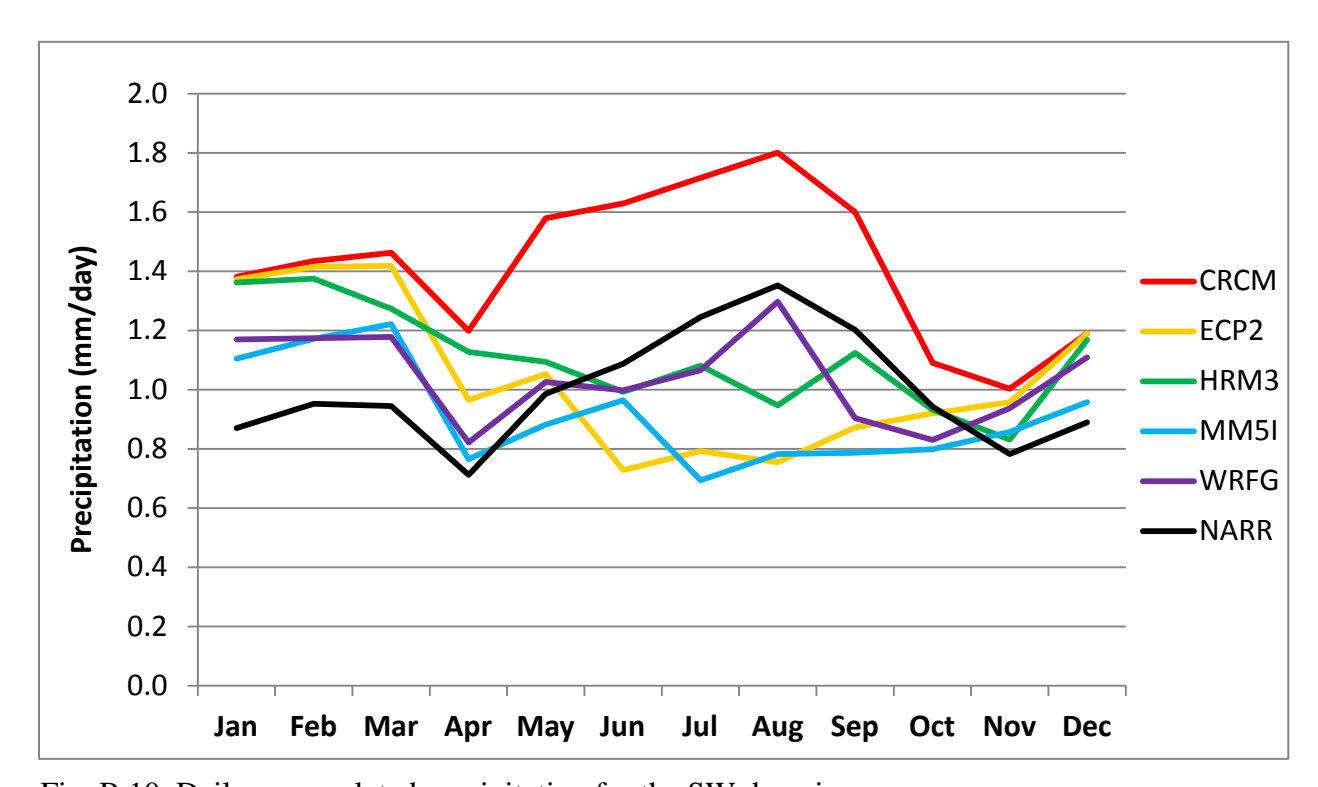


Fig. B.10. Daily accumulated precipitation for the SW domain.

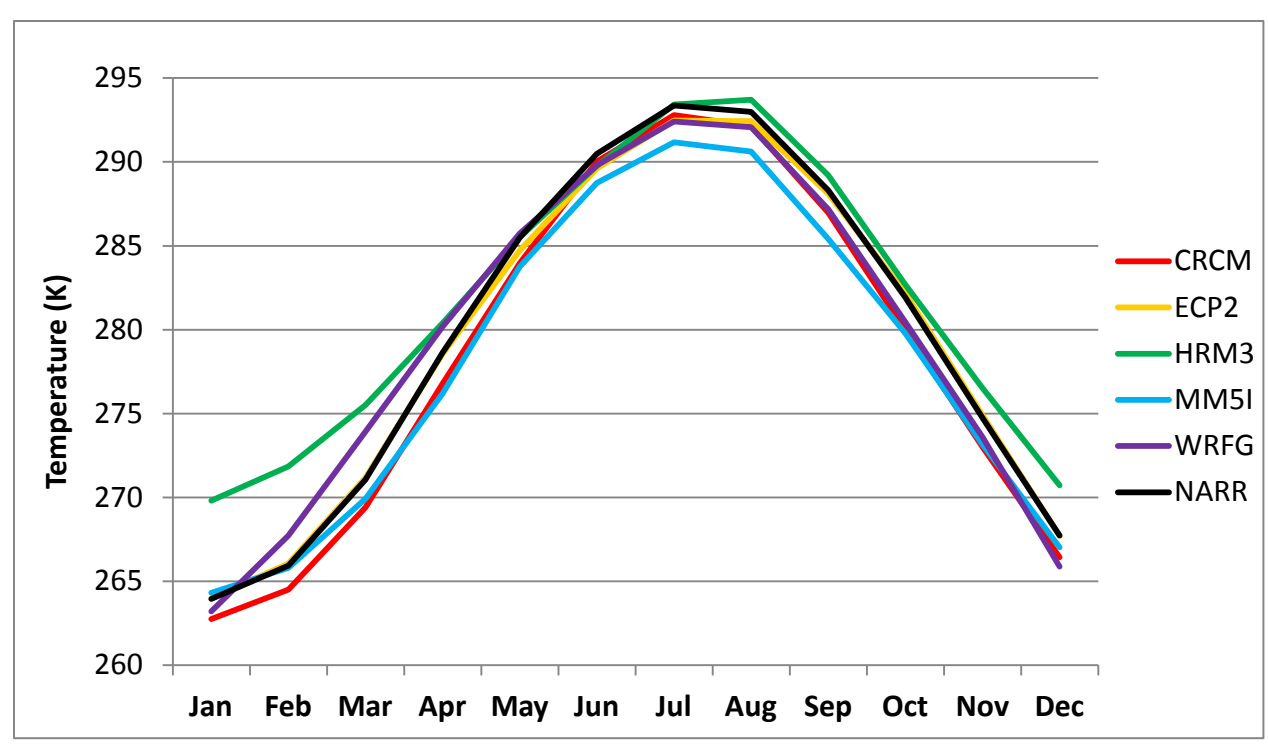


Fig. B.11. Monthly mean surface-air temperatures for the GLR domain.

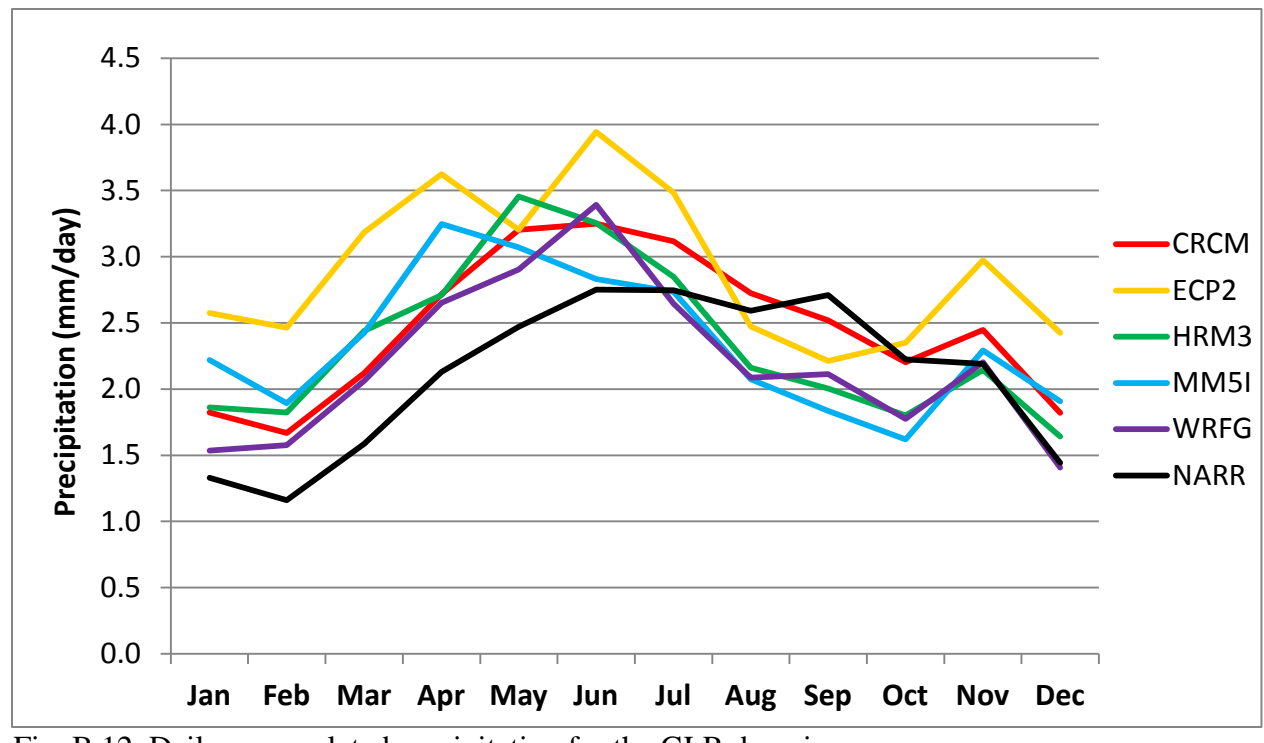


Fig. B.12. Daily accumulated precipitation for the GLR domain.

APPENDIX C STATISTICS

	CRCM	ECP2	HRM3	MM5I	WRFG
JAN	-1.57	-0.39	2.93	-0.53	-0.42
FEB	-2.16	-0.63	2.61	-1.11	0.20
MAR	-2.83	-1.12	1.43	-1.99	-0.16
APR	-3.05	-1.43	0.25	-2.58	-1.10
MAY	-2.78	-1.63	-0.33	-2.22	-1.78
JUN	-2.16	-1.70	-0.13	-1.95	-2.13
JUL	-2.16	-1.58	0.34	-2.18	-2.50
AUG	-2.24	-1.31	0.67	-2.19	-2.56
SEP	-2.54	-1.04	0.54	-2.64	-2.46
OCT	-2.71	-0.73	0.52	-2.40	-2.27
NOV	-2.25	-0.40	1.21	-1.63	-1.25
DEC	-1.70	-0.38	1.80	-0.93	-0.93
MAM	-2.88	-1.39	0.45	-2.26	-1.01
JJA	-2.19	-1.53	0.29	-2.11	-2.40
SON	-2.50	-0.72	0.76	-2.22	-1.99
DJF	-1.81	-0.47	2.44	-0.86	-0.38
ANN	-2.34	-1.03	0.99	-1.86	-1.45

Table C.1. Monthly mean surface-air temperature bias for the CONUS domain.

	CRCM	ECP2	HRM3	MM5I	WRFG
JAN	1.94	1.99	3.98	1.87	2.57
FEB	2.28	1.75	3.51	1.77	2.41
MAR	2.93	1.69	2.48	2.21	2.32
APR	3.26	1.81	1.57	2.80	2.08
MAY	3.09	2.04	1.30	2.54	2.18
JUN	2.56	2.13	1.43	2.29	2.43
JUL	2.60	2.04	1.78	2.47	2.75
AUG	2.51	1.79	1.95	2.41	2.78
SEP	2.66	1.50	1.67	2.76	2.58
OCT	2.76	1.42	1.66	2.51	2.36
NOV	2.31	1.64	2.33	1.89	1.81
DEC	2.03	2.07	3.14	1.99	2.51
MAM	3.09	1.85	1.78	2.52	2.19
JJA	2.55	1.98	1.72	2.39	2.65
SON	2.58	1.52	1.89	2.39	2.25
DJF	2.08	1.94	3.54	1.87	2.50
ANN	2.58	1.82	2.23	2.29	2.40

Table C.2. MAE for monthly mean surface-air temperatures for the CONUS domain.

	CRCM	ECP2	HRM3	MM5I	WRFG
JAN	2.42	2.56	4.79	2.40	3.38
FEB	2.74	2.19	4.33	2.23	3.07
MAR	3.51	2.15	3.13	2.63	2.78
APR	4.10	2.42	2.04	3.34	2.65
MAY	4.04	2.71	1.89	3.13	2.93
JUN	3.67	2.90	2.07	2.93	3.10
JUL	3.74	2.76	2.43	3.15	3.40
AUG	3.54	2.42	2.55	3.01	3.38
SEP	3.50	2.02	2.13	3.23	3.05
OCT	3.29	1.86	2.05	2.92	2.70
NOV	2.74	2.04	2.85	2.33	2.26
DEC	2.53	2.61	3.76	2.47	3.20
MAM	3.88	2.43	2.36	3.03	2.79
JJA	3.65	2.69	2.35	3.03	3.29
SON	3.18	1.97	2.34	2.83	2.67
DJF	2.56	2.46	4.29	2.36	3.22
ANN	3.32	2.39	2.83	2.81	2.99

Table C.3. RMSE for monthly mean surface-air temperatures for the CONUS domain.

	CRCM	ECP2	HRM3	MM5I	WRFG
JAN	0.99	0.98	0.98	0.99	0.96
FEB	0.99	0.99	0.97	0.99	0.97
MAR	0.97	0.98	0.97	0.98	0.97
APR	0.93	0.96	0.96	0.96	0.94
MAY	0.89	0.93	0.95	0.93	0.92
JUN	0.86	0.92	0.93	0.93	0.92
JUL	0.84	0.91	0.90	0.91	0.91
AUG	0.86	0.92	0.89	0.92	0.91
SEP	0.92	0.96	0.94	0.95	0.95
OCT	0.97	0.98	0.97	0.97	0.98
NOV	0.99	0.98	0.98	0.98	0.98
DEC	0.99	0.98	0.98	0.98	0.97
MAM	0.94	0.97	0.97	0.96	0.95
JJA	0.85	0.92	0.91	0.92	0.92
SON	0.97	0.98	0.97	0.98	0.98
DJF	0.99	0.99	0.98	0.99	0.97
ANN	0.99	0.98	0.98	0.99	0.96

Table C.4. Monthly mean surface-air temperature correlations between each RCM and NARR for the CONUS domain.

	CRCM	ECP2	HRM3	MM5I	WRFG
JAN	0.43	0.95	0.27	0.61	0.38
FEB	0.41	0.95	0.36	0.60	0.44
MAR	0.44	1.04	0.41	0.63	0.37
APR	0.51	0.97	0.40	0.71	0.48
MAY	0.59	0.68	0.29	0.52	0.34
JUN	0.60	0.53	0.16	0.48	0.17
JUL	0.52	0.36	-0.01	0.58	0.00
AUG	0.58	0.17	-0.21	0.51	-0.06
SEP	0.32	0.10	-0.02	0.44	0.15
OCT	0.15	0.22	-0.01	0.32	0.16
NOV	0.20	0.54	0.04	0.34	0.26
DEC	0.27	0.69	0.18	0.41	0.24
MAM	0.52	0.90	0.37	0.62	0.40
JJA	0.56	0.35	-0.02	0.52	0.04
SON	0.22	0.28	0.00	0.37	0.19
DJF	0.37	0.86	0.27	0.54	0.35
ANN	0.42	0.60	0.15	0.51	0.24

Table C.5. Daily accumulated precipitation bias for the CONUS domain.

	CRCM	ECP2	HRM3	MM5I	WRFG
JAN	0.65	1.05	0.76	0.88	0.70
FEB	0.64	1.06	0.76	0.92	0.74
MAR	0.59	1.11	0.78	0.85	0.63
APR	0.61	1.01	0.73	0.82	0.64
MAY	0.73	0.89	0.85	0.74	0.69
JUN	0.77	0.92	0.94	0.81	0.78
JUL	0.81	0.99	0.96	1.20	0.83
AUG	0.82	0.92	0.94	1.28	0.81
SEP	0.72	0.82	0.97	1.39	0.97
OCT	0.52	0.56	0.77	0.96	0.76
NOV	0.60	0.75	0.71	0.80	0.64
DEC	0.58	0.85	0.68	0.80	0.60
MAM	0.61	0.97	0.71	0.75	0.61
JJA	0.76	0.86	0.87	1.04	0.72
SON	0.56	0.60	0.75	0.94	0.71
DJF	0.61	0.96	0.69	0.85	0.65
ANN	0.53	0.72	0.60	0.76	0.59

Table C.6. MAE for daily accumulated precipitation for the CONUS domain.

	CRCM	ECP2	HRM3	MM5I	WRFG
JAN	0.94	0.92	1.48	1.31	0.60
FEB	0.91	0.94	1.39	1.36	0.54
MAR	0.79	0.91	1.20	1.11	0.56
APR	0.77	0.87	1.12	1.04	0.55
MAY	0.91	0.84	1.01	1.01	0.62
JUN	1.03	1.08	1.10	1.18	1.07
JUL	1.14	1.43	1.23	1.60	1.57
AUG	1.13	1.31	1.19	1.82	1.71
SEP	1.02	0.93	0.85	1.50	1.23
OCT	0.75	0.56	0.95	1.14	0.84
NOV	0.90	0.75	1.30	1.15	0.53
DEC	0.86	0.81	1.21	1.07	0.55
MAM	0.75	0.78	1.02	0.92	0.44
JJA	1.02	1.17	1.06	1.44	1.36
SON	0.77	0.60	0.90	1.08	0.73
DJF	0.88	0.86	1.32	1.21	0.51
ANN	0.71	0.68	0.89	0.99	0.61

Table C.7. RMSE for daily accumulated precipitation for the CONUS domain.

	CRCM	ECP2	HRM3	MM5I	WRFG
JAN	0.86	0.84	0.74	0.81	0.85
FEB	0.86	0.83	0.77	0.79	0.84
MAR	0.87	0.83	0.71	0.78	0.83
APR	0.87	0.84	0.68	0.81	0.83
MAY	0.83	0.77	0.61	0.80	0.72
JUN	0.81	0.77	0.66	0.79	0.71
JUL	0.73	0.75	0.65	0.66	0.67
AUG	0.79	0.78	0.66	0.70	0.68
SEP	0.77	0.77	0.72	0.69	0.74
OCT	0.81	0.81	0.74	0.72	0.77
NOV	0.84	0.83	0.75	0.78	0.84
DEC	0.84	0.82	0.76	0.78	0.84
MAM	0.87	0.82	0.68	0.81	0.81
JJA	0.79	0.79	0.68	0.73	0.72
SON	0.80	0.81	0.73	0.70	0.78
DJF	0.86	0.84	0.77	0.80	0.85
ANN	0.85	0.82	0.75	0.76	0.80

Table C.8. Daily accumulated precipitation correlations between each RCM and NARR for the CONUS domain.

	CRCM	ECP2	HRM3	MM5I	WRFG
JAN	-1.40	-0.44	4.53	-0.30	-1.42
FEB	-1.57	-0.37	4.61	-0.72	0.85
MAR	-1.66	-0.34	3.51	-1.46	1.94
APR	-1.51	-0.16	1.44	-2.27	1.27
MAY	-1.20	-0.56	0.13	-1.58	0.17
JUN	-0.30	-0.64	-0.44	-1.51	-0.66
JUL	-0.39	-0.65	0.19	-1.88	-0.99
AUG	-0.79	-0.52	0.61	-2.23	-1.16
SEP	-1.33	-0.32	0.55	-2.87	-1.34
OCT	-1.98	-0.07	0.31	-2.38	-1.67
NOV	-1.81	-0.14	1.06	-1.96	-1.40
DEC	-1.44	-0.44	2.03	-1.28	-2.25
MAM	-1.46	-0.36	1.69	-1.77	1.13
JJA	-0.49	-0.60	0.12	-1.87	-0.94
SON	-1.71	-0.18	0.64	-2.41	-1.47
DJF	-1.47	-0.42	3.72	-0.77	-0.94
ANN	-1.28	-0.39	1.54	-1.70	-0.55

Table C.9. Monthly mean surface-air temperature bias for the NE domain.

	CRCM	ECP2	HRM3	MM5I	WRFG
JAN	1.89	1.74	5.39	1.68	3.10
FEB	1.86	1.42	5.13	1.60	2.74
MAR	1.98	1.18	3.82	1.95	2.78
APR	2.23	1.15	1.81	2.86	1.76
MAY	-1.20	-0.56	0.13	-1.58	0.17
JUN	-0.30	-0.64	-0.44	-1.51	-0.66
JUL	-0.39	-0.65	0.19	-1.88	-0.99
AUG	-0.79	-0.52	0.61	-2.23	-1.16
SEP	-1.33	-0.32	0.55	-2.87	-1.34
OCT	-1.98	-0.07	0.31	-2.38	-1.67
NOV	-1.81	-0.14	1.06	-1.96	-1.40
DEC	-1.44	-0.44	2.03	-1.28	-2.25
MAM	-1.46	-0.36	1.69	-1.77	1.13
JJA	-0.49	-0.60	0.12	-1.87	-0.94
SON	-1.71	-0.18	0.64	-2.41	-1.47
DJF	-1.47	-0.42	3.72	-0.77	-0.94
ANN	-1.28	-0.39	1.54	-1.70	-0.55

Table C.10. MAE for monthly mean surface-air temperatures for the NE domain.

	CRCM	ECP2	HRM3	MM5I	WRFG
JAN	2.52	2.58	5.86	2.37	4.34
FEB	2.17	1.94	5.58	2.11	3.44
MAR	2.21	1.56	4.24	2.14	3.17
APR	2.56	1.67	2.33	3.14	2.38
MAY	2.70	2.19	2.10	2.83	2.04
JUN	2.13	2.21	2.24	2.70	2.14
JUL	1.98	1.98	2.28	2.82	2.16
AUG	1.72	1.48	2.55	2.83	2.04
SEP	1.89	1.13	1.87	3.22	1.77
OCT	2.26	1.23	1.57	2.66	1.95
NOV	2.22	1.78	2.39	2.41	2.36
DEC	2.48	2.54	3.79	2.44	4.25
MAM	2.28	1.55	2.38	2.56	2.11
JJA	1.85	1.82	2.17	2.72	2.02
SON	2.00	1.18	1.79	2.63	1.77
DJF	2.28	2.23	4.97	2.13	3.72
ANN	1.65	1.04	2.26	2.04	1.47

Table C.11. RMSE for monthly mean surface-air temperatures for the NE domain.

	CRCM	ECP2	HRM3	MM5I	WRFG
JAN	0.97	0.96	0.92	0.97	0.87
FEB	0.98	0.97	0.92	0.96	0.89
MAR	0.97	0.97	0.93	0.96	0.91
APR	0.89	0.93	0.92	0.89	0.91
MAY	0.82	0.87	0.87	0.83	0.88
JUN	0.87	0.88	0.87	0.86	0.88
JUL	0.87	0.88	0.87	0.84	0.87
AUG	0.91	0.91	0.88	0.86	0.88
SEP	0.95	0.95	0.90	0.92	0.94
OCT	0.97	0.96	0.93	0.96	0.97
NOV	0.97	0.95	0.94	0.97	0.94
DEC	0.96	0.96	0.93	0.97	0.88
MAM	0.92	0.94	0.93	0.91	0.92
JJA	0.88	0.89	0.88	0.85	0.88
SON	0.98	0.96	0.92	0.97	0.97
DJF	0.97	0.97	0.93	0.97	0.88
ANN	0.98	0.98	0.93	0.97	0.95

Table C.12. Monthly mean surface-air temperature correlations between each RCM and NARR for the NE domain.

	CRCM	ECP2	HRM3	MM5I	WRFG
JAN	0.47	1.37	0.40	0.79	0.26
FEB	0.50	1.34	0.64	0.73	0.45
MAR	0.51	1.61	0.73	0.88	0.45
APR	0.58	1.53	0.65	1.16	0.64
MAY	0.69	1.33	0.96	0.74	0.56
JUN	0.63	1.23	0.80	0.36	0.80
JUL	0.51	0.83	0.41	0.25	0.21
AUG	0.38	0.25	0.11	-0.13	-0.16
SEP	-0.09	-0.06	-0.22	-0.38	-0.21
OCT	0.00	0.29	-0.19	-0.19	-0.10
NOV	0.21	0.89	0.05	0.19	0.11
DEC	0.31	1.07	0.20	0.43	0.09
MAM	0.59	1.49	0.78	0.93	0.55
JJA	0.51	0.77	0.44	0.16	0.28
SON	0.04	0.37	-0.12	-0.13	-0.06
DJF	0.43	1.26	0.41	0.65	0.27
ANN	0.39	0.97	0.38	0.40	0.26

Table C.13. Daily accumulated precipitation bias for the NE domain.

	CRCM	ECP2	HRM3	MM5I	WRFG
JAN	0.54	1.37	0.75	0.87	0.49
FEB	0.52	1.34	0.75	0.83	0.56
MAR	0.56	1.61	0.92	0.95	0.60
APR	0.62	1.53	0.87	1.17	0.74
MAY	0.73	1.33	1.12	0.79	0.73
JUN	0.76	1.29	1.08	0.64	1.05
JUL	0.84	1.12	1.07	0.77	0.89
AUG	0.80	0.87	1.07	0.92	0.88
SEP	0.58	0.86	0.98	1.05	0.85
OCT	0.40	0.58	0.72	0.78	0.65
NOV	0.48	0.92	0.71	0.65	0.57
DEC	0.45	1.07	0.65	0.71	0.51
MAM	0.62	1.49	0.92	0.95	0.66
JJA	0.77	0.99	0.97	0.71	0.82
SON	0.43	0.65	0.75	0.71	0.63
DJF	0.48	1.26	0.68	0.78	0.47
ANN	0.46	0.98	0.68	0.60	0.55

Table C.14. MAE for daily accumulated precipitation for the NE domain.

	CRCM	ECP2	HRM3	MM5I	WRFG
JAN	0.68	1.01	1.33	0.94	0.75
FEB	0.65	0.92	1.01	0.84	0.48
MAR	0.71	1.15	1.15	0.83	0.55
APR	0.75	1.05	1.17	0.91	0.65
MAY	0.88	0.85	1.03	0.83	0.45
JUN	0.94	0.96	1.03	0.98	0.80
JUL	1.02	0.84	1.03	0.87	0.54
AUG	0.96	0.66	0.77	0.94	0.69
SEP	0.69	0.70	0.62	0.70	0.47
OCT	0.51	0.56	0.79	0.68	0.36
NOV	0.62	0.83	1.05	0.66	0.29
DEC	0.62	0.91	1.11	0.73	0.59
MAM	0.73	0.96	1.01	0.68	0.44
JJA	0.93	0.70	0.88	0.85	0.54
SON	0.54	0.59	0.74	0.59	0.26
DJF	0.63	0.93	1.13	0.81	0.58
ANN	0.61	0.68	0.84	0.61	0.26

Table C.15. RMSE for daily accumulated precipitation for the NE domain.

	CRCM	ECP2	HRM3	MM5I	WRFG
JAN	0.84	0.80	0.53	0.67	0.80
FEB	0.89	0.85	0.70	0.71	0.78
MAR	0.81	0.74	0.49	0.57	0.70
APR	0.78	0.73	0.32	0.60	0.54
MAY	0.77	0.72	0.27	0.67	0.43
JUN	0.62	0.57	0.35	0.41	0.15
JUL	0.40	0.31	0.01	0.15	-0.05
AUG	0.20	0.04	-0.21	-0.15	-0.17
SEP	0.36	-0.05	-0.16	-0.39	-0.23
OCT	0.30	0.32	0.08	0.00	0.10
NOV	0.50	0.51	0.32	0.32	0.36
DEC	0.77	0.74	0.55	0.58	0.73
MAM	0.79	0.75	0.36	0.59	0.55
JJA	0.42	0.34	0.04	0.09	-0.05
SON	0.28	0.19	0.07	-0.08	0.04
DJF	0.85	0.81	0.62	0.66	0.78
ANN	0.54	0.44	0.31	0.24	0.29

Table C.16. Daily accumulated precipitation correlations between each RCM and NARR for the NE domain.

	CRCM	ECP2	HRM3	MM5I	WRFG
JAN	-2.07	-2.32	-0.03	-2.39	-2.41
FEB	-1.96	-2.03	0.01	-2.14	-1.73
MAR	-1.97	-1.79	-0.43	-2.02	-1.62
APR	-1.44	-1.25	-0.40	-1.56	-1.33
MAY	-1.05	-1.07	-0.21	-1.10	-1.46
JUN	-0.64	-1.05	-0.03	-0.90	-1.61
JUL	-0.53	-1.19	0.19	-0.96	-2.01
AUG	-0.72	-1.42	0.45	-1.14	-2.19
SEP	-1.12	-1.34	-0.13	-1.78	-2.26
OCT	-1.68	-1.33	-0.49	-2.07	-2.48
NOV	-2.05	-1.56	-0.85	-2.25	-2.38
DEC	-2.11	-2.26	-0.99	-2.54	-2.67
MAM	-1.49	-1.37	-0.35	-1.56	-1.47
JJA	-0.63	-1.22	0.20	-1.00	-1.93
SON	-1.62	-1.41	-0.49	-2.03	-2.38
DJF	-2.05	-2.20	-0.34	-2.36	-2.27
ANN	-1.45	-1.55	-0.24	-1.74	-2.01

Table C.17. Monthly mean surface-air temperature bias for the SE domain.

	CRCM	ECP2	HRM3	MM5I	WRFG
JAN	2.09	2.38	2.66	2.42	2.66
FEB	1.98	2.08	2.19	2.16	2.22
MAR	1.98	1.82	1.52	2.03	1.86
APR	1.46	1.30	1.01	1.57	1.40
MAY	1.08	1.16	0.67	1.12	1.48
JUN	0.73	1.13	0.55	0.91	1.63
JUL	0.73	1.27	0.82	0.98	2.01
AUG	0.82	1.48	1.26	1.15	2.19
SEP	1.13	1.41	1.10	1.78	2.26
OCT	1.69	1.49	1.28	2.09	2.49
NOV	2.07	1.72	1.64	2.28	2.42
DEC	2.14	2.35	2.25	2.58	2.77
MAM	1.50	1.41	1.04	1.57	1.54
JJA	0.74	1.29	0.84	1.01	1.94
SON	1.63	1.51	1.33	2.05	2.39
DJF	2.07	2.26	2.36	2.39	2.50
ANN	1.46	1.59	1.36	1.74	2.03

Table C.18. MAE for monthly mean surface-air temperatures for the SE domain.

	CRCM	ECP2	HRM3	MM5I	WRFG
JAN	2.38	2.96	2.94	2.78	3.28
FEB	2.17	2.52	2.47	2.44	2.66
MAR	2.13	2.12	1.75	2.24	2.18
APR	1.61	1.54	1.21	1.76	1.62
MAY	1.29	1.32	0.84	1.34	1.63
JUN	1.00	1.30	0.79	1.25	1.75
JUL	0.93	1.47	1.16	1.32	2.13
AUG	0.99	1.63	1.74	1.43	2.27
SEP	1.33	1.54	1.30	2.17	2.35
OCT	1.88	1.71	1.44	2.35	2.58
NOV	2.25	2.08	1.91	2.48	2.69
DEC	2.44	2.91	2.58	2.89	3.32
MAM	1.65	1.62	1.23	1.75	1.75
JJA	0.95	1.45	1.16	1.32	2.04
SON	1.79	1.73	1.49	2.29	2.47
DJF	2.32	2.79	2.60	2.70	3.06
ANN	1.59	1.79	1.52	1.92	2.19

Table C.19. RMSE for monthly mean surface-air temperatures for the SE domain.

	CRCM	ECP2	HRM3	MM5I	WRFG
JAN	0.99	0.98	0.97	0.98	0.97
FEB	0.99	0.98	0.96	0.98	0.97
MAR	0.99	0.97	0.96	0.98	0.97
APR	0.98	0.97	0.95	0.98	0.97
MAY	0.95	0.95	0.94	0.95	0.95
JUN	0.91	0.91	0.91	0.90	0.94
JUL	0.85	0.81	0.72	0.83	0.87
AUG	0.89	0.86	0.46	0.90	0.92
SEP	0.97	0.96	0.87	0.97	0.98
OCT	0.99	0.98	0.96	0.99	0.99
NOV	0.99	0.98	0.97	0.99	0.98
DEC	0.99	0.98	0.97	0.98	0.98
MAM	0.98	0.97	0.95	0.98	0.97
JJA	0.89	0.87	0.74	0.88	0.91
SON	0.99	0.98	0.96	0.99	0.99
DJF	0.99	0.98	0.97	0.98	0.97
ANN	0.99	0.98	0.95	0.98	0.98

Table C.20. Monthly mean surface-air temperature correlations between each RCM and NARR for the SE domain.

	CRCM	ECP2	HRM3	MM5I	WRFG
JAN	0.03	0.78	-0.06	0.51	0.20
FEB	0.03	0.82	0.07	0.59	0.41
MAR	0.30	0.92	0.21	0.74	0.33
APR	0.49	0.83	0.29	1.06	0.76
MAY	0.25	0.49	0.16	1.16	0.65
JUN	0.39	0.78	0.38	1.58	0.04
JUL	0.52	1.15	0.34	2.77	0.29
AUG	1.03	1.40	0.07	2.95	0.29
SEP	0.83	0.98	0.87	3.02	1.52
OCT	0.31	0.28	0.58	1.66	0.89
NOV	-0.11	0.26	0.25	0.47	0.28
DEC	-0.14	0.50	0.09	0.32	0.15
MAM	0.34	0.75	0.22	0.99	0.58
JJA	0.64	1.11	0.27	2.44	0.21
SON	0.34	0.51	0.57	1.72	0.90
DJF	-0.03	0.70	0.03	0.47	0.25
ANN	0.33	0.77	0.27	1.40	0.48

Table C.21. Daily accumulated precipitation bias for the SE domain.

	CRCM	ECP2	HRM3	MM5I	WRFG
JAN	0.50	0.95	0.74	1.18	0.97
FEB	0.57	1.01	0.75	1.40	1.13
MAR	0.52	1.03	0.76	1.28	0.92
APR	0.67	0.89	0.78	1.22	0.97
MAY	0.58	0.94	1.06	1.32	1.18
JUN	0.75	1.14	1.42	1.72	1.09
JUL	0.95	1.50	1.41	2.88	1.25
AUG	1.16	1.53	1.27	3.10	1.23
SEP	1.28	1.48	1.62	3.38	1.92
OCT	0.86	0.79	1.16	2.25	1.41
NOV	0.67	0.70	0.90	1.33	0.90
DEC	0.55	0.79	0.78	1.19	0.85
MAM	0.51	0.91	0.76	1.18	0.95
JJA	0.88	1.31	1.21	2.53	1.06
SON	0.89	0.91	1.15	2.26	1.33
DJF	0.51	0.85	0.65	1.24	0.96
ANN	0.53	0.90	0.75	1.69	1.01

Table C.22. MAE for daily accumulated precipitation for the SE domain.

	CRCM	ECP2	HRM3	MM5I	WRFG
JAN	0.64	1.12	1.16	1.41	0.56
FEB	0.72	1.17	1.19	1.71	0.68
MAR	0.66	0.80	1.01	1.30	0.77
APR	0.84	0.64	0.83	1.20	0.68
MAY	0.75	0.70	0.81	1.48	0.98
JUN	1.00	1.08	1.22	1.86	1.86
JUL	1.28	1.98	1.76	2.86	2.98
AUG	1.49	1.60	1.96	3.36	3.23
SEP	1.56	1.19	1.18	2.81	2.37
OCT	1.03	0.62	0.97	1.88	1.57
NOV	0.80	0.69	0.83	1.17	0.81
DEC	0.70	0.95	0.73	0.90	0.63
MAM	0.66	0.59	0.77	1.14	0.60
JJA	1.11	1.44	1.49	2.56	2.57
SON	1.02	0.69	0.86	1.77	1.38
DJF	0.64	1.05	0.94	1.29	0.51
ANN	0.68	0.81	0.79	1.53	1.11

Table C.23. RMSE for daily accumulated precipitation for the SE domain.

	CRCM	ECP2	HRM3	MM5I	WRFG
JAN	0.61	0.63	0.55	0.30	0.34
FEB	0.54	0.47	0.59	0.10	0.13
MAR	0.62	0.52	0.45	-0.05	0.11
APR	0.70	0.67	0.39	0.16	0.31
MAY	0.67	0.42	0.11	0.47	0.02
JUN	0.39	0.18	-0.43	0.07	-0.30
JUL	0.28	0.53	-0.07	0.04	-0.01
AUG	0.45	0.63	0.16	0.35	0.23
SEP	0.54	0.49	0.31	0.45	0.46
OCT	0.55	0.43	0.51	0.51	0.51
NOV	0.27	0.35	0.30	-0.15	0.06
DEC	0.61	0.57	0.54	0.10	0.35
MAM	0.69	0.49	0.30	0.11	0.03
JJA	0.38	0.45	-0.19	0.11	-0.08
SON	0.24	0.05	0.14	0.18	0.16
DJF	0.59	0.57	0.63	0.15	0.24
ANN	0.07	0.02	-0.06	-0.32	-0.31

Table C.24. Daily accumulated precipitation correlations between each RCM and NARR for the SE domain.

	CRCM	ECP2	HRM3	MM5I	WRFG
JAN	-0.76	1.82	5.55	1.50	2.49
FEB	-2.29	0.97	4.79	-0.06	2.40
MAR	-4.19	-0.41	2.71	-2.12	0.88
APR	-5.66	-2.01	0.85	-3.62	-1.65
MAY	-5.31	-2.15	0.07	-3.16	-2.45
JUN	-4.33	-2.39	1.09	-2.70	-2.78
JUL	-4.40	-2.35	2.24	-3.46	-3.16
AUG	-4.20	-1.56	2.42	-3.17	-2.89
SEP	-4.29	-0.84	2.35	-3.07	-2.64
OCT	-3.88	-0.04	2.43	-2.08	-1.87
NOV	-2.13	1.09	3.67	-0.26	0.28
DEC	-0.85	1.99	4.61	1.36	1.86
MAM	-5.05	-1.53	1.21	-2.97	-1.08
JJA	-4.31	-2.10	1.92	-3.11	-2.94
SON	-3.43	0.07	2.82	-1.81	-1.41
DJF	-1.30	1.59	4.99	0.93	2.25
ANN	-3.52	-0.49	2.73	-1.74	-0.80

Table C.25. Monthly mean surface-air temperature bias for the NW domain.

	CRCM	ECP2	HRM3	MM5I	WRFG
JAN	1.56	2.31	5.61	1.88	2.83
FEB	2.42	1.85	4.84	1.52	2.92
MAR	4.24	1.62	2.98	2.33	2.30
APR	5.70	2.30	1.64	3.75	2.24
MAY	5.37	2.43	1.21	3.34	2.60
JUN	4.48	2.74	1.71	2.99	2.93
JUL	4.67	2.83	2.64	3.74	3.36
AUG	4.45	2.29	2.71	3.44	3.11
SEP	4.41	1.66	2.46	3.28	2.81
OCT	3.94	1.39	2.49	2.34	2.07
NOV	2.27	1.85	3.74	0.99	1.20
DEC	1.65	2.49	4.71	1.73	2.25
MAM	5.09	1.87	1.78	3.13	2.07
JJA	4.52	2.56	2.30	3.38	3.12
SON	3.49	1.38	2.86	2.06	1.66
DJF	1.77	2.16	5.05	1.56	2.64
ANN	3.59	1.35	2.81	1.97	1.63

Table C.26. MAE for monthly mean surface-air temperatures for the NW domain.

	CRCM	ECP2	HRM3	MM5I	WRFG
JAN	1.96	2.70	6.31	2.34	3.42
FEB	2.98	2.23	5.61	1.91	3.76
MAR	4.68	2.06	3.70	2.81	2.91
APR	6.13	2.79	2.02	4.16	2.72
MAY	5.89	2.91	1.69	3.72	3.19
JUN	5.09	3.27	2.28	3.40	3.50
JUL	5.41	3.46	3.29	4.23	3.98
AUG	5.15	2.97	3.34	3.91	3.69
SEP	4.96	2.23	2.90	3.62	3.25
OCT	4.29	1.83	2.84	2.63	2.40
NOV	2.72	2.20	4.11	1.38	1.53
DEC	2.12	2.91	5.23	2.12	2.72
MAM	5.50	2.41	2.17	3.49	2.47
JJA	5.19	3.17	2.86	3.82	3.70
SON	3.88	1.80	3.20	2.35	2.05
DJF	2.25	2.56	5.70	1.96	3.26
ANN	4.00	1.80	3.22	2.30	1.96

Table C.27. RMSE for monthly mean surface-air temperatures for the NW domain.

	CRCM	ECP2	HRM3	MM5I	WRFG
JAN	0.95	0.95	0.90	0.96	0.93
FEB	0.93	0.93	0.84	0.93	0.83
MAR	0.86	0.87	0.78	0.90	0.73
APR	0.76	0.81	0.85	0.82	0.78
MAY	0.75	0.84	0.89	0.84	0.85
JUN	0.80	0.87	0.89	0.89	0.88
JUL	0.77	0.86	0.87	0.88	0.87
AUG	0.77	0.84	0.87	0.88	0.87
SEP	0.77	0.83	0.89	0.86	0.86
OCT	0.86	0.84	0.90	0.88	0.89
NOV	0.92	0.90	0.91	0.95	0.94
DEC	0.93	0.93	0.91	0.96	0.94
MAM	0.80	0.82	0.85	0.84	0.77
JJA	0.78	0.86	0.89	0.89	0.88
SON	0.87	0.85	0.90	0.90	0.90
DJF	0.94	0.94	0.89	0.95	0.91
ANN	0.85	0.85	0.86	0.89	0.85

Table C.28. Monthly mean surface-air temperature correlations between each RCM and NARR for the NW domain.

	CRCM	ECP2	HRM3	MM5I	WRFG
JAN	0.70	1.13	0.23	0.91	0.75
FEB	0.62	1.15	0.32	0.83	0.68
MAR	0.44	1.13	0.34	0.61	0.44
APR	0.49	1.22	0.24	0.55	0.42
MAY	0.84	0.81	-0.08	0.26	0.11
JUN	0.84	0.42	-0.47	0.11	-0.09
JUL	0.57	-0.12	-0.64	-0.12	-0.32
AUG	0.46	-0.36	-0.61	-0.20	-0.31
SEP	0.16	-0.20	-0.64	-0.44	-0.40
OCT	0.16	0.31	-0.42	-0.02	-0.01
NOV	0.49	0.81	-0.19	0.64	0.47
DEC	0.61	0.85	0.15	0.80	0.49
MAM	0.59	1.05	0.17	0.47	0.32
JJA	0.62	-0.02	-0.57	-0.07	-0.24
SON	0.27	0.31	-0.42	0.06	0.02
DJF	0.64	1.04	0.23	0.85	0.64
ANN	0.53	0.60	-0.15	0.33	0.18

Table C.29. Daily accumulated precipitation bias for the NW domain.

	CRCM	ECP2	HRM3	MM5I	WRFG
JAN	0.97	1.31	0.85	1.08	0.90
FEB	0.90	1.31	0.88	1.00	0.83
MAR	0.70	1.24	0.86	0.77	0.61
APR	0.63	1.26	0.75	0.65	0.56
MAY	0.92	0.89	0.61	0.52	0.45
JUN	0.90	0.68	0.66	0.49	0.48
JUL	0.75	0.65	0.72	0.47	0.54
AUG	0.64	0.57	0.69	0.39	0.43
SEP	0.37	0.45	0.69	0.52	0.48
OCT	0.45	0.52	0.69	0.48	0.54
NOV	0.88	1.07	0.84	0.91	0.76
DEC	0.88	1.07	0.79	0.96	0.70
MAM	0.72	1.10	0.68	0.59	0.49
JJA	0.74	0.55	0.66	0.40	0.45
SON	0.51	0.55	0.67	0.47	0.49
DJF	0.91	1.22	0.82	1.01	0.80
ANN	0.65	0.69	0.55	0.50	0.47

Table C.30. MAE for daily accumulated precipitation for the NW domain.

	CRCM	ECP2	HRM3	MM5I	WRFG
JAN	1.45	0.98	2.13	1.74	0.67
FEB	1.33	1.03	2.03	1.66	0.61
MAR	1.02	1.06	1.62	1.38	0.51
APR	0.85	1.14	1.55	1.25	0.48
MAY	1.07	1.02	1.34	0.91	0.48
JUN	1.14	1.02	1.31	0.89	0.52
JUL	0.99	1.11	0.95	0.79	0.48
AUG	0.85	1.07	0.62	0.71	0.45
SEP	0.50	0.60	0.69	0.46	0.23
OCT	0.76	0.60	1.23	0.93	0.36
NOV	1.39	0.98	2.13	1.76	0.57
DEC	1.33	0.85	1.90	1.63	0.58
MAM	0.90	0.95	1.43	1.11	0.41
JJA	0.96	1.00	0.92	0.75	0.44
SON	0.81	0.59	1.25	0.98	0.32
DJF	1.36	0.93	2.00	1.65	0.59
ANN	0.88	0.62	1.24	0.99	0.36

Table C.31. RMSE for daily accumulated precipitation for the NW domain.

	CRCM	ECP2	HRM3	MM5I	WRFG
JAN	0.86	0.85	0.77	0.87	0.89
FEB	0.86	0.85	0.75	0.88	0.89
MAR	0.84	0.83	0.66	0.86	0.87
APR	0.79	0.76	0.51	0.82	0.83
MAY	0.70	0.67	0.54	0.72	0.72
JUN	0.67	0.64	0.75	0.77	0.76
JUL	0.62	0.51	0.75	0.77	0.74
AUG	0.54	0.50	0.61	0.78	0.69
SEP	0.64	0.51	0.62	0.60	0.58
OCT	0.79	0.79	0.67	0.78	0.80
NOV	0.85	0.85	0.75	0.87	0.89
DEC	0.87	0.85	0.77	0.88	0.89
MAM	0.78	0.76	0.55	0.81	0.82
JJA	0.61	0.56	0.77	0.80	0.75
SON	0.81	0.81	0.70	0.82	0.84
DJF	0.86	0.85	0.77	0.88	0.89
ANN	0.79	0.80	0.68	0.82	0.83

Table C.32. Daily accumulated precipitation correlations between each RCM and NARR for the NW domain.

	CRCM	ECP2	HRM3	MM5I	WRFG
JAN	-2.10	-0.68	1.52	-0.99	-0.36
FEB	-2.84	-1.13	0.85	-1.57	-0.82
MAR	-3.51	-1.98	-0.22	-2.38	-1.97
APR	-3.59	-2.34	-0.96	-2.88	-2.80
MAY	-3.56	-2.78	-1.37	-3.04	-3.47
JUN	-3.41	-2.76	-1.17	-2.73	-3.56
JUL	-3.37	-2.17	-1.32	-2.40	-3.92
AUG	-3.26	-1.77	-0.87	-2.18	-4.07
SEP	-3.43	-1.69	-0.67	-2.82	-3.65
OCT	-3.31	-1.54	-0.20	-3.08	-3.10
NOV	-3.02	-1.07	0.90	-2.07	-1.54
DEC	-2.42	-0.88	1.45	-1.33	-0.67
MAM	-3.55	-2.37	-0.85	-2.76	-2.75
JJA	-3.34	-2.23	-1.12	-2.44	-3.85
SON	-3.25	-1.43	0.01	-2.66	-2.76
DJF	-2.45	-0.90	1.27	-1.29	-0.62
ANN	-3.15	-1.73	-0.17	-2.29	-2.49

Table C.33. Monthly mean surface-air temperature bias for the SW domain.

	CRCM	ECP2	HRM3	MM5I	WRFG
JAN	2.24	1.54	2.14	1.49	1.67
FEB	2.89	1.67	1.75	1.81	1.72
MAR	3.54	2.19	1.54	2.53	2.30
APR	3.66	2.51	1.79	3.01	2.94
MAY	3.70	2.93	1.95	3.17	3.55
JUN	3.66	3.04	1.91	2.91	3.67
JUL	3.62	2.60	1.93	2.63	4.02
AUG	3.46	2.26	1.78	2.50	4.20
SEP	3.54	2.03	1.63	2.99	3.77
OCT	3.35	1.88	1.62	3.20	3.21
NOV	3.07	1.66	1.93	2.26	1.91
DEC	2.52	1.64	2.25	1.74	1.67
MAM	3.61	2.51	1.69	2.89	2.90
JJA	3.57	2.59	1.83	2.64	3.95
SON	3.29	1.77	1.57	2.78	2.90
DJF	2.47	1.31	1.78	1.46	1.30
ANN	3.19	1.92	1.39	2.39	2.61

Table C.34. MAE for monthly mean surface-air temperatures for the SW domain.

	CRCM	ECP2	HRM3	MM5I	WRFG
JAN	2.75	1.86	2.77	2.04	2.03
FEB	3.45	2.03	2.32	2.42	2.09
MAR	4.26	2.74	2.00	3.22	2.75
APR	4.52	3.26	2.37	3.77	3.54
MAY	4.65	3.83	2.53	3.95	4.20
JUN	4.76	4.08	2.52	3.73	4.35
JUL	4.69	3.55	2.47	3.45	4.64
AUG	4.46	3.13	2.29	3.29	4.81
SEP	4.39	2.80	2.10	3.67	4.29
OCT	4.06	2.48	2.06	3.85	3.64
NOV	3.59	2.08	2.44	2.81	2.32
DEC	3.01	1.98	2.78	2.35	2.03
MAM	4.45	3.25	2.22	3.62	3.45
JJA	4.60	3.52	2.36	3.44	4.56
SON	3.95	2.35	2.00	3.37	3.32
DJF	2.78	1.54	2.22	1.81	1.58
ANN	3.84	2.48	1.79	2.95	3.02

Table C.35. RMSE for monthly mean surface-air temperatures for the SW domain.

	CRCM	ECP2	HRM3	MM5I	WRFG
JAN	0.96	0.97	0.96	0.96	0.97
FEB	0.94	0.96	0.93	0.94	0.94
MAR	0.87	0.90	0.90	0.88	0.90
APR	0.79	0.85	0.87	0.83	0.87
MAY	0.81	0.87	0.91	0.88	0.89
JUN	0.84	0.88	0.93	0.92	0.92
JUL	0.86	0.91	0.94	0.93	0.92
AUG	0.86	0.91	0.93	0.92	0.91
SEP	0.81	0.88	0.91	0.87	0.88
OCT	0.87	0.90	0.89	0.86	0.90
NOV	0.95	0.96	0.94	0.94	0.96
DEC	0.97	0.98	0.96	0.96	0.97
MAM	0.79	0.86	0.88	0.84	0.87
JJA	0.85	0.90	0.94	0.93	0.92
SON	0.87	0.90	0.89	0.88	0.91
DJF	0.97	0.98	0.96	0.97	0.97
ANN	0.83	0.88	0.88	0.87	0.89

Table C.36. Monthly mean surface-air temperature correlations between each RCM and NARR for the SW domain.

	CRCM	ECP2	HRM3	MM5I	WRFG
JAN	0.51	0.50	0.49	0.23	0.30
FEB	0.48	0.46	0.42	0.22	0.22
MAR	0.52	0.47	0.33	0.28	0.23
APR	0.49	0.25	0.42	0.05	0.11
MAY	0.59	0.07	0.11	-0.10	0.04
JUN	0.54	-0.36	-0.10	-0.12	-0.09
JUL	0.47	-0.45	-0.16	-0.55	-0.18
AUG	0.45	-0.60	-0.40	-0.57	-0.05
SEP	0.40	-0.33	-0.08	-0.42	-0.30
OCT	0.15	-0.02	-0.01	-0.14	-0.11
NOV	0.22	0.18	0.05	0.08	0.16
DEC	0.30	0.30	0.28	0.07	0.22
MAM	0.53	0.26	0.28	0.08	0.13
JJA	0.49	-0.47	-0.22	-0.41	-0.11
SON	0.26	-0.06	-0.01	-0.16	-0.09
DJF	0.43	0.42	0.40	0.17	0.25
ANN	0.43	0.04	0.11	-0.08	0.05

Table C.37. Daily accumulated precipitation bias for the SW domain.

	CRCM	ECP2	HRM3	MM5I	WRFG
JAN	0.58	0.56	0.71	0.36	0.42
FEB	0.57	0.56	0.64	0.44	0.43
MAR	0.59	0.52	0.57	0.38	0.37
APR	0.51	0.34	0.51	0.24	0.29
MAY	0.69	0.39	0.58	0.32	0.42
JUN	0.67	0.53	0.61	0.40	0.48
JUL	0.70	0.68	0.63	0.69	0.63
AUG	0.70	0.72	0.75	0.76	0.73
SEP	0.67	0.51	0.57	0.62	0.64
OCT	0.40	0.35	0.49	0.33	0.44
NOV	0.36	0.29	0.37	0.30	0.33
DEC	0.44	0.42	0.48	0.33	0.35
MAM	0.57	0.36	0.46	0.26	0.32
JJA	0.66	0.61	0.63	0.56	0.55
SON	0.44	0.28	0.44	0.33	0.40
DJF	0.52	0.49	0.59	0.35	0.38
ANN	0.49	0.27	0.39	0.28	0.33

Table C.38. MAE for daily accumulated precipitation for the SW domain.

	CRCM	ECP2	HRM3	MM5I	WRFG
JAN	0.74	0.40	0.99	1.00	0.31
FEB	0.76	0.47	1.07	1.03	0.30
MAR	0.70	0.43	0.86	0.82	0.30
APR	0.61	0.45	0.71	0.71	0.28
MAY	0.89	0.76	0.74	0.60	0.41
JUN	1.02	1.26	0.72	0.64	0.47
JUL	1.23	1.55	0.98	0.90	0.75
AUG	1.12	1.66	0.92	0.87	0.86
SEP	1.04	1.10	0.82	0.70	0.46
OCT	0.57	0.42	0.72	0.62	0.38
NOV	0.47	0.32	0.60	0.62	0.27
DEC	0.55	0.41	0.68	0.73	0.31
MAM	0.67	0.47	0.66	0.62	0.26
JJA	1.06	1.41	0.81	0.73	0.60
SON	0.61	0.51	0.61	0.51	0.27
DJF	0.67	0.38	0.85	0.88	0.25
ANN	0.63	0.58	0.56	0.52	0.27

Table C.39. RMSE for daily accumulated precipitation for the SW domain.

	CRCM	ECP2	HRM3	MM5I	WRFG
JAN	0.71	0.76	0.55	0.78	0.76
FEB	0.74	0.75	0.73	0.74	0.76
MAR	0.83	0.86	0.69	0.86	0.87
APR	0.89	0.90	0.71	0.91	0.86
MAY	0.87	0.87	0.79	0.94	0.91
JUN	0.81	0.82	0.72	0.87	0.88
JUL	0.76	0.64	0.66	0.65	0.69
AUG	0.80	0.69	0.66	0.68	0.62
SEP	0.69	0.76	0.70	0.70	0.62
OCT	0.79	0.79	0.67	0.79	0.73
NOV	0.81	0.86	0.72	0.79	0.79
DEC	0.66	0.76	0.66	0.66	0.75
MAM	0.89	0.89	0.77	0.93	0.91
JJA	0.77	0.73	0.67	0.77	0.74
SON	0.74	0.84	0.70	0.79	0.73
DJF	0.70	0.76	0.68	0.74	0.77
ANN	0.79	0.83	0.75	0.84	0.79

Table C.40. Daily accumulated precipitation correlations between each RCM and NARR for the SW domain.

	CRCM	ECP2	HRM3	MM5I	WRFG
JAN	-1.20	0.03	5.87	0.36	-0.74
FEB	-1.42	0.15	5.93	-0.13	1.79
MAR	-1.66	0.12	4.45	-1.13	2.86
APR	-1.85	-0.07	1.75	-2.45	1.53
MAY	-1.53	-0.76	0.01	-1.73	0.24
JUN	-0.45	-0.88	-0.72	-1.73	-0.70
JUL	-0.57	-0.89	0.06	-2.19	-0.96
AUG	-0.84	-0.57	0.72	-2.37	-0.91
SEP	-1.34	-0.21	0.90	-2.90	-1.13
OCT	-1.94	0.24	0.75	-2.13	-1.47
NOV	-1.74	0.15	1.78	-1.58	-1.14
DEC	-1.30	-0.03	3.00	-0.72	-1.85
MAM	-1.68	-0.24	2.07	-1.77	1.54
JJA	-0.62	-0.78	0.02	-2.09	-0.86
SON	-1.67	0.06	1.14	-2.20	-1.25
DJF	-1.31	0.05	4.93	-0.16	-0.27
ANN	-1.32	-0.23	2.04	-1.56	-0.21

Table C.41. Monthly mean surface-air temperature bias for the GLR domain.

	CRCM	ECP2	HRM3	MM5I	WRFG
JAN	1.78	1.23	5.98	1.29	2.72
FEB	1.81	1.05	5.95	1.24	2.60
MAR	2.08	1.01	4.51	1.86	3.09
APR	2.63	1.24	2.05	3.26	1.87
MAY	2.61	1.93	1.50	2.82	1.23
JUN	1.54	1.82	1.71	2.57	1.63
JUL	1.56	1.63	1.78	2.80	1.70
AUG	1.45	1.15	2.05	2.69	1.58
SEP	1.68	0.89	1.51	3.03	1.40
OCT	2.09	0.85	1.17	2.24	1.56
NOV	1.84	1.23	2.07	1.71	1.57
DEC	1.75	1.52	3.37	1.50	3.11
MAM	2.40	1.21	2.29	2.61	1.84
JJA	1.47	1.48	1.72	2.68	1.60
SON	1.78	0.81	1.38	2.25	1.31
DJF	1.65	1.12	5.00	1.15	2.39
ANN	1.53	0.64	2.08	1.78	0.94

Table C.42. MAE for monthly mean surface-air temperatures for the GLR domain.

	CRCM	ECP2	HRM3	MM5I	WRFG
JAN	2.43	1.95	6.39	1.86	3.99
FEB	2.08	1.36	6.23	1.71	3.27
MAR	2.28	1.33	4.76	2.05	3.43
APR	2.87	1.82	2.56	3.46	2.48
MAY	3.08	2.49	2.33	3.09	2.23
JUN	2.44	2.52	2.50	2.91	2.30
JUL	2.22	2.22	2.38	3.03	2.19
AUG	1.84	1.51	2.51	2.91	1.92
SEP	2.00	1.09	1.92	3.25	1.64
OCT	2.25	1.08	1.50	2.45	1.75
NOV	2.20	1.72	2.46	2.08	2.26
DEC	2.46	2.24	3.92	1.97	4.19
MAM	2.53	1.66	2.63	2.74	2.24
JJA	2.07	2.01	2.25	2.88	2.04
SON	2.01	1.05	1.80	2.45	1.55
DJF	2.17	1.63	5.41	1.54	3.41
ANN	1.73	0.80	2.41	1.95	1.18

Table C.43. RMSE for monthly mean surface-air temperatures for the GLR domain.

	CRCM	ECP2	HRM3	MM5I	WRFG
JAN	0.93	0.93	0.88	0.94	0.73
FEB	0.95	0.96	0.90	0.94	0.84
MAR	0.93	0.96	0.92	0.92	0.90
APR	0.83	0.89	0.88	0.80	0.87
MAY	0.77	0.83	0.83	0.79	0.85
JUN	0.84	0.86	0.84	0.86	0.87
JUL	0.83	0.86	0.83	0.85	0.86
AUG	0.85	0.87	0.84	0.80	0.83
SEP	0.92	0.92	0.88	0.85	0.90
OCT	0.93	0.94	0.91	0.92	0.94
NOV	0.93	0.88	0.88	0.93	0.85
DEC	0.91	0.89	0.86	0.92	0.68
MAM	0.86	0.90	0.90	0.84	0.90
JJA	0.84	0.87	0.84	0.84	0.86
SON	0.95	0.94	0.90	0.94	0.95
DJF	0.95	0.94	0.88	0.95	0.75
ANN	0.95	0.97	0.92	0.93	0.94

Table C.44. Monthly mean surface-air temperature correlations between each RCM and NARR for the GLR domain.

	CRCM	ECP2	HRM3	MM5I	WRFG
JAN	0.49	1.24	0.53	0.89	0.21
FEB	0.51	1.30	0.66	0.73	0.42
MAR	0.53	1.60	0.85	0.84	0.48
APR	0.59	1.49	0.58	1.12	0.52
MAY	0.73	0.73	0.98	0.60	0.43
JUN	0.50	1.19	0.50	0.08	0.64
JUL	0.37	0.74	0.10	-0.01	-0.10
AUG	0.13	-0.12	-0.43	-0.52	-0.50
SEP	-0.19	-0.50	-0.71	-0.88	-0.60
OCT	-0.02	0.13	-0.42	-0.61	-0.45
NOV	0.25	0.78	-0.05	0.10	0.01
DEC	0.38	0.98	0.20	0.46	-0.04
MAM	0.62	1.27	0.81	0.85	0.48
JJA	0.33	0.60	0.06	-0.15	0.01
SON	0.01	0.14	-0.39	-0.46	-0.35
DJF	0.46	1.18	0.46	0.70	0.20
ANN	0.36	0.80	0.23	0.23	0.08

Table C.45. Daily accumulated precipitation bias for the GLR domain.

	CRCM	ECP2	HRM3	MM5I	WRFG
JAN	0.54	1.25	0.72	0.91	0.40
FEB	0.52	1.30	0.72	0.75	0.47
MAR	0.55	1.60	0.93	0.86	0.55
APR	0.60	1.49	0.75	1.12	0.60
MAY	0.75	0.75	1.05	0.64	0.54
JUN	0.65	1.22	0.82	0.39	0.86
JUL	0.70	1.00	0.85	0.55	0.67
AUG	0.67	0.68	0.81	0.65	0.74
SEP	0.54	0.73	0.87	0.94	0.75
OCT	0.32	0.42	0.60	0.66	0.56
NOV	0.41	0.79	0.57	0.51	0.42
DEC	0.46	0.98	0.55	0.63	0.41
MAM	0.63	1.27	0.86	0.86	0.55
JJA	0.64	0.81	0.71	0.47	0.61
SON	0.34	0.46	0.61	0.55	0.49
DJF	0.49	1.18	0.63	0.74	0.37
ANN	0.39	0.80	0.50	0.40	0.36

Table C.46. MAE for daily accumulated precipitation for the GLR domain.

	CRCM	ECP2	HRM3	MM5I	WRFG
JAN	0.66	1.35	0.93	1.08	0.53
FEB	0.63	1.38	0.91	0.93	0.65
MAR	0.66	1.68	1.10	1.04	0.69
APR	0.71	1.55	0.94	1.26	0.72
MAY	0.88	0.88	1.33	0.79	0.72
JUN	0.80	1.41	1.03	0.53	1.03
JUL	0.86	1.21	1.08	0.72	0.88
AUG	0.81	0.87	1.02	0.78	0.95
SEP	0.63	0.88	1.02	1.06	0.91
OCT	0.42	0.54	0.70	0.76	0.66
NOV	0.54	0.94	0.71	0.62	0.55
DEC	0.62	1.10	0.75	0.79	0.51
MAM	0.72	1.32	1.07	0.97	0.65
JJA	0.77	0.98	0.92	0.59	0.77
SON	0.44	0.57	0.72	0.66	0.59
DJF	0.62	1.26	0.83	0.91	0.51
ANN	0.52	0.92	0.68	0.50	0.47

Table C.47. RMSE for daily accumulated precipitation for the GLR domain.

	CRCM	ECP2	HRM3	MM5I	WRFG
JAN	0.74	0.67	0.45	0.57	0.65
FEB	0.81	0.75	0.63	0.54	0.65
MAR	0.78	0.68	0.48	0.46	0.61
APR	0.83	0.81	0.43	0.67	0.71
MAY	0.76	0.76	0.37	0.73	0.64
JUN	0.63	0.62	0.41	0.75	0.32
JUL	0.43	0.33	0.15	0.48	0.26
AUG	0.14	0.15	0.11	0.40	0.09
SEP	0.19	0.22	0.18	0.13	0.11
OCT	0.31	0.41	0.34	0.40	0.37
NOV	0.60	0.61	0.42	0.41	0.51
DEC	0.69	0.68	0.43	0.47	0.66
MAM	0.82	0.83	0.48	0.69	0.71
JJA	0.42	0.43	0.25	0.62	0.25
SON	0.30	0.36	0.36	0.32	0.39
DJF	0.75	0.71	0.51	0.53	0.66
ANN	0.60	0.53	0.43	0.45	0.49

Table C.48. Daily accumulated precipitation correlations between each RCM and NARR for the GLR domain.

REFERENCES

References

- Andresen, J. A., G. Alagarswamy, C. A. Rotz, J. T. Ritchie, and A. W. LeBaron, 2001: Weather Impacts on Maize, Soybean, and Alfalfa Production in the Great Lakes Region, 1895-1996. *Agron. J.*, **93**, 1059-1070.
- Bukovsky, Melissa S., David J. Karoly, 2007: A Brief Evaluation of Precipitation from the North American Regional Reanalysis. *J. Hydrometeor*, **8**, 837–846
- Caldwell, P., 2010: California Wintertime Precipitation Bias in Regional and Global Climate Models. *J. of Applied Meteorology and Climatology*, **49**, 2147-2158.
- Caya, D. and R. Laprise, 1999: A semi-implicit semi-langragian regional climate model: the Canadian RCM. *Mon. Wea. Rev*, **127**, 341-362.
- Climate Change Science Program (CCSP), 2008: Climate Models: An Assessment of Strengths and Limitations. A Report by the U.S. Climate Change Science Program and the Subcommittee on Global Change Research [Bader D.C., C. Covey, W.J. Gutowski Jr., I.M. Held, K.E. Kunkel, R.L. Miller, R.T. Tokmakian and M.H. Zhang (Authors)]. Department of Energy, Office of Biological and Environmental Research, Washington, D.C., USA, 124 pp.
- Côté, J. J-G Desmarais, S. Gravel, A. Méthot, A. Patoine, M Rochest and A. Staniforth, 1998: The operational CMC-MRB global environmental multiscale (GEM) model. Part I: design considerations and formulation. *Mon. Wea. Rev*, 126, 1371-1395.
- Déqué, M. and S. Somot, 2007: Variable resolution versus limited area modelling: perfect model approach. *Research Activities in Atmospheric and Oceanic Modelling*, **37**, 3.03–3.04.
- Doms, G., U. Schaettler, 1999: The Nonhydrostatic Limited-Area Model LM (Lokal Modell) of DVD. Part 1: Scientific Documentation. [Available from www.cosmomodel.org].
- Dudhia, J., 1993: A nonhydrostatic version of the Penn State NCAR mesoscale model: Validation tests and simulation of an atlantic cyclone and cold front. *Mon. Wea. Rev*, **121**, 1493-1513.
- Feng, J. and C. Fu, 2006: Inter-Comparison of 10-year Precipitation Simulated by Several RCMs for Asia. *Advances in Atmospheric Sciences*, **23**, 531-542.
- Gibson, J. K., P. Kallberg, S. Uppala, A. Hernandez, A. Nomura, and E. Serrano, 1997: *ERA Description*. ECMWF Reanalysis Project Report Series, Vol. 1, ECMWF, 72 pp.
- Grell, G.A., J. Dudhia, and D. R. Stauffer, 1994: A Description of the Fifth-Generation Penn State/NCAR Mesoscale Model (MM5). *NCAR Technical Note*, **TN-398** + **STR**, 1-128.

- Gutowski, William J., R. W. Arritt, S. Kawazoe, D. M. Flory, E. S. Takle, S. Biner, D. Caya, R. G. Jones, R. Laprise, L. R. Leung, L. O. Mearns, W. Moufouma-Okia, A. M. B. Nunes, Y. Qian, J. O. Roads, L. C. Sloan and M. A. Snyder, 2010: Regional extreme monthly precipitation simulated by narccap rcms. *J. Hydrometeor*, **11**, 1373–1379.
- Huffman, G. J., and Coauthors, 1997: The Global Precipitation Climatology Project (GPCP) combined precipitation dataset. *Bull. Amer. Meteor. Soc.*, **78**, 5–20.
- Jacob, D., 2001: A note to the simulation of the annual and inter-annual variability of the water budget over the Baltic Sea drainage basin. *Meteor. Atmos. Phys*, **77**, 61-73.
- Jacob, D., L. Bärring, O. Bøssing Christensen, J. Hesselbjerg Christensen, M. de Castro, M. Déqué, F. Giorgi, S. Hagemann, M. Hirschi, R. Jones, E. Kjellström, G. Lenderink, B. Rockel, E. Sánchez, C. Schär, S. I. Seneviratne, S. Somot, A. van Ulden, and B. van den Hurk, 2007: An inter-comparison of regional climate models for Europe: model performance in present-day climate. *Climatic Change*, 81, 31-52.
- Jones, C.G., U. Will'en, A. Ullerstig, and U. Hansson, 2004: The Rossby Centre regional atmospheric climate model part I: model climatology and performance for the present climate over Europe. *Ambio*, **33**, 199–210.
- Juang, H-M., and M. Kanamitsu, 1994: The NMC nested regional spectral model. *Mon. Wea. Rev.*, **122**, 3–26
- Kalnay, E., and Coauthors, 1996: The NCEP/NCAR 40-Year Reanalysis Project. *Bull. Amer. Meteor. Soc.*, **77**, 437–471.
- Kanamitsu, M., 2000: Latest GSM/RSM system. Preprints, Second Int. RSM Workshop, Maui, HI, MHPCC
- Kanamitsu, M., W. Ebisuzaki, J. Woollen, S-K. Yang, J. Hnilo, M. Fiorino, and J. Potter, 2002: NCEP–DOE AMIP-II reanalysis (R-2). *Bull. Amer. Meteor. Soc.*, **83**, 1631–1643.
- Karl, T.R., C.N. Williams, Jr., F.T. Quinlan, and T.A. Boden, 1990: United States Historical Climatology Network (HCN) Serial Temperature and Precipitation Data, Environmental Science Division, Publication No. 3404, Carbon Dioxide Information and Analysis Center, Oak Ridge National Laboratory, Oak Ridge, TN, 389 pp.
- Karl, T. R, J. M. Melillo, and T. C. Peterson, 2009: Global Climate Change Impacts in the United States. U.S. Global Change Research Program Report, 196 pp.
- Kim, J., H. Jung, C. R. Mechoso and H. Kang, 2008: Validation of a multidecadal RCM hindcast over East Asia. *Global and Planetary Change*, **61**, 225-241.

- Kjellström, E., L. Bärring, S. Gollvik, U. Hansson, C. Jones, P. Samuelsson, M. Rummukainen, A. Ullerstig, U. Willén, and K. Wyser, 2005: *A140-year simulation of European climate with the new version of theRossby Centre regional atmospheric climate model (RCA3)*. Reports Meteorology and Climatology, **108**, 54.
- Kostopoulou, E., K. Tolika, I. Tegoulias, C. Giannakopoulos, S. Somot, C. Anagnostropoulou, and P. Maheras, 2009: Evaluation of a regional climate model using in situ temperature observations over the Balkan Peninsula. *Tellus*, **61A**, 357-370.
- Kotroni, V., S. Lykoudis, K. Lagouvardos, and D. Lalas, 2008: A fine resolution regional climate change experiment for the Eastern Mediterranean: Analysis of the present climate simulations. *Global and Planetary Change*, 64, **93**-104.
- Leung, L. R., Y. Qian, J. Han and J. O. Roads, 2003: Intercomparison of Global Reanalyses and Regional Simulations of Cold Season Water Budgets in the Western United States. *J. Hydrometeor*, **4**, 1067-1087.
- Leung, L. R., Y. Qian and X. Bian, 2003: Hydroclimate of the Western United States Based on Observations and Regional Climate Simulations of 1981-2000. Part I: Seasonal Statistics. *J. Climatol*, **16**, 1892-1911.
- Li, X. S. Zhong, X. Bian, and W. Heilman. 2010: Hydroclimate variability in the Great Lakes region as derived from the North American Regional Reanalysis. *J. Geophys. Res.* (In press)
- Ma, Y., S. Chen, F. Hua, H. Wei and D. H. Bromwich, 2008: Evaluation of a regional climate model for atmospheric simulation over Arctic river basins. *Chin. J. Oceanol. Limnol*, **26**, 425-433.
- Mailhot, A., I. Beauregard, G. Talbot, D. Caya, and S. Biner, 2011: Future changes in intense precipitation over Canada assessed from multi-model NARCCAP ensemble simulations. *Int. J. Climatol.*
- Markovic, M., C. G. Jones, K. Winger, and D. Paquin, 2009: The surface radiation budget over North America: gridded data assessment and evaluation of regional climate models. *Int. J. Climatol*, **29**, 2226-2240.
- Maurer, E. P., A. W. Wood, J. C. Adam, D. P. Lettenmaier, and B. Nijssen, 2002: A long-term hydrologically based dataset of land surface fluxes and states for the conterminous United States. *J. Climate*, **15**, 3237–3251.
- McCarthy, J.J., O. F. Canziani, N. A. Leary, D. J. Dokken, and K. S. White (eds), 2001: *Climate Change 2001: Impacts, Adaptation, and Vulnerability*. Cambridge University Press.

- McGuire, A.D., J.E. Walsh, J.S. Kimball, J.S. Clein, S.E. Euskirchen, S. Drobot, U.C. Herzfeld, J. Maslanik, R.B. Lammers, M.A. Rawlins, C.J. Vorosmarty, T.S. Rupp, W. Wu, and M. Calef, 2008: The Western Arctic Linkage Experiment (WALE): Overview and Synthesis. *Earth Interactions*, **12**, 1–13.
- Mearns, L.O., et al., 2007, updated 2011. *The North American Regional Climate Change Assessment Program dataset*, National Center for Atmospheric Research Earth System Grid data portal, Boulder, CO. Data downloaded 2012-01-02. [http://www.earthsystemgrid.org/project/NARCCAP.html]
- Mearns, L. O., W. J. Gutowski, R. Jones, L.-Y. Leung, S. McGinnis, A. M. B. Nunes, and Y. Qian: A regional climate change assessment program for North America. *EOS*, Vol. 90, No. 36, 8 September 2009, pp. 311-312.
- Mesinger, F., G. DiMego, E. Kalnay, K. Mitchell, P. C. Shafran, W. Ebisuzaki, D. Jović, J. Woollen, E. Rogers, E. H. Berbery, M. B. Ek, Y. Fan, Ro. Grumbine. W. Higgins, H. Li, Y. Lin, G. Manikin, D. Parrish and W. Shi, 2006: North American Regional Reanalysis. *Bull Amer. Met. Soc.*, **87**, 343-360.
- Music, B., and D. Caya, 2007: Evaluation of the Hydrological Cycle over the Mississippi River Basin as Simulated by the Canadian Regional Climate Model (CRCM). *J. Hydrometeor*, **8**, 969–988.
- National Center for Atmospheric Research (NCAR), cited 2009: North American Regional Climate Change Assessment Program (NARCCAP). [Available online at http://www.narccap.ucar.edu/index.html]
- National Assessment Synthesis Team (NAST), 2001: Climate Change Impacts on the United States: The Potential Consequences of Climate Variability and Change. Report for the U.S. Global Change Research Program. Cambridge University Press, 620 pp.
- Radu, R., M. Déqué, and S. Somot, 2008: Spectral nudging in a spectral regional climate model. *Tellus*, **60A**, 885–897.
- Rivington, M., D. Miller, K. B. Matthews, G. Russell, G. Bellocchi, and K. Buchan, 2008: Evaluating regional climate model estimates against site-specific observed data in the UK. *Climatic Change*, **88**, 157-185.
- Sain, S. R., J. A. Hoeting, E. M. Schliep, 2010: A comparison study of extreme precipitation from six difference regional climate models via spatial hierarchical modeling. *Extremes*, **13**, 219-239.
- Southworth, J., J. C. Randolph, M. Habeck, O.C. Doering, R. A. Pfeifer, D. G. Rao, and J. J. Johnston, 2000: Consequences of future climate change and changing climate variability on maize yields in the Midwestern United States. *Agriculture, Ecosystems and Environment*, **82**, 139-158.

- Southworth, J., R. A. Pfeifer, M. Habeck, J. C. Randolph, O. C. Doering, J. J. Johnston, and D. G. Rao, 2002: Changes in Soybean Yields in the Midwestern United States as a Result of Future Changes in Climate, Climate Variability, and CO2 Fertilization. *Climatic Change*, **53**, 447-475.
- U.S. Department of Agriculture-National Agricultural Statistics Service, 1997: Census of Agriculture. [Available online at http://www.usda.gov/nass/]
- University Corporation for Atmospheric Research, cited 2012: Understanding Climate Change Multimedia Gallery. [Available online at http://www2.ucar.edu/news/understanding-climate-change-multimedia-gallery]
- Walter, A., K. Keuler, D. Jacob, R. Knoche, A. Block, S. Kotlarski, G. Müller-Westermeier, D. Rechid and W. Ahrens, 2006: A high resolution reference data set of German wind velocity 1951-2001 and comparison with regional climate model results. *Meteorologische Zeitschrift*, **15**, 585-596.
- Wang, S., R. R. Gillies, E. S. Takle, and W. J. Gutowski, 2009: Evaluation of precipitation in the Intermountain Region as simulated by the NARCCAP regional climate models. *Geophysical Research Letters*, **36**, 1-6.
- Watson, T. T., Zinyowera, M. C. and Moss, R. H. (eds), 1998: *The Regional Impacts of Climate Change*. Cambridge University Press.
- West, G. L., Steenburgh, J. W., Cheng, Y. Y., 2007. Spurious Grid-Scale Precipitation in the North American Regional Reanalysis. Monthly Weather Review, 135, 2168–2184. doi: 10.1175/MWR3375.1
- Winkler, J. A., J. A. Andresen, G. Guentchev, and R. D. Kriegel, 2002: Possible Impacts of Projected Temperature Change on Commercial Fruit Production in the Great Lakes Region. *J. Great Lakes Res*, **28**, 608-625.
- Wuebbles, D. J., and K. Hayhoe, 2004: Climate Change Projections for the United States Midwest. *Mitigation and Adaptation Strategies for Global Change*, **9**, 335-363.
- Wu, W., A. H. Lynch, S. Drobot, J. Maslanik, A. D. McGuire, and U. Herfeld, 2007: Comparative Analysis of the Western Arctic Surface Climate among Observations and Model Simulations. *Earth Interactions*, **11**, 1-24.
- Zhang, Y. C., W. B. Rossow, A. A. Lacis, V. Oinas, and M. I. Mishchenko, 2004: Calculation of radiative fluxes from the surface top of the atmosphere based on the ISCCP and other global data sets: Refinements of the radiative transfer model and the input data. *Journal of Geophysical Research*, **109**, D19105.